

I. CENOZOIC GEOLOGY OF IRAN: AN INTEGRATED STUDY OF  
EXTENSIONAL TECTONICS AND RELATED VOLCANISM

II. EDIACARAN STRATIGRAPHY OF THE NORTH AMERICAN  
CORDILLERA: NEW OBSERVATIONS FROM EASTERN CALIFORNIA AND  
NORTHERN UTAH

Thesis by  
Charles Verdel

In Partial Fulfillment of the Requirements

For the Degree of  
Doctor of Philosophy

California Institute of Technology

Pasadena, California

2009

(Defended August 27, 2008)

© 2009

Charles Verdel

All Rights Reserved

## ACKNOWLEDGEMENTS

Because of difficulties that arose in obtaining Iranian visas, my graduate student career has been spent working on a number of projects that are only loosely related. Although not the original plan, in the end I think I have become a better geologist for being exposed to a wide variety of topics. I would like to thank Brian Wernicke for his assistance in formulating the two major projects that comprise this thesis, and for the helpful discussions that we have had over the last six years. None of our work in Iran would have been possible without the efforts of Jamshid Hassanzadeh, and I would like to thank him for all of his contributions to the first half of this thesis. Discussions with Bernard Guest, Jahandar Ramezani, and Jean-Philippe Avouac on the subject of Iranian tectonics have been invaluable. John Eiler allowed me to measure O isotopes in his lab during my first year at Caltech, and ever since then he has been the source of useful (and entertaining) advice. Joe Kirschvink and Ken Farley graciously provided access to their labs. Lindsey Hedges invested a great deal of her time to help me obtain results from the He lab. Ryan Petterson's input was instrumental to the work I did in the Panamint Range, and he has always been a great person to go into the field with. I have benefited greatly from discussions about Neoproterozoic stratigraphy with Ryan, David Fike and John Grotzinger. Finally, I would like to thank my parents for their never-ending support.

## ABSTRACT

**I.**

The late Oligocene to Miocene collision of Arabia and Eurasia was preceded by ~175 My of subduction of Neotethyan oceanic crust. Associated magmatic activity includes late Triassic(?) to Jurassic plutons in the Sanandaj-Sirjan zone of southern Iran, limited Cretaceous magmatism in the Alborz Mountains of northern Iran, and widespread Eocene volcanism across central Iran. Metamorphic core complexes of Eocene age have recently been recognized in widely separated parts of Iran, suggesting that Tertiary volcanism was related to extension. Geochemical data indicate that Eocene volcanism was typical of continental arcs and was followed by less voluminous Oligocene basaltic volcanism of the type often associated with back-arc basins. This set of observations suggests that mid-Mesozoic plutons in southern Iran are the remnants of an original volcanic arc that was only weakly developed because of slow subduction rate. Magmatic activity largely ceased in southern and central Iran during the Cretaceous and shifted to the north, suggesting a period of flat slab subduction. Subsequent slab-rollback during the Eocene extended the overriding plate, forming metamorphic core complexes and inducing pressure-release melting of partially hydrated lithospheric mantle and upwelling of asthenosphere.

**II.**

The Ediacaran Period spans from the base of cap carbonates overlying glacial deposits of the Marinoan “Snowball Earth” event to the Precambrian-Cambrian boundary, ~635 to 542 Ma. Sediments deposited during the rifting of southwest Laurentia, which are now

exposed in a relatively narrow belt in the western US, are one of the best records on earth of the geological, geochemical, and geobiological events that occurred during this period. Evidence for one of the most significant of these, the final oxygenation of the oceans, is found within the upper Johnnie Formation in the southern Great Basin. C isotope data from thick, basinal facies of the Johnnie Fm. in the Panamint Range provide a more complete record of ocean chemistry associated with this event than previously determined from thinner, platformal facies. Strata in northern Utah of roughly the same age include a rift-related basalt, providing some of the youngest geologic evidence for the rifting of western Laurentia.

## TABLE OF CONTENTS

Acknowledgements.....	iii
Abstract.....	iv
Table of Contents.....	vi
List of Figures and Tables.....	ix
<b>Chapter 1:</b> Introduction.....	I-1
<b>PART I: CENOZOIC GEOLOGY OF IRAN: AN INTEGRATED STUDY OF EXTENSIONAL TECTONICS AND RELATED VOLCANISM</b>	
<b>Chapter 2:</b> Geology and thermochronology of Tertiary Cordilleran-style metamorphic core complexes in the Saghand region of central Iran.....	II-1
Abstract.....	II-1
Introduction.....	II-3
Tectonic setting.....	II-4
Geology of the Saghand region.....	II-6
Stratified rocks.....	II-7
Crystalline rocks.....	II-8
Structural and stratigraphic observations of the Neybaz-Chatak detachment system.....	II-10
Neybaz-Chatak detachment fault and hanging-wall splays.....	II-10
Mylonites.....	II-12
Supradetachment and postextensional basinal deposits and structures..	II-13
Geochronology and thermochronology.....	II-15
U-Pb geochronology.....	II-15
<sup>40</sup> Ar/ <sup>39</sup> Ar geochronology.....	II-16
(U-Th)/He thermochronology.....	II-17
Western domain.....	II-18
Eastern domain.....	II-19
Discussion and conclusions.....	II-20
Timing of extension.....	II-22
Kinematics of extension.....	II-23
Cretaceous and Miocene (U-Th)/He cooling ages.....	II-26
Regional significance.....	II-28
Acknowledgements.....	II-29
References.....	II-30
<b>Chapter 3:</b> Geochronology and geochemistry of Iranian Paleogene volcanism: an extensional arc flare-up.....	III-1
Abstract.....	III-1
Introduction.....	III-2
Regional geology.....	III-5
Arc stratigraphy.....	III-7
Geochronology.....	III-9
Urumieh-Dokhtar U-Pb and <sup>40</sup> Ar/ <sup>39</sup> Ar geochronology.....	III-9

Karaj Formation U-Pb geochronology.....	III-10
Additional U-Pb and $^{40}\text{Ar}/^{39}\text{Ar}$ geochronology and a composite stratigraphic section.....	III-10
Geochemistry.....	III-13
Previous work.....	III-13
Major and trace element data.....	III-14
Iranian shoshonites.....	III-21
Discussion.....	III-25
Mechanism for the Iranian Tertiary flare-up.....	III-26
Changes in subduction rate.....	III-27
Changes in subduction angle.....	III-28
Slab melting.....	III-29
Rifting/back-arc basin development.....	III-30
Conceptual model for the Eocene magmatic flare-up.....	III-31
Conclusions.....	III-37
References.....	III-37

## **PART II: EDIACARAN STRATIGRAPHY OF THE NORTH AMERICAN CORDILLERA: NEW OBSERVATIONS FROM EASTERN CALIFORNIA AND NORTHERN UTAH**

### **Chapter 4: Litho- and chemostratigraphy of the Johnnie Formation and Stirling**

Quartzite, Panamint Range and Funeral Mountains, eastern California: implications for the Death Valley record of Ediacaran ocean chemistry..	IV-1
Abstract.....	IV-1
Introduction.....	IV-2
Stratigraphic and tectonic setting.....	IV-3
Stratigraphy of the Johnnie Formation and Stirling Quartzite.....	IV-5
Background.....	IV-5
Lithostratigraphy and C isotope data from the Panamint Range.....	IV-9
Johnson Canyon.....	IV-10
South Fork of Hanaupah Canyon.....	IV-12
North Fork of Hanaupah Canyon.....	IV-13
Wildrose Peak area.....	IV-15
Trail Canyon.....	IV-17
Lithostratigraphy and C isotope data from the Funeral Mountains.....	IV-22
Discussion and conclusions.....	IV-24
Correlations within the Panamint Range.....	IV-24
Record of the Shuram anomaly in the Death Valley region.....	IV-27
Comparison with the Wonoka Formation, South Australia.....	IV-29
References.....	IV-31

### **Chapter 5: Geochemistry of the Ediacaran Browns Hole basalt, Utah: implications**

for the timing of western Laurentian rifting.....	V-1
Abstract.....	V-1
Introduction.....	V-1

Northern Utah Neoproterozoic-Cambrian stratigraphy.....	V-3
Analytical data.....	V-5
Trace element data, Browns Hole basalt.....	V-5
Geochronology.....	V-7
Paleomagnetic data.....	V-8
Discussion.....	V-10
Correlations with Death Valley.....	V-10
Conclusions.....	V-13
References.....	V-14

## FIGURES AND TABLES

**CHAPTER 1:**

Figure captions.....	I-10
<b>Fig. 1</b> Tectonic maps of Cordilleran-style metamorphic core complexes in eastern California and Iran.....	I-11
<b>Fig. 2</b> Shaded relief map of part of the Great Basin.....	I-12
<b>Fig. 3</b> Primitive mantle normalized trace element diagram.....	I-13

**CHAPTER 2:**

<b>Fig. 1</b> Geologic map of Iran.....	II-51
<b>Fig. 2</b> Geologic map of the Saghand area.....	II-52
<b>Fig. 3</b> Geologic map of Khoushoumi Mountain.....	II-53
<b>Fig. 4</b> High-resolution satellite images of the Saghand area.....	II-54
<b>Fig. 5</b> Field photographs of extensional features.....	II-55
<b>Fig. 6</b> Fault- and shear zone-related rocks .....	II-57
<b>Fig. 7</b> Mylonitic foliation and lineation orientations .....	II-58
<b>Fig. 8</b> U-Pb concordia plot.....	II-59
<b>Fig. 9</b> $^{40}\text{Ar}/^{39}\text{Ar}$ inverse isochron diagrams.....	II-60
<b>Fig. 10</b> Thermochronologic data from the eastern domain.....	II-61
<b>Fig. 11</b> Summary of superposition relationships for the Khoshoumi Mtn. area.....	II-63
<b>Fig. 12</b> Map of metamorphic core complexes along the Alpine-Himalaya orogen... ..	II-64
<b>Table S1</b> U-Pb data.....	II-65
<b>Table S2</b> $^{40}\text{Ar}/^{39}\text{Ar}$ data for western domain samples .....	II-66
<b>Table S3</b> $^{40}\text{Ar}/^{39}\text{Ar}$ data for eastern domain samples .....	II-68
<b>Table S4</b> (U-Th)/He data for western domain samples.....	II-71
<b>Table S5</b> (U-Th)/He data for eastern domain samples .....	II-73
<b>Table 1</b> Alpine-Himalayan metamorphic core complexes .....	II-76

**CHAPTER 3:**

Figure captions.....	III-56
<b>Fig. 1</b> Geologic map of Iran .....	III-59
<b>Fig. 2</b> Cretaceous through Miocene stratigraphy in the Tafresh area .....	III-60
<b>Fig. 3</b> U-Pb concordia diagrams/Ar spectra.....	III-61
<b>Fig. 4</b> Cretaceous through Miocene stratigraphy of the Chalus Road area .....	III-62
<b>Fig. 5</b> Tertiary stratigraphy of the Alborz Mtns.....	III-63
<b>Fig. 6</b> Tertiary stratigraphy of the Urumieh-Dokhtar arc .....	III-64
<b>Fig. 7</b> Total alkali-silica diagrams. ....	III-65
<b>Fig. 8</b> Primitive mantle normalized trace element diagrams. ....	III-66
<b>Fig. 9</b> Ti/V vs. Zr/Nb plot for primitive Iranian basalts .....	III-67
<b>Fig. 10</b> Generalized Tertiary stratigraphy of Iran .....	III-68
<b>Fig. 11</b> Iranian shoshonite.....	III-69
<b>Fig. 12</b> Diagram summarizing tectonic setting of Iranian Paleogene volcanism.....	III-70
<b>Table 1</b> U-Pb zircon age data .....	III-71
<b>Table 2</b> $^{40}\text{Ar}/^{39}\text{Ar}$ plagioclase age data.....	III-74

**CHAPTER 3 (continued):****Table 3** Major and trace element compositions of Iranian Paleogene volcanic rocks.III-76**CHAPTER 4:**

Figure captions.....	IV-40
<b>Fig. 1</b> Shaded relief map of part of the southern Great Basin .....	IV-45
<b>Fig. 2</b> Shaded relief map of the Panamint Range .....	IV-46
<b>Fig. 3</b> Proterozoic to earliest Cambrian stratigraphy of the Death Valley region ....	IV-47
<b>Fig. 4</b> Photographs from Johnson Canyon and Hanaupah Canyon.....	IV-48
<b>Fig. 5</b> C isotope data for the upper Johnnie Fm.....	IV-49
<b>Fig. 6</b> Johnnie Fm. and lower Stirling Quartzite, S. fork of Hanaupah Canyon .....	IV-50
<b>Fig. 7</b> Upper Johnnie Fm. dolostone, N. fork of Hanaupah Canyon.....	IV-51
<b>Fig. 8</b> Photographs of upper Johnnie Fm. carbonates.....	IV-52
<b>Fig. 9</b> Geologic map of the Johnnie-Stirling contact near Wildrose Peak .....	IV-53
<b>Fig. 10</b> Photograph of Trail Canyon.....	IV-54
<b>Fig. 11</b> Geologic map of the Trail Canyon area.....	IV-55
<b>Fig. 12</b> Johnnie Fm. breccia bed in Blackwater Wash. ....	IV-56
<b>Fig. 13</b> Giant limestone breccia clasts in Trail Canyon .....	IV-57
<b>Fig. 14</b> Photographs of the upper Johnnie Fm. in Trail Canyon.....	IV-58
<b>Fig. 15</b> Trail Canyon C isotope data.....	IV-59
<b>Fig. 16</b> Photographs of the lower Johnnie Fm. in Trail Canyon. ....	IV-60
<b>Fig. 17</b> C isotope data from the Funeral Mtns. ....	IV-61
<b>Fig. 18</b> Summary of C isotope data.....	IV-62
<b>Fig. 19</b> Correlation between Hanaupah Canyon and Trail Canyon.....	IV-63
<b>Fig. 20</b> Summary of C isotope data from the Wonoka Fm.....	IV-64
<b>Table 1</b> C and O isotope data tables.....	IV-65

**CHAPTER 5:**

Figure captions.....	V-22
<b>Fig. 1</b> Shaded relief map of northern Utah and southern Idaho .....	V-25
<b>Fig. 2</b> Late Proterozoic to Cambrian stratigraphy of the Browns Hole Quadrangle...V-26	
<b>Fig. 3</b> Geologic map of the Browns Hole quadrangle.....	V-27
<b>Fig. 4</b> Geochemical data from the Browns Hole basalt.....	V-28
<b>Fig. 5</b> U-Pb concordia diagram for Browns Hole basalt apatites.....	V-29
<b>Fig. 6</b> Paleomagnetic data from the Browns Hole quadrangle.....	V-30
<b>Fig. 7</b> Preexisting C isotope data .....	V-31
<b>Table 1</b> XRF major and trace element data from the Browns Hole basalt.....	V-32
<b>Table 2</b> U-Pb geochronology of the Browns Hole basalt.....	V-33

## **Chapter 1**

### **Introduction**

This thesis is divided into two sections that focus on different topics: the first part deals with Cenozoic metamorphic core complexes and volcanism in Iran, and the second part is a study of Neoproterozoic strata in the western United States. Despite the obvious differences in geographic locations and time periods, these two projects share common themes in extensional tectonism, volcanism, and sedimentation that are outlined in this introductory chapter.

In the North American Cordillera, the tectonic significance of scattered occurrences of high-grade metamorphic rocks structurally overlain by weakly metamorphosed to unmetamorphosed strata (i.e., “Cordilleran-style metamorphic core complexes”) was originally recognized in the 1960s. Early interpretations of these areas tended to link them with Mesozoic contractional structures exposed along the eastern margin of the Great Basin (e.g., Misch, 1960). When K-Ar ages revealed that the footwalls of these core complexes actually cooled in the Tertiary (e.g., Armstrong and Hansen, 1966), it became apparent that their formation was not directly related to the earlier period of shortening and paved the way for our current understanding of large magnitude Tertiary extension in the Basin and Range province.

Within the last few years, similar structures have been recognized in the Iranian segment of the Alpine-Himalayan orogen. Ramezani and Tucker (2003), in a study with

implications analogous to those of Armstrong and Hansen (1966), presented high-precision U-Pb data from Proterozoic through Tertiary rocks in eastern Iran. Among other things, their data demonstrated conclusively that mylonitic gneisses near the town of Saghand (Fig. 1), previously considered to be Precambrian based on high metamorphic grade (e.g., Stöcklin, 1968), are, in fact, Eocene. Subsequent field and analytical work (Chapter 2) has revealed that these gneisses form the footwalls of a belt of metamorphic core complexes that are similar in many ways to those found in the southwestern United States. New thermochronology data indicate that these eastern Iranian core complexes were active in the middle Eocene, and reinterpretation of existing geologic maps suggest that they locally accommodated  $\geq 30$  km of extension. An additional Eocene core complex has since been documented further west in Iran (Fig. 1, Moritz et al., 2006), and geologic descriptions from an area of recently discovered eclogites in southern Iran (Davoudian et al., 2007) suggest that it may be yet another Eocene core complex. With the recent recognition of these structures, along with evidence of Paleogene brittle normal faulting (Tillman et al., 1981, Guest et al., 2006), it has become reasonably clear that the Eocene epoch was a time of crustal extension in Iran. Extension was accompanied by very large volumes of shallow marine to continental volcanism and sedimentation, as confirmed by new geochronological data (Chapter 3). Primitive basalts erupted during this  $\sim 20$  My “flare-up” stage have trace element characteristics typical of most continental arcs. In contrast, trace element data from basalts erupted after the flare-up ended, during a much less extensive Oligocene phase of volcanism, suggest that they were generated from an asthenospheric source that was only slightly modified by fluxing from the subducted slab. This set of observations can be explained by a two-stage model

for Iranian Tertiary volcanism. In the first stage, previously hydrated lithospheric mantle melted due to pressure release associated with crustal thinning, thus producing large volumes of Eocene volcanic rocks with trace element compositions reflective of their source within the mantle wedge. In the second stage, beginning in the late Eocene or early Oligocene, the supply of previously fluxed lithospheric mantle was exhausted and the dominant source of volcanism became asthenospheric mantle, which continued to upwell in response to extension. It is suggested that slab-rollback was the driving force for extension and may have been preceded by a period of flat-slab subduction which both suppressed volcanism and preconditioned the overriding plate with slab-derived fluids.

In eastern California, metamorphic core complexes are found along both margins of Death Valley. In the Panamint Range (west side of Death Valley) and Funeral Mountains (east side), Miocene detachment faults separate underlying Proterozoic high-grade rocks from overlying Proterozoic through Tertiary low-grade to unmetamorphosed strata (Fig. 1, e.g., Hodges et al., 1990, Wright and Troxel, 1993). Late Proterozoic sedimentary rocks in these areas were deposited within the western Laurentian continental margin during the break-up of the supercontinent Rodinia (e.g., Hoffman, 1991) and the subsequent development of a passive-margin. These rocks comprise one of the world's most complete records of the geochemical and geobiological events that occurred during the Ediacaran Period, i.e., the time from cap carbonate deposition following the Marinoan "Snowball Earth" glaciation until the Precambrian-Cambrian boundary, roughly 635 to 542 Ma. Most modern studies of Ediacaran strata from the Death Valley region (e.g., Corsetti and Kaufman, 2003) have focused on platformal facies to the southeast of Death

Valley, where it has subsequently been shown that much of the rock record is missing along disconformities (Pettersen et al., 2007). Chapter 4 is focused on assembling a more complete Death Valley stratigraphic and isotopic record of the Johnnie Fm. and Stirling Quartzite from basinal facies exposed in the Panamint Range and Funeral Mountains. Isotopic data from these two formations in eastern California, as well as equivalent strata in Oman, Australia, and China, constitute evidence for the final oxygenation of the oceans during the Late Proterozoic (e.g., Fike et al., 2006).

These Death Valley strata are part of a westward-thickening package of Proterozoic rift-related sedimentary and volcanic rocks that extends from Mexico to Canada (Fig. 2, Stewart, 1972). A very generalized stratigraphy of these deposits consists of two parts: a lower section of Cryogenian (850-635 Ma) mafic volcanics, glacial diamictites, and shallow marine sedimentary rocks, and an upper section of Ediacaran to Cambrian sediments (e.g., Stewart, 1972). Most studies of these rocks have concluded that rifting of Laurentia occurred during deposition of the lower part, and post-rift subsidence is represented by the upper part (e.g., Stewart, 1972, Prave, 1999). In northern Utah, a spatially-restricted Proterozoic basalt flow is situated at a stratigraphic level above glacial sediments and below rocks containing Cambrian trace fossils. Previous correlations of the northern Utah section with better characterized strata in the Death Valley area have been tenuous at best (e.g., Corsetti et al., 2007). In Chapter 5, pre-existing C isotope data are used to show that eruption of the northern Utah basalt postdated deposition of the Marinoan cap carbonate sequence and is therefore within the upper part of the generalized Laurentian rift-to-drift stratigraphy. New trace element data

from the basalt share similarities with older Laurentian rift-related basalts (Harper and Link, 1986) and with Tertiary basalts in Iran that accompanied extension (Fig. 3, Chapter 3). These observations suggest that in at least one place, rifting of Laurentia seems to have continued later than estimated by most geological studies and is more consistent with the long-standing findings of tectonic subsidence models (e.g., Bond et al. 1985).

Both parts of this thesis therefore deal with large-magnitude extension and volcanic and sedimentary rocks deposited in rifts. An interesting outcome of the Iran project is the similarity in Cenozoic tectonic histories of Iran and the western U.S. Both regions were affected by Tertiary extension and volcanic flare-ups, and Iran may have experienced a Cretaceous period of flat-slab subduction analogous to the Laramide orogeny. Pre-extensional arc magmatism was more extensive in the western U.S., while syn-extensional volcanism was greater in Iran. This inverse relationship may be fundamentally related to convergence rate (which was 2 to 3 times greater in the North American Cordillera than in Iran) which at least partially controls the extent of mantle melting prior to the additional influence of decompression accompanying extension.

## **REFERENCES**

Armstrong, R.L., and Hansen, E., 1966, Cordilleran infrastructure in the eastern Great Basin: *American Journal of Science*, v. 264, p. 112-127.

Bond, G.C., Christie-Blick, N., Kominz, M.A., and Devlin, W.J., 1985, An early Cambrian rift to post-rift transition in the Cordillera of western North America: *Nature*, v. 315, p. 742-746.

Corsetti, F.A., and Kaufman, A.J., 2003, Stratigraphic investigations of carbon isotope anomalies and Neoproterozoic ice ages in Death Valley, California: *Geological Society of America Bulletin*, v. 115, p. 916-932.

Corsetti, F.A., Link, P.K., and Lorentz, N.J., 2007,  $\delta^{13}\text{C}$  chemostratigraphy of the Neoproterozoic succession near Pocatello, Idaho, U.S.A.: implications for glacial chronology and regional correlations: *SEPM Special Publication No. 86*, p. 193-205.

Davoudian, A.R., Genser, J., Dachs, E., and Shabanian, N., 2007, Petrology of eclogites from north of Shahrekord, Sanandaj-Sirjan zone, Iran: *Mineralogy and Petrology*, doi: 10.1007/s00710-007-0204-6.

Fike, D.A., Grotzinger, J.P., Pratt, L.M., and Summons, R.E., 2006, Oxidation of the Ediacaran ocean: *Nature*, v. 444, p. 744-747.

Guest, B., Axen, G.J., Lam, P.S., and Hassanzadeh, J., 2006a, Late Cenozoic shortening in the west-central Alborz Mountains, northern Iran, by combined conjugate strike-slip and thin-skinned deformation: *Geosphere*, v. 2, p. 35-52.

Harper, G.D., and Link, P.K., 1986, Geochemistry of Upper Proterozoic rift-related volcanics, northern Utah and southeastern Idaho: *Geology*, v. 14, p. 864-867.

Hodges, K.V., McKenna, L.W., and Harding, M.B., 1990, Structural unroofing of the central Panamint Mountains, Death Valley region, southeastern California, *in* Wernicke, B.P., ed., Basin and Range extensional tectonics near the latitude of Las Vegas, Nevada: Geological Society of America Memoir 176, Boulder, p. 377-390.

Hoffman, P.F., 1991, Did the breakout of Laurentia turn Gondwanaland inside-out?: *Science*, v. 252, p. 1409-1412.

Misch, P., 1960, Regional structural reconnaissance in central-northeast Nevada and some adjacent areas: observations and interpretations: Intermountain Association of Petroleum Geologists Guidebook for 11<sup>th</sup> Annual Field Conference, p. 17-42.

Moritz, R., Ghazban, F., and Singer, B.S., 2006, Eocene gold ore formation at Muteh, Sanandaj-Sirjan tectonic zone, western Iran: a result of late-stage extension and exhumation of metamorphic basement rocks within the Zagros orogen: *Economic Geology*, v. 101, p. 1497-1524.

Petterson, R., Prave, A., Wernicke, B., and Fallick, A.E., 2007, New stratigraphic and isotopic constraints on the Cryogenian-Ediacaran strata of Death Valley region, *Geological Society of America Abstracts with Programs*, v. 39, no. 6, p. 222.

Prave, A.R., 1999, Two diamictites, two cap carbonates, two  $\delta^{13}\text{C}$  excursions, two rifts: the Neoproterozoic Kingston Peak Formation, Death Valley, California: *Geology*, v. 27, p. 339-342.

Ramezani, J., and Tucker, R.D., 2003, The Saghand region, central Iran: U-Pb geochronology, petrogenesis and implications for Gondwana tectonics: *American Journal of Science*, v. 303, p. 622-665.

Stewart, J.H., 1972, Initial deposits in the Cordilleran geosyncline: evidence of a late Precambrian (<850 m.y.) continental separation: *Geological Society of America Bulletin*, v. 83, p. 1345-1360.

Stöcklin, J., 1968, Structural history and tectonics of Iran: a review: *American Association of Petroleum Geologists Bulletin*, v. 52, p. 1229-1258.

Sun, S.S., and McDonough, W.F., 1989, Chemical and isotopic systematics of oceanic basalts; implications for mantle composition and processes, *in* Saunders, A.D., and Norry, M.J., eds., *Magmatism in the oceanic basins*: *Geological Society of London Spec. Pub.* 42, p. 313-345.

Tillman, J.E., Poosti, A., Rossello, S., and Eckert, A., 1981, Structural evolution of Sanandaj-Sirjan ranges near Esfahan, Iran: American Association of Petroleum Geologists Bulletin, v. 65, p. 674-687.

Wright, L.A., and Troxel, B.W., 1993, Geologic map of the central and northern Funeral Mountains and adjacent areas, Death Valley region, southern California: U.S. Geological Survey Miscellaneous Investigations Series Map I-2305, scale 1:48,000, 1 sheet.

**FIGURE CAPTIONS**

**Figure 1.** Simplified tectonic maps of some Cordilleran-style metamorphic core complexes in eastern California and Iran, shown at the same scale. See Chapters 2 and 4 for references.

**Figure 2.** Shaded relief map showing locations of the Panamint Range (Chapter 4) and Huntsville, UT (Chapter 5) and thickness (in feet) of late Proterozoic to Cambrian strata in the western US (after Stewart, 1972). Blue arrow points to estimated original position of the Huntsville area prior to eastward transport in the hanging wall of the Willard thrust (Stewart, 1972).

**Figure 3.** Primitive mantle normalized trace element diagram. Note similarities between the Proterozoic Browns Hole basalt in Utah and a typical Oligocene basalt from Iran, both of which are believed to be rift-related. In contrast, Eocene basalts from Iran have trace element characteristics much more typical of volcanic arcs, for example the depletion of Nb. Primitive mantle composition from Sun and McDonough (1989).

Figure 1

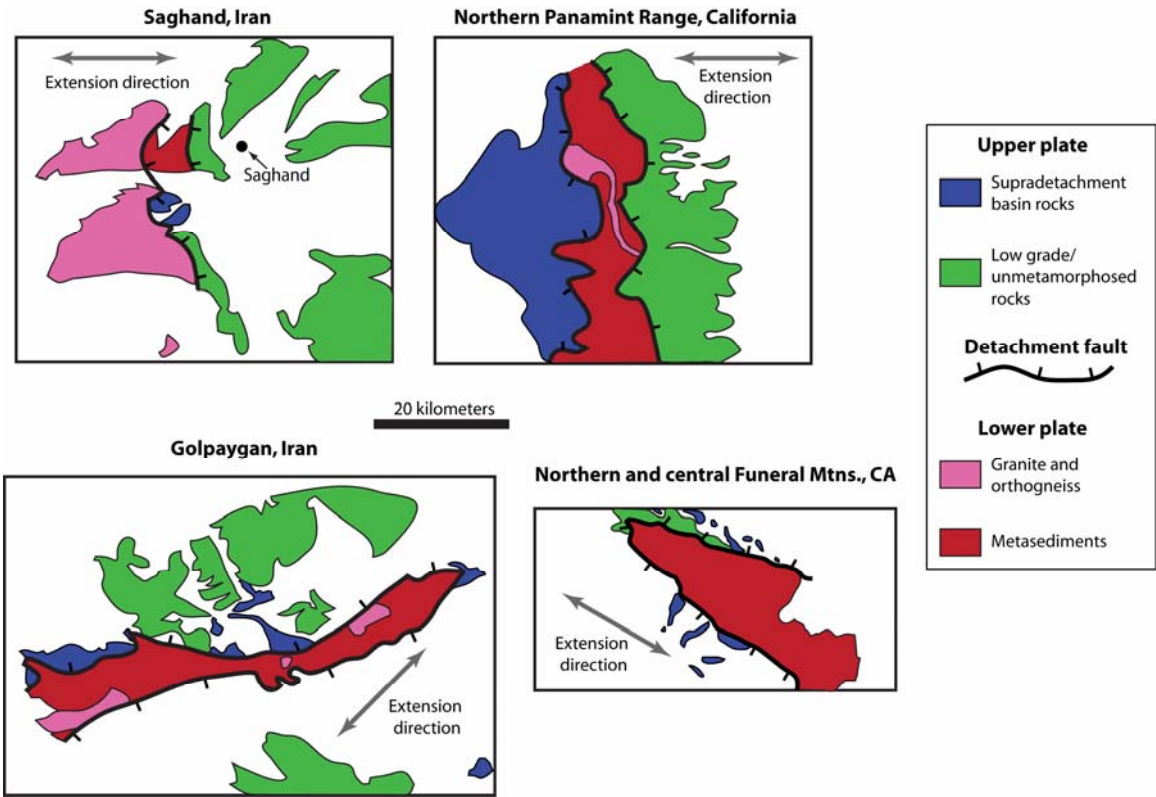
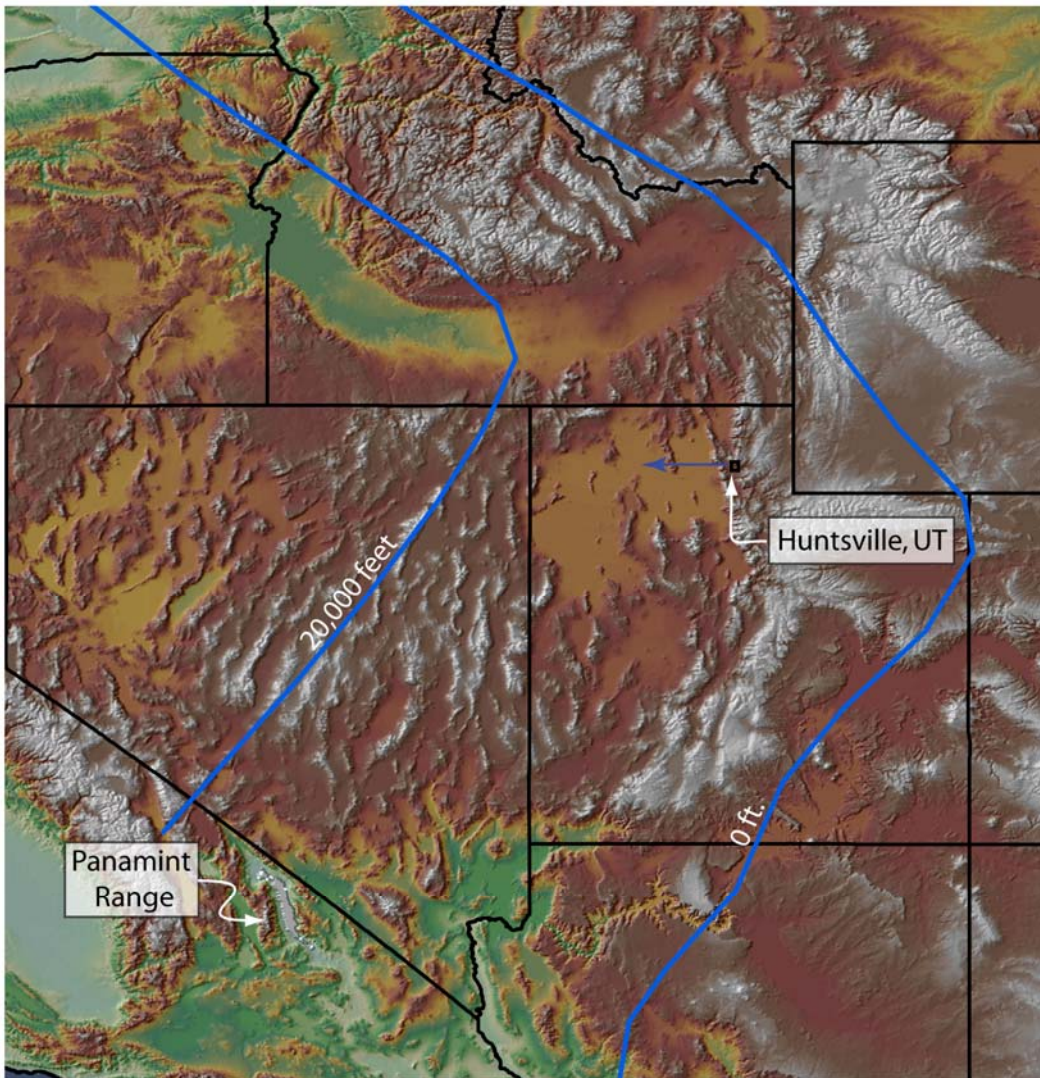
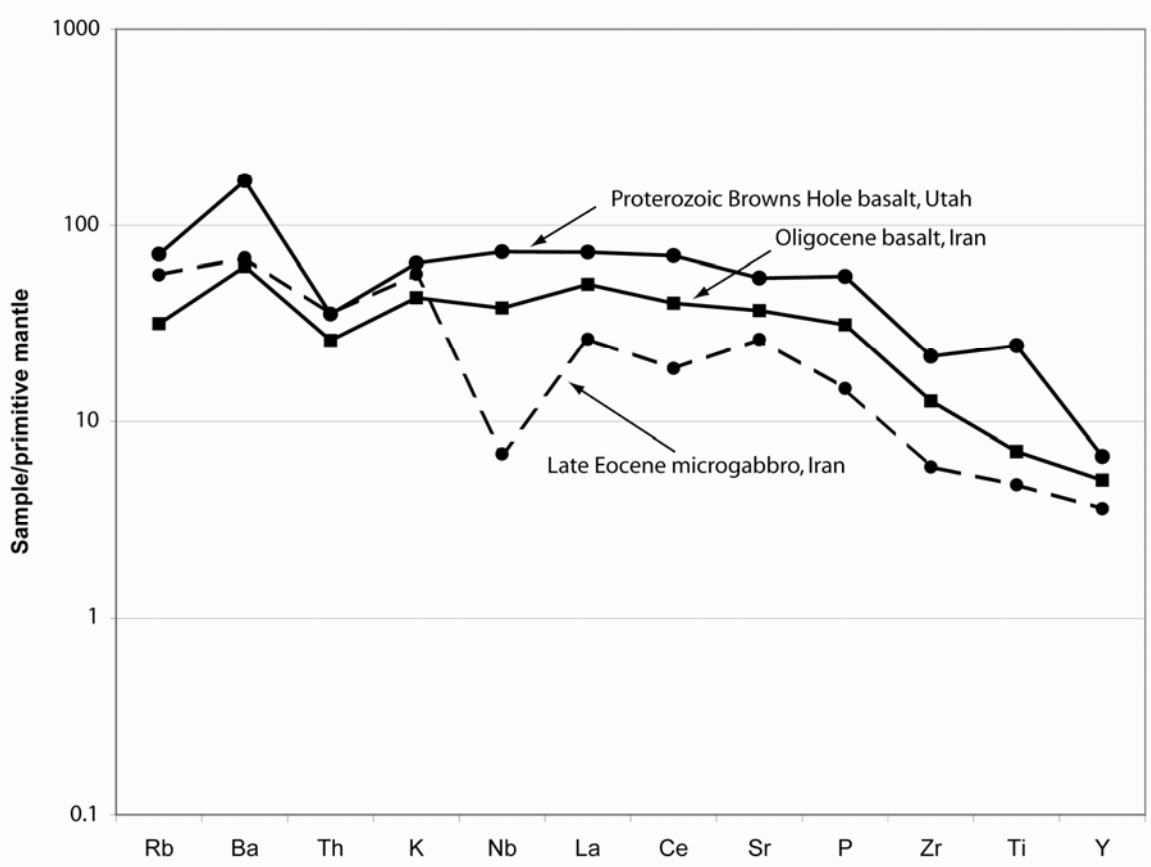


Figure 2



500 km

Figure 3



## **Chapter 2**

### **Geology and thermochronology of Tertiary Cordilleran-style metamorphic core complexes in the Saghand region of central Iran**

*Geological Society of America Bulletin, 2007, v. 119, p. 961-977.*

Charles Verdel<sup>1</sup>, Brian P. Wernicke<sup>1</sup>, Jahandar Ramezani<sup>2</sup>, Jamshid Hassanzadeh<sup>3</sup>, Paul R. Renne<sup>4</sup>, and Terry L. Spell<sup>5</sup>

(1) Division of Geological and Planetary Sciences, California Institute of Technology, Pasadena, CA 91125

(2) Department of Earth, Atmospheric and Planetary Sciences, Massachusetts Institute of Technology, Cambridge, MA 02139

(3) Department of Geology, University of Tehran, Tehran, Iran

(4) Berkeley Geochronology Center, 2455 Ridge Rd., Berkeley, CA 94709 *and*  
Department of Earth and Planetary Science, University of California, Berkeley, CA 94720

(5) Department of Geoscience, University of Nevada, Las Vegas, Las Vegas, NV 89154

#### **ABSTRACT**

An ~100 km long N-S belt of metamorphic core complexes is localized along the boundary between the Yazd and Tabas tectonic blocks of the central Iranian microcontinent, between the towns of Saghand and Posht-e-Badam. Amphibolite facies

mylonitic gneisses are structurally overlain by east-tilted supracrustal rocks including thick (>1 km), steeply dipping, nonmarine siliciclastic and volcanic strata. Near the detachment (the Neybaz-Chatak fault), the gneisses are generally overprinted by chlorite brecciation. Cross-cutting relationships along with U-Pb zircon and  $^{40}\text{Ar}/^{39}\text{Ar}$  age data indicate that migmatization, mylonitic deformation, volcanism and sedimentation all occurred in the middle Eocene, between ~49 and 41 Ma. The westernmost portion of the Tabas block immediately east of the complexes is an east-tilted crustal section of Neoproterozoic/Cambrian crystalline rocks and metasedimentary strata >10 km thick.  $^{40}\text{Ar}/^{39}\text{Ar}$  biotite ages of 150-160 Ma from structurally deep parts of the section contrast with ages of 218-295 Ma from shallower parts and suggest Late Jurassic tilting of the crustal section. These results define three events: (1) a Late Jurassic period of upper crustal cooling of the western Tabas block, which corresponds to regional Jurassic-Cretaceous tectonism and erosion recorded by a strong angular unconformity below mid-Cretaceous strata throughout central Iran; (2) profound ~EW middle Eocene crustal extension, plutonism and volcanism (ca. 44-40 Ma); and (3) ~2-3 km of early Miocene (ca. 20 Ma) erosional exhumation of both core complex and Tabas block assemblages at uppermost crustal levels, resulting from significant north-south shortening. The discovery of these and other complexes within the mid-Tertiary magmatic arcs of Iran demonstrates that Cordilleran-style core-complexes are an important tectonic element in all major segments of the Alpine-Himalayan orogenic system.

## INTRODUCTION

The Cenozoic geology of Iran has traditionally been viewed in terms of two dominant events: widespread and voluminous Eocene to Oligocene primarily arc-related volcanism (e.g., Forster et al., 1972) (Figure 1) and accompanying rapid sedimentation, and Miocene and younger folding, thrusting and strike-slip faulting accommodating the collision between Arabia and Eurasia (e.g., Stöcklin, 1968). More recently, some authors have proposed an Eocene to Miocene phase of crustal extension in Iran and adjacent regions to explain the local alkaline affinity of Tertiary volcanism and the onset of rapid sedimentation (Hassanzadeh et al., 2002; Vincent et al., 2005). Recognition of tectonic elements of Late Cretaceous and younger age associated with significant crustal extension in Iran has included reports of domino-style normal faulting in the Golpaygan region (Tillman et al., 1981) and rapid exhumation of mylonitic crystalline rocks along extensional detachment faults in the Takab, Biarjmand and Posht-e-Badam areas (Stockli et al., 2004; Hassanzadeh et al., 2005; Kargaran et al., 2006, respectively; Figure 1).

In this paper we present the results of field and analytical work in the Saghand and Posht-e-Badam area of central Iran, where we have documented a north-trending belt of domiform mountain ranges exhibiting the traits of the mid-Tertiary metamorphic core complexes in the Sonora Desert region of southwestern North America (e.g., Davis, 1980; Reynolds, 1985). These include mylonitized, high-grade granitic rocks lying below a low-angle detachment fault, with associated chlorite brecciation; low-grade to unmetamorphosed upper plate rocks; and a supradetachment basin containing a thick succession of scarp-facies nonmarine strata. We first describe the regional and local

geological setting of these central Iranian ranges based on previous work, and then systematically describe the extensional tectonic elements. Building on an extensive database of U-Pb geochronology of crystalline and volcanic rocks (Ramezani and Tucker, 2003) we then present new U-Pb, (U-Th)/He and  $^{40}\text{Ar}/^{39}\text{Ar}$  data that refine the timing of extensional deformation as well as earlier and later periods of major deformation, and discuss the significance of this data for the Tertiary evolution of the Tethysides.

### **TECTONIC SETTING**

The Iranian segment of the Alpine-Himalayan orogenic system has a complex Permian through Quaternary history of successive rifting and collision, but nonetheless most of Iran is underlain by a relatively concordant blanket of Paleozoic platform sediments similar to those on the Arabian platform (e.g., Stöcklin, 1968). It is therefore generally believed that the major continental blocks in Iran, as outlined by narrow belts of Mesozoic ophiolitic rocks, had a common origin in a cratonic platform along the northern flank of Gondwana in late Paleozoic time (e.g., Ramezani and Tucker, 2003). Permian through Quaternary reconstructions of the Tethysides in the Middle East accordingly involve progressive break up and transfer of fragments of northern Gondwana and their accretion to the southern flank of Eurasia (e.g., Sengör and Natal'in, 1996). The most recent event of this type is the mid-Tertiary rifting of Arabia away from Africa and its Miocene collision with Asia by closure of the Neotethys oceanic tract (e.g., Axen et al., 2001; McQuarrie et al., 2003), ultimately forming the folded belts of the Zagros Mountains to the south and the Alborz-Kopet Dagh ranges to the north (Figure 1). The collisional suture between Arabia and Eurasia lies along or perhaps somewhat north of

the Zagros thrust zone, which juxtaposes folded and thrust strata of the Arabian platform against a stratigraphically and structurally more complex, marginal assemblage referred to as the Sanandaj-Sirjan zone (Figure 1).

Prior to the collision, plate convergence involved northward subduction of ~1300 km of Neotethyan oceanic lithosphere (e.g., McQuarrie et al., 2003), resulting in Andean-type magmatic arcs on the overriding continental plates that reach from the Balkan Peninsula to Afghanistan. The bulk of the Paleogene magmatic rocks in Iran are traditionally grouped into three belts: Alborz in the north, Urumieh-Dokhtar across central Iran, and Lut in the east (Figure 1). Between the Alborz and Urumieh-Dokhtar belts lies a large region of relatively low topography that includes the Central-East Iranian Microcontinent (CEIM), as outlined by major faults (Takin, 1972).

The Saghand area lies in the western portion of the CEIM, about 100 km north-northeast of the axis of the Urumieh-Dokhtar arc (Figure 1). The CEIM is subdivided into three fault-bounded blocks, including (from east to west) the Lut, Tabas and Yazd blocks (Figure 1; e.g., Alavi, 1991). The boundary zone between the Tabas and Yazd blocks, the Kashmar-Kerman tectonic zone of Ramezani and Tucker (2003), forms a 50-100 km-wide, 600 km-long concave-east belt (Figure 1) that exposes stratigraphically and structurally deep crustal levels (Cambrian stratified rocks, various crystalline units) that contrast with predominantly unmetamorphosed Mesozoic and younger rocks exposed elsewhere in the two blocks.

## **GEOLOGY OF THE SAGHAND REGION**

Previous investigations in the Saghand area have included systematic mapping at scales of 1:100,000 to 1:500,000 (Valeh and Haghypour, 1970; Haghypour, 1977a and b; Haghypour et al., 1977), and the detailed U-Pb zircon study of magmatic rocks in the area (Ramezani and Tucker, 2003). The area is crossed by two strike-slip faults of unknown age and net slip, the Posht-e-Badam and Chapedony faults (Figure 2). Ramezani and Tucker (2003) subdivided the area into three lithotectonic domains, including an eastern, a central and a western domain, based on lithostratigraphic and age characteristics. The eastern and central domains are juxtaposed along the Posht-e-Badam fault. The central domain is faulted over the western domain along the Neybaz and Chatak faults, which dip shallowly to moderately east or northeast, and are not overlapped by any pre-Neogene strata. Although the contact between central and western domains is mainly exposed in two semi-continuous bands, it appears that a single low-angle fault system (the Neybaz-Chatak fault) juxtaposes the two domains over an along-strike distance of about 90 km (Figure 2).

Bedrock exposures in the central and eastern domains constitute 1) stratified rocks that range in age from Ediacaran/Cambrian to Neogene (Figure 2, upper left legend); 2) crystalline metamorphic complexes that include steeply foliated medium-grade felsic gneisses, schists, amphibolites and marble known as the Boneh-Shurow (eastern domain) and Posht-e-Badam (central domain) complexes, and 3) magmatic intrusive and sub-extrusive rocks of Early Cambrian (eastern domain) and Late Triassic (central domain) age (Figure 2, lower right legend). The western domain is dominated by Eocene deep-

seated metamorphic rocks and magmatic intrusions (Figure 2, see also units defined in the lower right legend). The rock units relevant to this study are described in more detail below. Stated age data in this section are those of Ramezani and Tucker (2003).

### **Stratified rocks**

The oldest stratified rocks include a thick succession of Ediacaran to early Cambrian weakly metamorphosed graywackes, volcanoclastic rocks and basaltic lavas, collectively referred to as the Tashk Formation. It contains detrital zircons as young as 627 Ma and was intruded by 533 Ma granitoid plutons. The Tashk Formation is overlain by the Cambrian Volcano-Sedimentary Unit (CVSU) of Ramezani and Tucker (2003). These units are overlain in angular unconformity by Permian and Triassic shallow marine carbonates.

Terrigenous and carbonaceous rocks of mid-Cretaceous age containing Aptian to Cenomanian fossils (e.g., *Orbitolina*) lie in angular unconformity on older units ranging in age from Cambrian through Triassic (Haghipour et al., 1977). Although the pre-Cretaceous hiatus spans between ca. 100 to 400 My within the Kashmar-Kerman tectonic zone, in the interior of the Yazd and Tabas blocks strongly folded marine strata as young as Middle Jurassic rest in angular unconformity beneath the mid-Cretaceous strata (Haghipour et al., 1977). The stratigraphic record thus indicates that significant crustal shortening occurred within the central Iranian structural blocks between mid-Jurassic and mid-Cretaceous time and was concomitant with substantial erosion, particularly within the Kashmar-Kerman tectonic zone.

Volcanic rocks and associated sedimentary strata of Eocene age are widespread within the CEIM and throughout Iran (Figure 1), but are restricted to two relatively small areas in the Saghand region (Haghipour et al., 1977), one along the northwest flank of Kalut-e-Chapedony and another along the northeast side of Khoshoumi Mountain (Figure 2). In the latter location, Haghipour et al. (1977) reported nummulitic marls indicating marine deposition, at least in part. As elaborated below, our observations of a steeply dipping section of these strata in excess of 1000 meters thick suggest primarily non-marine deposition in a rapidly subsiding basin, but confirm the Eocene age assignment of Haghipour et al. (1977).

The Eocene strata are overlain in angular unconformity by poorly consolidated evaporitic sandstones and mudstones which are probably Miocene or Pliocene in age (Haghipour et al., 1977). Near Saghand, these strata are at least several hundred meters thick and display a complex pattern of faulting and folding that suggests significant contractile deformation.

### **Crystalline rocks**

Within each of the five ranges that comprise the eastern domain, the first-order structural pattern is that of an east-tilted crustal section, with Cretaceous strata exposed in the eastern portions of the ranges, east-dipping stratified rocks of the Tashk Formation and CVSU occupying the central portions, and deep-seated crystalline rocks of the Boneh-Shurow complex cropping out in the west (Figure 2). The primary contact between the stratified rocks and subjacent crystalline rocks in both the central and eastern domains is

a moderately to steeply east-dipping ductile shear zone. Plutonism and metamorphism in the Boneh-Shurow complex occurred at ~545 Ma. Emplacement of granitoid plutons and intermediate to felsic volcanism associated with the CVSU occurred over a narrow temporal window of 533 to 525 Ma.

The western domain is composed almost entirely of high-grade gneissic rocks comprising the Chapedony complex. This complex was long considered the oldest of the Precambrian units in the Saghand region based on its high metamorphic grade (Stöcklin, 1968; Haghypour et al., 1977), but U-Pb zircon dating demonstrates a middle Eocene intrusive age for the oldest components of these gneisses. Zircons from both syn-kinematic gneiss and migmatitic leucosomes derived from them have previously yielded concordia lower intercept ages of ca. 46 Ma (Ramezani and Tucker, 2003). The majority of the Chapedony complex is comprised of gneiss, with lesser amounts of migmatite, anatectite, schist, marble and calc-silicate rock. The gneisses are locally amphibolitic but are predominantly medium to coarse biotite-kspar-plagioclase-quartz gneiss with rare clinopyroxene and garnet. Medium to high metamorphic grade is indicated by large areas of migmatite and anatectite within the complex (Ramezani and Tucker, 2003).

Two post-metamorphic intrusions crop out at Daranjir Mountain (Figure 2). The Daranjir diorite (U-Pb age 43.4 +/- 0.2 Ma) is apparently the older of the intrusions. The Khoshoumi granite (U-Pb age 44.3 +/- 1.1 Ma) overlaps in age, but intrudes both the Daranjir diorite and gneisses of the Chapedony complex. These ages and cross-cutting

relationships thus constrain metamorphism of the Chapedony complex to have occurred between 49 and 44 Ma (Ramezani and Tucker, 2003).

## **STRUCTURAL AND STRATIGRAPHIC OBSERVATIONS OF THE NEYBAZ-CHATAK DETACHMENT SYSTEM**

Our new field observations include 1) geological mapping of a ~6 km-long transect across the detachment system along the northeast flank of Khoshoumi Mountain (western domain), where all of the primary extensional tectonic elements are exposed; 2) mesoscopic structural data from mylonitic gneisses at Khoshoumi Mountain, Neybaz Mountain and Kalut-e-Chapedony; 3) structural microanalysis of lower plate mylonitic gneisses; 4) photo-documentation of key structural and stratigraphic relationships in the area; and 5) structural reconnaissance of the western end of Boneh-Shurow Mountain using high-resolution satellite imagery.

### **Neybaz-Chatak detachment fault and hanging wall splays**

The Neybaz-Chatak detachment system without exception emplaces lower temperature rock assemblages on top of higher. On the east side of Khoushoumi Mountain, the detachment emplaces Eocene supradetachment basin deposits and weakly metamorphosed to unmetamorphosed CVSU over mylonitic gneiss of the Chapedony complex (Figure 2). At Neybaz Mountain and Kalut-e-Chatak it emplaces medium-grade greenstones of the Posht-e-Badam complex over high-grade gneiss, and at the southeast tip of Kalut-e-Chapedony it emplaces unmetamorphosed Cretaceous limestone over high-grade gneiss. Above the main contact with Chapedony complex gneisses along the

eastern flanks of Neybaz Mountain and Khoshoumi Mountain, low- and high-angle splays juxtapose lower grade rocks on higher, or where both units are stratified, younger rocks on top of older.

Along the Khoshoumi Mountain transect, the detachment juxtaposes strongly gouged and brecciated CVSU over mylonitic gneiss, and a hanging wall normal fault juxtaposes Eocene sedimentary rocks against CVSU (Figure 3). The detachment contact in general dips gently to the north, but is strongly curvilinear, forming an E- to NE-trending antiform-synform pair (Figures 3 and 4a). In outcrop, the detachment varies from being a diffuse zone of gouge and breccia a few meters wide to a sharply defined plane (Figure 5a). The gouge zones associated with the detachment and its hanging wall splays are at least tens of meters thick (Figure 5b) and exhibit phacoidal structure, with lozenge-shaped blocks of ~1 to 10 m in maximum dimension set in a matrix of gouge (Figure 5c).

Immediately below exposures of the detachment, tabular zones of chlorite breccia were observed at Khoshoumi Mountain (Figure 5a), Neybaz Mountain (Figure 6a) and along the western flank of Kalut-e-Chapedony. At the latter locality the detachment emplaces Cretaceous limestone on chlorite breccia of mylonitic gneiss, with brecciation affecting a structural thickness of mylonite (measured perpendicular to foliation) of about 100 m. Brecciation and chloritization become much less intense downward through the zone, which has a well defined base (Figure 5d).

## **Mylonites**

As first observed by Haghypour et al. (1977), “huge parts” of the Chapedony complex are mylonitic. Mylonitization of augen gneiss and late-stage pegmatites within the gneiss is widespread on Khoshoumi Mountain, Neybaz Mountain (Figures 6b and 6c) and at Kalut-e-Chapedony (Figure 5e). The mylonites typically are composed of feldspar porphyroclasts in a matrix of biotite and fine-grained, recrystallized quartz and feldspar (Figure 6d). Recrystallized quartz and feldspar grains average  $\sim 100 \mu\text{m}$  and  $\sim 25 \mu\text{m}$  in diameter, respectively. Quartz is typically recrystallized by subgrain rotation, while recrystallization of feldspar is primarily from “bulging” recrystallization (e.g., Passchier and Trouw, 2005). These textures, along with abundant myrmekite, suggest that mylonitization occurred in the upper part of the medium-grade conditions field ( $450\text{-}600^\circ\text{C}$ ) of Passchier and Trouw (2005). Textures range from protomylonite to ultramylonite, often within single outcrops (Figure 6b). Although lineation or foliation may be difficult to detect in some outcrops, the mylonites tend to be well developed L-S tectonites with low to moderate dip and plunge, with the lineation bisecting conjugate joints (Figure 5e).

Foliation and lineation orientations were measured in three areas: on the south side of Neybaz Mountain, in the mapped transect on the east side of Khoshoumi Mountain (Figure 3), and in the central part of Kalut-e-Chapedony (Figure 2). In the latter two areas, measurements were distributed over an area of  $1\text{-}2 \text{ km}^2$ . The orientations at Kalut-e-Chapedony are distinctly different from those in the two areas to the south. At Kalut-e-Chapedony, foliation typically strikes roughly north-south and dips fairly gently to the west, with lineation plunging an average of  $12^\circ\text{WSW}$  (Figure 7a). At Neybaz and

Khoshoumi Mountains, attitudes are more scattered, but, on average, foliation dips north and lineation plunges  $43^{\circ}\text{N}$  (Figure 7b).

Well developed S-C texture is preserved in mylonitic orthogneiss along the southern flank of Neybaz Mountain, yielding top-to-the-north sense of shear (Figure 6c). Oriented samples of eight other mylonites, five from Kalut-e-Chapedony and three from Khoshoumi Mountain, were slabbed and sectioned parallel to lineation and perpendicular to foliation to evaluate sense of shear. The Kalut-e-Chapedony samples yielded three top-to-the-west determinations and one top-to-the-east (Figure 7a). The samples from Khoshoumi Mountain yielded two top-to-the-south and one top-to-the-north determinations (Figure 7b). The occurrence of oppositely directed shear sense indicators is quite common, if not ubiquitous, in mylonitic rocks (Hippertt and Tohver, 1999) and may suggest an important component of “pure shear” contraction normal to the flow direction (e.g., Lee et al., 1987).

### **Supradetachment and post-extensional basinal deposits and structures**

As mentioned above, at least 1000 m of Tertiary non-marine sandstone, siltstone, conglomerate, breccia and volcanic rocks are exposed on the northeast flank of Khoshoumi Mountain (Figure 4a). In the map transect (Figure 3), these strata dip steeply southeastward, and are truncated along a moderately to steeply north-dipping normal fault which emplaces them on top of brecciated Cambrian strata. Tectonic lenses of Cretaceous conglomerate are locally present along the fault contact. The Tertiary strata are intruded by a dacite plug, which exhibits well developed flow foliation and consists

of an older phase to the west (Tev1 on Figure 3) and a younger phase to the east (Tev2 on Figure 3). The intrusive contact is sub-parallel to the flow foliation, and both dip steeply inward toward the dome in a radial pattern. Attitudes of bedding in the country rock appear to be deflected into parallelism with the margins of the plug as a result of emplacement (Figure 3). Small outliers of the main intrusive occur on the southwestern side, one of which intrudes brecciated CVSU strata south of the normal fault that juxtaposes Cambrian and Tertiary rocks. Given the kilometer-scale offset along the normal fault and the lack of brecciation in the outlier within the Cambrian strata, we interpret these relations to indicate that intrusion occurred after faulting and brecciation of the CVSU. The steep inward dips of flow foliation around the dome further suggest that intrusion may also have post-dated most tilting of the Tertiary section, assuming the plug intruded vertically.

The lower part of the Tertiary section southwest of the intrusive plug is primarily sandstone and siltstone but contains at least one rock avalanche deposit a few meters thick containing clasts of Cambrian volcanic rocks (Figure 5f). As developed further after discussion of geochronological data from the area, we interpret these strata as a fault scarp facies developed in the early stages of detachment faulting, whereby the upper crust was fragmented into fault blocks, just prior to major rotation of hanging wall strata and final ascent of mylonitic gneisses to the surface.

Along the northeast margin of Khoshoumi Mountain, a marked angular unconformity is observed between the steeply tilted Tertiary strata and overlying Neogene(?) nonmarine

strata, which dip gently northeastward (Figures 3, 4a). The origin of tilting of the younger strata is not clear from relations around Khoshoumi Mountain. However, in the extensive exposures of these deposits in low-relief badlands just east of Saghand (Haghipour et al., 1977), a large, open, gently west-plunging anticline with gently to moderately dipping limbs is developed within these deposits. The anticline is cored by basement rocks of the Boneh Shurow complex, and is aligned with the long axis of the topographic ridge comprising Boneh-Shurow Mountain and Tashk Mountain (Figures 2 and 4b). This relationship indicates that some or all of the topography of the region may be controlled by post-extensional, approximately north-south tectonic shortening.

## **GEOCHRONOLOGY AND THERMOCHRONOLOGY**

### **U-Pb geochronology**

We determined one additional U-Pb zircon age from mylonitic (augen) orthogneiss of the Chapedony complex at Neybaz Mountain (sample 2604, Table S1, Figure 2; Figure 6c). This sample consists of mica-rich bands enveloping K-feldspar and plagioclase porphyroclasts. Six single zircon grains were analyzed for Pb and U by the ID-TIMS method at the Geochronology Laboratory at MIT (Lehrmann et al, 2006; Schoene et al, 2006). The U-Pb isotopic dates and the associated uncertainties are calculated using the error propagation algorithm of Ludwig (1980) and are plotted with  $2\sigma$  uncertainties on a conventional concordia plot (Figure 8). The final uncertainties reported here incorporate both the internal (analytical) and external (systematic) sources of error. The latter includes the U-Pb tracer calibration error as well as the U decay constant errors of Jaffey et al. (1971). The incorporation of systematic errors in the calculated dates is necessary

when results from different laboratories and/or different isotopic systems (*e.g.*, U-Pb versus  $^{40}\text{Ar}/^{39}\text{Ar}$ ) are compared (*e.g.*, Schoene et al., 2006). Details of the U-Pb procedure are provided in Appendix A and Table S1.

Six U-Pb zircon analyses from sample 2604 produced an array of mutually distinctive  $^{206}\text{Pb}/^{238}\text{U}$  dates ranging from 49.35 Ma to 48.97 Ma (Figure 8). Regression of these data to a straight line yields an upper concordia intercept date of  $49.66 \pm 0.96$  Ma (MSWD = 0.1). Alternatively, the three youngest analyses (z3, z5 and z6) overlap within error and yield a weighted mean  $^{206}\text{Pb}/^{238}\text{U}$  date of  $49.01 \pm 0.12$  Ma. The two calculated dates overlap within uncertainties and represent end-member estimates for the timing of zircon crystallization in the rock. These dates are consistent within uncertainties with a less precise  $46.8 \pm 2.5$  Ma zircon date from a nearby gneiss sample previously determined by Ramezani and Tucker (2003). Similarly, our measured ages can be interpreted as the timing of peak-metamorphic and/or anatectic zircon crystallization in the Chapedony complex.

#### **$^{40}\text{Ar}/^{39}\text{Ar}$ geochronology**

The ages of three samples from the Khoshoumi Mountain map transect were determined by  $^{40}\text{Ar}/^{39}\text{Ar}$  geochronology techniques using a  $\text{CO}_2$  laser and automated extraction line at the Berkeley Geochronology Center using the Fish Canyon sanidine (28.02 Ma; Renne et al., 1998) as a neutron flux monitor (Figures 3 and 9, Table S2).

Sample 1604 was collected from a layer of biotite-rich volcanic ash within sediments from the hanging wall of the detachment. Samples 1304 and 1404 were collected from the dacite plug that intrudes the sediments (Figure 3). Biotite from the ash has an  $^{40}\text{Ar}/^{39}\text{Ar}$  inverse isochron age of  $41.2 \pm 2.4$  Ma. Plagioclase from sample 1304 has an inverse isochron age of  $42.0 \pm 1.8$  Ma, which is indistinguishable (within uncertainties) from an alkali feldspar age of  $40.5 \pm 2.5$  Ma from sample 1404. Considering that the ash is near the top of the exposed section and assuming the dacite plug postdates both faulting and tilting as discussed in the previous section, these ages suggest that faulting and tilting occurred between 39 and 43 Ma.

In addition,  $^{40}\text{Ar}/^{39}\text{Ar}$  biotite ages were determined for six samples from a transect along Boneh-Shurow and Tashk Mountains (Figure 2, Table S3). These ages represent the time since the samples cooled below the Ar closure temperature in biotite, which is  $\sim 300$ - $350^\circ\text{C}$  under conditions of rapid cooling ( $\geq 10^\circ\text{C}/\text{My}$ ) (Harrison et al., 1985).  $^{40}\text{Ar}/^{39}\text{Ar}$  biotite ages were determined at the Nevada Isotope Geochronology Lab and are discussed in a later section. Details of the  $^{40}\text{Ar}/^{39}\text{Ar}$  procedure are provided in Appendix B.

### **(U-Th)/He thermochronology**

(U-Th)/He ages were determined on apatite and zircon from Chapedony complex gneiss and post-metamorphic plutons as well as from Ediacaran to Cambrian rocks in the tilted crustal section of the eastern domain. These ages represent the time since the samples cooled below the He closure temperatures of apatite and zircon, which are about  $70^\circ\text{C}$  and  $190^\circ\text{C}$ , respectively (Wolf et al., 1996, Reiners et al., 2002). Apatite grains were

placed in Pt tubes and heated with a Nd-YAG laser at the California Institute of Technology to extract helium, which was then analyzed by mass spectrometry (House et al., 2000). The grains were subsequently dissolved in nitric acid and analyzed with ICP-MS to determine U and Th concentrations. Zircon (U-Th)/He ages were determined using a similar procedure but utilizing a flux of lithium metaborate to facilitate the dissolution of zircon in nitric acid (Tagami et al., 2003). Details of the (U-Th)/He procedure are provided in Appendix C.

### ***Western domain***

(U-Th)/He ages were determined from gneisses at Kalut-e-Chapedony and postmetamorphic plutons at Daranjir Mountain (Table S4, Figure 2). Zircons from 0504, a sample of Chapedony gneiss, have an average (U-Th)/He age of  $43.0 \pm 7.8$  ( $2\sigma$ ) Ma; apatites from this sample have an age of  $20.3 \pm 5.8$  Ma. G18, another sample of Chapedony gneiss, has a zircon (U-Th)/He age of  $48.8 \pm 15.6$  Ma.

Zircons from samples G27 (Khoshoumi granite) and G30 (Daranjir diorite) yield (U-Th)/He ages of  $40.5 \pm 5.8$  Ma and  $40.6 \pm 5.2$  Ma, respectively. Apatites from these two samples have (U-Th)/He ages of  $22.8 \pm 3.3$  and  $15.4 \pm 8.4$  Ma, respectively.

These results suggest that both the gneisses of the Chapedony complex and the unmetamorphosed plutons cooled through the zircon He partial retention zone during middle Eocene core complex formation. The overlap, within error, of U-Pb and zircon

(U-Th)/He ages from the gneisses suggests rapid middle Eocene cooling. Subsequent cooling to  $\sim 70^{\circ}\text{C}$  by  $\sim 20\text{ Ma}$  occurred at a much lower rate.

### ***Eastern domain***

The presence of an east tilted crustal section with  $>10\text{ km}$  of structural relief immediately east of the core complexes raises the issue of whether the crustal section was generated by flexural isostasy accompanying Eocene extension along a west-dipping detachment system analogous to a number of examples in the North American Cordillera (Wernicke and Axen, 1988). In the Cordilleran examples, the tilting of crustal sections in the footwalls of major normal faults usually occurs rapidly, effectively “quenching” the thermal structure that existed within the crustal section just prior to unroofing (e.g., Fitzgerald et al., 1991; Reiners et al., 2000; Stockli, 2005). If the crustal section of the eastern domain was formed by Eocene extension, an east-west horizontal transect of cooling ages across the domain would be expected to yield progressively younger ages toward the west, reaching an Eocene minimum.

A  $\sim 20\text{ km}$  long horizontal depth profile along Boneh-Shurow and Tashk Mountains, from unmetamorphosed CVSU near the top of the crustal section in the east to crystalline rocks at significant structural depth within the Boneh-Shurow complex to the west (Figure 2), was sampled for (U-Th)/He and  $^{40}\text{Ar}/^{39}\text{Ar}$  dating to determine the age of tilting. (U-Th)/He apatite and zircon ages determined from this profile are primarily from detrital grains in sedimentary or metasedimentary rocks, and generally display a significant amount of scatter but do not vary systematically with structural position. Mean zircon

(U-Th)/He ages range from 100 to 134 Ma and overlap (using two-sigma errors) between 116 and 125 Ma. Mean apatite ages range from 17 to 20 Ma (Table S5). In contrast,  $^{40}\text{Ar}/^{39}\text{Ar}$  ages determined on metamorphic biotite from six of the samples do exhibit variation with position.  $^{40}\text{Ar}/^{39}\text{Ar}$  biotite ages vary from 150 to 160 Ma in structurally deeper parts of the section to 218 to 295 Ma in the upper part. As is apparent from a plot of age versus structural position (Figure 10a), the data indicate Late Jurassic tilting of the crustal section, followed by relatively uniform cooling of the entire section below  $\sim 190^\circ\text{C}$  in mid-Cretaceous time, and cooling of at least the westernmost half of the section below  $\sim 70^\circ\text{C}$  in latest Oligocene or early Miocene time. Late Jurassic tilting may also account for the ca. 150 Ma lower-intercept ages of zircons from the Boneh-Shurow complex (Figure 10b) since decompression accompanying rapid exhumation of these structurally deep rocks may have cracked the zircons and facilitated Pb-loss along microfractures.

## **DISCUSSION AND CONCLUSIONS**

The region of Eocene gneisses in the Saghand area clearly contains all of the major tectonic elements known from metamorphic core complexes in the North American Cordillera. Each of the four ranges in the western domain contains a brittle fault emplacing various upper crustal assemblages on deep-seated gneisses, which is a signature observation along the 2,000 km-long belt of core complexes in North America (e.g., Davis et al., 1980; Coney, 1980; Armstrong, 1982). The structural style of younger-over-older, moderate- to low-angle faults observed in central Iran is ubiquitous in the hanging wall structure of Cordilleran detachments. A distinctive structural style of

lozenge-shaped fault blocks bounded by gouge and breccia, termed *chaos structure*, has been described from a number of Cordilleran examples (Noble, 1941; Wernicke and Burchfiel, 1982; Wright and Troxel, 1984). Mylonitic gneisses are also ubiquitous in the footwalls of Cordilleran examples (e.g., Davis and Coney, 1979; Davis, 1980; Davis and Lister, 1988). In particular, where the footwalls of the Cordilleran examples are primarily granitic, as in the Sonoran Desert region, the development of L-S tectonite overprinted by chloritic brecciation (e.g., Reynolds, 1985; Spencer and Welty, 1986) bears strong similarity to the central Iran complexes. The development of thick deposits of primarily non-marine sedimentary and volcanic successions containing rock avalanche breccias, steeply tilted and juxtaposed on structurally lower rocks, referred to as supradetachment basins (e.g., Friedmann et al., 1994), are well described from most Cordilleran examples.

The topographic expression of the mountain ranges bearing the Chapedony complex has been given the special term *kalut* in the local Farsi dialect, which signifies a tendency toward having a broad, flat upland area, in contrast to the relatively narrow, cusped ridge lines characteristic of surrounding ranges (Ramezani and Tucker, 2003). This pattern is similar to that of Cordilleran metamorphic core complexes, especially in the southwestern U. S., where domes of variably mylonitic gneisses in the footwalls of extensional detachments are expressed by a domiform topography or *turtleback* (e.g. Wright et al., 1974; Coney, 1980).

In addition to these common features, we further note that the tectonic setting of the Cordilleran examples is that of a continental or Andean type magmatic arc (Coney, 1980; Armstrong, 1982; Armstrong and Ward, 1991). The middle Eocene timeframe for the development of the Saghand area core complexes (see below) coincides with peak production of arc magmas in the Urumieh-Dokhtar, Alborz, Lut and related magmatic arcs of central Iran. The protoliths of mylonitic plutons, the undeformed plutons of the Daranjir Mountain area and volcanic strata within the supradetachment basin are all contemporaneous with the mid-Tertiary magmatic arc system of central Iran and are broadly synchronous with development of extension in the back-arc region.

### **Timing of extension**

A summary of known (solid lines) and inferred (dashed lines) superposition relationships and relevant geochronologic data for the Khoshoumi Mountain transect is illustrated in Figure 11. Peak metamorphism (migmatization) and mylonitization of the Chapedony complex is bracketed between 44 and 49 Ma based on the oldest U-Pb zircon ages from Chapedony complex gneiss and the late-stage plutons at Daranjir Mountain.  $^{40}\text{Ar}/^{39}\text{Ar}$  age determinations indicate that as late as 41 Ma, a supradetachment basin had formed in the hanging wall of the detachment. Not long after this time, the basin fill was steeply tilted and intruded by the dacite plug, which yields the same age, within uncertainties, as the biotite tuff within the basin. Given uncertainties of ca.  $\pm 2$  Ma on both ages, the maximum time available for post tuff sedimentation, tilting, and final motion on the detachment and its hanging wall splays is 4 My. The age constraints therefore imply that mylonitization of extant igneous rock occurred between 49 and 44 Ma, and movement on

the Neybaz-Chatak fault and supradetachment basin development was completed no later than  $41 \pm 2$  Ma.

### **Kinematics of extension**

Present data from the Saghand area do not provide sufficient constraints on the magnitude and direction of extension that led to exhumation of the core complexes. The complete lithological mismatch between hanging wall and footwall of the Neybaz-Chatak detachment system suggests an amount of extension that is at least as wide as the complexes themselves, or at least 30 km. Assuming extension of this magnitude occurred over, at most, 4 My as outlined above, we obtain a minimum average horizontal extension rate of  $\sim 8$  mm/yr. The 4 My timescale is quite similar to that observed for similar geochronologic constraints on Cordilleran examples (e.g., Holm and Dokka, 1993; Niemi et al., 2001; Walker et al., 1990; Wells et al., 2000; Gans and Bohrsen, 1998), and the  $\sim 8$  mm/yr rate is similar to those measured in both the Cordillera and the Aegean region (e.g., Kumerics et al, 2005; Ring et al., 2003).

In Cordilleran examples, the extension direction is usually indicated by three major criteria, independent of piercing points that might be observed between hanging wall and footwall. These include 1) development of extensive areas of extension-parallel mylonitization (e.g., Rehrig and Reynolds, 1980; Davis, 1980); 2) the development of extension-parallel antiforms and synforms in the detachment surface at a variety of scales (e.g., John, 1987; Spencer and Reynolds, 1989); and 3) tilt direction of hanging wall fault blocks including supradetachment basin deposits, such that the tilt direction is opposite

the transport direction on the detachment fault (e.g., Davis et al., 1980; Shackelford, 1980). A fourth, perhaps less robust consideration is that in the Cordilleran examples, belts of core complex mountain ranges tend to be elongate perpendicular to the regional extension direction, as for example in the Lower Colorado River trough region of the Sonoran Desert (Spencer and Reynolds, 1989).

As detailed above, the orthogonality in the trend of lineations between Kalut-e-Chapedony and Khoshoumi Mountain, and the lack of clear cut asymmetry in shear direction make it difficult to apply the first criterion. Given the observation of significant post-Eocene deformation in the area, it is possible that the orthogonality of lineation trend is, at least in part, the result of vertical-axis rotations of the range blocks. In a paleomagnetic study of Cretaceous limestones just north of Saghand, Soffel et al. (1996) concluded that the tilt-corrected paleomagnetic pole for these strata is concordant with a modest number of other Cretaceous directions in the CEIM. We interpret this data to preclude major ( $>30^\circ$ ) differential rotation of the Neybaz Mountain-Khoshoumi Mountain area with respect to the remainder of the CEIM. Further, the continuity and general eastward dip of the Neybaz-Chatak fault along its entire length argues against major post-extensional dismemberment and vertical-axis rotation of the core complex belt, and hence we do not favor post-extensional vertical-axis rotation as an explanation for the differing trends in mylonitic lineation.

Despite the general occurrence of extension-parallel mylonites in many core complexes, it is not uncommon to observe more than one flow direction in footwall mylonites (e.g.,

MacCready et al., 1997). Although in some instances footwall mylonites may be interpreted as the down dip continuation of brittle simple shear on their overlying detachments (e.g., Wernicke, 1981; Lister et al., 1984), much of the mylonitic gneiss in Cordilleran and other examples is now regarded as the result of mid-crustal channel flows directed toward the area of maximum unroofing during extension (e.g., Wernicke, 1992; MacCready et al., 1997; Brun et al., 1994). Therefore, our preferred interpretation of the nearly orthogonal trends of the mylonitic lineations is that the Kalut-e-Chapedony mylonites represent eastward flow of middle crustal rocks toward the region of denudation early in the extension process, and the Khoshoumi Mountain and Neybaz Mountain mylonites, located along the southern margin of the extended region, record northerly flow toward the same region.

The criterion of antiforms and synforms is also difficult to evaluate. Neybaz and Khoshoumi Mountains and Kalut-e-Chatak are elongate roughly east-west, but Kalut-e-Chapedony is slightly elongate north-south. On the whole, this would appear to suggest east-west extension, but the topographic pattern is in general not as regular as that for the best Cordilleran examples. Furthermore, given the evidence for post-extensional folding in the area, the morphology of the core complex ranges could relate more to an episode of Neogene folding than to the episode of Eocene extension.

As regards hanging wall tilt direction, the supradetachment basin deposits along the northeast flank of Khoshoumi Mountain are tilted ~ESE, implying WNW displacement on the detachment system. As with the other criteria, tilt direction in Cordilleran

examples is not always opposite the direction of slip on the fault, and in several instances has been shown to be either in the same direction as slip (e.g., Wernicke, 1985), or significantly oblique to the extension direction (e.g., Hodges et al., 1989).

Although further work is clearly required to resolve the issue, the NNE trend of the belt of core complexes, the ESE tilt direction of the supradetachment basin at Khoshoumi Mountain, the ~E-W elongation direction of 3 of the 4 core complex ranges, and the WSW trend of mylonitic lineation at Kalut-e-Chapedony suggest an overall E-W extension direction, with transport on the detachment top to the west. We interpret the northerly lineation direction at Khoushoumi and Neybaz Mountains to be the result of extension-normal flow of deep-crustal rocks from unextended areas in the south toward the region of maximum unroofing to the north.

### **Cretaceous and Miocene (U-Th)/He cooling ages**

Although the eastern and western domains both yield Miocene apatite ages, the Cretaceous zircon cooling ages from the eastern domain contrast strongly with the Eocene zircon cooling ages from the western domain. As discussed above, the  $^{40}\text{Ar}/^{39}\text{Ar}$  biotite ages and uniformity of (U-Th)/He apatite and zircon ages across the crustal section indicates that tilting and rapid cooling, perhaps due to contactational deformation in the region, occurred in the Late Jurassic. As noted above, a regional angular unconformity separates Albian(?) to Cenomanian strata from Middle Jurassic and older rocks.

Miocene (U-Th)/He apatite ages obtained from both the western and eastern domains suggest a period of exhumation that postdates extension by approximately 20 My. Assuming a mid-Tertiary geothermal gradient of 30° C/km, appropriate for continental arc terrain, and a mean surface temperature of 10° C, a pre-Miocene depth of ~2000 m is indicated by these ages. We interpret these ages to reflect cooling related to ~N-S shortening of the region, as suggested by the folding of Neogene strata near Saghand as discussed above (Figure 4b). The development of a major early Miocene east-west trending fold raises the question of whether this deformation is related to the Arabia-Eurasia collision. According to the palinspastic and plate tectonic arguments presented by McQuarrie et al. (2003), 20 Ma is the earliest possible time of collision between Arabia and central Iran. If the age of initial collision is closer to 10 Ma as preferred by McQuarrie et al., then the fold would represent shortening in an Andean-type setting and would suggest a pre-collisional transition from extension to compression in the overriding plate at some time between ~40 and ~20 Ma as suggested by Vincent et al. (2005) based on stratigraphic data from Azerbaijan. Such a transition occurred there near the end of the Eocene, which they interpreted as supporting previous suggestions that the initial collision occurred at ca. 40 Ma. Although data collected during this study only indirectly bear on this issue, the simple plate tectonic and palinspastic arguments indicate that at 40 Ma there was >1000 km of separation between central Iran and the Zagros Mountains. Clearly the details of how various Neo-Tethyan continental fragments may have interacted with one another are at issue, but wholesale arrival of the Arabian subcontinent against contiguous, south Asian continental crust (i.e., the broadest possible

definition of the “initial collision” of Arabia with Eurasia, as opposed to the collision of intra-Tethyan continental fragments) by 40 Ma is unlikely.

### **Regional significance**

In addition to the core complexes exposed near Saghand, core complexes have also been reported in northwest (Stockli et al., 2004) and northeast (Hassanzadeh et al., 2005) Iran (Figure 1). Existing geologic maps (Thiele et al., 1967; Tillman et al., 1981) and satellite image reconnaissance strongly suggest the presence of a fourth Iranian core complex in southwest Iran near the town of Golpaygan (Figure 1). Available thermochronologic data indicate that the Iranian core complexes may span a range in age from late Cretaceous to early Miocene. Prior to these reports, there were no known regions of significant Tertiary extension within the Tethysides between the Bitlis suture in eastern Turkey and the western Himalayan syntaxis. The widespread occurrence of core complexes in Iran demonstrates that core complex development has affected every major segment of the Tethysides (Figure 12 and Table 1).

Formation of the Cretaceous to Cenozoic core complexes of the Alpine-Himalayan orogen is usually attributed to either back-arc extension associated with rapid subduction or “slab rollback,” such as in the Tyrrhenian basin (e.g., Royden, 1993), or to large gradients in gravitational potential energy within the lithosphere resulting from localized crustal thickening (e.g., Dewey, 1988). The former has been invoked by some authors to account for the numerous core complexes of Spain, western Turkey and the Tyrrhenian and Aegean Seas (e.g., Brunet et al., 2000; Buick, 1991; Dinter, 1998; Lonergan and

White, 1997; Okay and Satir, 2000; Thomson et al., 1999), while other authors have suggested that the latter process is responsible for extensional structures in Spain, the Himalayas and eastern China (Platt and Vissers, 1989; Burchfiel et al., 1992; Davis et al., 2002). Extension in the eastern Alps has been ascribed to a combination of gravitational collapse and tectonic escape (e.g., Ratschbacher et al., 1991a, b). Extension in the Saghand region long predated any intracontinental shortening resulting from direct contact between Arabia and Eurasia, which argues against core complex formation as the result of thickened crust or the eastward extrusion of the CEIM (Figure 1). The extension direction appears to be oblique, or perhaps sub-parallel, to the Urumieh-Dokhtar magmatic arc, but perpendicular to the north-south trending Lut segment of the Iranian arc, currently ~200 km east of the Saghand area. Kazmin et al. (1986) conclude that volcanism within the Lut arc resulted from the westward subduction of oceanic crust separating the CEIM from Afghanistan, as shown on the paleogeographic reconstructions of Dercourt et al. (1986). Eocene extension within the Saghand region therefore may be a pre-collisional back-arc spreading event associated with the eastern segment of the Iranian arcs.

## **ACKNOWLEDGEMENTS**

We would like to thank the University of Tehran Research Council for their support of this project and Ahmad Reza Malekpour for his efforts in the field. Ken Farley, Rebecca Flowers, and Lindsey Hedges provided assistance with the (U-Th)/He analyses. Bernard Guest and Kevin Mahan conducted informal reviews of a pre-submission version of the manuscript. Kevin Mahan also offered helpful advice in microstructural analysis.

Comments from Mark Allen, David Foster and Uwe Ring greatly improved the manuscript. Financial support for this project was provided by the Caltech Tectonics Observatory and NSF grant EAR-0511054.

## **REFERENCES**

Alavi, M., 1991, Sedimentary and structural characteristics of the Paleo-Tethys remnants in northeastern Iran: *Geological Society of America Bulletin*, v. 103, p. 983-992.

Argles, T.W., and Edwards, M.A., 2002, First evidence for high-grade, Himalyan-age synconvergent extension recognized within the western syntaxis; Nanga Parbat, Pakistan: *Journal of Structural Geology*, v. 24, p. 1327-1344.

Armstrong, R.L., 1982, Cordilleran metamorphic core complexes; from Arizona to southern Canada: *Annual Review of Earth and Planetary Sciences*, v.10, p.129-154.

Armstrong, R.L., and Ward, P.L., 1991, Evolving geographic patterns of Cenozoic magmatism in the North American Cordillera; the temporal and spatial association of magmatism and metamorphic core complexes: *Journal of Geophysical Research, B, Solid Earth and Planets*, v.96, p. 13201-13224.

Axen, G.J., Bartley, J.M., and Selverstone, J., 1995, Structural expression of a rolling hinge in the footwall of the Brenner Line normal fault, eastern Alps: *Tectonics*, v. 14, p. 1380-1392.

Axen, G.J., Lam, P.S., Grove, M., Stockli, D.F., and Hassanzadeh, J., 2001, Exhumation of the west-central Alborz Mountains, Iran, Caspian subsidence, and collision-related tectonics: *Geology*, v. 29, p. 559-562.

Brun, J.-P., Sokoutis, D., and van den Driessche, J., 1994, Analogue modeling of detachment fault systems and core complexes: *Geology*, v. 22, p. 319-322.

Brunel, M., Arnaud, N., Tapponnier, P., Pan, Y., and Wang, Y., 1994, Kongur Shan normal fault: type example of mountain building assisted by extension (Karakoram fault, eastern Pamir): *Geology*, v. 22, p. 707-710.

Brunet, C., Monie, P., Jolivet, L., and Cadet, J.-P., 2000, Migration of compression and extension in the Tyrrhenian Sea, insights from  $^{40}\text{Ar}/^{39}\text{Ar}$  ages on micas along a transect from Corsica to Tuscany: *Tectonophysics*, v. 321, p. 127-155.

Buick, I.S., 1991, The late Alpine evolution of an extensional shear zone, Naxos, Greece: *Journal of the Geological Society, London*, v. 148, p. 93-103.

Burchfiel, B.C., Chen, Z., Hodges, K.V., Yuping, L., Royden, L.H., Changrong, D., and Jiene, X., 1992, The South Tibetan detachment system, Himalayan Orogen; extension contemporaneous with and parallel to shortening in a collisional mountain belt: *GSA Special Paper*, v. 269, 41 p.

Caby, R., Hammor, D., and Delor, C., 2001, Metamorphic evolution, partial melting and Miocene exhumation of lower crust in the Edough metamorphic core complex, west Mediterranean orogen, eastern Algeria: *Tectonophysics*, v. 342, p. 239-273.

Carmignani, L., Decandia, F.A., Fantozzi, P.L., Lazzarotto, A., Liotta, D., and Meccheri, M., 1994, Tertiary extensional tectonics in Tuscany (Northern Apennines, Italy): *Tectonophysics*, v. 238, p. 295-315.

Carmignani, L., and Roy, K., 1990, Crustal extension in the Northern Apennines; the transition from compression to extension in the Alpi Apuane core complex: *Tectonics*, v. 9, p. 1275-1303.

Chen, Z., Liu, Y., Hodges, K.V., Burchfiel, B.C., Royden, L.H., and Deng, C., 1990, The Kangmar Dome; a metamorphic core complex in southern Xizang (Tibet): *Science*, v. 250, p. 1552-1556.

Coney, P.J., 1980, Cordilleran metamorphic core complexes; an overview: *Geological Society of America Memoir*, no. 153, p. 7-31.

Davis, G.A., Anderson, J.L., Frost, E.G., and Shackelford, T.J., 1980, Mylonitization and detachment faulting in the Whipple-Buckskin-Rawhide Mountains terrane, southeastern

California and western Arizona: Geological Society of America Memoir, no. 153, p. 79-129.

Davis, G.A., Darby, B.J., Yadong, Z., and Spell, T.L., 2002, Geometric and temporal evolution of an extensional detachment fault, Hohhot metamorphic core complex, Inner Mongolia, China: *Geology*, v. 30, p. 1003-1006.

Davis, G.A., and Lister, G.S., 1988, Detachment faulting in continental extension; perspectives from the Southwestern U.S. Cordillera, *in* Clark, S.P., Burchfiel, B.C., Suppe, J., Processes in continental lithospheric deformation, Geological Society of America Special Paper, v. 218, p.133-159.

Davis, G.H., 1980, Structural characteristics of metamorphic core complexes, southern Arizona: Geological Society of America Memoir, no. 153, p. 35-77.

Davis, G.H., and Coney, P.J., 1979, Geologic development of the Cordilleran metamorphic core complexes: *Geology*, v. 7, p. 120-124.

Dercourt, J., L. P. Zonenshain, L. E. Ricou, V. G. Kazmin, X. Le Pichon, A. L. Knipper, C. Grandjacquet, I. M. Sbertshikov, J. Geysant, C. Lepvrier, D. H. Pechersky, J. Boulin, J.-C. Sibuet, L. A. Savostin, O. Sorokhtin, M. Westphal, M. L. Bazhenov, J. P. Lauer, and B. Biju-Duval, 1986, Geological evolution of the Tethys belt from the Atlantic to the Pamirs since the Lias: *Tectonophysics*, v. 123, p. 241–315.

Dewey, J.F., 1988, Extensional collapse of orogens: *Tectonics*, v. 7, p. 1123-1139.

Dinter, D.A., 1998, Late Cenozoic extension of the Alpine collisional orogen, northeastern Greece: origin of the north Aegean basin: *GSA Bulletin*, v. 110, p. 1208-1230.

Dinter, D.A., Macfarlane, A., Hames, W., Isachsen, C., Bowring, S., and Royden, L., 1995, U-Pb and  $^{40}\text{Ar}/^{39}\text{Ar}$  geochronology of the Symvolon granodiorite: Implications for the thermal and structural evolution of the Rhodope metamorphic core complex, northeastern Greece: *Tectonics*, v. 14, p. 886-908.

Fitzgerald, P.G., Fryxell, J.E, and Wernicke, B.P., 1991, Miocene crustal extension and uplift in southeastern Nevada; constraints from fission track analysis: *Geology*, v. 19, p. 1013-1016.

Forster, H., Fesefeldt, K., and Kursten, M., 1972, Magmatic and orogenic evolution of the central Iranian volcanic belt: 24<sup>th</sup> International Geologic Congress, Section 2, p. 198-210.

Fournier, M., Jolivet, L., Goffe, B., and Dubois, R., 1991, Alpine Corsica metamorphic core complex: *Tectonics*, v. 10, p. 1173-1186.

Friedmann, S.J., Davis, G.A., Fowler, T.K., Brudos, T., Parke, M., Burbank, D.W., and Burchfiel, B.C., 1994, Stratigraphy and gravity-glide elements of a Miocene supradetachment basin, Shadow Valley, East Mojave Desert *in* McGill, S.F. and Ross, T.M., Geological investigations of an active margin: Geological Society of America, Cordilleran Section, Annual Meeting, Guidebook., v. 27, p. 302-318.

Fugenschuh, B., and Schmid, S.M., 2005, Age and significance of core complex formation in a very curved orogen: evidence from fission track studies in the South Carpathians (Romania): *Tectonophysics*, v. 404, p. 33-53.

Gans, P.B., and Bohron, W.A., 1998, Suppression of volcanism during rapid extension in the Basin and Range Province, United States: *Science*, v. 279, p. 66-68.

Gautier, P., and Brun, J.-P., 1994, Crustal-scale geometry and kinematics of late-orogenic extension in the central Aegean (Cyclades and Evvia Island): *Tectonophysics*, v. 238, p. 399-424.

Gessner, K., Ring, U., Johnson, C., Hetzel, R., Passchier, C.W., and Gungor, T., 2001, An active bivergent rolling-hinge detachment system: central Menderes metamorphic core complex in western Turkey: *Geology*, v. 29, p. 611-614.

Grassl, H., Neubauer, F., Millahn, K., and Weber, F., 2004, Seismic image of the deep crust at the eastern margin of the Alps (Austria): indications for crustal extension in a convergent orogen: *Tectonophysics*, v. 380, p. 105-122.

Haghipour, A., 1977a, Geological map of the Biabanak-Bafq area: Geological Survey of Iran, scale 1:500,000.

Haghipour, A., 1977b, Geological map of the Posht-e-Badam area: Geological Survey of Iran, scale 1:100,000.

Haghipour, A., and Aghanabati, A. (compilers), 1985, Geological map of Iran, Ministry of Mines and Metals, Geological Survey of Iran.

Haghipour, A., Valeh, N., Pelissier, G., and Davoudzadeh, 1977, Explanatory text of the Ardekan quadrangle map, Geological Survey of Iran, Geological Quadrangle H8, 114 p.

Harrison, T.M., Duncan, I., and McDougal, I., 1985, Diffusion of  $^{40}\text{Ar}$  in biotite: Temperature, pressure and compositional effects: *Geochimica et Cosmochimica Acta*, v. 49, p. 2461-2468.

Hassanzadeh, J., Ghazi, A.M., Axen, G., and Guest, B., 2002, Oligomiocene mafic-alkaline magmatism in north and northwest of Iran: evidence for the separation of the

Alborz from the Urumieh-Dokhtar magmatic arc: Geological Society of America Abstracts with Programs, v. 34, no. 6, p. 331.

Hassanzadeh, J., Malekpour, A., Grove, M., Axen, G.J., Horton, B.K., Stockli, D.F., Farley, K., Schmitt, A.K., Mohajjel, M., and Ghazi, A.M., 2005, Biarjmand metamorphic core complex; new evidence for Late Cretaceous-Paleocene extensional tectonics along the northern margin of central Iranian Plateau: Geological Society of America Abstracts with Programs, v. 37, no. 7, p. 71.

Hippertt, J., and Tohver, E., 1999, On the development of zones of reverse shearing in mylonitic rocks: Journal of Structural Geology, v.21, p. 1603-1614.

Hodges, K.V., McKenna, L.W., Stock, J., Knapp, J., Page, L., Sternlof, K., Wuest, G., and Walker, J.D., 1989, Evolution of extensional basins and basin and range topography west of Death Valley, California: Tectonics, v. 8, p. 453-467.

Holm, D.K., and Dokka, R.K., 1993, Interpretation and tectonic implications of cooling histories; an example from the Black Mountains, Death Valley extended terrane, California: Earth and Planetary Science Letters, v. 116, p.63-80.

House, M.A., Farley, K.A., Stockli, D., 2000, Helium chronometry of apatite and titanite using Nd-YAG laser heating: Earth and Planetary Science Letters, v. 183, p. 365-368.

Hubbard, M.S., Spencer, D.A., and West, D.P., 1995, Tectonic exhumation of the Nanga Parbat massif, northern Pakistan: *Earth and Planetary Science Letters*, v. 133, p. 213-225.

Jaffey, A. H., Flynn, K. F., Glendenin, L. E., Bentley, W. C., and Essling, A. M., 1971, Precision Measurement of Half-Lives and Specific Activities of  $^{235}\text{U}$  and  $^{238}\text{U}$ : *Physical Review C*, v. 4, no. 5, p. 1889-1906.

Janak, M., Plasienska, D., Frey, M., Cosca, M., Schmidt, S.T., Luptak, B., and Meres, S., 2001, Cretaceous evolution of a metamorphic core complex, the Veporic unit, Western Carpathians (Slovakia): P-T conditions and in situ  $^{40}\text{Ar}/^{39}\text{Ar}$  UV laser probe dating of metapelites: *Journal of Metamorphic Geology*, v. 19, p. 197-216.

John, B.E., 1987, Structural and intrusive history of the Chemehuevi Mountains area, southeastern California and western Arizona: Doctoral thesis, University of California, Santa Barbara, 344 p.

Jolivet, L., Faccenna, C., Goffe, B., Mattei, M., Rossetti, F., Brunet, C., Storti, F., Funicello, R., Cadet, J.P., d'Agostino, N., and Parra, T., 1998, Midcrustal shear zones in postorogenic extension: example from the northern Tyrrhenian Sea: *Journal of Geophysical Research*, v. 103, p. 12123-12160.

Junlai, L., Davis, G.A., Zhiyong, L., and Fuyuan, W., 2005, The Liaonan metamorphic core complex, Southeastern Liaoning Province, North China: a likely contributor to

Cretaceous rotation of Eastern Liaoning, Korea and contiguous areas: *Tectonophysics*, v. 407, p. 65-80.

Kargaran, F., Neubauer, F., Genser, J., and Houshmandzadeh, A., 2006, The Eocene Chapedony metamorphic core complex in central Iran: preliminary structural results: *European Geosciences Union Geophysical Research Abstracts*, v. 8.

Kazmin, V.G., Sbertshikov, I.M., Ricou, L.-E., Zonenshain, L.P., Boulin, J., and Knipper, A.L., 1986, Volcanic belts as markers of the Mesozoic-Cenozoic active margin of Eurasia: *Tectonophysics*, v. 123, p. 123-152.

Kounov, A., Seward, D., Bernoulli, D., Burg, J.-P., and Ivanov, Z., 2004, Thermotectonic evolution of an extensional dome: the Cenozoic Osogovo-Lisets core complex (Kraishte zone, western Bulgaria): *Geologische Rundschau*, v. 93, p. 1008-1024.

Kumerics, C., Ring, U., Bricchau, S., Glodny, J., and Monie, P., 2005, The extensional Messaria shear zone and associated brittle detachment faults, Aegean Sea, Greece: *Journal of the Geological Society, London*, v. 162, p. 701-721.

Lee, J., Miller, E.L., and Sutter, J.F., 1987, Ductile strain and metamorphism in an extensional tectonic setting: a case study from the northern Snake Range, Nevada, USA *in* Coward, M.P., Dewey, J.F., and Hancock P.L., eds., *Continental extensional tectonics*, Geological Society Special Publication No. 28, p. 267-298.

Lee, J., Hacker, B.R., Dinklage, W.S., Wang, Y., Gans, P., Calvert, A., Wan, J., Chen, W., Blythe, A.E., and McClelland, W., 2000, Evolution of the Kangmar Dome, southern Tibet: structural, petrologic and thermochronologic constraints, *Tectonics*, v. 19, p. 872-895.

Lee, J., Hacker, B., and Wang, Y., 2004, Evolution of north Himalyan gneiss domes: structural and metamorphic studies in Mabja Dome, southern Tibet: *Journal of Structural Geology*, v. 26, p. 2297-2316.

Lee, J., and Lister, G.S., 1992, Late Miocene ductile extension and detachment faulting, Mykonos, Greece: *Geology (Boulder)*, v. 20, p. 120-124.

Lehrmann, D. J., Ramezani, J., Bowring, S. A., Martin, M. W., Montgomery, P., Enos, P., Payne, J. L., Orchard, M. J., Wang, H., and Wei, J., 2006, Timing of recovery from the end-Permian extinction; geochronologic and biostratigraphic constraints from south China: *Geology (Boulder)*, v. 34, no. 12, p. 1053-1056.

Lister, G.S., Banga, G., and Feenstra, A., 1984, Metamorphic core complexes of Cordilleran type in the Cyclades, Aegean Sea, Greece: *Geology (Boulder)*, v. 12, p. 221-225.

Lonergan, L., and White, N., 1997, Origin of the Betic-Rif mountain belt: *Tectonics*, v. 16, p. 504-522.

Ludwig, K. R., 1980, Calculation of uncertainties of U-Pb isotope data: *Earth and Planetary Science Letters*, v. 46, no. 2, p. 212-220.

MacCready, T., Snoke, A.W., Wright, J.E., and Howard, K.A., 1997, Mid-crustal flow during Tertiary extension in the Ruby Mountains core complex, Nevada: *Geological Society of America Bulletin*, v. 109, p. 1576-1594.

Mancktelow, N.S., and Pavlis, T.L., 1994, Fold-fault relationships in low-angle detachment systems: *Tectonics*, v. 13, p. 668-685.

McQuarrie, N., Stock, J.M., Verdel, C., and Wernicke, B.P., 2003, Cenozoic evolution of Neotethys and implications for the causes of plate motions: *Geophysical Research Letters*, v. 30, 2036, doi:10.1029/2003GL017992.

Niemi, N.A., Wernicke, B.P., Brady, R.J., Saleeby, J.B., and Dunne, G.C., 2001, Distribution and provenance of the middle Miocene Eagle Mountain Formation, and implications for regional kinematic analysis of the Basin and Range Province: *Geological Society of America Bulletin*, v. 113, p. 419-442.

Noble, L.F., 1941, Structural features of the Virgin Spring area, Death Valley, California: Geological Society of America Bulletin, v. 52, p. 941-999.

Okay, A.I., and Satir, M., 2000, Coeval plutonism and metamorphism in a latest Oligocene metamorphic core complex in northwest Turkey: Geological Magazine, v. 137, p. 495-516.

Passchier, C.W., and Trouw, R.A.J., 2005, Microtectonics: Berlin, Springer, 366 p.

Platt, J.P., and Compagnoni, R., 1990, Alpine ductile deformation and metamorphism in a Calabrian basement nappe (Aspromonte, South Italy): Eclogae Geologicae Helvetiae, v. 83, p. 41-58.

Platt, J.P., and Vissers, R.L.M., 1989, Extensional collapse of thickened continental lithosphere: a working hypothesis for the Alboran sea and Gibraltar arc: Geology, v. 17, p.540-543.

Platzman, E., and Platt, J.P., 2004, Kinematics of a twisted core complex: Oblique axis rotation in an extended terrane (Betic Cordillera, southern Spain): Tectonics, v. 23, TC6010, doi:10.1029/2003TC001549.

Ramezani, J., and Tucker, R.D., 2003, The Saghand region, central Iran: U-Pb geochronology, petrogenesis and implications for Gondwana tectonics: *American Journal of Science*, v. 303, p. 622-665.

Ratschbacher, L., Behrmann, J.H., and Pahr, A., 1990, Penninic windows at the eastern end of the Alps and their relation to the intra-Carpathian basins: *Tectonophysics*, v. 172, p. 91-105.

Ratschbacher, L., Merle, O., Davy, P., and Cobbold, P., 1991a, Lateral extrusion in the eastern Alps, part I, boundary conditions and experiments scaled for gravity: *Tectonics*, v. 10, p. 245-256.

Ratschbacher, L., Frisch, W., and Linzer, H.-G., 1991b, Lateral extrusion in the eastern Alps, part II, structural analysis: *Tectonics*, v. 10, p. 257-271.

Rehrig, W.A., and Reynolds, S.J., 1980, Geologic and geochronologic reconnaissance of a northwest-trending zone of metamorphic core complexes in southern and western Arizona: *Geological Society of America Memoir*, no. 153, p. 131-157.

Reiners, P.W., Brady, R., Farley, K.A., Fryxell, J.E., Wernicke, B., and Lux, D., 2000, Helium and argon thermochronometry of the Gold Butte Block, South Virgin Mountains, Nevada: *Earth and Planetary Science Letters*, v. 178, p. 315-326.

Reiners, P.W., Farley, K.A., and Hickey, H.J., 2002, He diffusion and (U-Th)/He thermochronometry of zircon; initial results from Fish Canyon Tuff and Gold Butte: *Tectonophysics*, v. 349, p. 297-308.

Renne, P.R., Swisher, C.C., Deino, A.L., Karner, D.B., Owens, T., and DePaolo, D.J., 1998, Intercalibration of Standards, Absolute Ages and Uncertainties in  $^{40}\text{Ar}/^{39}\text{Ar}$  Dating: *Chemical Geology (Isotope Geoscience Section)*, v. 145 (1-2), p. 117-152.

Reynolds, S.J., 1985, *Geology of the South Mountains, central Arizona*: Arizona Bureau of Geology and Mineral Technology, Geological Survey Branch, Bulletin 195, 61 p.

Ring, U., and Collins, A.S., 2005, U-Pb SIMS dating of synkinematic granites: timing of core-complex formation in the northern Anatolide belt of western Turkey: *Journal of the Geological Society, London*, v. 162, p. 289-298.

Ring, U., Thomson, S.N., and Brocker, M., 2003, Fast extension but little exhumation: the Vari detachment in the Cyclades, Greece: *Geological Magazine*, v. 140, p. 245-252.

Royden, L.H., 1993, Evolution of retreating subduction boundaries formed during continental collision: *Tectonics*, v. 12, p. 629-638.

Schmid, S.M., Berza, T., Diaconescu, V., Froitzheim, N., and Fugenschuh, B., 1998, Orogen-parallel extension in the Southern Carpathians: *Tectonophysics*, v. 297, p. 209-228.

Schoene, B., Crowley, J. L., Condon, D. J., Schmitz, M. D., and Bowring, S. A., 2006, Reassessing the uranium decay constants for geochronology using ID-TIMS U–Pb data: *Geochimica et Cosmochimica Acta*, v. 70, p. 426-445.

Sengor, A.M.C., 1987, Tectonics of the Tethysides; orogenic collage development in a collisional setting: *Annual Review of Earth and Planetary Sciences*, v. 15, p. 213-244.

Sengor, A.M.C., and Natal'in, B.A., 1996, Paleotectonics of Asia: fragments of a synthesis, *in* Yin, A., and Harrison, M., *The tectonic evolution of Asia*: Cambridge University Press, p.486-640.

Shackelford, T.J., 1980, Tertiary tectonic denudation of a Mesozoic-early Tertiary(?) gneiss complex, Rawhide Mountains, western Arizona: *Geology*, v. 8, p.190-194.

Soffel, H.C., Davoudzadeh, M., Rolf, C., and Schmidt, S., 1996, New palaeomagnetic data from central Iran and a Triassic palaeoreconstruction, *Geologische Rundschau*, v. 85, p. 293-302.

Spencer, J.E., and Reynolds, S.J., 1989, Middle Tertiary tectonics of Arizona and adjacent areas: Arizona Geological Society Digest, v. 17, p. 539-574.

Spencer, J.E., and Welty, J.W., 1986, Possible controls of base- and precious-metal mineralization associated with Tertiary detachment faults in the lower Colorado River trough, Arizona and California: *Geology*, v. 14, p. 195-198.

Stockli, D.F., 2005, Application of low-temperature thermochronometry to extensional tectonic settings: *Reviews in Mineralogy and Geochemistry*, v. 58, p.411-448.

Stockli, D.F., Hassanzadeh, J., Stockli, L.D., Axen, G.J., Walker, J.D., and Dewane, T.J., 2004, Structural and geochronological evidence for Oligo-Miocene intra-arc low-angle detachment faulting in the Takab-Zanjan area, NW Iran: *Geological Society of America Abstracts with Programs*, v. 36, no. 5, p. 319.

Stöcklin, J., 1968, Structural history and tectonics of Iran: a review: *AAPG Bulletin*, v. 52, p. 1229-1258.

Tagami, T., Farley, K.A., and Stockli, D.F., 2003, (U-Th)/He geochronology of single zircon grains of known Tertiary eruption age: *Earth and Planetary Science Letters*, v. 207, p. 57-67.

Takin, M., 1972, Iranian geology and continental drift in the Middle East: *Nature*, v.235, p.147-150.

Thiele, O., Alavi, M., Assefi, R., Hushmand-zadeh, A., Sayed-Emami, K., and Zahedi, M., 1967, Geological map of Golpaygan: Geological Survey of Iran, scale 1:250,000.

Thomson, S.N., 1994, Fission track analysis of the crystalline basement rocks of the Calabrian Arc, southern Italy; evidence of Oligo-Miocene late-orogenic extension and erosion: *Tectonophysics*, v. 238, p. 331-352.

Thomson, S.N., Stoeckhert, B., and Brix, M.R., 1999, Miocene high-pressure metamorphic rocks of Crete, Greece; rapid exhumation by buoyant escape, *in* Ring, U., Brandon, M.T., Lister, G.S., and Willett, S.D., eds., *Exhumation processes: normal faulting, ductile flow and erosion*: Geological Society Special Publications, v. 154, p. 87-107.

Tillman, J.E., Poosti, A., Rossello, S., and Eckert, A., 1981, Structural evolution of Sanandaj-Sirjan Ranges near Esfahan, Iran: *AAPG Bulletin*, v. 65, p. 674-687.

Valeh, N., and Haghypour, A., 1970, Geological map of Ardekan: Geological Survey of Iran, scale 1:250,000.

van Hinsbergen, D.J.J., and Meulenkamp, J.E., 2006, Neogene supradetachment basin development on Crete (Greece) during exhumation of the South Aegean core complex: *Basin Research*, v. 18, p. 103-124.

Vincent, S.J., Allen, M.B., Ismail-Zadeh, A.D., Flecker, R., Foland, K.A., and Simmons, M.D., 2005, Insights from the Talysh of Azerbaijan into the Paleogene evolution of the south Caspian region: *Geological Society of America Bulletin*, v. 117, p. 1513-1533.

Walker, J.D., Bartley, J.M., and Glazner, A.F., 1990, Large-magnitude Miocene extension in the central Mojave Desert; implications for Paleozoic to Tertiary paleogeography and tectonics: *Journal of Geophysical Research, B, Solid Earth and Planets*, v. 95, p. 557-569.

Wallis, S.R., Platt, J.P., and Knott, S.D., 1993, Recognition of syn-convergence extension in accretionary wedges with examples from the Calabrian Arc and the Eastern Alps: *American Journal of Science*, v. 293, p. 463-494.

Wawrzenitz, N., and Krohe, A., 1998, Exhumation and doming of the Thasos metamorphic core complex (S Rhodope, Greece): structural and geochronological constraints: *Tectonophysics*, v. 285, p. 301-332.

Wawrzyniec, T.F., Selverstone, J., and Axen, G.J., 2001, Styles of footwall uplift along the Simplon and Brenner normal fault systems, central and Eastern Alps: *Tectonics*, v. 20, p. 748-770.

Wells, M.L., Snee, L.W., and Blythe, A.E., 2000, Dating of major normal fault systems using thermochronology; an example from the Raft River detachment, Basin and Range, Western United States: *Journal of Geophysical Research, B, Solid Earth and Planets*, v.105, p.16303-16327.

Wernicke, B., 1981, Low-angle normal faults in the Basin and Range Province; nappe tectonics in an extending orogen: *Nature*, v. 291, p. 645-648.

Wernicke, B., 1985, Uniform-sense normal simple shear of the continental lithosphere: *Canadian Journal of Earth Sciences*, v. 22, p. 108-125.

Wernicke, B., 1992, Cenozoic extensional tectonics of the U.S. Cordillera, *in* Burchfiel, B.C., Lipman, P.W., and Zoback, M.L., *The Cordilleran Orogen; conterminous U.S.*, p. 553-581.

Wernicke, B., and Axen, G.J., 1988, On the role of isostasy in the evolution of normal fault systems: *Geology*, v. 16, p. 848-851.

Wernicke, B., and Burchfiel, B.C., 1982, Modes of extensional tectonics: *Journal of Structural Geology*, v. 4, p. 105-115.

Whitney, D.L., and Dilek, Y., 1997, Core complex development in central Anatolia, Turkey: *Geology*, v. 25, p. 1023-1026.

Wolf, R.A., Farley, K.A., Silver, L.T., 1996, Helium diffusion and low-temperature thermochronometry of apatite: *Geochimica et Cosmochimica Acta*, v. 60, p. 4231-4240.

Wright, L.A., Otton, J.K., and Troxel, B.W., 1974, Turtleback surfaces of Death Valley viewed as phenomena of extensional tectonics: *Guidebook; Death Valley region, California and Nevada*, p. 79-80

Wright, L.A., and Troxel, B.W., 1984, *Geology of the northern half of the Confidence Hills 15-minute Quadrangle, Death Valley region, eastern California; the area of the Amargosa chaos: Map Sheet - California Division of Mines and Geology*, v.34, 31 p.

Yin, A., Harrison, T.M., Murphy, M.A., Grove, M., Nie, S., Ryerson, F.J., Feng, W.X., and Chen, Z.L., 1999, Tertiary deformation history of southeastern and southwestern Tibet during the Indo-Asian collision: *GSA Bulletin*, v. 111, p.1644-1664.

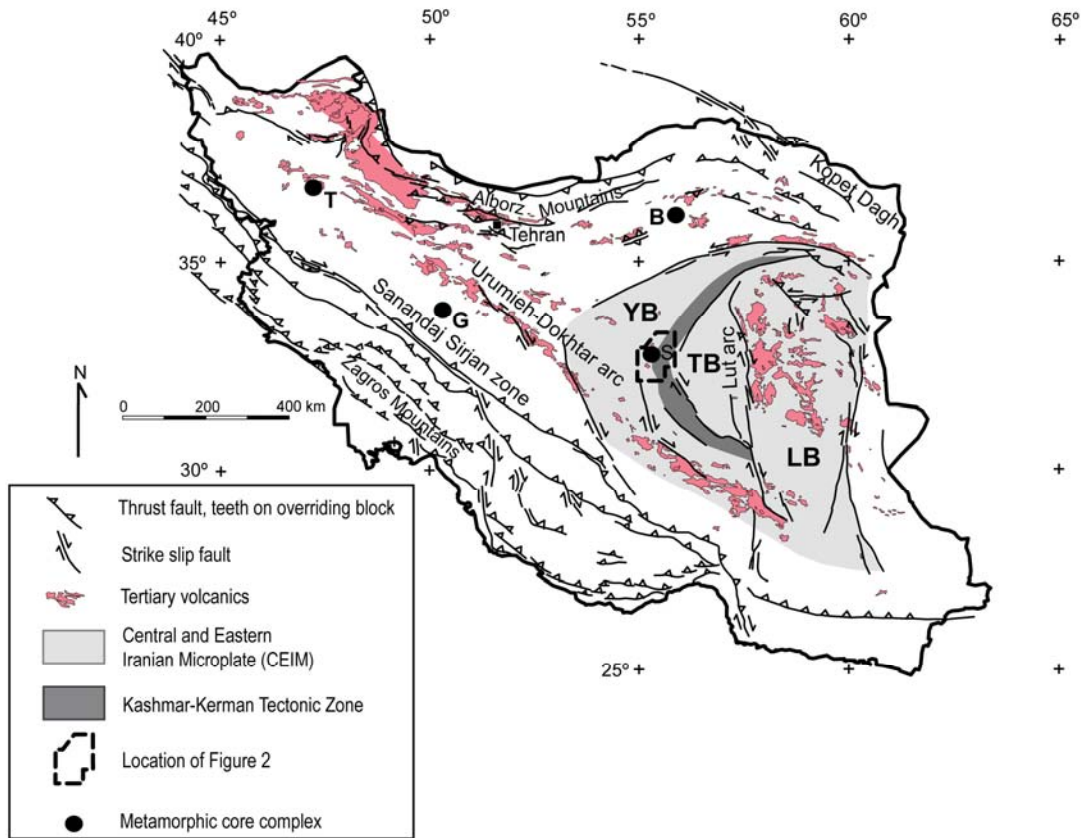


**Figure 1.** Distribution of Tertiary volcanic rocks, major faults (modified from Haghypour and Aghanabati, 1985) and known or suspected metamorphic core complexes in Iran. The location of the Saghand region is outlined within the Yazd Block of the Central Iranian Microcontinent. Abbreviations: B=Biarjmand core complex (Hassanzadeh et al., 2005), G=Golpaygan core complex (Thiele et al., 1967), S=Saghand core complex (this paper), T=Takab-Zanjan core complex (Stockli et al., 2004), LB=Lut Block, TB=Tabas Block, YB=Yazd Block

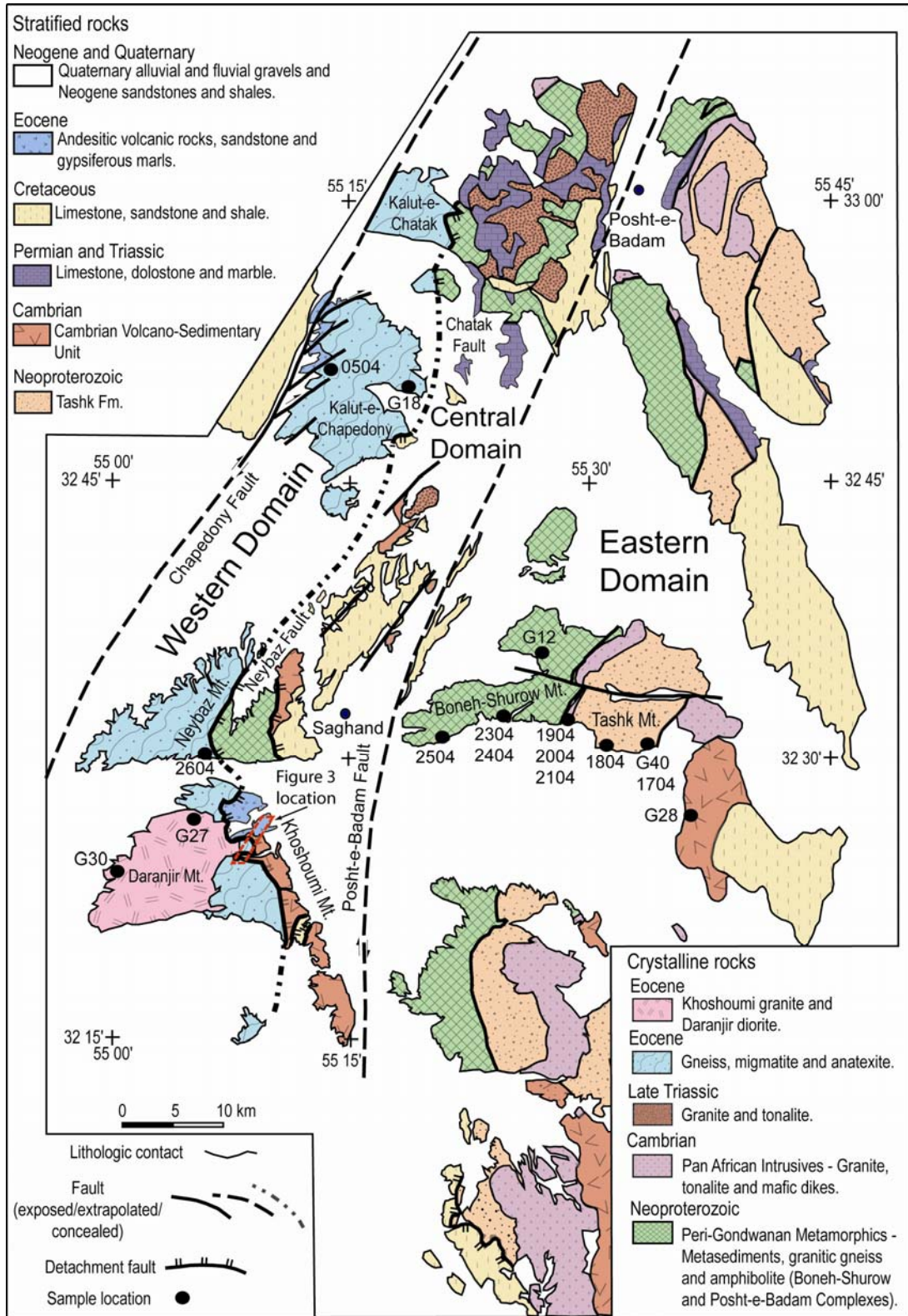


**Figure 2.** Geologic map of the Saghand area, modified from Ramezani and Tucker (2003).

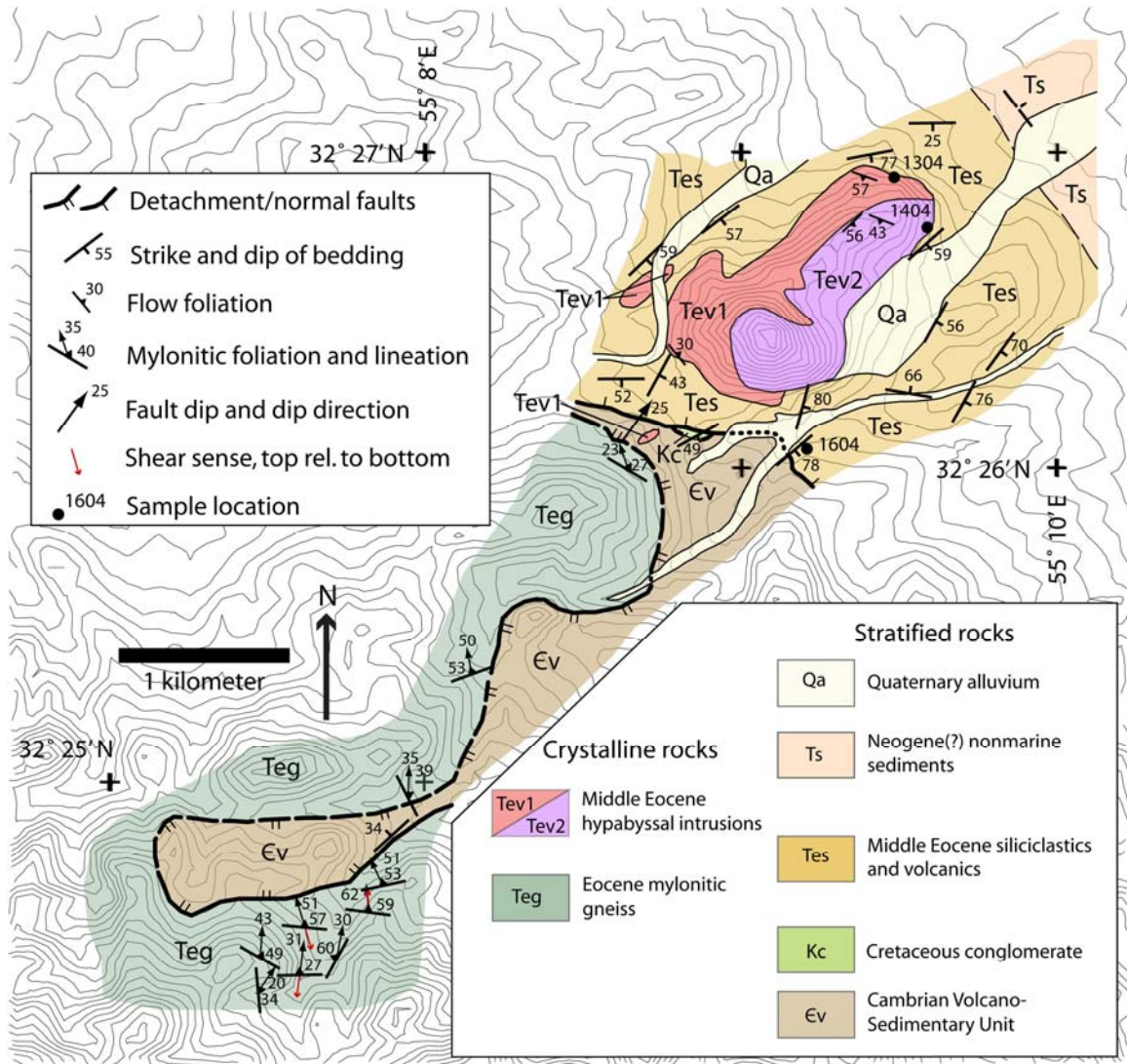


**Figure 3.** Geologic map of a portion of the east side of Khoushoumi Mountain showing  $^{40}\text{Ar}/^{39}\text{Ar}$  sampling locations. See Figure 2 for location.

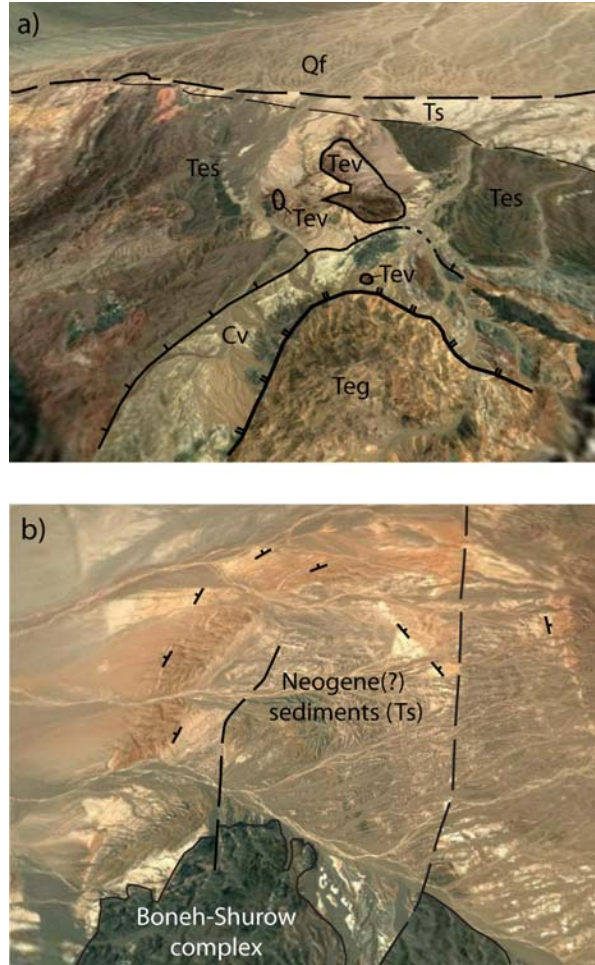


**Figure 4.** Oblique high-resolution satellite images. a) View northeast along the eastern edge of Khoshoumi Mountain showing ESE dipping Eocene supradetachment basin deposits (Tes) intruded by Eocene hypabyssal rocks (Tev), faulted over CVSU (Cv) and Eocene gneiss (Teg). The Eocene sediments and volcanics are unconformably overlain by Neogene(?) sediments (Ts) and alluvial fan deposits (Qf). See Figure 3 for geologic map of this area. Width of view at center of image is 4.5 km. b) View west of the western margin of Boneh-Shurow Mountain showing broad, ~EW trending fold and opposing dips of Neogene(?) sediments. Width of view at center of image is 4.6 km. Images from Google Earth, ©2006 Google™, ©2007 Europa Technologies, ©2007 Digital Globe, ©2007 TerraMetrics

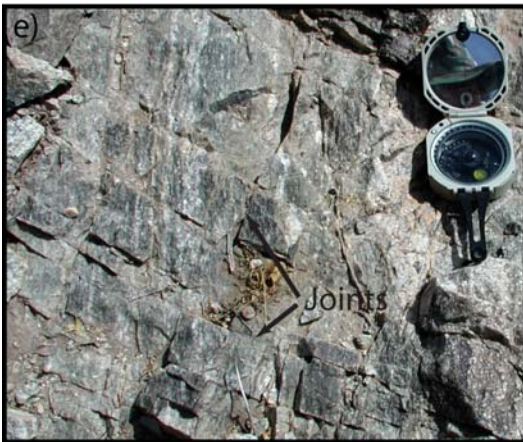
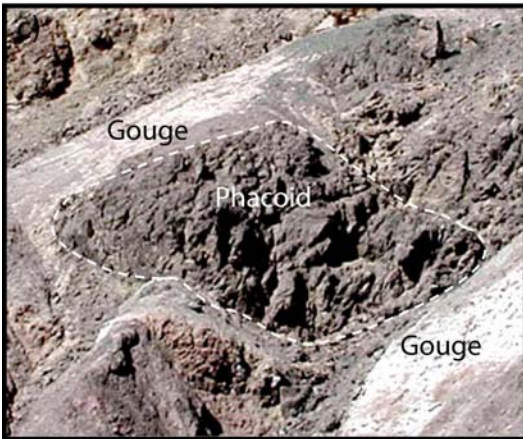


**Figure 5.** Field photographs of extensional features in the Saghand area. a) View NNE of detachment fault emplacing Cambrian volcanic strata over chlorite breccia of mylonitic Chapedony gneiss, Khoshoumi Mountain (locality of fault plane attitude, Figure 3). b) View north of steeply west tilted Cretaceous limestone faulted over cataclastic Cambrian shale and volcanics exhibiting chaos structure. Width of view is ~200 m. c) Close-up view of chaos structure showing phacoid (~3 m wide) surrounded by gouge. d) View west showing base of chlorite breccia zone (dark band in middle ground), west side of Kalut-e-Chapedony. Light-grey rocks in the foreground are mylonitic gneiss of the Chapedony complex. Width of view in foreground is ~200 m. e) S70W lineation in mylonitic Chapedony gneiss, with foliation-normal conjugate joints, west side of Kalut-e-Chapedony. Width of view is 42 cm. f) Monolithic scarp breccia of Cambrian volcanic rocks in Tertiary supradetachment basin, Khoshoumi Mountain. Width of view is 0.7 m.

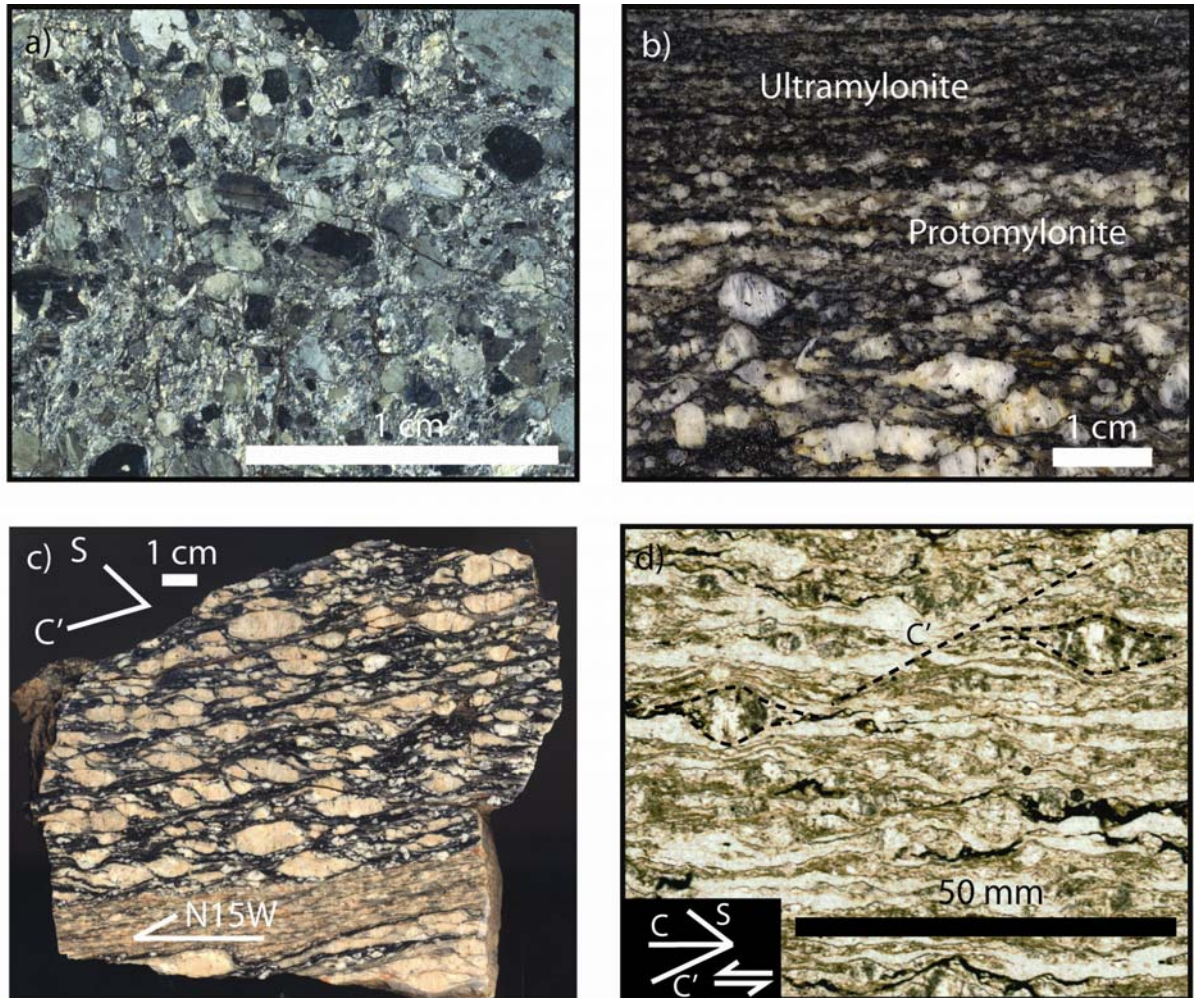


**Figure 6.** Photomicrographs/hand sample photos of fault- and shear zone-related rocks in the area. a) Photomicrograph of chlorite breccia from Neybaz Mountain. b) Polished slab of mylonitic Chapedony gneiss showing abrupt transition from ultramylonite to protomylonite, Kalut-e-Chapedony. c) Polished slab of S-C mylonite with top to the N15W shear sense, Neybaz Mountain. d) Photomicrograph of mylonitic gneiss showing sigmoid porphyroclasts and extensional shear bands indicating top to the left shear sense, Kalut-e-Chapedony.

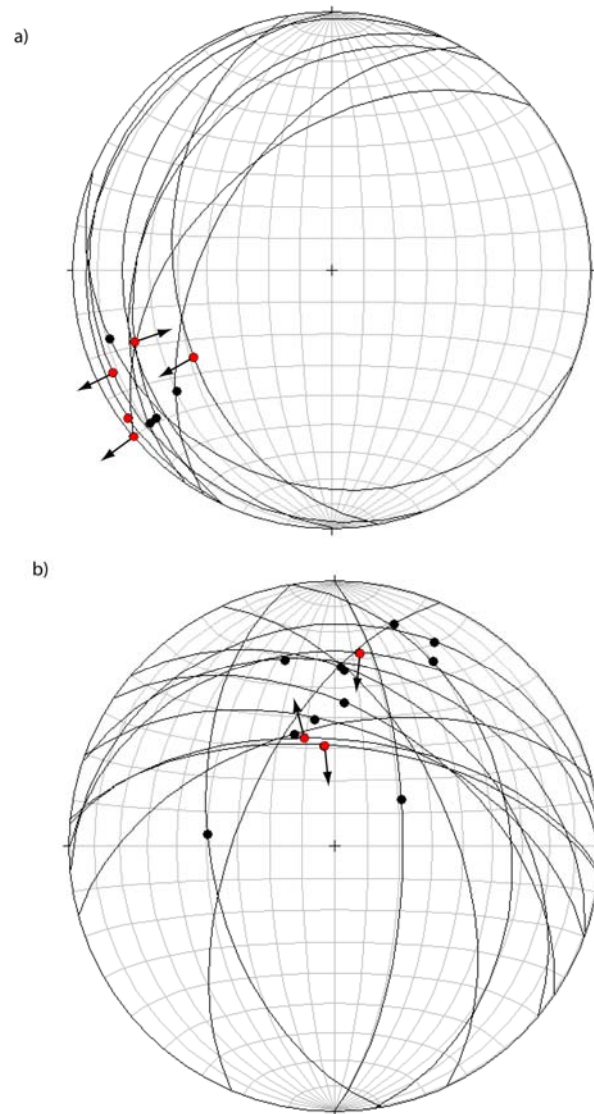


**Figure 7.** Lower-hemisphere equal-area plots of mylonitic foliation and lineation orientations from a) Kalut-e-Chapedony and b) Khoushoumi Mountain. Red dots indicate oriented samples from which sense-of-shear directions were determined, arrows indicate relative motion of the top with respect to the bottom.

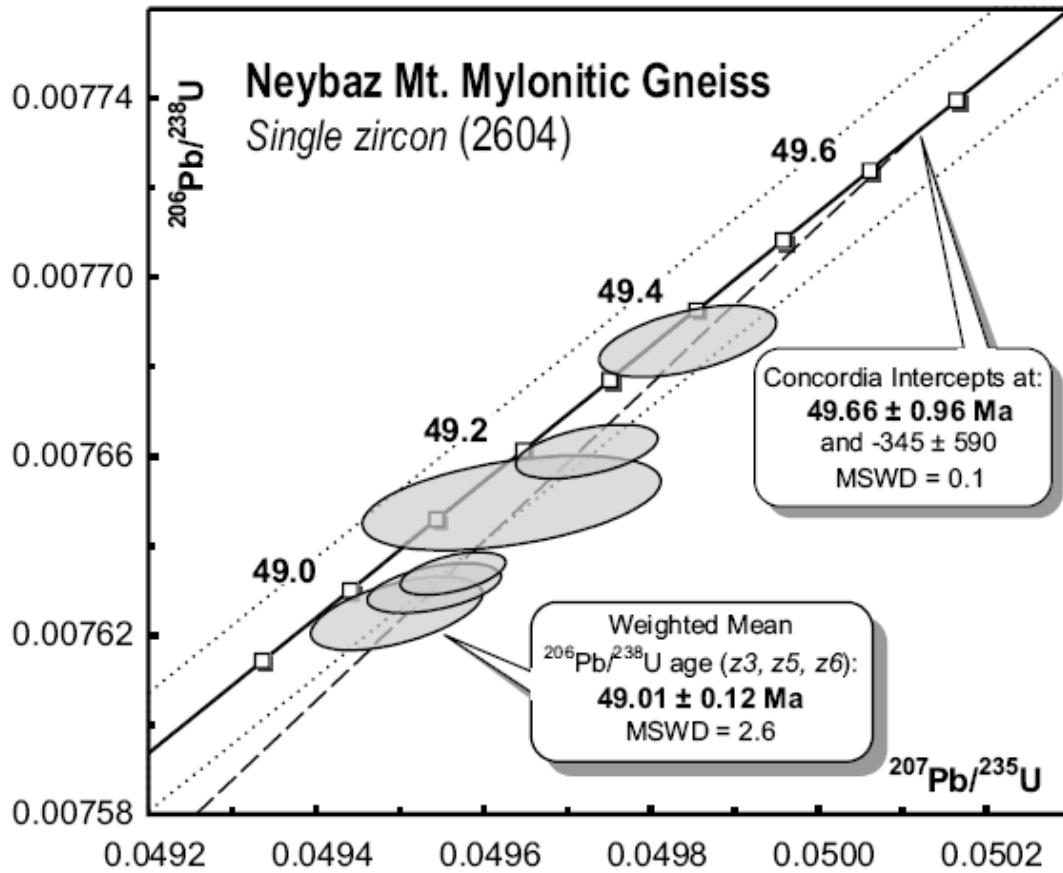


**Figure 8.** Concordia plot for zircons from sample 2604, a mylonitic gneiss from the southern edge of Neybaz Mountain (see Figure 6c).

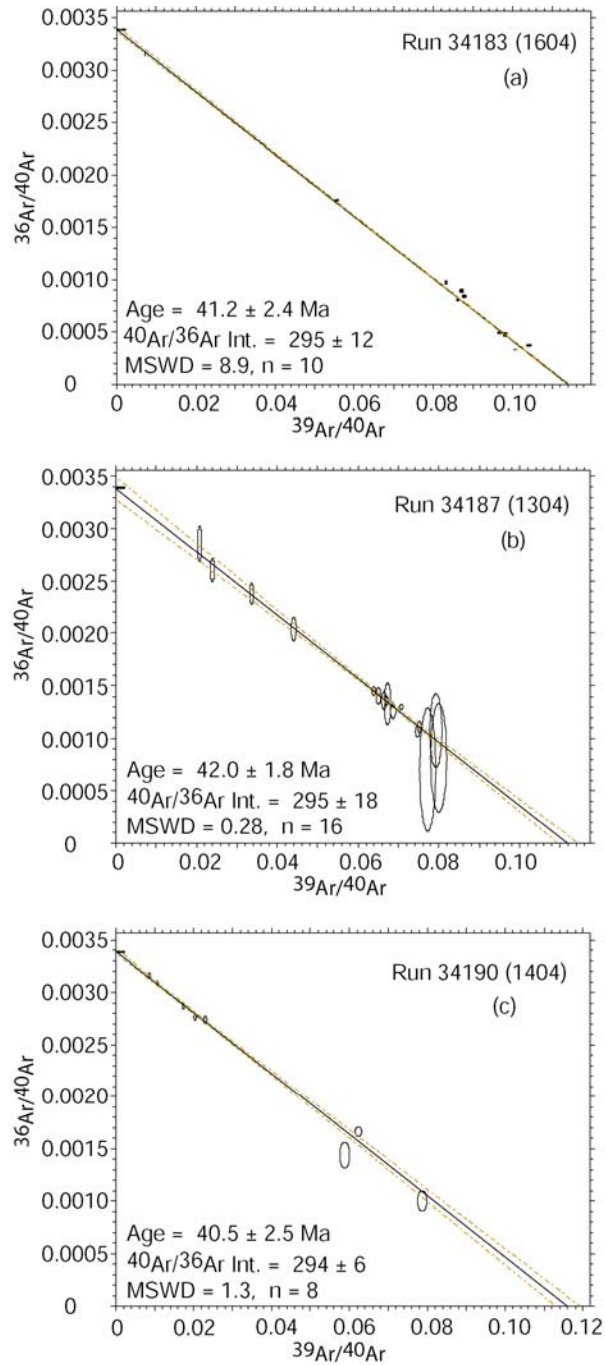


**Figure 9.**  $^{40}\text{Ar}/^{39}\text{Ar}$  inverse isochron diagrams. All uncertainties are given at 95% confidence level. a) 1604 biotite single grain total fusion analyses. The isochron exhibits excess scatter and the age uncertainty is expanded by  $t \cdot \sqrt{\text{MSWD}}$ . b) 1304 plagioclase step-heating of two multi-grain aliquots. c) 1404 alkali feldspar single grain total fusion analyses.

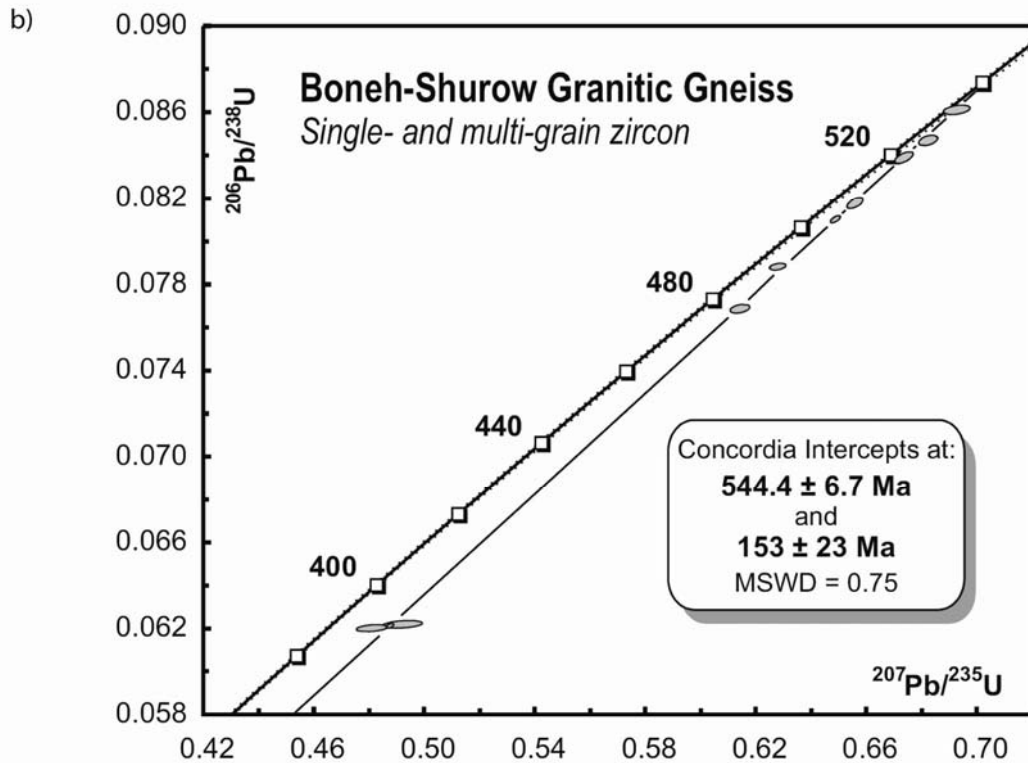
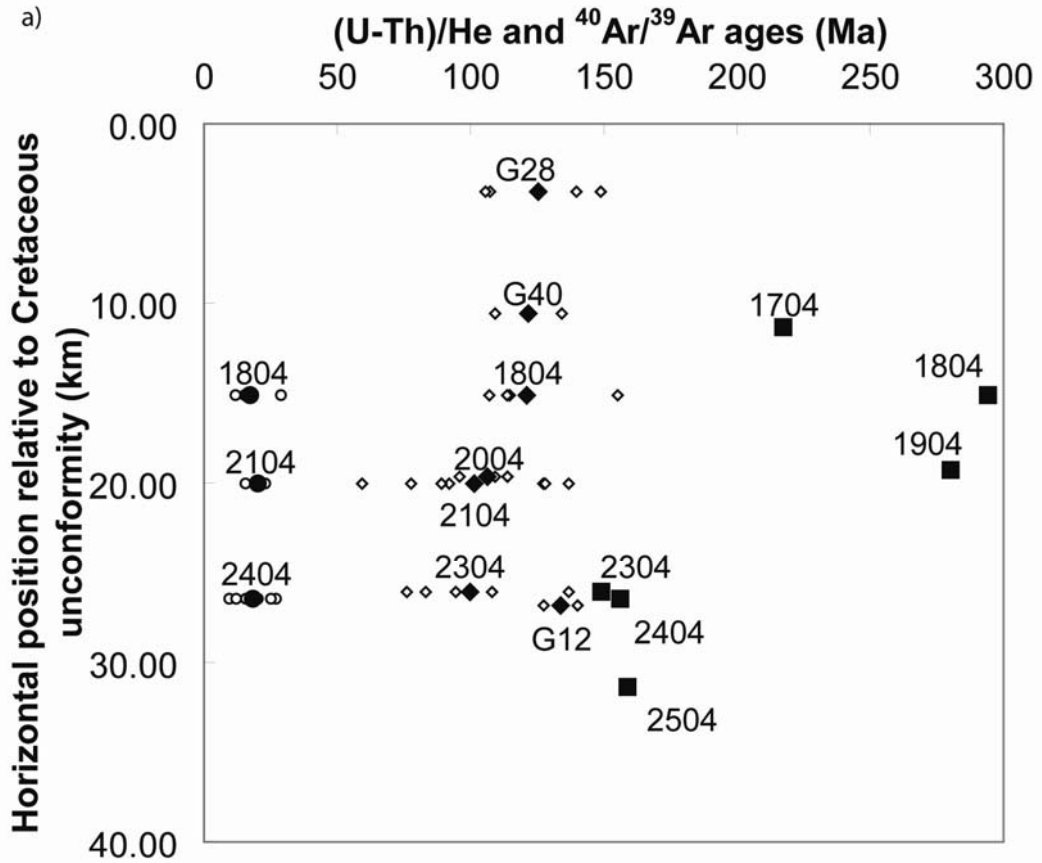


**Figure 10.** Thermochronologic data from the eastern domain. a) (U-Th)/He apatite (circles) and zircon (diamonds) ages, along with  $^{40}\text{Ar}/^{39}\text{Ar}$  biotite ages (squares) from eastern domain samples, plotted as a function of horizontal position within the east-tilted crustal section. For (U-Th)/He data, individual replicates are shown with open symbols, and mean ages are shown with filled symbols. Sample positions were determined by projection onto the direction N60W. b) U-Pb concordia diagram for zircons from the Boneh-Shurow complex (see Ramezani and Tucker (2003) for analytical details). The upper intercept age is interpreted as the crystallization age of the protoliths, while the lower intercept age may reflect Pb loss resulting from rapid uplift.

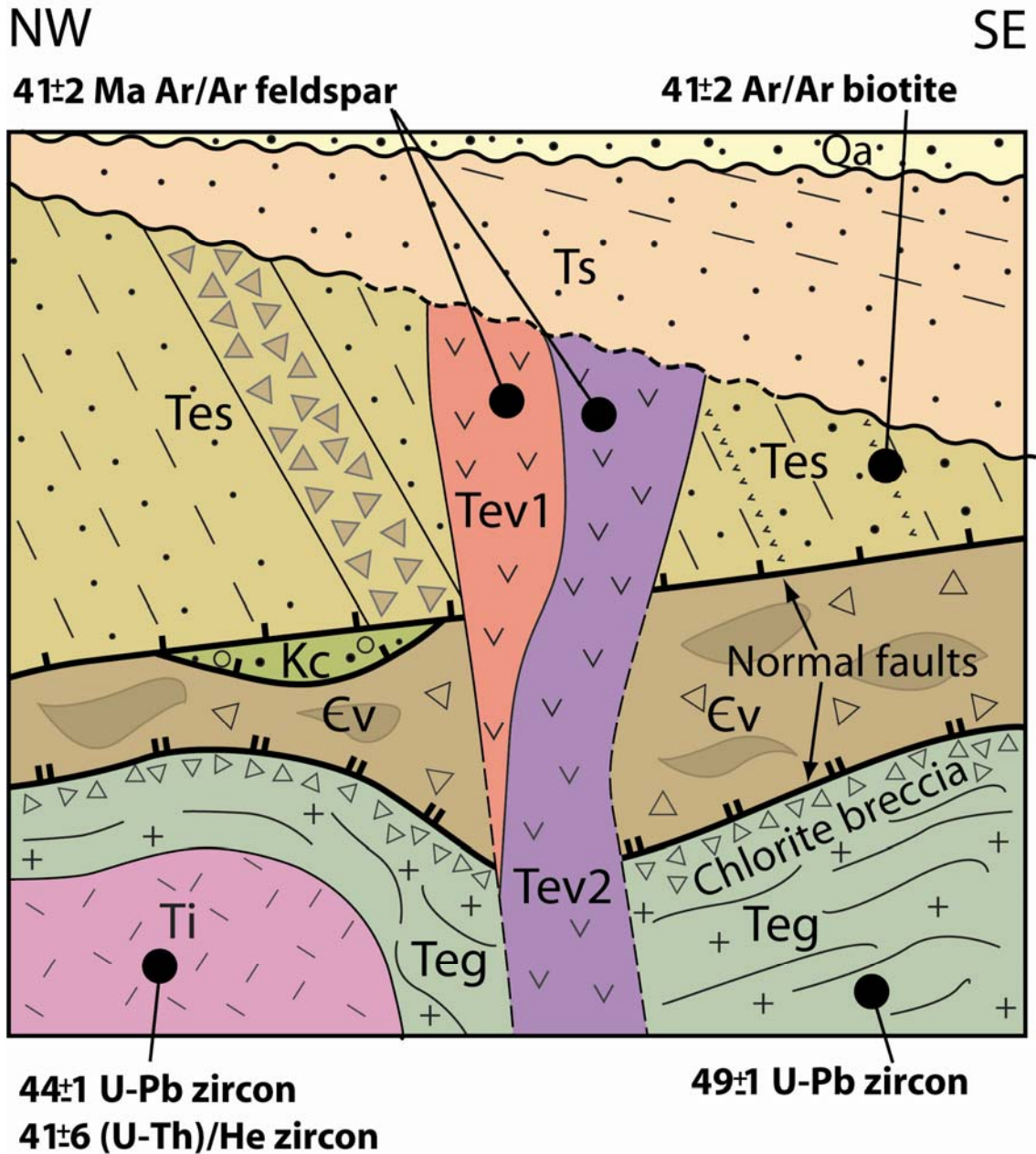


**Figure 11.** Summary of superposition relationships and  $^{40}\text{Ar}/^{39}\text{Ar}$  data for the Khoshoumi Mountain area (Figures 2 and 3). Solid lines indicate mapped relationships, and dashed lines indicate inferred relationships discussed in text.

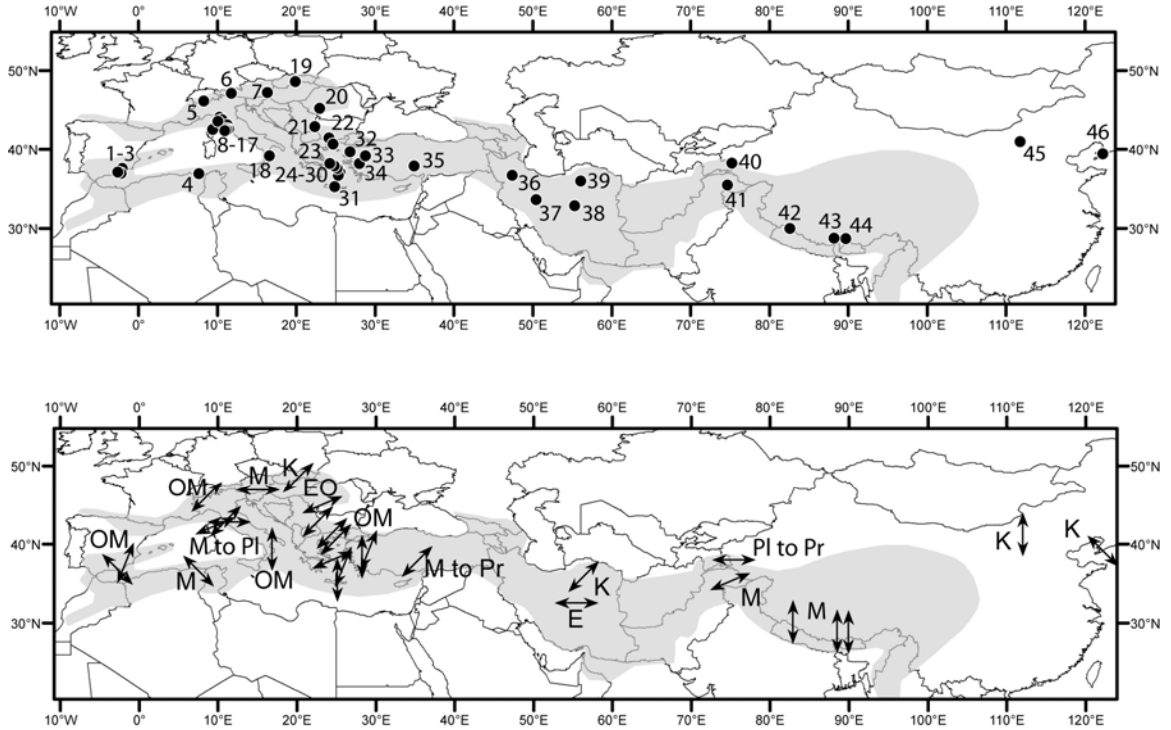


**Figure 12.** Map of Cretaceous to Tertiary metamorphic core complexes along the Alpine-Himalaya orogen, showing context of Iranian examples. (a) Locations of core complexes, (b) Extension directions and ages of selected core complexes. Shaded area is the approximate limit of the Tethysides, modified from Sengor (1987). Abbreviations: K=Cretaceous, E=Eocene, O=Oligocene, M=Miocene, Pl=Pliocene, Pr=Present. References in Table 1.

TABLE S1. U-Pb DATA

Sample	Pb <sub>c</sub> <sup>‡</sup> Fract'ns <sup>†</sup> (pg)	Pb* <sup>‡</sup> Pb <sub>c</sub>	Th U	Ratios								Age (Ma)			corr. coef.
				<sup>206</sup> Pb <sup>§</sup> <sup>204</sup> Pb	<sup>208</sup> Pb <sup>#</sup> <sup>206</sup> Pb	<sup>206</sup> Pb <sup>††</sup> <sup>238</sup> U	error (2σ%)	<sup>207</sup> Pb <sup>††</sup> <sup>235</sup> U	error (2σ%)	<sup>207</sup> Pb <sup>††</sup> <sup>206</sup> Pb	error (2σ%)	<sup>206</sup> Pb <sup>238</sup> U	<sup>207</sup> Pb <sup>235</sup> U	<sup>207</sup> Pb <sup>206</sup> Pb	
<b>Mylonitic gneiss – Neybaz Mountain (2604)</b>															
32° 29.952' N, 55° 6.343' E															
z2	0.7	48	0.52	2944.4	0.166	0.007686	(.09)	0.04984	(.17)	0.04704	(.15)	<b>49.35</b>	<b>49.39</b>	<b>51.1</b>	0.521
z4	0.3	63	0.52	3848.4	0.166	0.007661	(.06)	0.04972	(.14)	0.04707	(.12)	<b>49.20</b>	<b>49.27</b>	<b>53.0</b>	0.494
z1	0.6	34	0.40	2137.8	0.128	0.007650	(.11)	0.04963	(.29)	0.04706	(.26)	<b>49.12</b>	<b>49.19</b>	<b>52.3</b>	0.451
z3	0.7	96	0.37	6080.9	0.120	0.007630	(.06)	0.04954	(.13)	0.04709	(.12)	<b>49.00</b>	<b>49.10</b>	<b>53.8</b>	0.477
z5	0.7	41	0.53	2509.4	0.170	0.007625	(.09)	0.04950	(.17)	0.04708	(.14)	<b>48.97</b>	<b>49.06</b>	<b>53.3</b>	0.551
z6	0.3	107	0.52	6489.2	0.166	0.007634	(.05)	0.04957	(.10)	0.04709	(.09)	<b>49.02</b>	<b>49.12</b>	<b>53.9</b>	0.517

<sup>†</sup> All analyses are annealed and chemically treated single zircon grains.

<sup>‡</sup> Pb<sub>c</sub> is total common Pb in analysis. Pb\* is radiogenic Pb concentration.

<sup>§</sup> Measured ratio corrected for spike and fractionation only.

<sup>#</sup> Radiogenic Pb ratio.

<sup>††</sup> Corrected for fractionation, spike, blank, and initial common Pb. Mass fractionation correction of 0.25%/amu ± 0.04%/amu (atomic mass unit) was applied to single-collector Daly analyses. Total procedural blank was less than 0.7 pg for Pb and less than 0.1 pg for U. Blank isotopic composition: <sup>206</sup>Pb/<sup>204</sup>Pb = 18.27 ± 0.1, <sup>207</sup>Pb/<sup>204</sup>Pb = 15.59 ± 0.1, <sup>208</sup>Pb/<sup>204</sup>Pb = 38.12 ± 0.1.

Corr. coef. = correlation coefficient.

Age calculations are based on the decay constants of Steiger and Jäger (1977).

**TABLE S2.**  $^{40}\text{Ar}/^{39}\text{Ar}$  data for western domain samples

Sample Run ID	Power (W)	$^{40}\text{Ar}$ (nA)	$\sigma$ (nA)	$^{39}\text{Ar}$ (nA)	$\sigma$ (nA)	$^{38}\text{Ar}$ (nA)	$\sigma$ (nA)	$^{37}\text{Ar}$ (nA)	$\sigma$ (nA)	$^{36}\text{Ar}$ (nA)	$\sigma$ (nA)	$^{40}\text{Ar}^*/^{39}\text{Ar}_K$	$\sigma$	% $^{40}\text{Ar}^*$	Age (Ma)	$\sigma$ Ma
<b>Sample 1604, biotite</b>																
<i>32° 25.849' N, 55° 9.516' E</i>																
34183-01	5	1.00664	0.00102	0.08679	0.00022	0.00128	0.00002	0.00440	0.00005	0.00081	0.00001	8.8459	0.0603	76.27	41.56	0.28
34183-02	5	1.48920	0.00096	0.14991	0.00038	0.00207	0.00003	0.00152	0.00005	0.00048	0.00001	8.9835	0.0412	90.44	42.20	0.19
34183-03	5	12.12987	0.00531	0.08692	0.00022	0.00849	0.00004	0.00149	0.00004	0.03813	0.00005	9.9132	1.0836	7.10	46.51	5.02
34183-04	5	0.92257	0.00133	0.05141	0.00017	0.00098	0.00002	0.00253	0.00005	0.00162	0.00001	8.6378	0.1218	48.13	40.59	0.57
34183-05	5	0.36978	0.00053	0.03632	0.00013	0.00054	0.00002	0.00149	0.00005	0.00018	0.00001	8.7524	0.0827	85.96	41.13	0.38
34183-06	5	1.31457	0.00143	0.12734	0.00026	0.00179	0.00002	0.00437	0.00007	0.00065	0.00002	8.8185	0.0552	85.42	41.43	0.26
34183-07	5	0.68070	0.00090	0.07099	0.00022	0.00099	0.00002	0.00106	0.00004	0.00025	0.00001	8.5315	0.0520	88.98	40.10	0.24
34183-08	5	0.68510	0.00100	0.05976	0.00015	0.00101	0.00002	0.00124	0.00004	0.00061	0.00002	8.4544	0.0928	73.75	39.74	0.43
34183-09	5	0.65149	0.00113	0.05718	0.00021	0.00086	0.00002	0.00295	0.00005	0.00055	0.00001	8.5656	0.0739	75.19	40.26	0.34
34183-10	5	0.77398	0.00104	0.06435	0.00012	0.00103	0.00002	0.00221	0.00005	0.00075	0.00002	8.6000	0.0989	71.51	40.42	0.46
<b>Sample 1304, plagioclase</b>																
<i>32° 26.779' N, 55° 9.707' E</i>																
34187-01B	0.6	0.30214	0.00132	0.01339	0.00013	0.00031	0.00004	0.06957	0.00039	0.00063	0.00003	9.0081	0.7937	39.77	42.31	3.68
34187-01C	0.9	0.44673	0.00129	0.02925	0.00013	0.00049	0.00004	0.21280	0.00073	0.00068	0.00003	8.9763	0.3534	58.49	42.17	1.64
34187-01D	1.2	0.66043	0.00202	0.04975	0.00018	0.00077	0.00004	0.39962	0.00139	0.00081	0.00003	9.1415	0.2127	68.48	42.93	0.99
34187-01E	1.7	0.65136	0.00164	0.04940	0.00018	0.00076	0.00004	0.45224	0.00159	0.00084	0.00003	8.9209	0.2129	67.23	41.91	0.99
34187-01F	2.2	0.09436	0.00079	0.00757	0.00010	0.00015	0.00004	0.09685	0.00074	0.00013	0.00003	8.5925	1.3303	68.29	40.38	6.18
34187-01G	2.7	0.05402	0.00083	0.00421	0.00008	0.00008	0.00003	0.05682	0.00052	0.00005	0.00003	10.2622	2.2736	79.33	48.13	10.52
34187-01H	3.2	0.06241	0.00079	0.00504	0.00009	0.00008	0.00003	0.06581	0.00053	0.00007	0.00003	9.5098	1.9512	76.14	44.64	9.05

TABLE S2, continued.  $^{40}\text{Ar}/^{39}\text{Ar}$  data for western domain samples

Sample Run ID	Power (W)	$^{40}\text{Ar}$ (nA)	$\sigma$ (nA)	$^{39}\text{Ar}$ (nA)	$\sigma$ (nA)	$^{38}\text{Ar}$ (nA)	$\sigma$ (nA)	$^{37}\text{Ar}$ (nA)	$\sigma$ (nA)	$^{36}\text{Ar}$ (nA)	$\sigma$ (nA)	$^{40}\text{Ar}^*/^{39}\text{Ar}_K$	$\sigma$	% $^{40}\text{Ar}^*$	Age (Ma)	$\sigma$ Ma
<b>Sample 1304, plagioclase</b>																
<i>32° 26.779' N, 55° 9.707' E</i>																
34187-02B	0.4	0.17395	0.00076	0.00364	0.00007	0.00012	0.00003	0.00995	0.00020	0.00050	0.00003	7.5722	2.5565	15.81	35.64	11.91
34187-02C	0.6	0.29381	0.00094	0.00998	0.00009	0.00023	0.00003	0.04958	0.00032	0.00071	0.00003	8.8459	0.9521	29.94	41.56	4.42
34187-02D	0.9	0.36705	0.00110	0.02455	0.00012	0.00035	0.00003	0.17074	0.00075	0.00054	0.00003	8.9863	0.3875	59.83	42.21	1.80
34187-02E	1.2	0.70299	0.00192	0.04745	0.00020	0.00087	0.00004	0.34992	0.00110	0.00105	0.00003	8.9026	0.2173	59.78	41.82	1.01
34187-02F	1.5	0.90571	0.00211	0.06439	0.00024	0.00111	0.00004	0.52063	0.00140	0.00131	0.00003	8.7347	0.1671	61.75	41.04	0.78
34187-02G	1.8	0.73461	0.00173	0.04732	0.00020	0.00090	0.00004	0.42391	0.00111	0.00117	0.00003	8.9623	0.2202	57.38	42.10	1.02
34187-02H	2.2	0.43084	0.00116	0.02987	0.00017	0.00052	0.00004	0.32917	0.00083	0.00063	0.00003	9.1683	0.3291	63.08	43.06	1.53
34187-02I	3.5	0.15289	0.00081	0.01039	0.00009	0.00016	0.00003	0.13484	0.00087	0.00024	0.00003	9.0646	0.9086	61.03	42.58	4.22
34187-02J	7	0.29046	0.00093	0.00707	0.00009	0.00024	0.00003	0.08577	0.00046	0.00078	0.00003	9.5838	1.3943	23.13	44.98	6.46
<b>Sample 1404, alkali feldspar</b>																
<i>32° 26.599' N, 55° 9.830' E</i>																
34190-02	4	0.35877	0.00059	0.00388	0.00003	0.00029	0.00001	0.00308	0.00009	0.00111	0.00001	8.2742	1.0551	8.93	38.90	4.91
34190-03	4	0.12340	0.00044	0.00774	0.00007	0.00015	0.00001	0.03317	0.00024	0.00021	0.00001	8.1706	0.2620	51.08	38.42	1.22
34190-04	4	0.04751	0.00036	0.00284	0.00004	0.00006	0.00001	0.05492	0.00023	0.00008	0.00001	9.7939	0.6852	57.79	45.96	3.17
34190-05	4	0.60345	0.00067	0.00530	0.00004	0.00045	0.00001	0.00341	0.00008	0.00191	0.00001	7.4245	1.0795	6.52	34.95	5.03
34190-06	4	0.48638	0.00093	0.01001	0.00008	0.00041	0.00001	0.01475	0.00012	0.00135	0.00001	8.8744	0.4743	18.25	41.69	2.20
34190-07	4	0.33082	0.00076	0.00773	0.00007	0.00026	0.00001	0.09542	0.00034	0.00093	0.00001	8.2171	0.4738	19.02	38.64	2.20
34190-10	4	0.42792	0.00059	0.00744	0.00007	0.00040	0.00001	0.00309	0.00009	0.00123	0.00001	8.7855	0.6084	15.27	41.28	2.83
34190-11	4	0.05779	0.00033	0.00461	0.00005	0.00009	0.00001	0.07763	0.00030	0.00008	0.00001	8.9412	0.4044	70.52	42.00	1.88

**TABLE S3.**  $^{40}\text{Ar}/^{39}\text{Ar}$  data for eastern domain samples

<b>Sample 1704, biotite, 1.50 mg, J = 0.00151862 ± 0.0952%</b>													
<i>32° 30.712' N, 55° 33.490' E</i>													
Step	T (C)	t (min.)	36Ar	37Ar	38Ar	39Ar	40Ar	%40Ar*	% 39Ar released	Ca/K	40Ar*/39ArK	Age (Ma)	1 s.d.
1	650	12	1.185	0.489	0.234	0.123	355.438	5.2	0.1	14.559186	159.044460	390.30	63.44
2	725	12	1.174	0.142	0.236	0.933	377.176	12.3	0.6	0.55502762	47.501559	125.66	5.75
3	790	12	6.450	0.583	1.280	6.770	2330.42	21.5	4.4	0.31401927	74.009831	192.16	2.14
4	850	12	5.760	0.484	1.429	25.468	3750.04	56.6	16.7	0.06929389	83.637632	215.72	1.02
5	905	12	0.666	0.286	0.367	18.285	1695.17	90.0	12.0	0.05703138	76.650557	198.65	0.67
6	960	12	0.676	0.363	0.364	19.795	1802.18	90.6	12.9	0.06686444	82.111305	212.00	0.71
7	1015	12	0.692	0.592	0.458	25.864	2329.33	92.6	16.9	0.08345883	83.238422	214.75	0.67
8	1055	12	0.566	7.725	0.548	32.568	3071.00	95.6	21.3	0.86507904	90.257038	231.74	0.75
9	1095	12	0.435	11.578	0.260	13.478	1237.73	92.0	8.8	3.13511068	83.669016	215.79	0.69
10	1135	12	0.228	2.297	0.092	4.805	421.639	89.9	3.1	1.74393691	73.373017	190.59	0.65
11	1180	12	0.289	2.719	0.109	2.372	254.683	74.1	1.6	4.18481533	70.228433	182.82	0.71
12	1250	12	0.272	3.454	0.089	0.979	151.366	55.9	0.6	12.9139448	68.771262	179.21	1.50
13	1400	12	0.527	8.581	0.116	1.436	621.574	78.8	0.9	21.9318247	327.440483	728.19	3.44
								Cumulative %39Ar released =	100.0		Total gas age =	218.27	0.51
<b>Sample 1804, biotite, 0.80 mg, J = 0.00149439 ± 0.1458%</b>													
<i>32 30.554' N, 55 31.001' E</i>													
Step	T (C)	t (min.)	36Ar	37Ar	38Ar	39Ar	40Ar	%40Ar*	% 39Ar released	Ca/K	40Ar*/39ArK	Age (Ma)	1 s.d.
1	650	12	1.796	0.074	0.343	0.046	522.880	2.2	0.1	5.95967947	318.279303	701.94	130.97
2	725	12	0.813	0.270	0.187	0.235	253.190	9.7	0.6	4.25424452	99.455224	249.98	15.85
3	790	12	2.886	1.506	0.553	1.425	929.788	12.1	3.9	3.91284014	78.089842	199.13	6.23
4	840	12	11.986	2.349	2.338	4.194	3852.95	11.6	11.5	2.07250874	107.299564	268.30	5.57
5	890	12	0.657	0.462	0.175	3.853	630.711	73.4	10.5	0.44347792	116.639294	289.87	1.33
6	940	12	0.473	1.198	0.178	7.582	1024.44	89.1	20.7	0.58441382	118.678318	294.55	1.10
7	990	12	0.382	4.314	0.165	8.278	1093.15	92.3	22.6	1.92831363	120.332481	298.33	1.03
8	1040	12	0.362	8.471	0.126	5.903	857.919	90.8	16.1	5.31528882	129.773723	319.78	1.13
9	1100	12	0.284	6.263	0.080	3.317	501.455	88.6	9.1	6.9971508	129.026930	318.09	2.15
10	1180	12	0.157	3.610	0.034	0.727	144.996	83.2	2.0	18.4650128	131.332632	323.29	5.00
11	1400	12	0.593	9.159	0.134	1.005	314.117	44.8	2.7	34.046981	122.095747	302.36	3.17
								Cumulative %39Ar released =	100.0		Total gas age =	295.36	1.08

**TABLE S3, continued.**  $^{40}\text{Ar}/^{39}\text{Ar}$  data for eastern domain samples

<b>Sample 1904, biotite, 1.40 mg, J = 0.00151068 ± 0.0997%</b>													
32° 31.949' N, 55° 28.705' E													
Step	T (C)	t (min.)	36Ar	37Ar	38Ar	39Ar	40Ar	%40Ar*	% 39Ar released	Ca/K	40Ar*/39ArK	Age (Ma)	1 s.d.
1	670	12	2.619	0.074	0.505	0.085	760.456	2.0	0.3	3.29046746	199.846312	475.97	76.49
2	750	12	1.167	1.361	0.272	2.426	400.266	18.3	8.5	2.11962627	28.717012	76.62	1.71
3	810	12	8.146	0.950	1.618	3.833	2590.26	10.7	13.4	0.9360999	72.270577	186.94	4.28
4	860	12	1.858	0.754	0.368	2.841	836.066	38.0	10.0	1.00241183	109.783520	276.83	2.03
5	910	12	0.284	1.139	0.118	3.425	541.73	89.3	12.0	1.25615248	136.359062	337.91	1.52
6	960	12	0.336	3.017	0.119	3.520	617.767	88.2	12.4	3.23944637	150.548182	369.70	1.69
7	1010	12	0.400	8.050	0.256	5.937	843.91	89.4	20.8	5.12759068	124.761893	311.51	1.14
8	1060	12	0.248	6.288	0.123	3.689	533.269	91.3	12.9	6.44852923	127.512595	317.81	1.56
9	1120	12	0.199	6.095	0.131	1.914	292.433	88.3	6.7	12.0675928	121.608253	304.27	1.72
10	1190	12	0.152	2.269	0.029	0.465	113.326	77.9	1.6	18.5272295	139.225482	344.38	9.22
11	1400	12	0.564	1.633	0.115	0.360	215.684	13.0	1.3	17.2163975	70.060261	181.50	10.22
								Cumulative %39Ar released =	100.0		Total gas age =	281.32	1.17
<b>Sample 2304, biotite, 1.40 mg, J = 0.0053346 ± 0.1091%</b>													
32° 31.914' N, 55° 28.775' E													
Step	T (C)	t (min.)	36Ar	37Ar	38Ar	39Ar	40Ar	%40Ar*	% 39Ar released	Ca/K	40Ar*/39ArK	Age (Ma)	1 s.d.
1	680	12	2.871	0.025	0.541	0.382	816.288	-0.1	0.2	0.2535515	-2.737221	-7.61	-16.88
2	760	12	3.065	0.212	0.655	7.524	1167.750	25.9	4.1	0.10915855	39.781554	107.12	1.06
3	810	12	9.132	0.373	2.014	22.983	3845.67	32.7	12.4	0.06287337	54.849739	146.09	1.08
4	855	12	3.572	0.314	1.071	29.818	2716.07	63.2	16.1	0.04079556	57.564565	153.02	0.65
5	900	12	0.632	0.223	0.564	33.838	2156.4	92.8	18.3	0.02553054	58.971072	156.61	0.50
6	945	12	1.104	0.626	1.057	62.222	3799.98	92.4	33.7	0.03897552	56.539535	150.41	0.48
7	990	12	0.339	0.362	0.265	15.118	968.434	92.5	8.2	0.09276471	58.218381	154.69	0.54
8	1035	12	0.195	0.298	0.109	5.923	404.808	92.1	3.2	0.19492001	59.550334	158.08	0.65
9	1085	12	0.117	0.775	0.066	3.081	217.681	96.0	1.7	0.97475115	60.499413	160.49	1.12
10	1150	12	0.107	0.689	0.043	1.641	128.919	95.0	0.9	1.62734494	55.533265	147.84	0.99
11	1400	12	0.376	1.726	0.092	2.271	242.653	57.0	1.2	2.94689669	45.989171	123.28	1.96
								Cumulative %39Ar released =	100.0		Total gas age =	149.75	0.46

**TABLE S3, continued.**  $^{40}\text{Ar}/^{39}\text{Ar}$  data for eastern domain samples

<b>Sample 2404, biotite, 1.40 mg, J = 0.0015473 ± 0.1123%</b>														
32° 32.028' N, 55° 24.747' E														
Step	T (C)	t (min.)	36Ar	37Ar	38Ar	39Ar	40Ar	%40Ar*	% 39Ar released	Ca/K	40Ar*/39ArK	Age (Ma)	1 s.d.	
1	690	12	3.406	0.024	0.639	0.635	991.380	2.2	0.3	0.32679748	35.408661	96.23	11.56	
2	770	12	1.193	0.060	0.306	6.072	638.441	48.8	2.6	0.08543369	49.847487	134.04	0.92	
3	810	12	6.691	0.108	1.513	18.082	2947.75	35.8	7.8	0.05163956	58.354398	155.95	1.07	
4	850	12	2.619	0.144	0.983	33.458	2686.04	73.0	14.4	0.03721053	58.575993	156.52	0.60	
5	890	12	0.164	0.041	0.332	23.681	1430.37	98.5	10.2	0.01496871	59.000941	157.61	0.52	
6	930	12	0.393	0.089	0.928	64.871	3879.12	97.8	28.0	0.0118615	58.610905	156.61	0.48	
7	970	12	0.241	0.024	0.317	22.562	1369.27	96.8	9.7	0.00919673	58.185798	155.52	0.55	
8	1050	12	0.301	0.059	0.448	30.953	1918.05	96.8	13.3	0.01647972	59.750226	159.52	0.49	
9	1140	12	0.141	0.051	0.375	26.447	1605.70	99.1	11.4	0.01667226	59.428109	158.70	0.48	
10	1400	12	0.348	0.097	0.150	5.271	417.979	80.7	2.3	0.15911019	54.983769	147.30	0.69	
									Cumulative %39Ar released =	100.0	Total gas age =		156.20	0.40
											Plateau age (steps 3-6) =		156.86	0.58
<b>Sample 2504, biotite, 1.80 mg, J = 0.00152694 ± 0.0993%</b>														
32° 30.865' N, 55° 21.087' E														
Step	T (C)	t (min.)	36Ar	37Ar	38Ar	39Ar	40Ar	%40Ar*	% 39Ar released	Ca/K	40Ar*/39ArK	Age (Ma)	1 s.d.	
1	770	12	3.697	1.031	0.730	3.543	1178.11	10.6	4.8	1.21176812	37.252676	99.81	2.18	
2	810	12	10.177	1.758	1.973	5.023	3212.25	9.8	6.8	1.45753771	63.094333	165.94	4.32	
3	850	12	3.093	0.796	0.699	6.586	1255.83	30.1	8.9	0.50318861	57.018796	150.61	1.32	
4	890	12	0.265	0.551	0.132	6.623	475.911	86.7	9.0	0.3463505	60.406719	159.17	0.52	
5	930	12	0.341	1.193	0.237	11.971	818.517	90.7	16.2	0.41489475	60.692591	159.89	0.63	
6	970	12	0.415	6.291	0.259	14.750	1004.91	90.4	20.0	1.7763699	60.653963	159.79	0.58	
7	1050	12	0.565	30.581	0.310	15.826	1211.34	88.8	21.5	8.06318088	67.369872	176.65	0.63	
8	1140	12	0.310	21.154	0.152	6.708	586.271	89.0	9.1	13.1792775	75.506441	196.86	0.72	
9	1400	12	0.540	8.639	0.138	2.641	367.089	66.8	3.6	13.6726099	82.230342	213.39	1.84	
									Cumulative %39Ar released =	100.0	Total gas age =		165.38	0.53
											Pseudo plateau age (steps 4-6) =		159.57	0.65











TABLE 1. Alpine-Himalayan metamorphic core complexes

Number (Fig. 12)	Location/Name	Age	Extension direction	Reference
<b>Spain</b>				
1	Nevado-Filabrides	Late Oligocene-Late Miocene	NW-SE	Platt and Vissers, 1989
2	Sierra Alhamilla	Late Oligocene-Late Miocene	NNE-SSW	Platt and Vissers, 1989
3	Sierra de las Estancias	Late Oligocene-Early Miocene	NNE-SSW	Platzman and Platt, 2004
<b>Algeria</b>				
4	Edough	Late Miocene	NW-SE	Caby et al., 2001
<b>Alps</b>				
5	Simplon	Oligocene-Miocene	NE-SW	Mancktelow and Pavlis, 1994; Wawrzyniec et al., 2001
6	Brenner	Early Oligocene-Early Miocene	E-W	Axen et al., 1995; Wawrzyniec et al., 2001
7	Rechnitz	Miocene	E-W	Grassl et al., 2004; Ratschbacher et al., 1990
<b>Italy/Tyrrhenian Sea</b>				
8	Corsica	Late Oligocene-Early Miocene	ENE-WSW	Brunet et al., 2000; Fournier et al., 1991
9	Alpi Apuane	Miocene	NE-SW	Carmignani and Roy, 1990; Carmignani et al., 1994
10	Monte Pisano	Pliocene	NE-SW	Brunet et al., 2000
11	Monticciano-Roccastrada	Pliocene	E-W	Brunet et al., 2000
12	Elba	Miocene	E-W	Brunet et al., 2000
13	Monte Romani	Miocene-Pliocene	ENE-WSW	Brunet et al., 2000
14	Uccellina	Miocene		Brunet et al., 2000
15	Monte Argentario	Miocene	ENE-WSW	Brunet et al., 2000
16	Gorgona	Miocene	NW-SE	Brunet et al., 2000
17	Giglio	Miocene	ENE-WSW	Jolivet et al., 1998
18	Calabrian	Middle Oligocene-Middle Miocene	N-S	Platt and Compagnani, 1990; Thomson, 1994; Wallis et al., 1993
<b>Carpathians</b>				
19	Vepor	Cretaceous	NE-SW	Janak et al., 2001
20	Getic	Late Eocene-Oligocene	WSW-ENE	Fugenschuh and Schmid, 2005; Schmid et al., 1998
<b>Bulgaria/ Northern Greece</b>				
21	Osogovo-Lisets	Middle Eocene-Early Oligocene	NE-SW	Kounov et al., 2004
22	Rhodope	Miocene	NE-SW	Dinter et al., 1995; van Hinsbergen and Meulenkamp, 2006
<b>Greece/Aegean Sea</b>				
23	Thasos	Early-Middle Miocene	NE-SW	Wawrenitz and Krohe, 1998
24	Mykonos	Late Miocene	NE-SW	Lee and Lister, 1992
25	Naxos	Miocene	NNE-SSW	Lister et al., 1984
26	Ios	Miocene	NNE-SSW	Lister et al., 1984
27	Tinos	Miocene	NNE-SSW	Gautier and Brun, 1994; Ring et al., 2003
28	Andros	Miocene	NNE-SSW	Gautier and Brun, 1994
29	Evvia	Oligocene-Early Miocene	ENE-WSW	Gautier and Brun, 1994
30	Ikaria	Late Miocene-Pliocene	NNE-SSW	Kumerics et al., 2005
31	South Aegean (Cretan)	Early-Middle Miocene	N-S	Thomson et al., 1999; van Hinsbergen and Meulenkamp, 2006
<b>Turkey</b>				
32	Kazdag	Late Oligocene	NNW-SSE	Okay and Satir, 2000
33	Simav	Early-Middle Miocene	NNE-SSW	Ring and Collins, 2005
34	Central Menderes	Miocene-Present	N-S	Gessner et al., 2001
35	Nigde	Miocene-Present	NE-SW	Whitney and Dilek, 1997
<b>Iran</b>				
36	Takab-Zanjan	Miocene	NW-SE	Stockli et al., 2004
37	Golpaygan			Thiele et al., 1967; Tillman et al., 1981
38	Saghand	Middle Eocene	E-W	This paper
39	Biarjmand	Cretaceous	NE-SW	Hassanzadeh et al., 2005
<b>Himalaya</b>				
40	Kongur Shan	Early Pliocene-Present	E-W	Brunel et al., 1994
41	Nanga Parbat	Early Miocene	WSW-ENE	Argles and Edwards, 2002; Hubbard et al., 1995
42	N. Himalayan gneiss domes	Miocene	N-S	Burchfiel et al., 1992; Yin et al., 1999
43	Mabja Dome	Miocene	N-S	Lee et al., 2004
44	Kangmar Dome	Miocene	N-S	Chen et al., 1990; Lee et al., 2000
<b>Eastern China</b>				
45	Hohhot	Cretaceous	N-S	Davis et al., 2002
46	Liaonan	Early Cretaceous	NW-SE	Junlai et al., 2005

**APPENDIX A. ANALYTICAL METHODS FOR U-Pb GEOCHRONOLOGY**

Zircon was separated from bulk rock samples by standard crushing, heavy liquid, and magnetic separation techniques, and was subsequently handpicked using a binocular microscope, with selection based on clarity and crystal morphology. All grains were pre-treated to minimize the effects of Pb loss, by the method of thermal annealing and chemical leaching (chemical abrasion or CA-TIMS technique: Mattinson, 2005; Mundil et al., 2004) designed to preferentially remove the high-U parts of the zircon crystal that are most susceptible to Pb loss. Zircon grains are first annealed at 900°C for 60 hours and leached in 29M HF inside high-pressure Parr® vessels at 180°C for 12 hours. The partially dissolved sample is then fluxed successively with hot 4N HNO<sub>3</sub> and 6N HCl and thoroughly rinsed with ultra-pure water in between. Pre-treated and rinsed zircons were spiked with a mixed <sup>205</sup>Pb-<sup>233</sup>U-<sup>235</sup>U tracer solution and dissolved completely in 29M HF inside Parr® vessels at 220°C for 48-60 hours.

Dissolved Pb and U were chemically separated using a miniaturized HCl-based ion-exchange chromatography procedure modified after Krogh (1973), using 50 µl columns of AG1x8 anion-exchange resin. Both Pb and U were loaded with a silica gel - H<sub>3</sub>PO<sub>4</sub> emitter solution (Gerstenberger and Haase, 1997) on single degassed Re filaments and their isotopic compositions were measured on the VG Sector 54 multi-collector thermal ionization mass spectrometer at MIT. Lead isotopic measurements were made in a peak-switching mode by ion counting using a Daly photomultiplier detector with a <sup>206</sup>Pb ion beam intensity of 0.5 to 2.0 x 10<sup>-13</sup> Amps usually maintained in the course of data

acquisition. Uranium isotopes were measured as oxide ions on three Faraday detectors in a static mode with an average  $^{235}\text{U}^{16}\text{O}_2^+$  ion-beam intensity of  $8.0 \times 10^{-13}$  Amps.

Measured isotopic ratios were corrected for mass-dependent isotope fractionation in the mass spectrometer, as well as for U and Pb contributions from the spike, laboratory blanks and initial Pb in the sample. Details of fractionation and blank corrections are given in Table S1. The U-Pb data reduction, age calculation and error propagation follow the algorithm of Ludwig (1980) and the program ISOPLOT (Ludwig, 1991; version 3.14, 2004). All U-Pb dates are reported at 95% confidence levels.

- Gerstenberger, H., and Haase, G., 1997, A highly effective emitter substance for mass spectrometric Pb isotope ratio determinations: *Chemical Geology*, v. 136, no. 3-4, p. 309-312.
- Krogh, T.E., 1973, A low-contamination method for hydrothermal decomposition of zircon and extraction of U and Pb for isotopic age determinations: *Geochimica et Cosmochimica Acta*, v. 37, no. 3, p. 485-494.
- Ludwig, K.R., 1980, Calculation of uncertainties of U-Pb isotope data: *Earth and Planetary Science Letters*, v. 46, no. 2, p. 212-220.
- Ludwig, K.R., 1991, ISOPLOT; a plotting and regression program for radiogenic-isotope data; version 2.53: Open-File Report - U. S. Geological Survey, OF 91-0445.
- Mattinson, J.M., 2005, Zircon U-Pb chemical abrasion (CA-TIMS) method; combined annealing and multi-step partial dissolution analysis for improved precision and accuracy of zircon ages: *Chemical Geology*, v. 220, no. 1-2, p. 47-66.
- Mundil, R., Ludwig, K.R., Metcalfe, I., and Renne, P.R., 2004, Age and timing of the Permian mass extinctions; U-Pb dating of closed-system zircons: *Science*, v. 305, no. 5691, p. 1760-1763.

## APPENDIX B. ANALYTICAL METHODS FOR $^{40}\text{Ar}/^{39}\text{Ar}$ GEOCHRONOLOGY

### Berkeley Geochronology Center

Samples analyzed at the Berkeley Geochronology Center were irradiated in the cadmium-lined in-core irradiation tube (CLICIT) facility at the Oregon State University TRIGA research reactor. Samples were irradiated in wells in an Al disk of the type depicted by Renne et al. (1998) along with crystals of Fish Canyon sanidine. J-values were determined as the weighted mean of values (N=8) determined for each of three wells bracketing the samples, and the arithmetic mean and standard deviation ( $0.0026345 \pm 0.0000024$ ) of values for these three positions was used for age calculations. Ages are based on the constants of Steiger and Jäger (1977). Age uncertainties do not include contributions from decay constants or age of the standard.

Samples were degassed with a CO<sub>2</sub> laser either by step-wise power increase or by total fusion. Stepwise heating utilized an integrator lens to enhance uniformity of laser power distribution. Analysis with an MAP 215C mass spectrometer followed methods described by Renne et al. (1998). Procedural blanks were measured between every three unknowns and were similar to values reported by Knight et al. (2004). Blank correction was based on regression of data spanning the runs. Mass discrimination ( $1.00755 \pm 0.00185$  per amu) was determined from analyses of 12 aliquots from an automated on-line air pipette system, regularly interspersed with the unknowns and standards, and the discrimination correction was applied as a power law function (Renne, 2000). Interfering Ar isotopes from Ca, K and Cl were corrected for using production ratios summarized by Renne et al. (2005).

### References

- Knight K.B., Nomade, S., Renne, P.R., Marzoli, A., Bertrand, H., and Youbi, N., 2004, The Central Atlantic Magmatic Province at the Triassic-Jurassic boundary: Paleomagnetic and  $^{40}\text{Ar}/^{39}\text{Ar}$  evidence from Morocco for brief, episodic volcanism: *Earth and Planetary Science Letters* v. 228, p. 143-160.
- Renne, P.R., Knight, K.B., Nomade, S., Leung, K.-N., and Lou, T.-P., 2005, Application of deuterium-deuterium (D-D) fusion neutrons to  $^{40}\text{Ar}/^{39}\text{Ar}$  geochronology: *Applied Radiation and Isotopes*, v. 62, p. 25-32.
- Renne, P.R., 2000, K-Ar and  $^{40}\text{Ar}/^{39}\text{Ar}$  Dating, in *Quaternary Geochronology: Methods and Applications* (J.S. Noller, J.M. Sowers, and W.R. Lettis, Eds.): American Geophysical Union Reference Shelf Series, v. 4, p. 77-100.
- Renne, P.R., Swisher, C.C., Deino, A.L., Karner, D.B., Owens, T., and DePaolo, D.J., 1998, Intercalibration of Standards, Absolute Ages and Uncertainties in  $^{40}\text{Ar}/^{39}\text{Ar}$  Dating: *Chemical Geology (Isotope Geoscience Section)*, v. 145, p. 117-152.

Steiger, R. H., and Jäger, E., 1977, Subcommission on geochronology: Convention on the use of decay constants in geo- and cosmochronology: Earth and Planetary Science Letters, v. 36, p. 359-362.

### University of Nevada, Las Vegas

Samples analyzed by the  $^{40}\text{Ar}/^{39}\text{Ar}$  method at the University of Nevada Las Vegas were wrapped in Al foil and stacked in 6 mm inside diameter Pyrex tubes. Individual packets averaged 3 mm thick and neutron fluence monitors (FC-2, Fish Canyon Tuff sanidine) were placed every 5-10 mm along the tube. Synthetic K-glass and optical grade  $\text{CaF}_2$  were included in the irradiation packages to monitor neutron induced argon interferences from K and Ca. Loaded tubes were packed in an Al container for irradiation. Samples irradiated at the Nuclear Science Center at Texas A&M University were in-core for 14 hours in the D3 position on the core edge (fuel rods on three sides, moderator on the fourth side) of the 1MW TRIGA type reactor. Irradiations are performed in a dry tube device, shielded against thermal neutrons by a 5 mm thick jacket of  $\text{B}_4\text{C}$  powder, which rotates about its axis at a rate of 0.7 revolutions per minute to mitigate horizontal flux gradients. Correction factors for interfering neutron reactions on K and Ca were determined by repeated analysis of K-glass and  $\text{CaF}_2$  fragments. Measured  $(^{40}\text{Ar}/^{39}\text{Ar})_{\text{K}}$  values were  $0.0002 (\pm 150\%)$ . Ca correction factors were  $(^{36}\text{Ar}/^{37}\text{Ar})_{\text{Ca}} = 3.134 (\pm 7.09\%) \times 10^{-4}$  and  $(^{39}\text{Ar}/^{37}\text{Ar})_{\text{Ca}} = 7.357 (\pm 9.92\%) \times 10^{-4}$ . J factors were determined by fusion of 4-5 individual crystals of neutron fluence monitors which gave reproducibility's of 0.15% to 0.44% at each standard position. Variation in neutron flux along the 100 mm length of the irradiation tubes was <4%. An error in J of 0.1458% was used in age calculations. No significant neutron flux gradients were present within individual packets of crystals as indicated by the excellent reproducibility of the single crystal flux monitor fusions.

Irradiated crystals together with  $\text{CaF}_2$  and K-glass fragments were placed in a Cu sample tray in a high vacuum extraction line and were fused using a 20 W  $\text{CO}_2$  laser. Sample viewing during laser fusion was by a video camera system and positioning was via a motorized sample stage. Samples analyzed by the furnace step heating method utilized a double vacuum resistance furnace similar to the Staudacher et al. (1978) design. Reactive gases were removed by a single MAP and two GP-50 SAES getters prior to being admitted to a MAP 215-50 mass spectrometer by expansion. The relative volumes of the extraction line and mass spectrometer allow 80% of the gas to be admitted to the mass spectrometer for laser fusion analyses and 76% for furnace heating analyses. Peak intensities were measured using a Balzers electron multiplier by peak hopping through 7 cycles; initial peak heights were determined by linear regression to the time of gas admission. Mass spectrometer discrimination and sensitivity was monitored by repeated analysis of atmospheric argon aliquots from an on-line pipette system. Measured  $^{40}\text{Ar}/^{36}\text{Ar}$  ratios were  $284.31 \pm 0.23\%$  during this work, thus a discrimination correction of 1.03938 (4 AMU) was applied to measured isotope ratios. The sensitivity of the mass spectrometer was  $\sim 6 \times 10^{-17}$  mol  $\text{mV}^{-1}$  with the multiplier operated at a gain of 52 over the Faraday. Line blanks averaged 2.04 mV for mass 40 and 0.002 mV for mass 36 for laser fusion analyses and 33.36 mV for mass 40 and 0.08 mV for mass 36 for furnace

heating analyses. Discrimination, sensitivity, and blanks were relatively constant over the period of data collection. Computer automated operation of the sample stage, laser, extraction line and mass spectrometer as well as final data reduction and age calculations were done using LabSPEC software written by B. Idleman (Lehigh University). An age of 28.02 Ma was used for the Fish Canyon Tuff sanidine flux monitor in calculating ages for samples.

For  $^{40}\text{Ar}/^{39}\text{Ar}$  analyses a plateau segment consists of 3 or more contiguous gas fractions having analytically indistinguishable ages (i.e. all plateau steps overlap in age at  $\pm 2\sigma$  analytical error) and comprising a significant portion of the total gas released (typically  $>50\%$ ). Total gas (integrated) ages are calculated by weighting by the amount of  $^{39}\text{Ar}$  released, whereas plateau ages are weighted by the inverse of the variance. For each sample inverse isochron diagrams are examined to check for the effects of excess argon. Reliable isochrons are based on the MSWD criteria of Wendt and Carl (1991) and, as for plateaus, must comprise contiguous steps and a significant fraction of the total gas released. All analytical data are reported at the confidence level of  $1\sigma$  (standard deviation).

Staudacher, T.H., Jessberger, E.K., Dorflinger, D., and Kiko, J., A refined ultrahigh-vacuum furnace for rare gas analysis, *J. Phys. E: Sci. Instrum.*, 11, 781-784, 1978.  
Wendt, I., and Carl, C., 1991, The statistical distribution of the mean squared weighted deviation, *Chemical Geology*, v. 86, p. 275-285.

## APPENDIX C. ANALYTICAL METHODS FOR (U-Th)/He THERMOCHRONOLOGY

Apatites and zircon grains were separated from bulk rock samples by standard crushing, heavy liquid, and magnetic separation techniques and were subsequently handpicked using a binocular microscope. Apatite crystals were selected based on morphology, clarity, and lack of inclusions using a binocular microscope with crossed polars. Zircon selection was based on clarity and crystal morphology. Prior to analysis, grains were photographed and dimensions were measured. Grains were packaged in Pt packets and heated to 1065° C for eight minutes. Extracted He gas was spiked with  $^3\text{He}$ , purified using cryogenic and gettering methods, and analyzed on a quadrupole mass spectrometer.

Degassed apatites were retrieved, spiked with a  $^{235}\text{U}$ - $^{230}\text{Th}$ - $^{51}\text{V}$  tracer, dissolved in  $\text{HNO}_3$  at ~90 °C for 1 hour, and analyzed on a Finnigan Element ICP-MS. Degassed zircons were retrieved, placed in a larger Pt packet with a flux of Li metaborate, heated in a muffle furnace to 1000° C for two hours, and allowed to cool. The resultant bead was spiked with a  $^{235}\text{U}$ - $^{230}\text{Th}$ - $^{51}\text{V}$  tracer, dissolved in  $\text{HNO}_3$  and analyzed on a Finnigan Element ICP-MS. A hexagonal prism morphology was used to make an alpha-ejection corrections for each crystal to account for He ejected from crystal margins (Farley et al., 1996). Fragments of the Durango apatite standard were analyzed by the same procedures with the batch of unknowns.

Farley, K.A., Wolf, R.A., and Silver, L.T., 1996, The effects of long alpha-stopping distances on (U-Th)/He ages: *Geochimica et Cosmochimica Acta*, v. 60, p. 4223-4229.

## Chapter 3

### **Geochronology and geochemistry of Iranian Paleogene volcanism: an extensional arc flare-up**

#### **ABSTRACT**

New U-Pb and  $^{40}\text{Ar}/^{39}\text{Ar}$  geochronology demonstrate that shallow marine to continental volcanism within the Iranian Urumieh-Dokhtar arc was dominated by an Eocene pulse, ~20 My in duration, that is not readily explainable by changes in the subduction rate of Neotethyan oceanic crust. Tertiary submarine volcanic and volcanoclastic deposits in the Alborz Mountains of northern Iran as well as volcanic rocks in the Lut block of eastern Iran are also primarily Eocene in age. Eocene volcanism was enriched in large ion lithophile elements (LILE) and depleted in high-field strength elements (HFSE), a pattern typical of arc magmatism. In contrast, Oligocene basalts from the Urumieh-Dokhtar arc and the Alborz Mtns. are enriched in both LILE and HFSE, features consistent with the generation of magmas from undepleted, asthenospheric mantle. Zr/Nb and Ti/V ratios suggest that the Oligocene basalts were derived from a relatively unoxidized mantle source that is unexpected in volcanic arcs. Together with the recent recognition of Eocene metamorphic core complexes in central and east-central Iran and stratigraphic evidence for Eocene subsidence, these geochemical and geochronological data suggest that the magmatic pulse was related to extension, in contrast to compression-driven flare-ups in the western North American batholith and the Andean volcanic arc. Geochemical, geochronological, and stratigraphic data from the Iranian arc are consistent with an Eocene magmatic pulse that was generated by decompression melting of hydrated, slab-fluid modified lithospheric mantle in the mantle wedge, followed by Oligocene upwelling

and melting of asthenospheric mantle that was less extensively modified by hydrous fluids. Slab-rollback, facilitated by the particularly slow Arabia-Eurasia convergence rate and possibly preceded by a Cretaceous period of flat-slab subduction, may have initiated extension and ignited the flare-up. Neogene volcanism in the eastern Mediterranean region and along the western Trans Mexican Volcanic belt may be well-characterized, recent analogs for the Iranian Eocene flare-up.

## **INTRODUCTION**

Flux-melting models of arc volcanism predict that magma production is closely related to the supply of slab-derived hydrous fluids (e.g., Gill, 1981, McCulloch and Gamble, 1991, Davies and Stevenson, 1992). Regardless of whether these fluids originate from subducted sediments (e.g., Plank and Langmuir, 1993) or hydrous melts of oceanic crust (e.g., Elliott, 2003), the rate at which they are replenished is closely tied to subduction rate (e.g., Davies and Bickle, 1991). Although subduction rate and volcanic output are correlated in some cases (Huang and Lundstrom, 2007), it has become increasingly clear that magmatic production in some arcs is distinctly episodic and that the “flare-ups” responsible for the actual creation of these arcs are not related to changes in subduction rate (Ducea, 2001; Ducea and Barton, 2007). These observations suggest that conventional flux-melting models do not fully account for magma generation processes that operate at some convergent margins. One of these processes may be mantle upwelling, which is linked with volcanism in back-arc basins (e.g., Gribble et al., 1998) and may generate melting beneath volcanic fronts as well (e.g., Sisson and Bronto, 1998).

Two notable examples of magmatic flare-ups are 1) the Cretaceous arc of western North America, where despite a >100 My history of subduction, the batholith is dominated by two pulses, each lasting only 10-15 My (Ducea, 2001); and 2) episodic Miocene to Recent mafic volcanism in the Andean Puna Plateau (e.g., Kay et al., 2005). In both of these examples geologic evidence of syn-magmatic compression has led to models that link flare-ups to shortening of the overriding tectonic plate. In the model of Kay and Kay (1993), shortening and thickening increase the density of the base of the crust, eventually leading to delamination of the lower crust and lithospheric mantle. Partial melting of rising asthenospheric mantle subsequently generates a volcanic pulse. Ducea and Barton (2007) presented isotopic evidence that the North American arcs were derived from the crust and therefore proposed that flare-ups can occur when thickening leads to melting of the lower crust.

In this paper we address one of the most impressive yet understudied magmatic flare-ups in earth history, the Paleogene volcanism in Iran. Mixed volcanic and sedimentary sequences of this age in both the Urumieh-Dokhtar arc in central Iran and the Alborz Mountains in northern Iran are ~3-9 km thick (Figure 1, e.g., Förster et al., 1972, Hassanzadeh, 1993). Marine fossil assemblages within these strata are indicative of a pulse of Eocene submarine volcanism (e.g., Berberian and King, 1981) related to the slow (~3 cm/yr) subduction of Neotethys beneath Iran (McQuarrie et al., 2003). Mesozoic igneous rocks are virtually non-existent within both ranges despite a history of subduction that probably began in late Triassic time, as discussed below. Proposed explanations for the Eocene flare-up have included rifting/back-arc basin development

(Amidi et al., 1984, Amidi and Michel, 1985, Kazmin et al., 1986), changes in subduction angle (Berberian and Berberian, 1981, Shahabpour, 2007), and changes in subduction rate (Takin, 1972, Pazirandeh, 1973, Kazmin et al., 1986). Many previous geochemical studies of Iranian volcanism have been hindered by a lack of stratigraphic context or geochronological data and have not fully addressed complicating issues such as crustal assimilation and secondary alteration, leading to a regional dataset of major and trace element analyses that is difficult to interpret in terms of mantle processes.

In order to clarify these issues, we have conducted a study that 1) places U-Pb and  $^{40}\text{Ar}/^{39}\text{Ar}$  age constraints on the duration of the flare-up, and 2) utilizes major and trace element data from primitive mafic rocks erupted during and after the flare-up to identify temporal changes in the source(s) of magmas. Our geochronology data indicate that the magmatic pulse manifested in the Urumieh-Dokhtar arc and the Alborz Mtns. overlaps in time with the formation of Eocene metamorphic core complexes in central and east-central Iran (Moritz et al., 2006, Verdel et al., 2007) and Eocene normal faulting in the Alborz Mtns. (Guest et al., 2006a). Thus, in contrast to the examples from Cordilleran arcs, in Iran there is clear geologic evidence that the flare-up occurred at a time when the overriding plate was being extended. When placed in the context of regional volcanic and sedimentary stratigraphy, new geochemical data from a subset of primitive lavas illustrate a late Eocene-early Oligocene transition from a period of extensive, basaltic to rhyolitic, late Paleocene to Eocene volcanism with typical arc trace element compositions to a later period of limited mafic Oligocene magmatism with trace element compositions similar to those of oceanic island basalts (OIB). We propose that the Eocene flare-up was

generated by decompression melting of preconditioned, hydrated peridotite in the mantle wedge in response to crustal thinning associated with extension. Subsequent Oligocene OIB-type volcanism was produced as upwelling asthenosphere replaced the thinned lithospheric mantle.

We begin by reviewing the Mesozoic and Cenozoic history of Tethyan subduction and the Tertiary stratigraphic record of volcanism and basin formation within Iran. We then present U-Pb,  $^{40}\text{Ar}/^{39}\text{Ar}$ , and major and trace element data from Tertiary volcanic rocks in the Urumieh-Dokhtar arc and the Alborz Mountains. Finally, we propose a mechanism for generating extension-related magmatic flare-ups that accounts for the geochronological, geochemical, and stratigraphic observations from Iran.

## **REGIONAL GEOLOGY**

Complete discussions of the tectonics and paleogeographic evolution of Iran can be found in Stöcklin (1968), Berberian and King (1981), Dercourt et al. (1986), Ramezani and Tucker (2003), and McQuarrie et al. (2003). Summarized here are the events most pertinent for the generation of arc magmas across central Iran. The various continental blocks that comprise Iran are believed to have been situated along the Paleotethyan margin of Gondwana prior to Permian rifting that separated Iran from Gondwana and opened the Neotethys oceanic basin in its wake (e.g., Ramezani and Tucker, 2003, Hassanzadeh et al., 2008), leaving the Iranian fragments situated between one ocean basin that was expanding and another that was being consumed (Berberian and King, 1981). Neotethys thus widened as Iran was pulled away from Gondwana by the

subduction of Paleotethys beneath the southern margin of Eurasia. A regional unconformity separating rocks as young as Middle Triassic from overlying strata as old as Rhaetic-Liassic is generally interpreted as marking the Middle to Late Triassic closure of Paleotethys (e.g., Stöcklin, 1968, Horton et al., 2008). Plutons of roughly the same age in the Sanandaj-Sirjan zone of southwest Iran (Fig. 1) suggest that subduction of Neotethys beneath Iran initiated at about this time (Berberian and Berberian, 1981, Berberian et al., 1982, Kazmin et al., 1986, Arvin et al., 2007), and may, in fact, have been a direct consequence of the collision between northern Iran and Eurasia (Berberian and King, 1981). Continued subduction and arc magmatism through the Mesozoic is indicated by scattered Jurassic to Cretaceous intrusive rocks within the Sanandaj-Sirjan zone (Fig. 1, Berberian and Berberian, 1981). The distribution of these Mesozoic arc remnants relative to Tertiary volcanic rocks within the Urumieh-Dokhtar arc suggests that the axis of magmatism shifted to the northeast from its initial position within the Sanandaj-Sirjan zone in late Cretaceous or early Tertiary time. On the basis of recent paleogeographic reconstructions (McQuarrie et al., 2003), thermochronometry data from the Alborz Mountains (Axen et al., 2001, Guest et al., 2006b), and new estimates for the age of synorogenic sediments in the Zagros Mtns (Fakhari et al., 2008), Neotethys is believed to have closed from Late Oligocene to Miocene time, initiating the collision between Arabia and Eurasia. Ophiolite outcrops near the Main Zagros reverse fault, which generally separates the Sanandaj-Sirjan zone from the Zagros Mountains (Fig. 1), are believed to mark the suture between Arabia and Eurasia. This interpretation of Iranian regional geology suggests that subduction of Neotethys beneath Iran was on-

going from approximately Late Triassic until at least Late Oligocene time, some 175 million years.

### **ARC STRATIGRAPHY**

Paleogene volcanic rocks crop out in three general regions within Iran (Fig. 1). The first is along a NW-SE belt that extends ~1500 km across the central part of the country. This belt, named the Urumieh-Dokhtar arc in reference to localities at either end, terminates rather abruptly to the southeast near the Pakistan border and merges with volcanic rocks in the Lesser Caucasus and Alborz Mtns. to the northwest. The arc is subparallel to, and approximately 175-200 km northeast of, the Main Zagros reverse fault, although Neogene compression within the Sanandaj-Sirjan zone may have shortened this arc-trench gap since the time of active subduction (Berberian and Berberian, 1981). The Lesser Caucasus/Alborz outcrop belt extends southeast to near Semnan, where it becomes discontinuous and extends into eastern Iran. The third region is a large area of Tertiary volcanic rocks in the Lut block of eastern Iran. Our study is focused on the first two regions. Geochemical studies of volcanism in eastern Iran have been particularly sparse; Jung et al. (1984) is one of the few publications available.

Tertiary volcanic rocks in the Alborz Mtns. and Urumieh-Dokhtar arc unconformably overlie Mesozoic sections generally consisting of marine carbonates and siliciclastic rocks. Although separated by up to several hundred km, the general Tertiary stratigraphy in these ranges is remarkably similar. In both, the older part of the Tertiary section is made up of volcanic rocks of wide-ranging composition interbedded with marine and

continental sedimentary strata. Evidence for submarine volcanism, including pillow lavas, has been widely reported (Stöcklin, 1968, Förster et al., 1972, Alberti et al., 1979, Amidi et al., 1984, Spies et al., 1984, Amidi and Michel, 1985, Hassanzadeh, 1993).

This volcanic and sedimentary part of the section, which makes up the majority of the Tertiary outcrops shown on Fig. 1, is typically overlain, in both arc segments, by the late Eocene-early Oligocene Lower Red Formation, consisting of conglomerate, sandstone, shale, and gypsum, as well as relatively limited pyroclastics and volcanic flows.

Conformably overlying the Lower Red Fm. are ~1200 meters of marine limestones and marls comprising the Oligocene to early Miocene Qom Formation. Mafic lava flows are present within the Qom Formation in the Urumieh-Dokhtar arc and immediately below the Qom-correlative Gand Ab limestones in the western Alborz Mtns., where they have yielded  $^{40}\text{Ar}/^{39}\text{Ar}$  whole rock ages of ~33 Ma (Guest et al., 2007b). The Qom Fm. is conformably overlain by gypsum-bearing red beds of the Miocene Upper Red Formation and continental Pliocene and Quaternary sediments.

The Cenozoic stratigraphic record in the Alborz Mtns and Urumieh-Dokhtar arc, and across much of Iran, thus suggests a Tertiary history that began with a large pulse of shallow marine Eocene magmatism and sedimentation. As volcanism diminished and sea-level fell near the end of the Eocene, gypsum-bearing red beds of the early Oligocene Lower Red Fm. were deposited. Subsidence in the early Oligocene (Guest et al., 2007b) was accompanied by limited basaltic magmatism and led to deposition of the Qom Fm. in central Iran and correlative shallow marine limestones in northern Iran. Deposition of the Miocene Upper Red Formation marks the end of marine conditions over most of Iran.

## GEOCHRONOLOGY

### Urumieh-Dokhtar U-Pb and $^{40}\text{Ar}/^{39}\text{Ar}$ geochronology, Tafresh region

North of the town of Tafresh in central Iran, ~200 km southwest of Tehran, a cross-section through the Urumieh-Dokhtar arc is exposed as the relatively undeformed limb of a northwest-southeast trending syncline. In this area, complexly faulted Mesozoic carbonates and siliciclastic strata are unconformably overlain by the typical arc sequence described above: Paleocene-Eocene volcanic and sedimentary rocks, the Lower Red Fm, carbonates and mafic volcanics of the Qom Fm, and the Upper Red Fm. (Fig. 2). We collected a transect of silicic to intermediate volcanic samples that extends from the base of the volcanic sequence through the Lower Red Formation (Fig. 2). U-Pb zircon ages for the majority of these samples were determined with the UCLA ims1270 ion probe.  $^{40}\text{Ar}/^{39}\text{Ar}$  plagioclase dates were determined at the Nevada Isotope Geochronology Lab.

An andesite flow near the base of the volcanic section has a U-Pb zircon age of  $54.7 \pm 3.1$  Ma ( $2\sigma$ ) (Figs. 2 and 3, Table 1). A sample of green tuff from slightly higher in the section has a plagioclase  $^{40}\text{Ar}/^{39}\text{Ar}$  isochron of  $50.9 \pm 4.4$  Ma and a plateau of  $56.6 \pm 3.9$  Ma (Figs. 2 and 3, Table 2), both of which are statistically indistinguishable from the U-Pb age of the underlying andesite. We consider  $54.7 \pm 3.1$  Ma to be our best estimate for the age of the oldest Tertiary arc volcanism preserved along the transect. Ages decrease up section and reach  $44.3 \pm 2.2$  Ma in the middle of the volcanic section (Fig. 2).

### **Karaj Formation U-Pb geochronology, Chalus Road region**

The Eocene Karaj Formation in the Alborz Mtns. of northern Iran is comprised of 3000-4000 meters of volcanic, volcanoclastic, and sedimentary strata that has been subdivided into the following members: lower shale, middle tuff, Asara shale, and upper tuff (e.g., Stöcklin and Setudehnia, 1977). The conspicuously green tuffs and tuffaceous sediments of some renown in Iranian geology are most prevalent within the middle part of this formation, and in some sections within the Alborz Mtns., lavas of dacitic to basaltic composition are present between the Asara shale and the upper tuff member. Samples of tuffaceous material within the Karaj Fm. were collected along the Chalus Road north of Tehran (Figs. 1 and 4). We determined U-Pb ages of  $49.3 \pm 2.9$  Ma for the middle tuff member,  $45.3 \pm 2.3$  Ma for a tuff within the Asara shale, and  $41.1 \pm 1.6$  Ma for the upper tuff member (Figs. 3 and 4).

### **Additional U-Pb and $^{40}\text{Ar}/^{39}\text{Ar}$ geochronology and a composite stratigraphic section**

Building on the extensive geologic mapping performed by the Geological Survey of Iran and previous studies of Iranian Tertiary volcanism, we have assembled a regional volcanic and sedimentary stratigraphy for the Tertiary sections in the Alborz Mtns and Urumieh-Dokhtar arc. In the Alborz Mtns., this regional correlation encompasses geologic maps from the Saveh, Qazvin and Rasht, Tehran, Semnan, and Torud quadrangles (Fig. 5). In each of these areas, Cretaceous rocks, usually limestones, are separated from overlying Tertiary rocks by a prominent unconformity. The oldest Tertiary rocks exposed above the unconformity are conglomerates of the Fajan Formation, or “Eocene basal conglomerate,” which are thought to be Paleocene to early Eocene in

age (Stöcklin and Setudehnia, 1977). In the Tehran and Semnan quadrangles, the Fajan Fm is overlain by 400-500 m of marine limestones and marls comprising the Eocene Ziarat Formation. Conformably above the Ziarat Fm. are ~4000 m of sediments and volcanics of the Karaj Formation and equivalent Eocene strata as described above. We determined an additional U-Pb age of  $52.2 \pm 3.4$  Ma for a rhyolitic tuff in the lower part of the Eocene volcanic section ~80 km west of Torud in the eastern Alborz Mtns. (Figs. 1 and 3, Alavi and Hushmandzādeh, 1976). This age is indistinguishable from the oldest Tertiary volcanic ages obtained from both the Tafresh transect in the Urumieh-Dokhtar arc and the Chalus Road transect in the western Alborz Mtns. In addition, we obtained an  $^{40}\text{Ar}/^{39}\text{Ar}$  biotite age of  $37.2 \pm 0.38$  Ma from gabbros that intrude the Karaj Fm near Mobarak-abad, ENE of Tehran. This age is slightly younger than the U-Pb age of  $41.1 \pm 1.6$  Ma determined for the upper tuff member and places a radiometric age constraint on the end of Karaj Fm. deposition. Geochemical data from these late Eocene mafic intrusions are discussed below. Unconformably overlying the Karaj Fm. are sandstones, evaporites, marls, and limestones of the late Eocene Kond Formation which are unconformably overlain by the Oligo-Miocene Lower Red Formation, and the remainder of the section is as described above. The stratigraphic positions of mafic to intermediate samples collected for major and trace element geochemistry and described below are illustrated in Figure 5.

The Tertiary stratigraphy of the Urumieh-Dokhtar arc was compiled in a similar fashion from geologic maps of the Ahar, Saveh, Qom, Aran, Anarak, and Nain geologic quadrangle maps and several studies focused on Tertiary magmatism within the arc (Fig.

6). As noted above, the Tertiary stratigraphy of the Urumieh-Dokhtar arc is essentially the same as in the Alborz Mtns. We determined a U-Pb age of  $37.3 \pm 1.2$  Ma for a welded tuff ~60 km east of Saveh in the northwestern part of the Urumieh-Dokhtar arc (Fig. 3). This age is slightly younger than that determined for the Upper Tuff Member of the Karaj Fm. from the Chalus Road transect but overlaps with the  $^{40}\text{Ar}/^{39}\text{Ar}$  biotite age of gabbros intruding the Karaj Fm. in the Alborz Mtns. We interpret this age as marking the end of the magmatic flare-up. Based on the oldest and youngest U-Pb ages from the main period of volcanism, which are corroborated by  $^{40}\text{Ar}/^{39}\text{Ar}$  ages, we estimate that the magmatic flare-up lasted from  $54.7 \pm 3.1$  Ma (late Paleocene-early Eocene) until  $37.3 \pm 1.2$  Ma (late Eocene), implying a duration of ~13-22 million years. Given the prominent unconformity at the base of the Eocene volcanic section in both the Urumieh-Dokhtar arc and the Alborz Mtns., this is a minimum estimate for the duration of the flare-up.

In general, Mesozoic volcanic strata beneath the Eocene basal conglomerate are thin or absent, although there are exceptions. For instance, up to 1 km of middle to late Cretaceous intermediate to mafic lavas are present in the northern Alborz Mtns. in the Qazvin and Rasht quadrangle (Fig. 1, Annells et al., 1975). In this area the Karaj Fm. reaches a thickness of 6 km, however, suggesting that even in areas where Cretaceous volcanism occurred it was subsidiary to Eocene volcanism and sedimentation. As discussed below, the general distribution of Cretaceous volcanic and intrusive rocks to the northeast of late Triassic and Jurassic plutons (Fig. 1) may imply a Cretaceous period of flat-slab subduction.

Previous radiometric age constraints from the Urumieh-Dokhtar arc as well as our new ages are summarized in Figure 6, as are the stratigraphic positions of samples from the arc that were collected for geochemical investigation. The main pulse of volcanism occurred in the Eocene, but outcrops of younger intrusive and extrusive rocks indicate that magmatic activity continued after the Eocene pulse. This younger phase of magmatism spans from the early Oligocene until Recent time and has been widespread across Iran but volumetrically small compared with the Eocene flare-up. We next discuss geochemical differences that distinguish primitive volcanism erupted during the Eocene and Oligocene periods.

## **GEOCHEMISTRY**

### **Previous work**

Modern, high-quality geochemical investigations of Iranian Tertiary volcanism have been limited compared with many other arcs. We compiled ~275 major element analyses from 10 previous studies focused on the Iranian arcs (see Fig. 1 for the locations of these prior studies). These analyses were compared with large datasets from the Andes and Cascades which typify the basic geochemical attributes of continental arc volcanism. First-order compositional differences between volcanism in Iran and these well-characterized arcs are evident by comparing datasets from each region on total alkali-silica (TAS) diagrams (Figs. 7A, B, C and D). As these diagrams make clear, previous data from Iran suggest that Iranian Tertiary volcanism was significantly more alkaline than arc magmatism in more extensively studied regions. This characteristic of Iranian volcanism has been noted previously (e.g., Amidi et al, 1984, Kazmin et al., 1986, Aftabi

and Atapour, 2000), but has not been fully explained. We discuss the most likely possibilities for the generation of these alkaline lavas later in the paper. A more rigorous analysis of the older Iranian data is difficult because many of the analyses lack trace element, petrographic, and/or stratigraphic information. We discuss below a new suite of samples that, although limited in number, come from key stratigraphic intervals within the Tertiary arcs and capture much of the compositional diversity that has been established by previous studies.

### **Major and trace element data**

Twenty-one new samples of mafic to intermediate lavas and subvolcanic intrusions were collected in the Alborz Mtns., mainly north of Tehran, and in the Urumieh-Dokhtar arc, primarily between the cities of Saveh and Nain (Fig. 1). Mafic samples were preferentially collected in order to minimize the potential effects of differentiation from crustal contamination and fractional crystallization (e.g., DePaolo, 1981). A disadvantage of this approach is that these mafic rocks generally do not contain minerals suitable for U-Pb geochronology. In order to overcome this problem, plagioclase  $^{40}\text{Ar}/^{39}\text{Ar}$  ages were determined for some samples, and relative ages of the remainder were estimated from their stratigraphic position as discussed above.

Major element oxide and trace element (Nb, Zr, Y, Sr, U, Rb, Th, Pb, Ga, Zn, Ni, Cr, V, Ce, Ba, La, and Ti) compositions of these 21 samples were determined using X-ray fluorescence (XRF) at the Ronald B. Gilmore XRF laboratory at the University of Massachusetts (Table 3). Details of the analytical procedure can be found in Rhodes

(1996). The samples range from 44 to 59 wt.% SiO<sub>2</sub>. On a TAS diagram (Fig. 7E), 18 of the 21 samples plot within the field defined by the datasets from the Andes and Cascades, and the remainder (samples TA5, NA3, and TRD5) are unusually alkaline. The alkaline samples, all of which contain the zeolite mineral analcime (NaAlSi<sub>2</sub>O<sub>6</sub>·2H<sub>2</sub>O), would conventionally be called shoshonites. Due to their unusual composition and potential evidence for low-grade metamorphism they are discussed separately below. The 18 remaining “normal” samples can be subdivided into two groups based on the SiO<sub>2</sub> content normally specified as the divide between basalts and andesites: five have >53 wt.% SiO<sub>2</sub>, and 13 have <53 wt.% SiO<sub>2</sub>. Of the basaltic andesite and andesite samples with >53 wt.% SiO<sub>2</sub>, four of them (AN3, DEHNAR1, QM2 and AN5) are classified as medium-K andesites using the scheme proposed by Gill (1981), and the other (AR3) is high-K. Eight of the 13 samples with <53 wt.% SiO<sub>2</sub> are classified as basalts, and the remainder are basanites, trachybasalts, or basaltic trachyandesites. Eight of these mafic samples are alkalic according to the definition of Macdonald and Katsura (1964), three should probably be called “transitional” (Sheth et al., 2002), and the remaining two are sub-alkalic.

The transfer of incompatible elements from subducting slabs to the mantle wedge often results in distinctive trace element compositions of arc volcanism that can be illustrated on normalized trace element diagrams (Fig. 8, e.g., Pearce and Cann, 1973, Gill, 1981). The most common traits of arc volcanism are enrichment, relative to mid-ocean ridge basalts (MORB), of large ion lithophile elements (LILE) such as K, Rb, Sr, Ba, Th, U, and the light rare earth elements (REE), and the relative depletion of high field strength

elements (HFSE) such as Ti, Y, Zr, Nb, and the heavy REE. Enrichment of LILE is generally attributed to the addition of these water-soluble elements by fluids derived from the dehydration of the subducted slab (e.g., Tatsumi et al., 1986), while depletion of the generally fluid-immobile HFSE is thought to reflect a pre-existing depletion within the mantle wedge (e.g., McCulloch and Gamble, 1991, Woodhead et al., 1993, Elliott, 2003). The combination of enrichment in one group of elements and depletion in another results in characteristic “spiked” trace element diagrams. In contrast, back-arc basin basalts (BABB) are normally undepleted in their HFSE compositions (e.g., Woodhead et al., 1993). Because BABB are typically enriched in both LILE and HFSE, they tend to have relatively smooth trace element diagrams. From a practical perspective, trace element compositions of volcanic rocks may not provide any meaningful information about mantle compositions if those rocks did not originate from mantle melts or if extensive differentiation has occurred. This important caveat is discussed at length below, but first we describe the overall major and trace element compositions of our samples.

Trace element data from the five andesitic lavas and intrusions (Fig. 8A) are the most likely to have been affected by assimilation and fractional crystallization, and it is therefore difficult to draw conclusions about mantle compositions from these data. Three of the andesites (AN5, DEHNAR1, and AR3) are Eocene and have strong depletions in Nb, which is probably the most characteristic trace-element feature of arc magmatism (e.g., Gill, 1981). AN3, an Oligocene dike that is the most mafic of the andesite samples, has small positive spikes for the LILE Ba, K, and Sr, possibly related to slab contributions of these elements, but essentially no depletions of the HFSE. QM2, an

Eocene andesite flow from the Urumieh-Dokhtar arc near Tafresh, is Nb depleted and has a positive K spike, typical arc traits, but also contains little La and Ce, which is somewhat unusual because these LREE are fluid mobile and expected to be contributed more extensively by the subducting slab. LREE abundances are often observed to negatively correlate with SiO<sub>2</sub> content, however, so fractional crystallization is a likely explanation for the low LREE concentrations of this lava.

The subalkaline and transitional basalts, all of which are Eocene, have quite uniform trace element compositions (Fig. 8B). These basalts have relative depletions of the HFSE Nb, Zr, Ti, and Y and positive spikes for the LILE Ba, K, and Sr. These characteristics, as well as the general abundance of incompatible elements relative to MORB, can be explained as contributions from a subducting slab and/or assimilation of continental crust, as discussed below. Trace-element diagrams of the eight alkalic basalts (Fig. 8C) are more complicated. Four of these (QM6, SV4, TA1, and TA3) have prominent negative Nb spikes and positive Ba spikes, features consistent with an arc setting. The remaining alkalic basalts lack the characteristic Nb depletion.

As this description makes clear, some samples have all of the trace element characteristics of arc volcanics, e.g., the subalkaline basalts, some have virtually none, e.g., alkaline basalt samples MSHK1 and 7453, and other samples have some of the common characteristics but not all, e.g., QM6 has a negative Nb spike but no positive Sr spike. One complicating factor in evaluating these data is that the samples are of different ages, which has motivated the preceding discussion of geochronology and arc

stratigraphy. Another potential problem inherent to interpreting trace element data from continental arcs is the effect of crustal assimilation (e.g., DePaolo, 1981, Dungan and Davidson, 2004). The trace element composition of bulk continental crust (e.g., Taylor and McLennan, 1985) is quite similar to the composition of typical arc magmas, so extensive assimilation of crustal material can impart an “arc signature” to melts regardless of their original composition. Assuming that assimilation will lead to more silicic compositions, the problem can be minimized to some degree by filtering out all but the most primitive samples. Geochemical criteria modified from Collins (2002) were used to screen out samples that are the most likely to have been affected by crustal contamination and fractional crystallization.

A subset of our samples that meet these criteria ( $<53$  wt.%  $\text{SiO}_2$ ,  $>5$  wt.%  $\text{MgO}$ ,  $>130$  ppm Cr,  $\geq 50$  ppm Ni) are still somewhat removed from mantle compositions, but are nevertheless the most likely to provide insight into mantle compositions (Figs. 8D and E). Sample AN3 has also been included in this group despite containing 53.02 wt.%  $\text{SiO}_2$  because it meets the other geochemical criteria. Three of the basalts within the subset (SV4, TA1 and QZ2; Fig. 8D) contain analcime and will be discussed separately because their original trace element compositions have quite possibly been modified during the formation of analcime (Prelević et al., 2004). Major and trace element data for the remaining primitive and unaltered basalts suggest a key geochemical distinction between the Eocene and Oligocene samples (Fig. 8E). Two Late Eocene subvolcanic mafic intrusions from the Alborz Mtns. have typical arc characteristics, in particular the prominent Nb depletion. Although there are only two Eocene samples in this subset of

primitive basalts, the trace element patterns of all of the Eocene andesites (Fig. 8A) and Eocene shoshonites (Fig. 8F) also have characteristic Nb depletions. In contrast, the four Oligocene samples have quite different trace element compositions, with no Nb depletion and overall flat trace element diagrams. These characteristics are quite similar to OIB (Fig. 8E), but there are some subtle differences. Unlike OIB, sample AR5 has a small positive Sr spike, and three of the four samples have small negative Th spikes. Both of these features are consistent with contributions from slab-derived fluids (Elliott 2003). The fundamental difference between the Eocene and Oligocene samples is that while both groups are enriched in LILE, only the Eocene samples are depleted in HFSE. Both groups display evidence for modification by slab-derived fluids which would suggest continued subduction through the Eocene and early Oligocene.

In addition to trace-element diagrams, ratios of various incompatible elements are often used to infer the tectonic settings of ancient volcanic rocks. In the case of Iranian volcanism, two commonly-used trace element ratios, Zr/Nb and Ti/V, are particularly effective in illustrating the compositional differences between volcanics of different age. Both Zr and Nb are fluid-immobile and resistant to secondary alteration. Because arc lavas are characteristically depleted in Nb, Zr/Nb ratios are typically greater for arc volcanics than MORB or OIB. This ratio can therefore provide some insight into the contributions of subducted slabs in arc and back-arc environments. The basis for tectonic discriminations utilizing Ti and V is the sensitivity of V partitioning to oxygen fugacity ( $fO_2$ ) (Shervais, 1982). Oxidizing environments favor the partitioning of V into melt, whereas Ti partitioning is relatively unaffected by  $fO_2$ . Thus, to first order, oxidizing

conditions will lead to the production of magmas with relatively low Ti/V. MORB, produced under conditions of low  $fO_2$ , typically have Ti/V of 20 to 50, while arc volcanism, generated under more oxidizing conditions, generally has Ti/V of 10 to 20. On plots of Ti/V vs. Zr/Nb, primitive rocks from volcanic arcs would be predicted to have Ti/V of ~10-20 (Shervais, 1982) and Zr/Nb of ~10-100 (Davidson, 1996). In the case of our subset of samples, the two late Eocene intrusions have ratios that are generally in this range (Fig. 9). The Oligocene samples, however, have Zr/Nb ratios of ~3 to 9, and Ti/V ratios of 41 to 56. These values are unusual in arc settings and suggest that the source of the Oligocene volcanism was relatively undepleted in HFSE and unoxidized compared with the Eocene mantle source.

We conclude from this dataset that major and trace element compositions of several Oligocene Iranian basalts contrast with the typical compositions of lavas erupted during the Eocene main phase of volcanism in two fundamental ways. First, the Oligocene magmatism appears to be more mafic overall. These lavas are often primitive basalts, whereas Eocene volcanism was of wide-ranging composition but seldom included primitive mafic lavas. Second, the Oligocene basalts exhibit fewer of the classic geochemical traits of arc volcanism, i.e., Nb and Zr depletions, distinct positive Sr spikes, high Zr/Nb and low Ti/V ratios, which are usually found during the older phase of volcanism. Assuming that the compositions of these basalts are, in fact, related to the trace element compositions of their source, the difference in trace element compositions suggests that the source of magmatism changed in the early Oligocene. The timing of this transition is fairly well-constrained by geochronology data, although it is quite

conceivable that the change was not synchronous over a large area. Sample 7453, an Oligocene basalt flow at the base of the Gand Ab limestones in the Alborz Mtns., has OIB-type trace element characteristics (Fig. 8E) and is stratigraphically equivalent to a basalt dated by  $^{40}\text{Ar}/^{39}\text{Ar}$  whole rock at  $32.7 \pm 0.3$  Ma (Guest et al., 2007b). Comparison of this date with the  $^{40}\text{Ar}/^{39}\text{Ar}$  biotite age of  $37.2 \pm 0.38$  Ma from the Mobarak-abad gabbro, equivalent in age to samples DV1 and DV4 which have typical arc trace element compositions (Fig. 8E), suggests that the transition in magma sources occurred between  $\sim 37$  and 33 Ma. In terms of field relationships, the later period of OIB-type magmatism often occurs as basalt flows just below and within the Qom Fm. and mafic subvolcanic intrusions into the Karaj Formation and equivalent Eocene strata. However, some of the intrusions into the Karaj Fm., such as those represented by samples DV1 and DV4, seem to be slightly older and are part of the earlier period of magmatism with typical arc characteristics. Although additional fieldwork is required in order to fully establish the cross-cutting relationships between these intrusions and overlying formations, the late Eocene-early Oligocene Lower Red Fm. seems to be the key marker bed that separates underlying volcanic rocks with typical arc trace element compositions from overlying OIB-type volcanism. These stratigraphic relationships and a summary of our geochronology and geochemical data are illustrated in Figure 10.

### **Iranian shoshonites**

Shoshonites are high-K volcanic rocks with the following major and trace element characteristics from Morrison (1980): near silica saturated,  $\text{Na}_2\text{O} + \text{K}_2\text{O} > 5$  wt.%,  $\text{K}_2\text{O}/\text{Na}_2\text{O} > 0.5$  at 50 wt.%  $\text{SiO}_2$ , and  $> 1$  at 55 wt.%  $\text{SiO}_2$ ;  $\text{TiO}_2 < 1.3$  wt.%,  $\text{Al}_2\text{O}_3 > 14$

wt.%, low Fe enrichment, and high LILE. Shoshonites of Tertiary age have been widely described in Iran (e.g., Alberti et al., 1979, Amidi et al., 1984, Kazmin et al., 1986, Aftabi and Atapour, 2000). Three of our new samples (TRD5, NA3, and TA5) meet the preceding definition and form an outlying group on a TAS diagram (Fig. 7E). These samples all contain analcime, and previous descriptions of Iranian shoshonites usually mention the presence of analcime (Alberti et al., 1979, Amidi et al., 1984, Hassanzadeh, 1993, Aftabi and Atapour, 2000). As discussed above, three samples that are not shoshonites and which meet our geochemical criteria for primitive volcanism also contain analcime. In all of these samples, analcime occurs as small grains within the groundmass, and in the three shoshonitic samples it also occurs as larger crystals that superficially appear to be phenocrysts (Fig. 11). The widespread occurrence of analcime in Iranian arc rocks, and in particular the close association between analcime and the alkaline rocks that seem to define the first-order compositional difference between the Iranian arc and many other continental arcs (compare Figs. 7B, C, and E), necessitate a closer examination of how analcime formed and its effect on the trace element compositions of the rocks in which it occurs.

Hassanzadeh (1993) and Aftabi and Atapour (2000) suggested that analcime in Tertiary volcanic rocks of the Urumieh-Dokhtar arc formed after leucite ( $\text{KAlSi}_2\text{O}_6$ ). We found no trace of leucite in our analcime-bearing samples using a scanning-electron microscope, although this does not rule out the possibility that it was replaced entirely. Given the lack of clear evidence for a secondary origin, another possibility is that analcime is primary. Debates about the primary or secondary origin of analcime in potassic volcanic rocks

similar to those in Iran have arisen in several locations worldwide (see discussion and references in Prelević et al., 2004). The consensus that has developed in most of these cases is that analcime formed by replacement of a precursor mineral, usually leucite or nepheline, by hydrothermal fluids or during the late stages of crystallization from a hydrous melt (e.g., Karlsson and Clayton, 1991). Although we cannot rule out the primary origin of analcime, descriptions of Tertiary basalts and andesites containing nepheline from the Urumieh-Dokhtar arc (Hassanzadeh, 1993) suggest that the alteration hypothesis is more likely. This explanation, if true, raises doubts about the reliability of geochemical data from analcime-bearing samples because these compositions have almost certainly been modified by reactions with water-rich fluids (Gianetti and Masi, 1989, Prelević et al., 2004). In particular, the scatter displayed by the analcime-bearing samples on the plot of Zr/Nb vs. Ti/V (Fig. 9) may be attributable to changes in the concentration of one or more of these elements during the formation of analcime.

These concerns notwithstanding, analcime-bearing shoshonites are still fairly uncommon rocks, and their presence in Iran may have petrologic and tectonic significance. If the alteration hypothesis is true, it implies that the protoliths of these rocks were highly potassic (Prelević et al., 2004) and contained feldspathoids. The shoshonites analyzed during this study have Rb, Ba, Th, and K concentrations that are 2 to 6 times higher than OIB (Fig. 8F). Potential explanations for enrichment of these elements include addition by hydrous fluids during the formation of analcime, crustal assimilation, extreme additions of fluid-mobile LILE from a subducting slab, derivation from a highly enriched source, and low degrees of partial melting. Additional work is needed to fully understand

the petrogenesis of these lavas, but with the data available it is possible to evaluate the viability of these various options. First, it is important to note that the analcime-bearing primitive basalts have significantly lower LILE concentrations than the shoshonites: the late Eocene to Oligocene basaltic trachyandesite (SV4) has Rb, Ba, Th, and K contents that are only slightly higher than OIB, while the two Eocene basalts (QZ2 and TA1) have less Rb, Th and K than OIB and similar Ba (Fig. 8D). The discrepancy in the concentrations of these elements between the high-K and normal-K samples suggests that the process of forming analcime is not fully responsible for the extreme LILE enrichment and that at least some of this enrichment is a primary feature of the lavas.

While the slightly elevated  $\text{SiO}_2$  content of the shoshonites may indicate some crustal contamination, somewhat specialized and arguably unlikely conditions would be necessary to contribute sufficient LILE through crustal assimilation to match the compositions of the shoshonites while keeping  $\text{SiO}_2$  below 56 wt.%, the highest shoshonite value. For instance, the shoshonites typically contain about twice as much Ba, ~4 times as much K, ~6 times as much Th, and ~10 times as much Rb as the most enriched andesites despite having lower  $\text{SiO}_2$  contents. There is also no obvious correlation between  $\text{SiO}_2$  or MgO and Rb, Ba, Th, or K within the three shoshonite samples. In fact, the shoshonite lava with the highest MgO content (TRD5, 8.02 wt. % MgO) is also the most potassic, ~6 wt. %  $\text{K}_2\text{O}$ .

Large continuous additions of LILE from the subducted slab are unlikely given the slow subduction rate, but pulses of LILE related to slab melting are a possibility, as suggested

by Aftabi and Atapour (2000). The shoshonites analyzed in this study have elevated Sr/Y ratios ( $>40$ ), one of the geochemical traits of adakites, i.e., volcanic rocks thought to be derived from slab melting (Defant and Drummond, 1990). The shoshonites are slightly too mafic to meet the definition of adakite, but Defant and Drummond (1990) note that adakites may be associated with mafic volcanism that is highly enriched in LILE. With the available data, we cannot rule out the possibility that the shoshonites are related to slab melting, nor can we eliminate the possibility that LILE enrichment is due to low degrees of partial melting and/or derivation from an enriched source. These latter two possibilities were proposed by Stern et al. (1988) for the generation of shoshonites with similar LILE enrichments in the Mariana arc, where assimilation of continental crust is a non-factor and secondary enrichment is unlikely. Either explanation is consistent with the Tertiary tectonic setting of Iran: low degrees of partial melting could have been caused by a limited supply of slab fluids resulting from the slow subduction rate, or from mantle upwelling accompanying lithospheric thinning. Alternatively, the subsequent Oligocene OIB-type volcanism suggests that an enriched mantle source may have been available as well.

## **DISCUSSION**

Paleogeographic reconstructions and geologic evidence suggest that Neotethyan oceanic crust was subducted beneath Iran from approximately Late Triassic to Late Oligocene time. Despite this ~175 My history, geochronology data indicate that extensive arc volcanism within the Urumieh-Dokhtar arc and Alborz Mtns. occurred over a period of ~17 My, only 10% of the duration of subduction. Furthermore, volcanic rocks in the arcs

are typically interbedded with sediments containing shallow marine fossil and occasionally display textures suggestive of submarine eruption, i.e., pillows, indicating that shallow marine conditions were maintained despite the accumulation of several km of volcanic and sedimentary rocks. This juxtaposition of continental arc volcanism with marine sedimentation is most readily explained by syn-volcanic subsidence that compensated for the addition of volcanic material during the magmatic flare-up. Eocene extension and associated volcanism and basin formation in Iran have been suggested many times before (Takin, 1972, Pazirandeh, 1973, Amidi et al., 1984, Jung et al., 1984, Amidi and Michel, 1985, Kazmin et al., 1986, Emami, 1991, Hassanzadeh, 1993, Soltani, 2000, Hassanzadeh et al., 2002, Vincent et al., 2005, Guest et al., 2006a and b, Guest et al., 2007b, Shahabpour, 2007) and have recently gained additional support with the recognition of Eocene metamorphic core complexes in central (Moritz et al., 2006) and east-central (Verdel et al., 2007) Iran. Geologic maps and descriptions of the local geology of recently reported eclogite outcrops in the Sanandaj-Sirjan zone near Shahr-e-Kord (Fig. 1, Davoudian et al., 2007) suggest that this area, located in the forearc of Urumieh-Dokhtar, may be another Eocene metamorphic core complex.

### **Mechanism for the Iranian Tertiary flare-up**

Several explanations have been proposed for the Iranian flare-up and shoshonitic volcanism. In this section we evaluate the plausibility of the following mechanisms: change in subduction rate, change in subduction angle, slab melting, and back-arc basin development/rifting. In evaluating these explanations, four key observations must be considered: 1) the Eocene magmatic pulse was largely submarine, 2) Eocene volcanism

occurred ~100 km inland from the remnants of the Mesozoic arc, 3) Oligocene OIB-type mafic magmatism followed the Eocene flare-up, and 4) parts of Iran underwent Eocene extension as indicated by the presence of Eocene metamorphic core complexes.

#### *Changes in subduction rate*

Increased subduction rate would add a proportionally larger supply of hydrous fluids to the subduction zone per unit time, presumably leading to an increase in volcanic activity as predicted by conventional models of flux melting. Kazmin et al. (1986) proposed an explanation analogous to this for the Iranian flare-up while Takin (1972), Pazirandeh (1973), and Hassanzadeh (1993) held the opposite view and argued that subduction slowed in the Eocene because of diminished spreading in the Indian Ocean, leading to extension and volcanism within the Iranian arc. Kinematic reconstructions of Arabia-Eurasia convergence offer a direct means of evaluating these hypotheses. These plate reconstructions show that the rate and obliquity of convergence between Arabia and Eurasia was nearly constant from ~56 to 20 Ma (McQuarrie et al., 2003), signifying that the end of the pulse was not coincident with a change in subduction rate. Longer-term reconstructions by Savostin et al. (1986) suggest that the convergence rate was about 0.7 cm/yr faster during the Eocene than in the Paleocene, lending some support to the notion that the pulse was caused by increased subduction rate. However, considering that many arcs form in settings where convergence rates are ~10 cm/yr (DeMets et al., 1994), it would seem unlikely that an increase of less than 1 cm/yr would generate a sudden magmatic pulse of the magnitude seen in Iran. The Paleogene Arabia-Eurasia convergence rate of ~3 cm/yr is less than half of the present-day Andean convergence

rate (DeMets et al., 1994) and approximately one-third to one-half of the Cretaceous to Jurassic rate between the Farallon and North American plates when nearly all of the plutons in the North American arcs were emplaced (Page and Engebretson, 1984). If first-order comparisons are drawn between the Iranian arc and the Cordilleran arcs of North and South America based on subduction rate, magmatic production should have been relatively limited in Iran, perhaps one half of that in the Cordilleran examples. The limited extent of Mesozoic plutons in the Sanandaj-Sirjan zone suggests that this may, in fact, have been true for the initial axis of the Iranian arc.

#### *Changes in subduction angle*

The Late Cretaceous-early Tertiary inland shift in the locus of arc activity from the Sanandaj-Sirjan zone to the Urumieh-Dokhtar arc (Fig. 1) could be linked to a shallow subduction angle. Berberian and Berberian (1981) and Shahabpour (2007) proposed that various changes in subduction angle could account for the spatial pattern of magmatism within Iran, as well as transitions from compressional to extensional tectonic regimes. In other areas it has been suggested that flat-slab subduction could remove the lithospheric mantle from the overriding plate and trigger upwelling of asthenospheric mantle, potentially explaining the Oligocene OIB-type magmatism. However, this explanation is at odds with the evidence for submarine deposition of the Eocene volcanic and sedimentary strata and the existence of Eocene metamorphic core complexes, both of which suggest a syn-volcanic period of extension and subsidence. Flat-slab subduction is normally associated with contractional deformation and uplift due to increased coupling between the subducting slab and overriding plate, such as in the Laramide orogeny of

western North America (e.g., Bird, 1984). We therefore conclude that it is unlikely that flat-slab subduction was responsible for the key attributes of the Eocene flare-up.

There is some indirect evidence, however, that flat-slab subduction may have occurred during the Cretaceous. First, with the exception of some Cretaceous volcanic rocks in the northwesternmost part of the Sanandaj-Sirjan zone, most Cretaceous magmatism occurred in the northern part of Iran, in contrast to late Triassic to Jurassic plutonism which was concentrated in the southwestern part of the country, i.e., the relict magmatic arc in the Sanandaj-Sirjan zone. Second, a regional unconformity separating Cretaceous sediments from overlying Paleogene volcanic rocks implies a phase of contractional deformation that preceded the Eocene flare-up (e.g., Stöcklin, 1968). This event may correspond with Late Cretaceous to Paleocene cooling of a middle Cretaceous pluton in the Alborz Mtns. (Guest et al., 2006b) and Late Cretaceous folding and thrust faulting in the Sanandaj-Sirjan zone (e.g., Tillman, 1981). We suggest that the apparent Cretaceous shift in magmatism from the Sanandaj-Sirjan zone to northern Iran as well as Late Cretaceous to Paleogene shortening may have resulted from a period of flat-slab subduction that preceded the Eocene flare-up.

#### *Slab melting*

In recent years geochemical evidence has emerged from some arcs which suggests that slab melting may play a role in generating volcanism (e.g., Defant and Drummond, 1990, Gómez-Tuena et al., 2007). The slow convergence rate between Arabia and Eurasia implies that the downgoing slab had a long residence time in the subduction zone which

would have allowed it to heat up and potentially melt. None of the samples analyzed during this study are adakites based on the geochemical criteria specified by Defant and Drummond (1990), but a few samples from Hassanzadeh (1993) do meet these criteria. As discussed above, slab melting may be a viable explanation for generating the extreme LILE enrichment of the Iranian shoshonites. However, aside from the potential for generating volcanism with unusual compositions, slab melting does not explain geologic observations associated with the flare-up such as the inland position of the Tertiary arc or evidence for syn-volcanic subsidence. Furthermore, based on available, albeit limited, geochemical data, Paleogene volcanism with trace element compositions suggestive of slab melting (Defant and Drummond, 1990) seems to be rare in Iran. The absence of data in support of this hypothesis, in conjunction with geologic observations that are not explained by it, lead us to conclude that while slab melting may have occurred, it was not the key process in generating the Eocene flare-up.

#### *Rifting/back-arc basin development*

On the basis of major element data from alkaline Tertiary volcanics, Amidi et al. (1984) and Amidi and Michel (1985) argued that the Urumieh-Dokhtar arc was a linear rift basin unrelated to subduction. While parts of this idea may have some merit as discussed below, the geological and geochemical evidence linking subduction to volcanism within the Iranian arc is overwhelming (e.g., Förster et al., 1972, Takin, 1972, Dewey et al., 1973, Sengör et al., 1993). Kazmin et al. (1986) proposed a related explanation that much of the Eocene volcanism in Iran and throughout the Middle East and Mediterranean was related to back-arc basin development. This mechanism accounts for many of the

characteristics of the Eocene flare-up: the inland position of the Urumieh-Dokhtar arc relative to the Mesozoic arc, syn-extensional volcanism, development of shallow submarine basins, and the BABB geochemical affinity of the Oligocene basalts. However, Eocene volcanism, which was much more voluminous, has trace element compositions that are typical of arcs, not back arcs, and accumulated in many of the same basins as the Oligocene basalts. As an explanation for this discrepancy, we suggest that the mantle source of the Eocene volcanism was metasomatized by slab-derived fluids over the course of ~150 My, from the time of subduction initiation in the late Triassic until the flare-up began in the late Paleocene-early Eocene. Convergence rate was never greater than 3 cm/yr during this period (Savostin et al., 1986), which would have limited the volume of fluids released to the mantle wedge over any given period of time and which may be responsible for the restricted development of the Mesozoic arc. We suggest that this supply of fluids was sufficient to partially hydrate and alter the trace element composition of the mantle wedge but insufficient to induce significant magmatism until extension and decompression melting began. As a result, trace element compositions of Eocene lavas related to decompression but derived from a metasomatized source are indistinguishable from volcanism in other arcs where flux-melting predominates.

### **Conceptual model for the Eocene magmatic flare-up**

Trace element characteristics of Eocene volcanism within the Urumieh-Dokhtar arc, along with the linear trend of the range parallel to the Arabia-Eurasia suture, have led to the predominant view that the belt is a conventional arc analogous to the Andes. We

suggest, alternatively, that the magmatic flare-up was a hybrid of two common end-member mechanisms for generating volcanism: hydration of the mantle wedge by slab fluids as in subduction zones and decompression melting as in mid-ocean ridges (Plank and Langmuir, 1988, Pearce and Parkinson, 1993, Sisson and Bronto, 1998, Conder et al., 2002, Gaetani and Grove, 2003). Geochronology and geochemical data, together with observations of the Iranian Cenozoic stratigraphic record, are consistent with the following two-stage scenario for the Eocene magmatic flare-up and subsequent Oligocene magmatism (Fig. 12).

In the first stage, Eocene extension and crustal thinning, possibly related to slab rollback, generated decompression melting of the sub-arc mantle. Hydrated peridotite in the lithospheric mantle partially melted due to the combined effects of decompression and heating from the underlying upwelling asthenosphere. Both the lithospheric and asthenospheric mantle would have undergone partial melting during this period (Fig. 12). Melting was particularly extensive in the HFSE-depleted lithospheric mantle during this stage because it had been partially hydrated, i.e., preconditioned, during the ~150 My of slow subduction that preceded the flare-up. Melts from the asthenosphere would have been volumetrically small in comparison. Volcanics erupted during this period accumulated in continental and shallow submarine extensional basins, along with abundant sedimentary strata. Slow subduction established the conditions for slab rollback and generated only a limited extent of trench-perpendicular horizontal and downwelling flow within the mantle wedge. Upwelling mantle would therefore have been relatively unencumbered by pre-existing lateral or downward flow. As crustal

thinning progressed, the extent of decompression melting would have increased (Plank and Langmuir, 1988).

Extension directions in the Eocene Golpaygan metamorphic core complex (Moritz et al., 2006) and the suspected Eocene core complex near Shahr-e-Kord (Davoudian et al., 2007) are trench perpendicular. The parallel trends of the Urumieh-Dokhtar extension-related arc, the Mesozoic conventional arc in the Sanandaj-Sirjan zone, and the suture between Arabia and Eurasia also suggest that extension was trench-perpendicular. The most obvious explanation for trench-perpendicular extension is slab rollback (e.g., Lonergan and White, 1997). Rollback and associated extension occur when the subduction rate is large compared to the convergence rate, a condition that has been shown experimentally to be more likely in low convergence rate settings (Schellart, 2005) where coupling and shear stresses between the downgoing slab and overriding plate are relatively small, facilitating extension in the overlying crust (e.g., Jarrard, 1986, Northrup et al., 1995, Gorczyk et al., 2007). Given the evidence for nearly constant, slow Arabia-Eurasia convergence during the Paleogene, it is unclear if extension and resulting volcanism in Iran was triggered by a specific event or was the final result of protracted tension in the overriding plate. As described above, slab rollback may have followed a Cretaceous to Paleocene period of flat-slab subduction, in which case rollback might have accompanied the return to a normal slab dip, as has been suggested for the western U.S. (Humphreys, 1995).

In the second stage, upwelling asthenosphere replaced the thinned lithosphere. Partial melts of the asthenospheric source were responsible for the OIB-like Oligocene magmatism in much the same fashion as widely proposed for generating back-arc basin basalts (e.g., Gribble et al., 1998). Basalts may have been the dominant volcanic lithology during this period because the thinned crust contributed relatively little contamination and was an ineffective density barrier to primitive magmas (Plank and Langmuir, 1988). Trace-element evidence for slab contributions to the Oligocene basalts suggests that subduction was still occurring during this stage. Given the stratigraphic evidence for Oligocene extension, the late Eocene-early Oligocene transition from extensive arc magmatism to limited OIB volcanism probably occurred when the supply of preconditioned mantle wedge was exhausted.

The overall Paleocene to Miocene geologic history thus began with the accumulation of late Paleocene-early Eocene volcanic and sedimentary strata in extensional subsiding submarine basins developed inland of the Mesozoic arc. Deposition continued until at least early Oligocene time, although the continental redbeds of the Lower Red Fm. may mark a latest Eocene to earliest Oligocene hiatus in submarine deposition. The basins were inverted in Late Oligocene or Miocene time (Emami, 2001, Guest et al., 2007a), accompanying the collision of Arabia with Eurasia and are still being uplifted as the collision continues. The best documented example of basin inversion is near Saghand in eastern Iran (Fig. 1, Verdel et al., 2007), where syn-extensional Eocene volcanic and sedimentary strata were deposited in supradetachment basins (see e.g., Friedmann et al., 1994) during core complex formation and were subsequently exhumed by ~N-S

shortening at ~20 Ma (Verdel et al., 2007). Metamorphic core complexes in the Sanandaj-Sirjan zone also have Eocene supradetachment basins (Moritz et al., 2006, Davoudian et al. 2007), although the timing of exhumation is unknown in these areas. These and other outcrops of Eocene volcanic rocks in central Iran are the remnants of small extensional basins, but the two largest in terms of area are the linear basins of Paleogene strata in the Alborz Mtns. and Urumieh-Dokhtar arc. This history of slab rollback, basin formation, OIB-type volcanism, and subsequent basin inversion perhaps represents one cycle in the growth of an extensional-accretionary orogen, according to the definition of Collins (2002). Abundant Eocene and Oligocene volcanism in the Lut block of eastern Iran (Fig. 1) may have developed in a similar tectonic setting as suggested by Jung et al. (1984), although our data do not bear directly on that region.

A similar model for extensional flare-ups was proposed by Lawton and McMillan (1999) for the development of Cenozoic and Mesozoic continental rift magmatism in western North America. There, a remarkably similar transition occurred from an earlier phase of voluminous arc magmatism to a later period of relatively restricted OIB-type volcanism. In the eastern Mediterranean region, it has been argued that an analogous transition was related to extension of the Aegean and Anatolian plates as the result of slab rollback (e.g., Agostini et al., 2007). Wallace and Carmichael (1999), Verma (2002), and Blatter et al. (2007) suggested that decompression melting of asthenospheric mantle was responsible for Neogene extension-related volcanism in the Mexican volcanic belt. In fact, there are several similarities between the Iranian arc and the western part of the central Mexican arc. Subduction of the Rivera plate beneath Mexico has been quite slow (~1-5 cm/yr)

over much of the last 10 million years (DeMets and Traylen, 2000). Some Pliocene-Quaternary lavas from the western part of the Mexican arc were erupted at particularly high rates and have OIB geochemical attributes (Wallace et al., 1992). On a TAS diagram, ~1200 analyses from the Mexican volcanic belt, compiled from the GEOROC database, are scattered toward high alkalinity, similar to Iranian Tertiary volcanism (Fig. 7F). Furthermore, much of the controversy surrounding the primary or secondary nature of analcime has focused on Neogene shoshonites from the Mexican volcanic belt (e.g., Luhr and Kyser, 1989, Karlsson and Clayton, 1991). Not surprisingly, the unusual compositions of these volcanics have prompted a wide range of tectonic and petrologic explanations, including rifting (Verma et al., 2002), slab melting (Gómez-Tuena et al., 2007), interaction with a mantle plume (Márquez et al., 1999), and slab break-off (Ferrari, 2004). However, there seems to be little disagreement that extension played a role in generating volcanism associated with grabens in the western part of the belt (e.g., Wallace et al., 1992).

These similarities suggest that the Mexican volcanic belt and the eastern Mediterranean region may be well-characterized, recent analogs to the Iranian Eocene volcanism. The Iranian case is distinct from these in that the main pulse of Tertiary magmatism in Iran was coeval with extension but had trace element characteristics typical of arcs. OIB type volcanism did not occur until ~15-20 My later. The sheer amount of volcanism and sedimentation accompanying the Iranian example also appears to be a unique characteristic. Extensive preconditioning of the mantle wedge during the ~150 My of subduction preceding the magmatic pulse may be an important factor in the explanation

of both of these differences. Slow subduction rate, coupled with the relatively large consumption of oceanic crust necessary to close the Tethys from Iran's position in the middle to eastern part of Gondwana may have been a unique combination that facilitated extraordinary "preconditioning" and the subsequent Eocene flare-up during rollback.

## **CONCLUSIONS**

We conclude that subduction of Neotethys beneath Iran generated a poorly developed Late-Triassic to Jurassic magmatic arc in the Sanandaj-Sirjan zone. Magmatism seems to have shifted to northern Iran during the Cretaceous, perhaps as the result of flat-slab subduction. Eocene slab rollback extended the overriding plate, creating metamorphic core complexes and rift basins. Large volumes of volcanism were generated for ~20 My during decompression melting of the preconditioned mantle wedge. Subsequent Oligocene basaltic volcanism was sourced from upwelling asthenosphere. Extension ended and the rift basins were inverted when Arabia and Eurasia collided in the Late Oligocene to Miocene.

## **REFERENCES**

Aftabi, A., and Atapour, H., 2000, Regional aspects of shoshonitic volcanism in Iran: Episodes, v.23, p.119-125.

Agostini, S., Doglioni, C., Innocenti, F., Manetti, P., Tonarini, S., and Savaşçin, M.Y., 2007, The transition from subduction-related to intraplate Neogene magmatism in the western Anatolia and Aegean area, *in* Beccaluva, L., Bianchini, G., and Wilson, M., eds.,

Cenozoic volcanism in the Mediterranean area: Geological Society of America Special Paper 418, p. 1-15, doi 10.1130/2007.2418(01).

Alavi, M., and Hushmandzādeh, A., 1976, Geological map of the Torud quadrangle: Tehran, Geological Survey of Iran, scale 1:250,000.

Alberti, A., Comin-Chiaramonti, P., Di Battistini, G., Sinigoi, S., and Zerbi, M., 1979, Upper Eocene to early Oligocene shoshonitic volcanism in eastern Azerbaijan: Neues Jahrbuch für Mineralogie (Abhandlungen): v. 134, p. 248-264.

Amidi, S.M., Emami, M.H., and Michel, R., 1984, Alkaline character of Eocene volcanism in the middle part of central Iran and its geodynamic situation: Geologische Rundschau, v. 73, p. 917-932.

Amidi, S.M. and Michel, R., 1985, Cenozoic magmatism of the Surk area (central Iran) stratigraphy, petrography, geochemistry and their geodynamic implications: Geologie Alpine, v.61, p. 1-16.

Anells, R.N., Arthurton, R.S., Bazley, R.A., and Davies, R.G., 1975, Explanatory text of the Qazvin and Rasht quadrangles map: Geological Survey of Iran Geological Quadrangles E3, E4, 94 p.

Arvin, M., Pan, Y., Dargahi, S., Malekizadeh, A., and Babaei, 2007, Petrochemistry of the Siah-Kuh granitoid stock southwest of Kerman, Iran: implications for initiation of Neotethys subduction: *Journal of Asian Earth Sciences*, v. 30, p. 474-489.

Axen, G.J., Lam, P.S., Grove, M., Stockli, D.F., and Hassanzadeh, J., 2001, Exhumation of the west-central Alborz Mountains, Iran, Caspian subsidence, and collision-related tectonics: *Geology*, v. 29, p. 559-562.

Berberian, F., and Berberian, M., 1981, Tectono-plutonic episodes in Iran, *in* Gupta, H.K. and Delany, F.M., eds., *Zagros, Hindu Kush, Himalaya, geodynamic evolution*: Washington, D.C., American Geophysical Union, 323 p.

Berberian, F., Muir, I.D., Pankhurst, R.J., and Berberian, M., 1982, Late Cretaceous and early Miocene Andean-type plutonic activity in northern Makran and central Iran: *Journal of the Geological Society of London*, v. 139, p. 605-614.

Berberian, M., and King, G.C.P., 1981, Towards a paleogeography and tectonic evolution of Iran: *Canadian Journal of Earth Sciences*, v. 18, p. 210-265.

Bird, P., 1984, Laramide crustal thickening event in the Rocky Mountain foreland and Great Plains: *Tectonics*, v. 3, p.741-758.

Blatter, D.L., Farmer, G.L., and Carmichael, I.S.E., 2007, A north-south transect across the central Mexican volcanic belt at ~100°W: spatial distribution, petrological, geochemical, and isotopic characteristics of Quaternary volcanism: *Journal of Petrology*, v. 48, p. 901-950.

Boccaletti, M., Innocenti, F., Manetti, P., Mazzuoli, R., Motamed, A., Pasquare', G., Radicati di Brozolo, F., and Amin Sobhani, E., 1976, Neogene and Quaternary volcanism of the Bijar area (western Iran): *Bulletin Volcanologique*, v. 40-2, p. 121-132.

Collins, W., 2002, Nature of extensional accretionary orogens: *Tectonics*, v. 21, doi:10.1029/2000TC001272.

Conder, J.A., Wiens, D.A., and Morris, J., 2002, On the decompression melting structure at volcanic arcs and back-arc spreading centers: *Geophysical Research Letters*, v. 29, doi: 10.1029/2002GL015390.

Davidson, J.P., 1996, Deciphering mantle and crustal signatures in subduction zone magmatism, *in* Bebout, G.E., Scholl, D.W., Kirby, S.H., and Platt, J.P., eds., *Subduction top to bottom*, American Geophysical Union, *Geophysical Monograph* 96, 384 p.

Davies, J.H., and Bickle, M.J., 1991, A physical model for the volume and composition of melt produced by hydrous fluxing above subduction zones: *Royal Society of London Philosophical Transactions*, v. 335, p. 355-364.

Davies, J.H., and Stevenson, D.J., 1992, Physical model of source region of subduction zone volcanics: *Journal of Geophysical Research*, v.97, p. 2037-2070

Davoudian, A.R., Genser, J., Dachs, E., and Shabanian, N., 2007, Petrology of eclogites from north of Shahrekord, Sanandaj-Sirjan zone, Iran: *Mineralogy and Petrology*, doi: 10.1007/s00710-007-0204-6.

Defant, M., and Drummond, M., 1990, Derivation of some modern arc magmas by melting of young subducted lithosphere: *Nature*, v. 347, p. 662-665.

DeMets, C., Gordon, R.G., Argus, D.F., and Stein, S., 1994, Effect of recent revisions to the geomagnetic reversal time scale on estimates of current plate motions: *Geophysical Research Letters*, v. 21, p. 2191-2194.

DeMets, C., and Traylen, S., 2000, Motion of the Rivera plate since 10 Ma relative to the Pacific and North American plates and the mantle: *Tectonophysics*, v. 318, p. 119-159.

DePaolo, D.J., 1981, Trace element and isotopic effects of combined wallrock assimilation and fractional crystallization: *Earth and Planetary Science Letters*, v. 53, p. 189-202.

Dercourt, J., Zonenshain, L.P., Ricou, L.E., Kazmin, V.G., Lepichon, X., Knipper, A.L., Grandjacquet, C., Sbertshikov, I.M., Geysant, J., Lepvrier, C., Pechersky, D.H., Boulin, J., Sibuet, J.C., Savostin, L.A., Sorokhtin, O., Westphal, M., Bazhenov, M.L., Lauer, J.P., and Bijuduval, B., 1986, Geological evolution of the Tethys belt from the Atlantic to the Pamirs since the Lias: *Tectonophysics*, v.123, p.241-315.

Dewey, J.F., Pitman, W.C., III, Kyan, W.B.F., and Bonnin, J., 1973, Plate tectonics and the evolution of the Alpine system: *Geological Society of America Bulletin*, v. 84, p.3137-3180.

Ducea, M.N., and Barton, M.D., 2007, Igniting flare-up events in Cordilleran arcs: *Geology*, v.35, p.1047-1050.

Dungan, M.A., and Davidson, J., 2004, Partial assimilative recycling of the mafic plutonic roots of arc volcanoes: an example from the Chilean Andes: *Geology*, v. 32, p. 773-776.

Dupuy, C., and Dostal, J., 1978, Geochemistry of calc-alkaline volcanic rocks from southeastern Iran (Kouh-e-Shahsavaran): *Journal of Volcanology and Geothermal Research*, v. 4, p. 363-373.

Elliott, T., 2003, Tracers of the slab, *in* Eiler, J., ed., *Inside the subduction factory*, American Geophysical Union, *Geophysical Monograph* 138, p. 23-45.

Emami, M.H., 1991, Explanatory text of the Qom quadrangle map, Geological Quadrangle No. E6, Geological Survey of Iran.

Fakhari, M.D., Axen, G.J., Horton, B.K., Hassanzadeh, J., and Amini, A., 2008, Revised age of proximal deposits in the Zagros foreland basin and implications for Cenozoic evolution of the High Zagros: Tectonophysics, doi:10.1016/j.tecto.2007.11.064.

Ferrari, L., 2004, Slab detachment control on mafic volcanic pulse and mantle heterogeneity in central Mexico: *Geology*, v. 32, p. 77-80.

Förster, H., Fesefeldt, K., and Kürsten, M., 1972, Magmatic and orogenic evolution of the central Iranian volcanic belt: 24<sup>th</sup> International Geologic Congress, p.198-210.

Friedmann, S.J., Davis, G.A., Fowler, T.K., Brudos, T., Parke, M., Burbank, D.W., and Burchfiel, B.C., 1994, Stratigraphy and gravity-slide elements of a Miocene supradetachment basin, Shadow Valley, East Mojave Desert, *in* McGill, S.F., and Ross, T.M., eds., Geological investigations of an active margin: Geological Society of America Cordilleran Section guidebook: Redlands, California, San Bernardino County Museum Association, p. 302-318.

Gaetani, G.A., and Grove, T.L., Experimental constraints on melt generation in the mantle wedge, *in* Eiler, J., ed., Inside the subduction factory, American Geophysical Union, Geophysical Monograph 138, p. 107-133.

Ghorbani, M.R., 2006, Lead enrichment in Neotethyan volcanic rocks from Iran: the implications of a descending slab: *Geochemical Journal*, v. 40, p. 557-568.

Gianetti, B., and Masi, U., 1989, Trace-element behavior during weathering of leucite in potassic rocks in potassic rocks from the Roccamonfina volcano (Campania, southern Italy) and environmental implications: *Lithos*, v. 22, p. 317-324.

Gill, J.B., 1981, *Orogenic andesites and plate tectonics*: Springer-Verlag, 390 p.

Gómez-Tuena, A., Langmuir, C.H., Goldstein, S.L., Straub, S.M., and Ortega-Gutiérrez, F., 2007, Geochemical evidence for slab melting in the Trans-Mexican volcanic belt: *Journal of Petrology*, v. 48, p.537-562.

Gorczyk, W., Willner, A.P., Gerya, T.V., Connolly, J.A.D., and Burg, J-P., 2007, Physical controls of magmatic productivity at Pacific-type convergent margins: numerical modeling: *Physics of the Earth and Planetary Interiors*, v. 163, p. 209-232.

Gribble, R.F., Stern, R.J., Newman, S., Bloomer, S.H., and O'Hearn, T., 1998, Chemical and isotopic composition of lavas from the northern Mariana trough: implications for magmagenesis in back-arc basins: *Journal of Petrology*, v. 39, p.125-154.

Guest, B., Axen, G.J., Lam, P.S., and Hassanzadeh, J., 2006a, Late Cenozoic shortening in the west-central Alborz Mountains, northern Iran, by combined conjugate strike-slip and thin-skinned deformation: *Geosphere*, v. 2, p. 35-52.

Guest, B., Stockli, D.F., Grove, M., Axen, G.J., Lam, P.S., and Hassanzadeh, J., 2006b, Thermal histories from the central Alborz Mountains, northern Iran: implications for the spatial and temporal distribution of deformation in northern Iran: *Geological Society of America Bulletin*, v. 118, p. 1507-1521.

Guest, B., Guest, A., and Axen, G., 2007a, Late Tertiary tectonic evolution of northern Iran: a case for simple crustal folding: *Global and Planetary Change*, v. 58, p. 435-453

Guest, B., Horton, B.K., Axen, G.J., Hassanzadeh, J., and McIntosh, W.C., 2007b, Middle to late Cenozoic basin evolution in the western Alborz Mountains: implications for the onset of collisional deformation in northern Iran: *Tectonics*, v. 26,  
doi:10.1029/2006TC002091.

Haghipour, A., and Aghanabati, A., compilers, 1985, Geological map of Iran: Geological Survey of Iran Ministry of Mines and Metals, scale 1:2,500,000.

Haghipour, A., Taraz, H., and Vahdati Daneshmand, F., compilers, 1987, Geological map of the Tehran quadrangle: Geological Survey of Iran, scale 1:250,000.

Hassanzadeh, J., 1993, Metallogenic and tectonomagmatic events in the SE sector of the Cenozoic active continental margin of central Iran (Shahr e Babak area, Kerman Province) [Ph.D. thesis]: Los Angeles, University of California, 204 p.

Hassanzadeh, J., Ghazi, A.M., Axen, G., Guest, B., Stockli, D., and Tucker, P., 2002, Oligocene mafic-alkaline magmatism in north and northwest of Iran: evidence for the separation of the Alborz from the Urumieh-Dokhtar magmatic arc: Geological Society of America Abstract with Programs, v. 34, no. 6, p.331.

Hassanzadeh, J., Stockli, D.F., Horton, B.K., Axen, G.J., Stockli, L.D., Grove, M., Schmitt, A.K., and Walker, J.D., 2008, U-Pb zircon geochronology of late Neoproterozoic-Early Cambrian granitoids in Iran: implications for paleogeography, magmatism, and exhumation history of Iranian basement: Tectonophysics, v.451, p. 71-96.

Hickey, R.L., Frey, F.A., and Gerlach, D.C., 1986, Multiple sources for basaltic arc rocks from the southern volcanic zone of the Andes (34-41°S): trace element and isotopic evidence for contributions from subducted oceanic crust, mantle and continental crust: Journal of Geophysical Research, v. 91, p. 5963-5983.

Horton, B.K., Hassanzadeh, J., Stockli, D.F., Axen, G.J., Gillis, R.J., Guest, B., Amini, A., Fakhari, M.D., Zamanzadeh, S.M., and Grove, M., 2008, Detrital zircon provenance of Neoproterozoic to Cenozoic deposits in Iran: implications for chronostratigraphy and collisional tectonics: *Tectonophysics*, doi: 10.1016/j.tecto.2007.11.063.

Huang, F., and Lundstrom, C.C., 2007,  $^{231}\text{Pa}$  excesses in arc volcanic rocks: constraint on melting rates at convergent margins: *Geology*, v. 35, p.1007-1010.

Humphreys, E.D., 1995, Post-Laramide removal of the Farallon slab, western United States: *Geology*, v.23, p. 987-990.

Jarrard, R.D., 1986, Relations among subduction parameters: *Reviews in Geophysics*, v. 24, p. 217-284.

Jung, D., Keller, J., Khorasani, R., Marcks, C, Baumann, A., and Horn, P., 1984, Petrology of the Tertiary magmatic activity in the northern Lut area, east Iran: *Neues Jahrbuch für Geologie und Paläontologie Abhandlungen*, v. 160, p. 417-467.

Karlsson, H.R., and Clayton, R.N., 1991, Analcime phenocrysts in igneous rocks: primary or secondary?: *American Mineralogist*, v. 76, p. 189-199.

Kay, R.W., and Kay, S.M., 1993, Delamination and delamination magmatism: *Tectonophysics*, v. 219, p. 177-189.

Kay, S.M., Godoy, E., and Kurtz, A., 2005, Episodic arc migration, crustal thickening, subduction erosion, and magmatism in the south-central Andes: *Geological Society of America Bulletin*, v. 117, p.67-88.

Kazmin, V.G., Sbortshikov, I.M., Ricou, L-E., Zonenshain, L.P., Boulin, J., and Knipper, A.L., 1986, Volcanic belts as markers of the Mesozoic-Cenozoic active margin of Eurasia: *Tectonophysics*, v. 123, p. 123-152.

Lawton, T.F., and McMillan, 1999, Arc abandonment as a cause for passive continental rifting: comparison of the Jurassic Mexican Borderland rift and the Cenozoic Rio Grande rift: *Geology*, v. 27, p. 779-782.

Lonergan, L., and White, N., 1997, Origin of the Betic-Rif mountain belt: *Tectonics*, v. 16, p. 504-522.

Macdonald, G.A., and Katsura, T., 1964, Chemical composition of Hawaiian lavas: *Journal of Petrology*, v. 5, p. 82-133.

Márquez, A., Oyarzun, R., Doblas, M., and Verma, S.P., 1999, Alkalic (ocean-island basalt type) and calc-alkalic volcanism in the Mexican volcanic belt: a case for plume-related magmatism and propagating rifting at an active margin?: *Geology*, v. 27, p. 51-54

McCulloch, M.T., and Gamble, J.A., 1991, Geochemical and geodynamical constraints on subduction zone magmatism: *Earth and Planetary Science Letters*, v. 102, p.358-374.

McQuarrie, N., Stock, J.M., Verdel, C., and Wernicke, B.P., 2003, Cenozoic evolution of Neotethys and implications for the causes of plate motions: *Geophysical Research Letters*, v. 30, 2036, doi:10.1029/2003GL017992.

Moritz, R., Ghazban, F., and Singer, B.S., 2006, Eocene gold ore formation at Muteh, Sanandaj-Sirjan tectonic zone, western Iran: a result of late-stage extension and exhumation of metamorphic basement rocks within the Zagros orogen: *Economic Geology*, v. 101, p. 1497-1524.

Morrison, G.W., 1980, Characteristics and tectonic setting of the shoshonite rock association: *Lithos*, v. 13, p. 97-108.

Northrup, C.J., Royden, L.H., and Burchfiel, B.C., 1995, Motion of the Pacific plate relative to Eurasia and its potential relation to Cenozoic extension along the eastern margin of Eurasia: *Geology*, v. 23, p. 719-722.

Page, B.M., and Engebretson, D.C., 1984, Correlation between the geologic record and computed plate motions for central California: *Tectonics*, v. 3, p. 133-155.

Pazirandeh, M, 1973, Distribution of volcanic rocks in Iran and a preliminary discussion of their relationship to tectonics: *Bulletin Volcanologique*, v. 37, p. 573-585.

Pearce, J.A. and Cann, J.R., 1973, Tectonic setting of basic volcanic-rocks determined using trace-element analyses: *Earth and Planetary Science Letters*, v. 19, p. 290-300.

Pearce, J.A., Harris, N.B.W, and Tindle, A.G., 1984, Trace-element discrimination diagrams for the tectonic interpretation of granitic-rocks: *Journal of Petrology*, v. 25, p.956-983.

Pearce, J.A., and Parkinson, I.J., 1993, Trace element models for mantle melting: application to volcanic arc petrogenesis, *in* Prichard, H.M., Alabaster, T., Harris, N.B.W., and Neary, C.R., eds., *Magmatic processes and plate tectonics*, Geological Society Special Publication no.76, p. 373-403.

Plank, T., and Langmuir, C.H., 1988, An evaluation of the global variations in the major element chemistry of arc basalts: *Earth and Planetary Science Letters*, v. 90, p. 349-370.

Pollastro, R.M., Persits, F.M., and Steinshouer, D.W., compilers, 1999, Map showing geology, oil and gas fields, and geologic provinces of Iran: USGS Open-file report 97-470-G, on compact disc.

Prelević, D., Foley, S.F., Cvetković, V., and Romer, R.L., 2004, The analcime problem and its impact on the geochemistry of ultrapotassic rocks from Serbia: *Mineralogical Magazine*, v. 68, p. 633-648.

Ramezani, J., and Tucker, R.D., 2003, The Saghand region, central Iran: U-Pb geochronology, petrogenesis and implications for Gondwana tectonics: *American Journal of Science*, v. 303, p. 622-665.

Rhodes, J.M., 1996, Geochemical stratigraphy of lava flows sampled by the Hawaii Scientific Drilling Project: *Journal of Geophysical Research*, v. 101, p. 11729-11746.

Savostin, L.A., Sibuet, J-C., Zonenshain, L.P., Le Pichon, X., and Roulet, M-J., 1986, Kinematic evolution of the Tethys belt from the Atlantic Ocean to the Pamirs since the Triassic: *Tectonophysics*, v. 123, p. 1-35.

Schellart, W.P., 2005, Influence of the subducting plate velocity on the geometry of the slab and migration of the subduction hinge: *Earth and Planetary Science Letters*, v.231, p.197-219.

Sengör, A.M.C., Cin, A., Rowley, D.B., and Nie, S-Y., 1993, Space-time patterns of magmatism along the Tethysides: a preliminary study: *The Journal of Geology*, v. 101, p. 51-84.

Shahabpour, J., 2007, Island-arc affinity of the central Iranian volcanic belt: *Journal of Asian Earth Sciences*, v. 30, p. 652-665.

Shervais, J.W., 1982, Ti-V plots and the petrogenesis of modern and ophiolitic lavas: *Earth and Planetary Science Letters*, v. 59, p. 101-118.

Sheth, H.C., Torres-Alvarado, I.S., and Verma, S.P., 2002, What is the “calc-alkaline rock series”? : *International Geology Review*, v. 44, p. 686-701.

Sisson, T.W., and Bronto, S., 1998, Evidence for pressure-release melting beneath magmatic arcs from basalt at Galunggung, Indonesia: *Nature*, v. 391, p. 883-886.

Soltani, A., 2000, Geochemistry and geochronology of I-type granitoid rocks in the northeastern Central Iran Plate [Ph.D. thesis]: Australia, University of Wollongong, 300 p.

Spies, O., Lensch, G., and Mihm, A., 1984, Petrology and geochemistry of the post-ophiolitic Tertiary volcanics between Sabzevar and Quchan, NE Iran: *Neues Jahrbuch für Geologie und Palaontologie Abhandlungen*, v. 168, p. 389-408.

Stern, R.J., Bloomer, S.H., Lin, P-N., Ito, E., and Morris, J., 1988, Shoshonitic magmas in nascent arcs: new evidence from submarine volcanoes in the northern Marianas: *Geology*, v. 16, p. 426-430.

Stöcklin, J., 1968, Structural history and tectonics of Iran: a review: *American Association of Petroleum Geologists Bulletin*, v. 52, p. 1229-1258.

Stöcklin, J., and Setudehnia, A., 1977, Stratigraphic lexicon of Iran, Geological Survey of Iran, Report no. 18, second edition, 376 p.

Sun, S.S., and McDonough, W.F., 1989, Chemical and isotopic systematics of oceanic basalts; implications for mantle composition and processes, *in* Saunders, A.D. and Norry, M.J., eds., *Magmatism in the oceanic basins: Geological Society of London Spec. Pub.* 42, p. 313-345

Takin, M., 1972, Iranian geology and continental drift in the Middle East: *Nature*, v. 235, p.147-150.

Taylor, S.R., and McLennan, S.M., 1985, *The continental crust: its composition and evolution, an examination of the geochemical record preserved in sedimentary rocks:* Oxford, Blackwell Scientific Publications, 312 p.

Tillman, J.E., Poosti, A., Rossello, S., and Eckert, A., 1981, Structural evolution of Sanandaj-Sirjan Ranges near Esfahan, Iran: *AAPG Bulletin*, v. 65, p. 674-687.

Verdel, C., Wernicke, B.P., Ramezani, J., Hassanzadeh, J., Renne, P.R., and Spell, T.L., 2007, Geology and thermochronology of Tertiary Cordilleran-style metamorphic core complexes in the Saghand region of central Iran: *Geological Society of America Bulletin*, v. 119, p. 961-977.

Verma, S.P., 2002, Absence of Cocos plate subduction-related basic volcanism in southern Mexico: a unique case on earth?: *Geology*, v. 30, p. 1095-1098.

Vincent, S.J., Allen, M.B., Ismail-Zadeh, A.D., Flecker, R., Foland, K.A., and Simmons, M.D., 2005, Insights from the Talysh of Azerbaijan into the Paleogene evolution of the South Caspian region: *Geological Society of America Bulletin*, v. 117, p. 1513-1533.

Wallace, P., Carmichael, I.S.E, Righter, K., and Becker, T.A., 1992, Volcanism and tectonism in western Mexico: a contrast of style and substance: *Geology*, v. 20, p. 625-628.

Wallace, P.J., and Carmichael, I.S.E., 1999, Quaternary volcanism near the Valley of Mexico: implications for subduction zone magmatism and the effects of crustal thickness variations on primitive magma compositions: *Contributions to Mineralogy and Petrology*, v. 135, p. 291-314.

Woodhead, J.D., Eggins, S.E., and Gamble, J.G., 1993, High field strength and transition element systematics in island arc and back-arc basin basalts: evidence for multi-phase extraction and a depleted mantle wedge: *Earth and Planetary Science Letters*, v. 114, p. 491-504.

**FIGURE CAPTIONS**

**Figure 1.** Map of Iran highlighting Cenozoic and Mesozoic igneous rocks (modified from Haghypour and Aghanabati, 1985 and Pollastro et al., 1999). Eocene metamorphic core complexes from Moritz et al., 2006, Davoudian et al., 2007, and Verdel et al., 2007. Previous geochemical studies: A-Alberti et al., 1979, B-Boccaletti et al., 1976, C-Ghorbani, 2006, D-Amidi et al., 1984, E-Amidi and Michel, 1985, F-Förster et al., 1972, G-Hassanzadeh, 1993, H-Spies et al., 1984, I-Jung et al., 1984, J-Dupuy and Dostal, 1978.

**Figure 2.** Composite stratigraphy of Cretaceous through Miocene volcanic and sedimentary rocks in the Tafresh area showing geochronology sample locations (modified from Emami, 1991).

**Figure 3.** U-Pb concordia and Tera-Wasserburg plots and  $^{40}\text{Ar}/^{39}\text{Ar}$  spectra and isochrons for volcanic rocks from the Alborz Mtns. and Urumieh-Dokhtar arc.  $^{40}\text{Ar}/^{39}\text{Ar}$  data are from plagioclase; all errors are  $2\sigma$ .

**Figure 4.** Cretaceous through Miocene stratigraphy of the Chalus Road area showing geochronology results (modified from Haghypour et al., 1987).

**Figure 5.** Generalized Tertiary stratigraphy of the Alborz Mtns. showing positions of geochronology and geochemistry samples. Shaded region indicates time of Eocene magmatic flare-up.

**Figure 6.** Generalized Tertiary stratigraphy of the Urumieh-Dokhtar arc showing positions of geochronology and geochemistry samples. Shaded region indicates time of Eocene magmatic flare-up.

**Figure 7.** Total alkali-silica diagrams. (A) Nomenclature. (B) Data from ~1500 Andean samples and ~1000 Cascades samples, compiled from the GEOROC database. (C) Data from ~275 Iranian Tertiary samples, compiled from various sources. (D) Same data as (C) coded by age. (E) 21 new Iranian Tertiary samples, oval drawn around shoshonitic samples. (F) ~1100 samples from the Mexican volcanic belt, compiled from the GEOROC database.

**Figure 8.** Primitive mantle normalized trace element diagrams. (A) Andesites. (B) Subalkaline and transitional basalts. (C) Alkaline basalts. (D) Primitive basalts with analcime. (E) Primitive basalts without analcime. (F) Shoshonites. Primitive mantle, N-MORB and OIB values from Sun and McDonough, 1989. Volcanic arc basalt (VAB) values from Hickey et al., 1986.

**Figure 9.** Ti/V vs. Zr/Nb plot for primitive Iranian basalts.

**Figure 10.** Generalized Tertiary stratigraphy of Iran with radiometric age constraints.

**Figure 11.** Iranian shoshonite sample NA3.

**Figure 12.** Diagram summarizing development of the Eocene arc flare-up and subsequent OIB-type Oligocene magmatism. The continental lithosphere is area-balanced in these schematic cross-sections and is held constant at 100 km thickness at the right edge of the diagram. Abbreviations: UD-Urumieh-Dokhtar magmatic arc, AB-Alborz Mtns, CI-Central Iranian Eocene volcanics between Urumieh-Dokhtar and the Alborz Mtns.

Figure 1

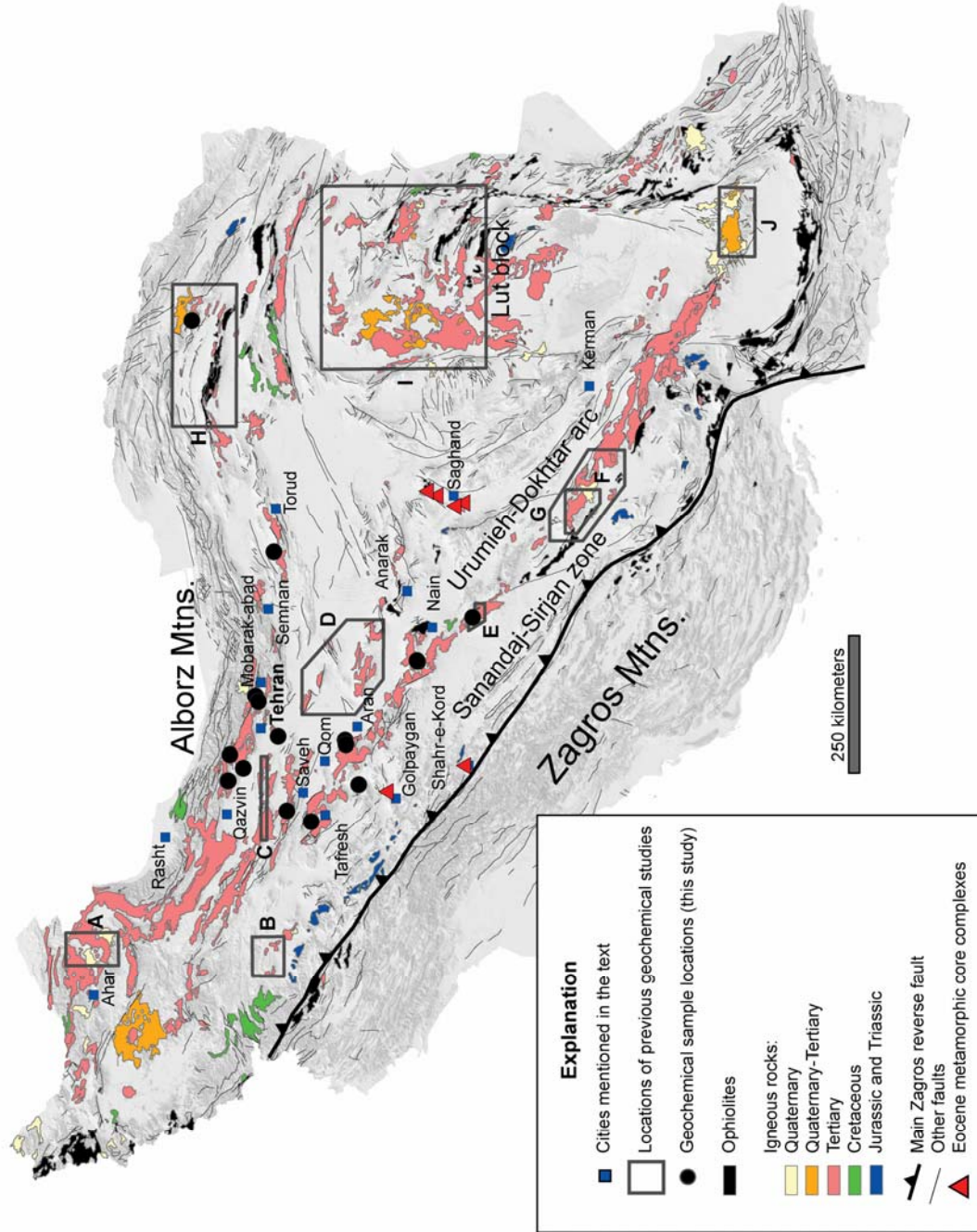


Figure 2

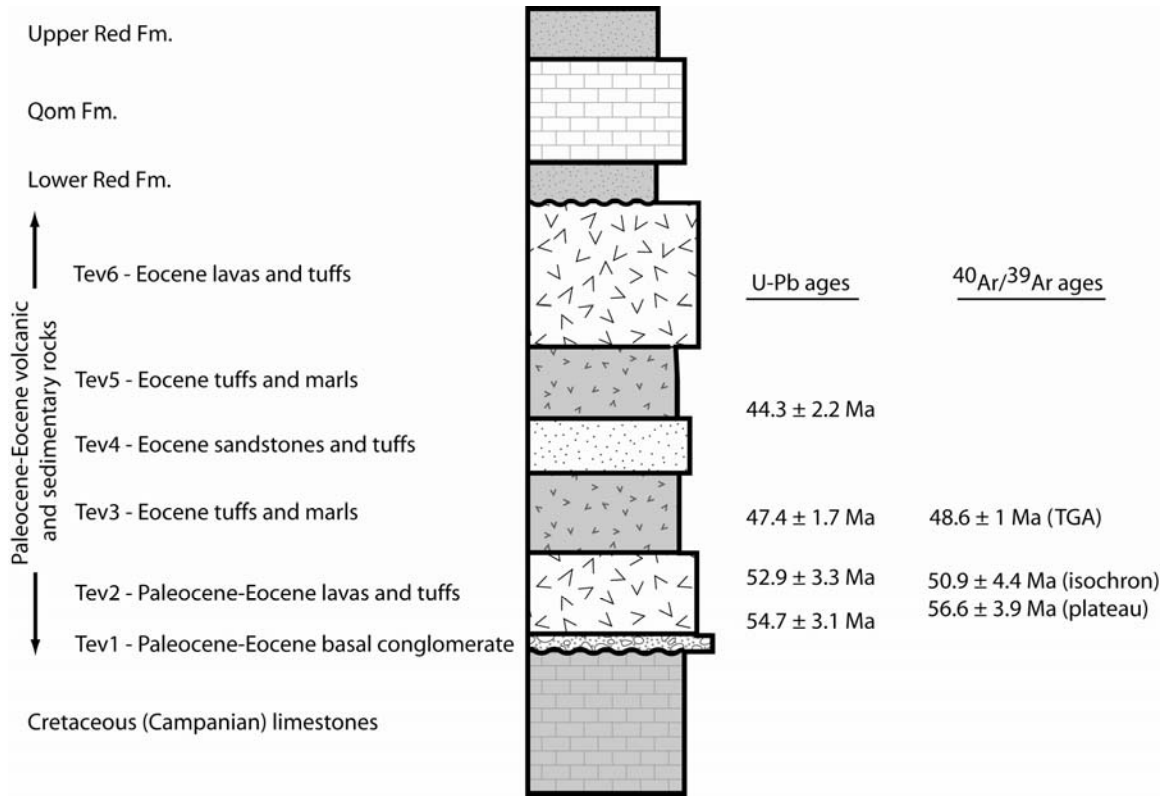


Figure 3

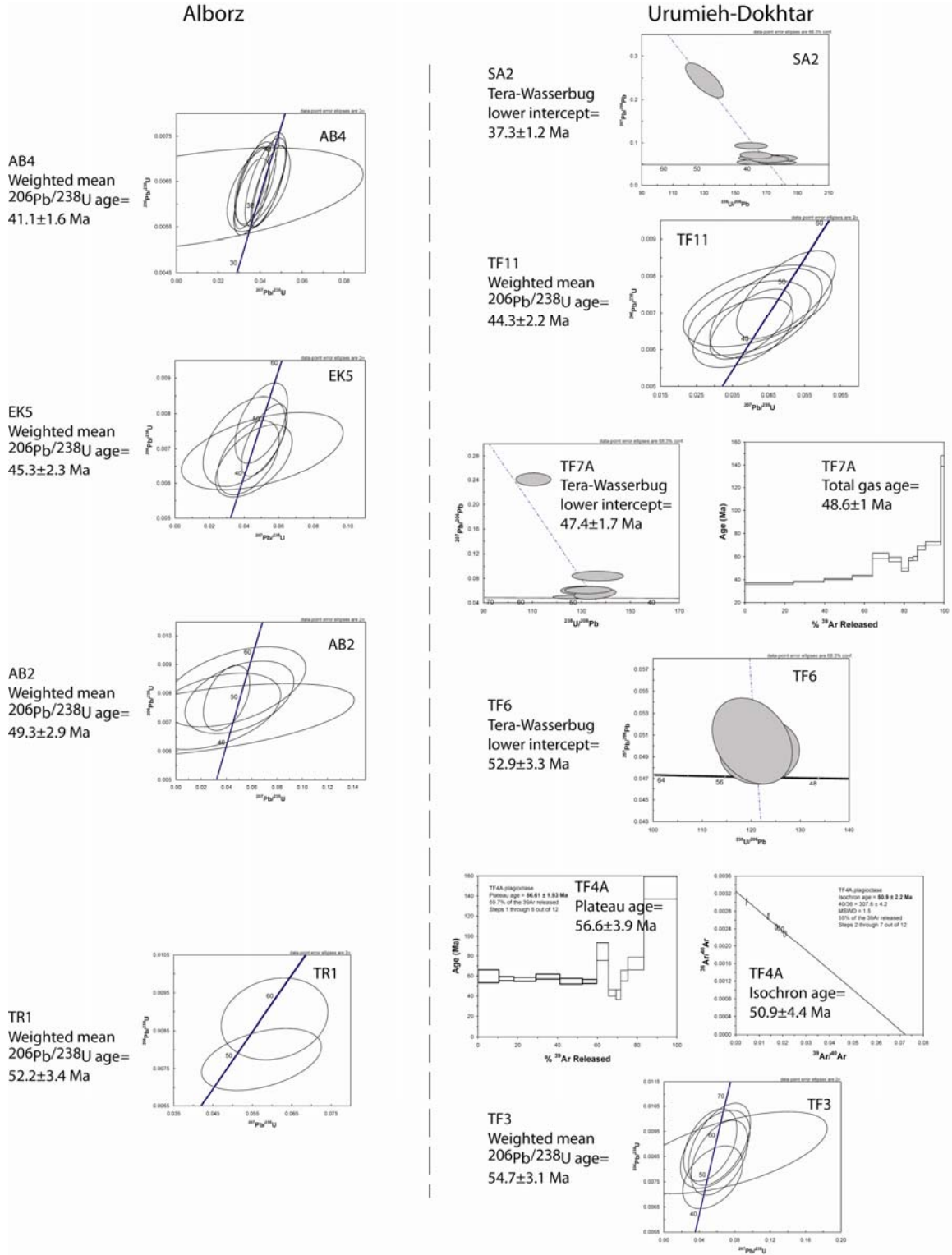


Figure 4

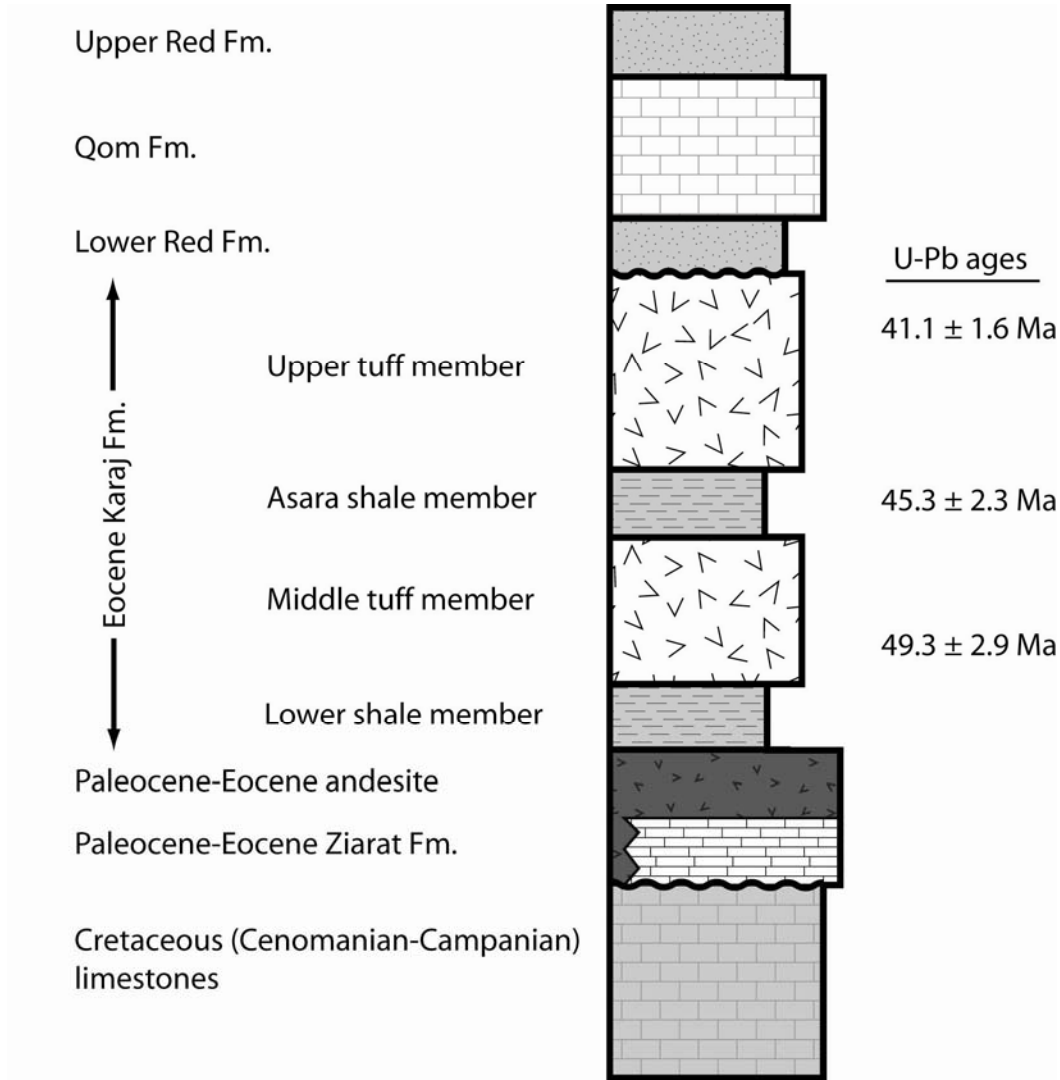


Figure 5

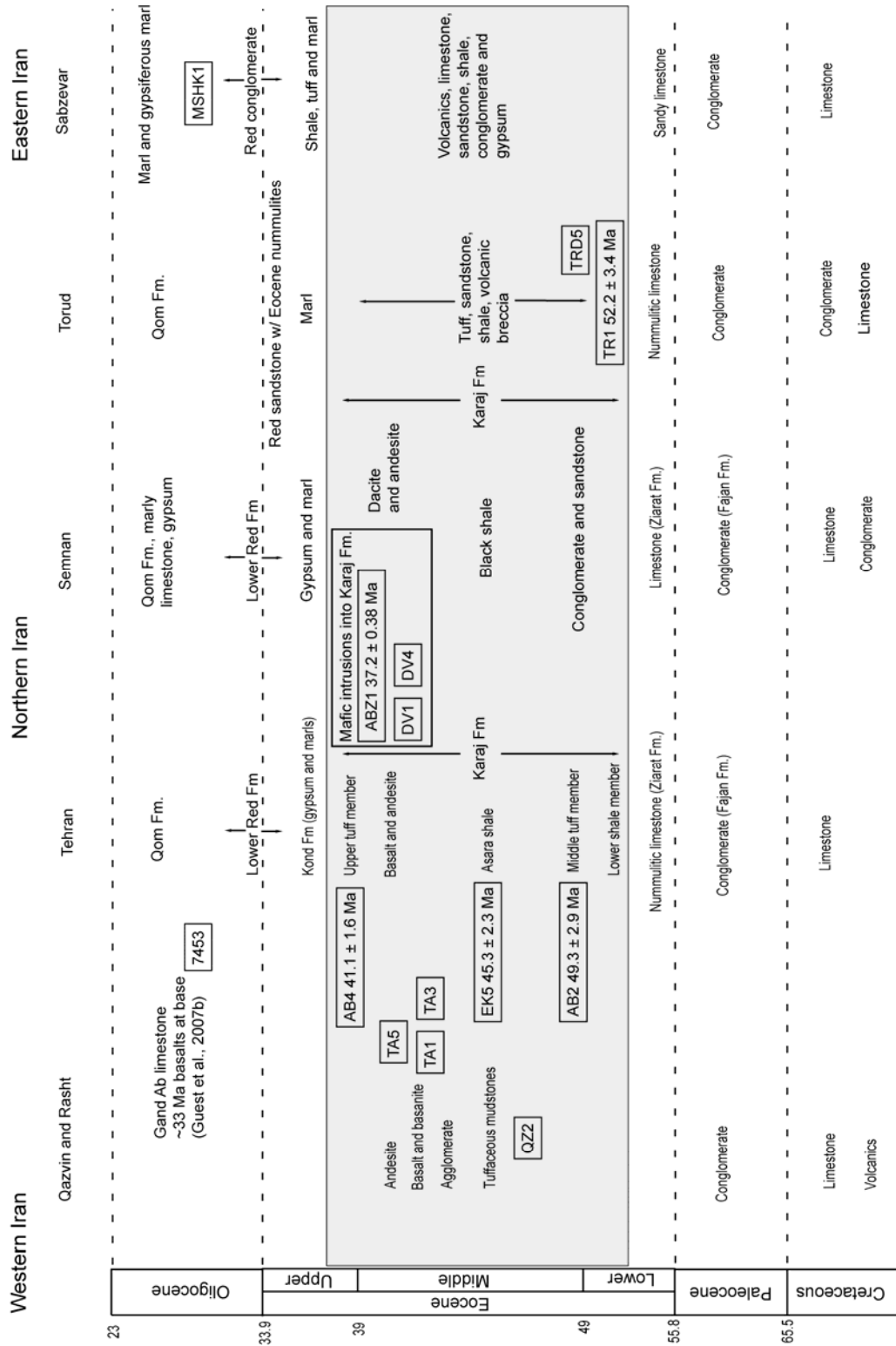


Figure 6

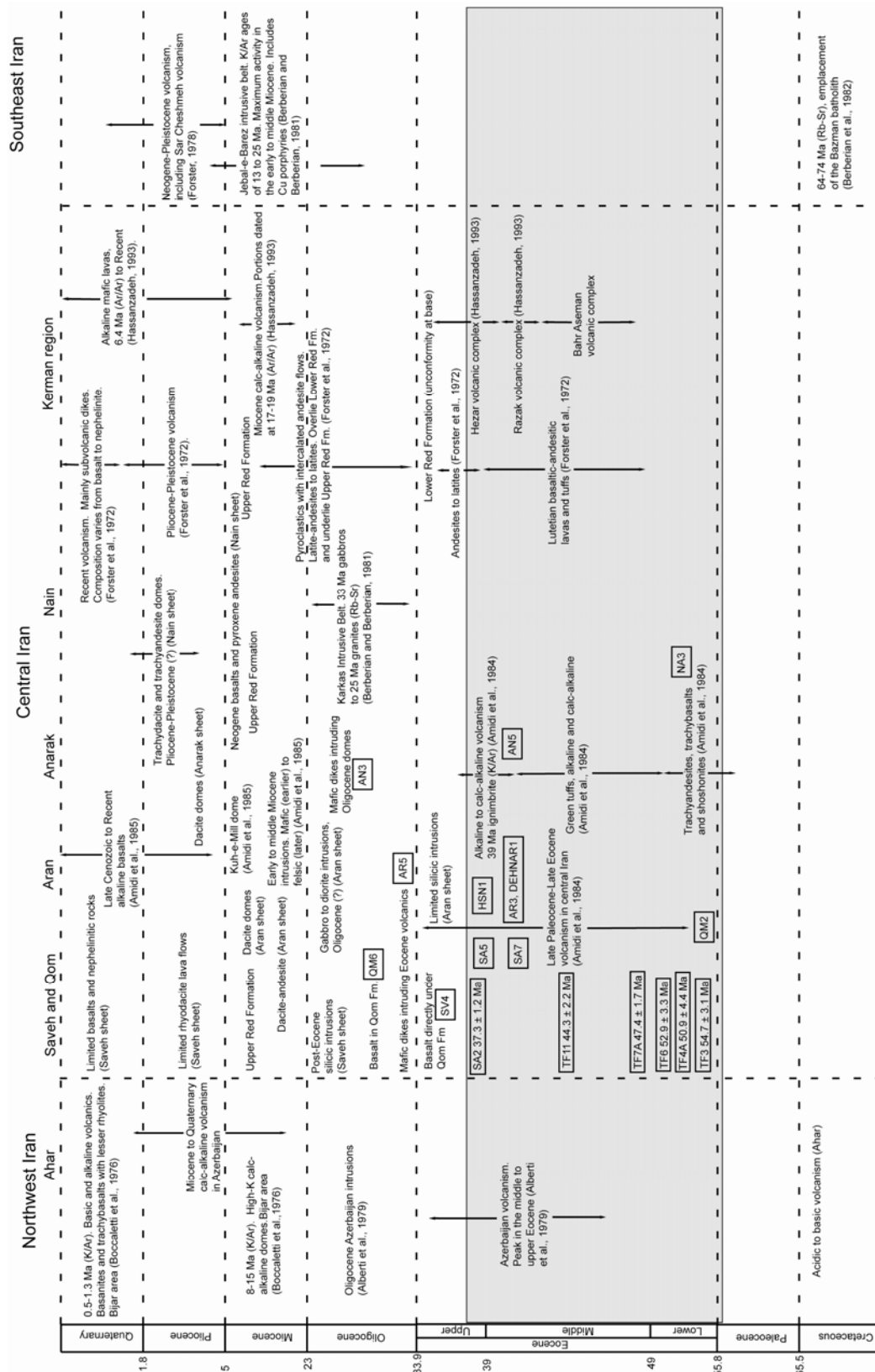


Figure 7

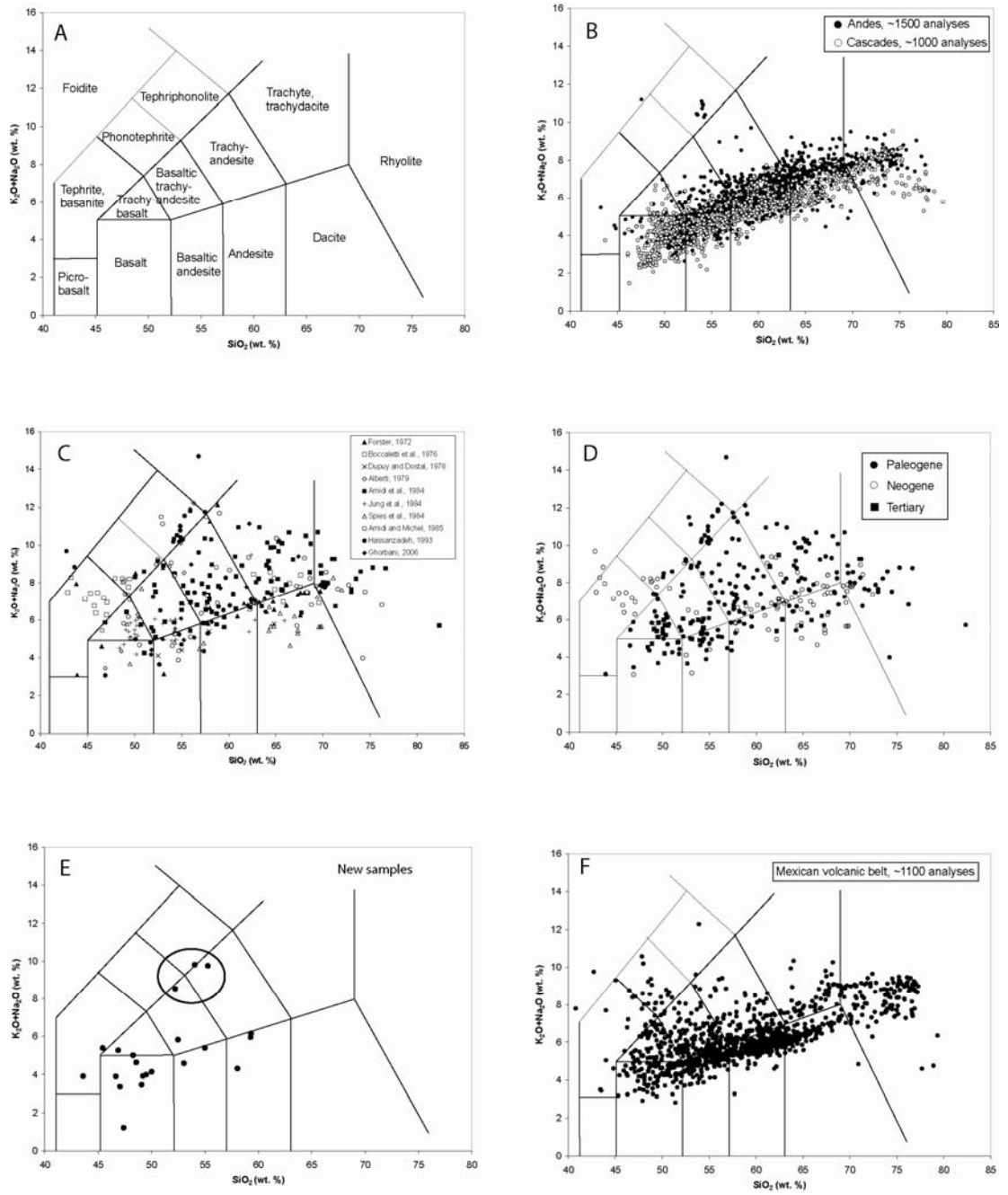


Figure 8

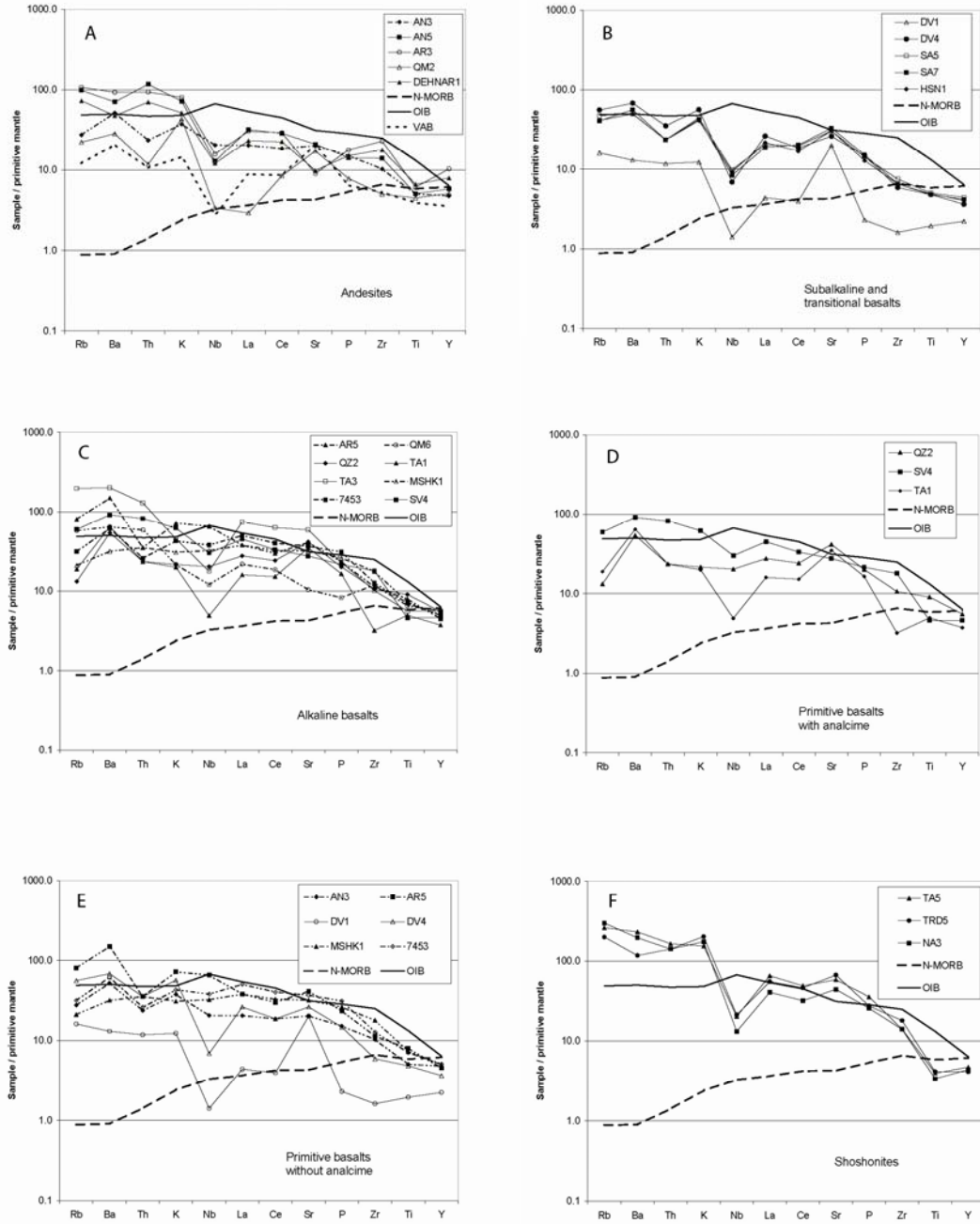


Figure 9

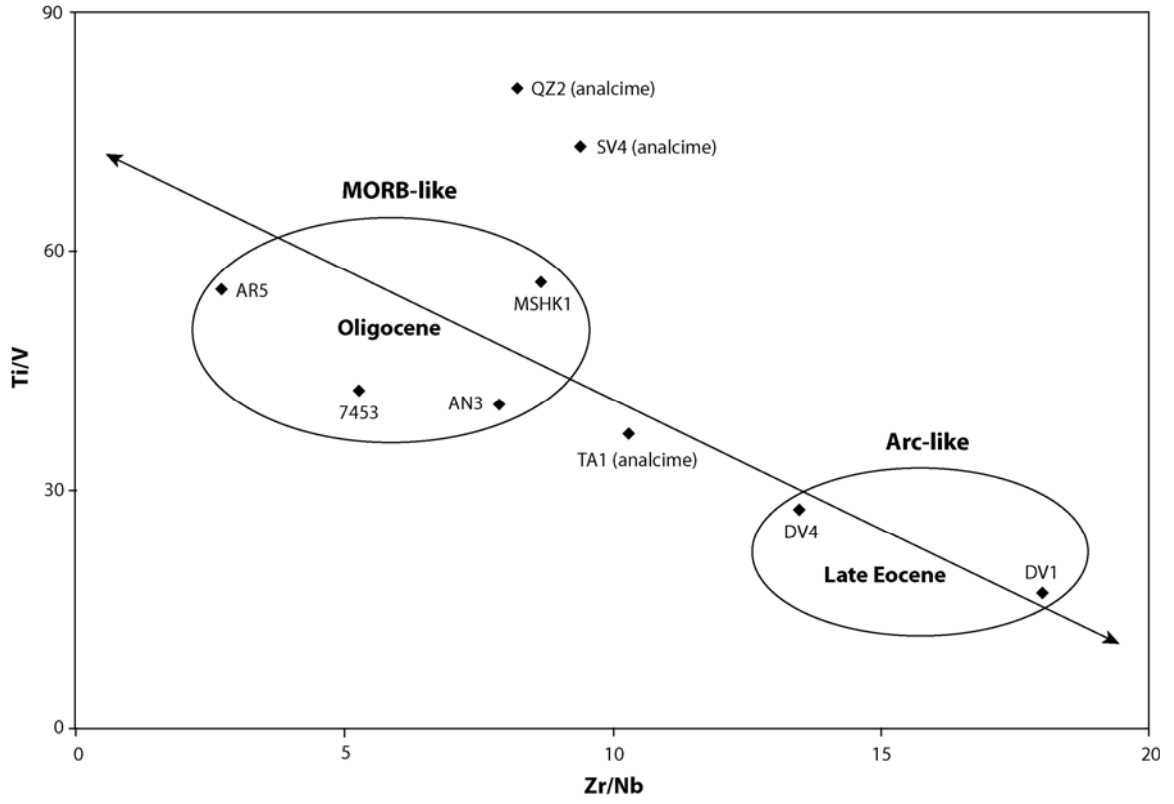
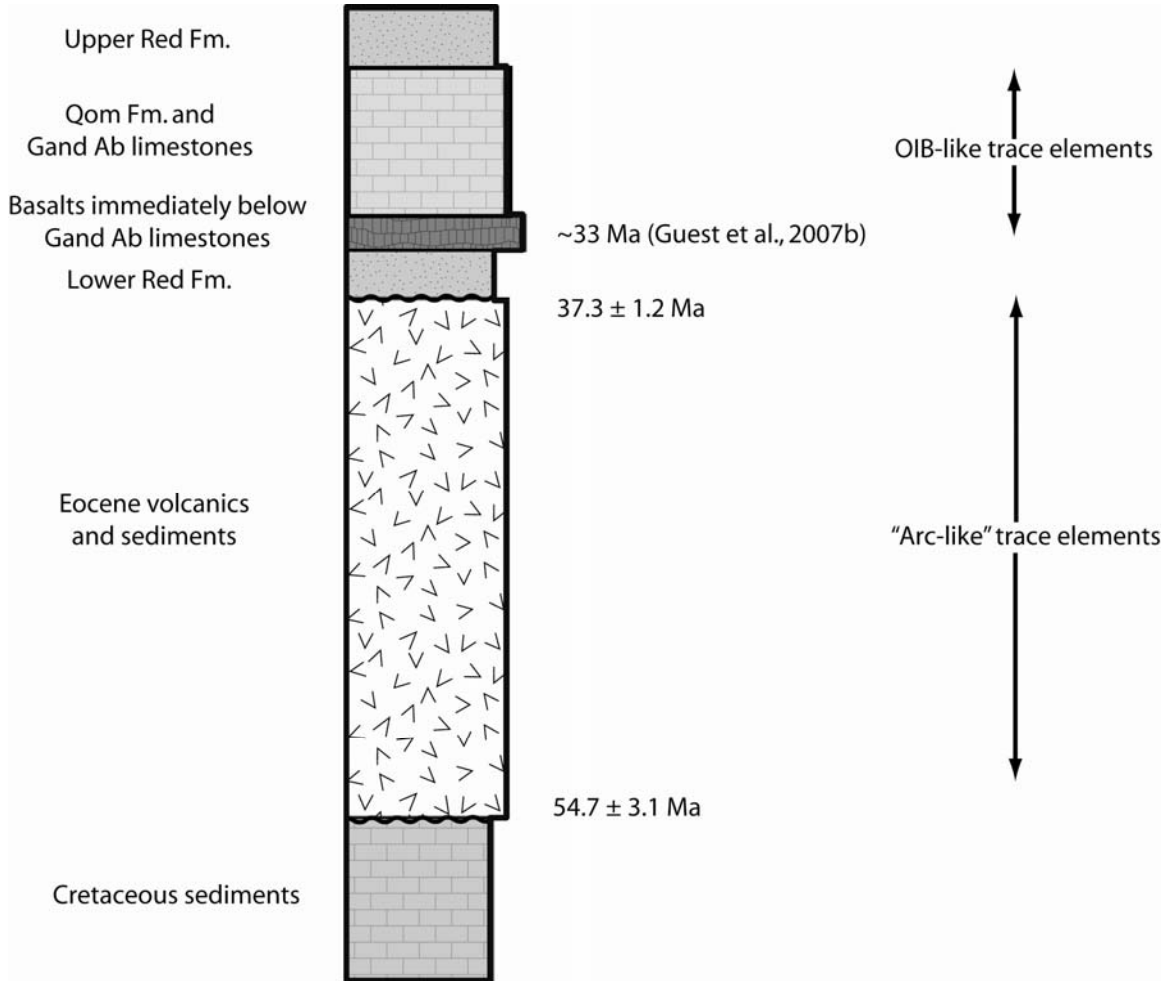


Figure 10



III-69

Figure 11

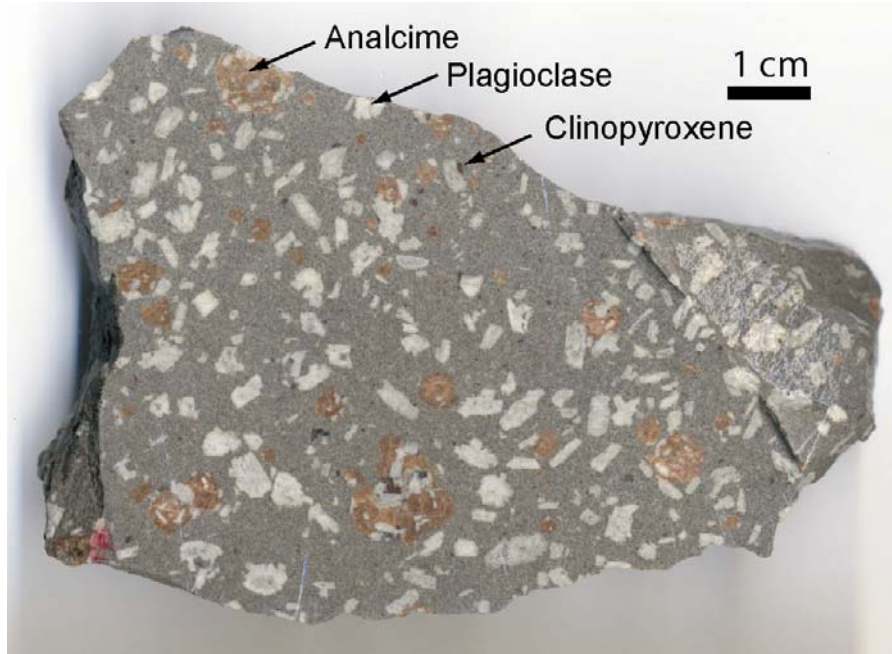


Figure 12

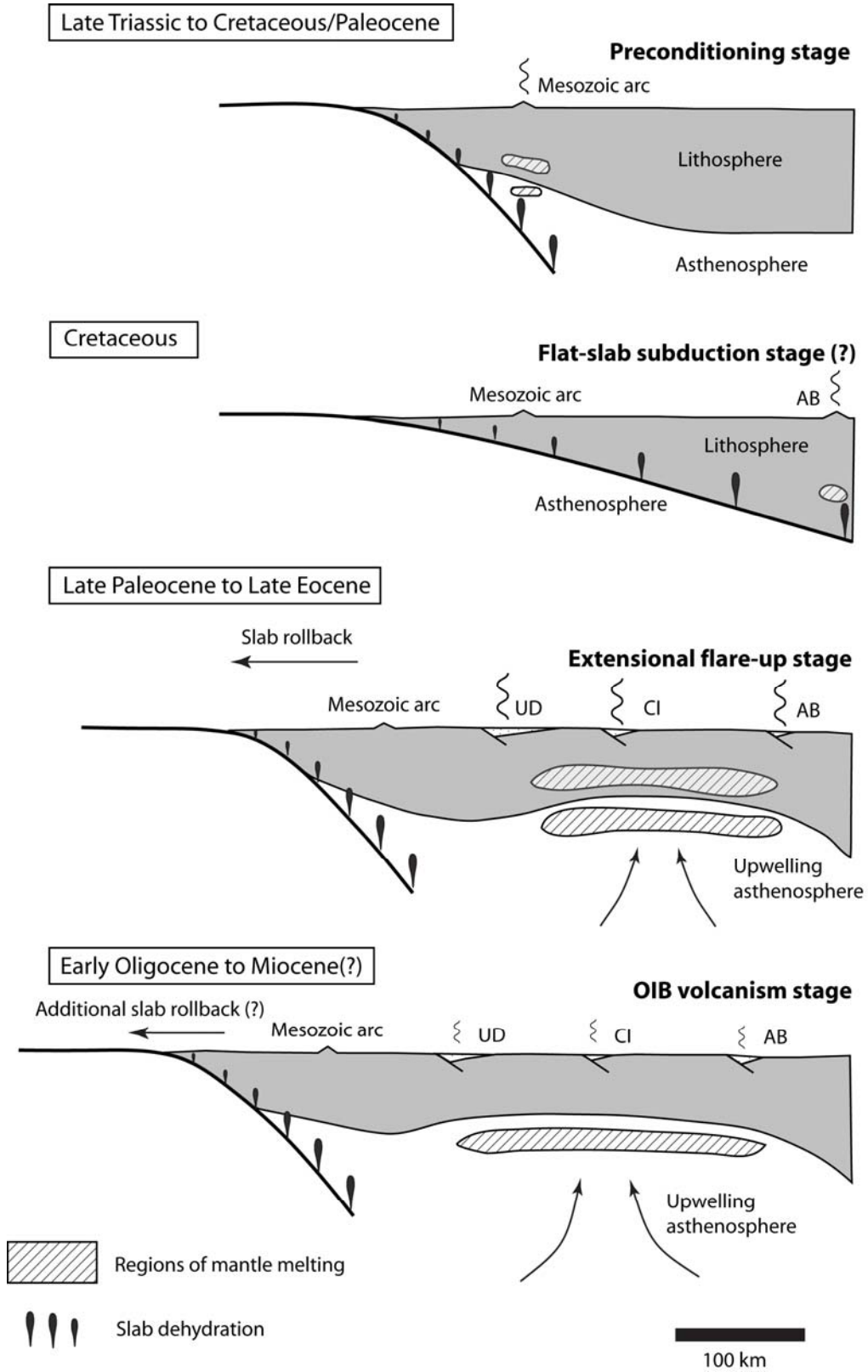


TABLE 1: U-Pb zircon age data

Sample/grain	Age (Ma) $^{206}\text{Pb}/^{238}\text{U}$	Age (Ma) $^{206}\text{Pb}/^{238}\text{U}$ 1 s.e.	Age (Ma) $^{207}\text{Pb}/^{235}\text{U}$	Age (Ma) $^{207}\text{Pb}/^{235}\text{U}$ 1 s.e.	$^{206}\text{Pb}^*/^{238}\text{U}$	$^{206}\text{Pb}^*/^{238}\text{U}$ 1 s.e.	$^{207}\text{Pb}^*/^{235}\text{U}$	$^{207}\text{Pb}^*/^{235}\text{U}$ 1 s.e.	Correlation of Concordia ellipses	UO/U	UO/U 1 s.e.
AB4_z1	42.13	2.71	40.22	4.81	0.00656	0.00042	0.04040	0.00493	0.6158	9.566	0.079
AB4_z2	41.57	2.36	37.49	3.92	0.00647	0.00037	0.03761	0.00401	0.5811	9.723	0.034
AB4_z3	39.33	2.95	7.63	33.60	0.00612	0.00046	0.00754	0.03330	0.4703	9.490	0.062
AB4_z4	41.61	2.58	42.34	3.90	0.00648	0.00040	0.04258	0.00401	0.6695	9.453	0.034
AB4_z5	42.53	2.44	42.37	2.57	0.00662	0.00038	0.04261	0.00264	0.9310	9.681	0.041
AB4_z6	40.88	2.37	35.83	3.28	0.00636	0.00037	0.03592	0.00335	0.6885	9.697	0.049
AB4_z7	41.12	2.35	43.54	3.31	0.00640	0.00037	0.04382	0.00340	0.7629	9.684	0.037
AB4_z8	39.62	2.22	35.80	3.38	0.00617	0.00035	0.03589	0.00345	0.6036	9.765	0.047
AB4_z9	40.84	2.51	39.08	6.00	0.00636	0.00039	0.03924	0.00615	0.5390	9.689	0.069
Ek5_z1	49.61	2.97	49.49	5.99	0.00773	0.00047	0.04995	0.00619	0.5246	8.086	0.062
Ek5_z2	46.20	3.36	39.96	9.51	0.00719	0.00053	0.04014	0.00974	0.4695	7.935	0.072
Ek5_z3	43.28	2.80	42.22	7.13	0.00674	0.00044	0.04246	0.00732	0.4878	8.172	0.071
Ek5_z4	46.49	2.70	51.16	5.20	0.00724	0.00042	0.05168	0.00539	0.6480	8.189	0.052
Ek5_z5	42.70	2.73	45.29	8.80	0.00665	0.00043	0.04561	0.00906	0.5404	8.178	0.069
Ek5_z6	44.48	2.90	49.98	18.44	0.00692	0.00045	0.05045	0.01910	0.4783	8.177	0.076
AB2_z1	45.44	3.30	23.26	47.82	0.00707	0.00052	0.02317	0.04820	0.5504	8.364	0.112
AB2_z2	52.86	3.62	46.04	22.32	0.00823	0.00057	0.04638	0.02300	0.4682	8.076	0.106
AB2_z3	47.39	3.45	29.60	21.55	0.00738	0.00054	0.02958	0.02180	0.4238	8.167	0.092
AB2_z4	50.37	2.95	39.96	7.31	0.00784	0.00046	0.04014	0.00748	0.4413	8.060	0.036
AB2_z5	50.52	3.28	49.78	17.05	0.00787	0.00051	0.05025	0.01760	0.4244	8.273	0.076
TR1_z1	56.56	2.81	59.79	5.30	0.00881	0.00044	0.06066	0.00554	0.1685	8.192	0.101
TR1_z2	49.72	2.14	56.60	5.98	0.00774	0.00034	0.05732	0.00622	0.4122	8.105	0.039

TABLE 1 (continued): U-Pb zircon age data

Sample/grain	Age (Ma) $^{206}\text{Pb}/^{238}\text{U}$	Age (Ma) $^{206}\text{Pb}/^{238}\text{U}$ 1 s.e.	Age (Ma) $^{207}\text{Pb}/^{235}\text{U}$	Age (Ma) $^{207}\text{Pb}/^{235}\text{U}$ 1 s.e.	$^{206}\text{Pb}^*/^{238}\text{U}$	$^{206}\text{Pb}^*/^{238}\text{U}$ 1 s.e.	$^{207}\text{Pb}^*/^{235}\text{U}$	$^{207}\text{Pb}^*/^{235}\text{U}$ 1 s.e.	Correlation of Concordia ellipses	UO/U	UO/U 1 s.e.
SA2_z1	40.12	1.75	77.70	5.29	0.00624	0.00027	0.07953	0.00562	0.6664	8.082	0.053
SA2_z2	49.23	3.03	232.90	33.10	0.00767	0.00047	0.25780	0.04100	0.8883	8.362	0.056
SA2_z3	36.11	1.55	48.07	4.45	0.00562	0.00024	0.04848	0.00460	0.3963	8.130	0.042
SA2_z4	38.91	2.05	53.73	4.17	0.00605	0.00032	0.05434	0.00433	0.4152	8.067	0.079
SA2_z5	39.29	1.95	44.12	3.96	0.00611	0.00031	0.04441	0.00408	0.5818	7.973	0.044
SA2_z6	36.34	1.62	40.75	2.97	0.00565	0.00025	0.04095	0.00304	0.6314	8.018	0.028
SA2_z7	37.40	1.82	48.36	4.84	0.00582	0.00028	0.04878	0.00500	0.4712	8.061	0.052
SA2_z8	39.34	1.63	58.25	5.35	0.00612	0.00025	0.05904	0.00558	0.5481	8.204	0.056
TF11_z1	44.89	3.19	43.98	6.19	0.00699	0.00050	0.04426	0.00637	0.5426	7.814	0.056
TF11_z2	48.13	3.13	49.39	5.42	0.00749	0.00049	0.04985	0.00560	0.6469	7.818	0.032
TF11_z3	44.07	2.66	39.54	6.77	0.00686	0.00042	0.03971	0.00693	0.4502	8.133	0.073
TF11_z4	46.17	2.91	41.75	8.21	0.00719	0.00046	0.04198	0.00843	0.4943	8.061	0.049
TF11_z5	43.01	2.51	39.92	4.53	0.00669	0.00039	0.04009	0.00464	0.6287	8.127	0.050
TF11_z6	41.54	2.49	37.81	5.55	0.00646	0.00039	0.03794	0.00568	0.4699	8.004	0.042
TF7A_z1	50.76	2.21	52.48	2.88	0.00791	0.00035	0.05304	0.00298	0.7204	7.995	0.018
TF7A_z2	47.06	2.41	82.04	6.45	0.00733	0.00038	0.08415	0.00689	0.6509	7.811	0.065
TF7A_z3	58.26	2.49	268.00	12.10	0.00908	0.00039	0.30200	0.01560	0.8331	8.174	0.033
TF7A_z4	49.53	2.09	62.27	5.16	0.00771	0.00033	0.06325	0.00541	0.4524	8.193	0.040
TF7A_z5	47.43	1.99	54.33	5.32	0.00739	0.00031	0.05497	0.00553	0.0726	8.285	0.105
TF7A_z6	48.44	2.29	61.59	4.64	0.00754	0.00036	0.06253	0.00486	0.5367	7.887	0.030
TF6_z1	52.77	2.36	55.43	3.24	0.00822	0.00037	0.05611	0.00337	0.7346	7.954	0.019
TF6_z2	53.40	2.41	57.01	4.30	0.00832	0.00038	0.05775	0.00447	0.7661	8.143	0.053

TABLE 1 (continued): U-Pb zircon age data

Sample/grain	Age (Ma) $^{206}\text{Pb}/^{238}\text{U}$	Age (Ma) $^{206}\text{Pb}/^{238}\text{U}$ 1 s.e.	Age (Ma) $^{207}\text{Pb}/^{235}\text{U}$	Age (Ma) $^{207}\text{Pb}/^{235}\text{U}$ 1 s.e.	$^{206}\text{Pb}^*/^{238}\text{U}$	$^{206}\text{Pb}^*/^{238}\text{U}$ 1 s.e.	$^{207}\text{Pb}^*/^{235}\text{U}$	$^{207}\text{Pb}^*/^{235}\text{U}$ 1 s.e.	Correlation of Concordia ellipses	UO/U	UO/U 1 s.e.
TF3_z1	49.31	3.25	54.54	13.28	0.00768	0.00051	0.05518	0.0138	0.4258	8.400	0.104
TF3_z2	55.54	4.25	73.49	42.19	0.00865	0.00066	0.07506	0.0447	0.5969	8.348	0.086
TF3_z3	57.48	3.74	51.92	11.84	0.00896	0.00059	0.05247	0.0123	0.4407	7.914	0.050
TF3_z4	56.40	4.04	57.21	15.35	0.00879	0.00063	0.05796	0.0160	0.4796	7.920	0.070
TF3_z5	54.29	3.87	61.87	12.51	0.00846	0.00061	0.06283	0.0131	0.4633	7.984	0.076
TF3_z6	57.71	4.24	61.84	13.62	0.00899	0.00066	0.06279	0.0143	0.5228	7.848	0.052

TABLE 2:  $^{40}\text{Ar}/^{39}\text{Ar}$  plagioclase age dataTF7A, plagioclase, 19.35 mg,  $J = 0.0019841 \pm 0.2384\%$ 

Step	T (°C)	t (min.)	$^{36}\text{Ar}$	$^{37}\text{Ar}$	$^{38}\text{Ar}$	$^{39}\text{Ar}$	$^{40}\text{Ar}$	% $^{40}\text{Ar}^*$	% $^{39}\text{Ar}$ rlsd	Ca/K	$^{40}\text{Ar}^*/^{39}\text{ArK}$	Age (Ma)	1 s.d.
1	550	12	7.346	4.420	3.885	82.942	2972.64	28.8	24.3	0.45520565	10.350785	36.68	0.72
2	580	12	1.689	5.754	1.224	52.422	1048.65	54.4	15.4	0.93773296	10.834842	38.37	0.43
3	610	12	1.716	14.953	1.229	48.219	1037.62	53.4	14.1	2.65067641	11.450196	40.53	0.48
4	640	12	1.649	26.719	0.907	34.55	884.597	47.9	10.1	6.618146	12.209336	43.18	0.58
5	680	12	6.944	61.270	1.937	28.272	2466.82	19.6	8.3	18.6130145	17.226681	60.63	2.18
6	730	12	5.969	105.38	1.923	21.502	2034.78	17.1	6.3	42.3919228	16.369872	57.66	1.96
7	800	12	2.116	16.430	1.204	12.568	773.931	22.6	3.7	11.202965	13.797554	48.72	1.38
8	890	12	1.485	2.802	0.947	7.484	545.841	23.0	2.2	3.20075722	16.431603	57.88	1.38
9	1000	12	1.800	2.049	1.241	7.566	641.048	20.1	2.2	2.31461268	16.607316	58.49	1.85
10	1140	12	3.146	1.928	3.120	13.428	1164.63	22.6	3.9	1.22675081	19.110076	67.14	1.70
11	1290	12	4.454	1.509	5.580	26.394	1820.21	29.8	7.7	0.48836917	20.295339	71.22	1.41
12	1400	12	3.873	1.061	4.020	5.874	1363.21	18.9	1.7	1.54341761	41.775679	143.66	4.62
								Cumulative % $^{39}\text{Ar}$ released =	100.0	<b>Total gas age</b>		<b>48.55</b>	<b>0.48</b>

TABLE 2 (continued):  $^{40}\text{Ar}/^{39}\text{Ar}$  plagioclase age dataTF4A, plagioclase, 20.90 mg,  $J = 0.0020690 \pm 0.2015\%$ 

Step	T (°C)	t (min.)	$^{36}\text{Ar}$	$^{37}\text{Ar}$	$^{38}\text{Ar}$	$^{39}\text{Ar}$	$^{40}\text{Ar}$	% $^{40}\text{Ar}^*$	% $^{39}\text{Ar}$ rlsd	Ca/K	$^{40}\text{Ar}^*/^{39}\text{ArK}$	Age (Ma)	1 s.d.	
1	480	12	11.906	0.404	2.968	24.177	385.11	10.2	10.5	0.17313885	16.247516	59.65	6.42	
2	515	12	2.323	0.322	0.746	17.069	937.763	28.6	7.4	0.19546378	15.601342	57.31	2.02	
3	550	12	2.847	0.536	0.947	25.384	1214.62	32.3	11.1	0.2187894	15.408620	56.62	1.95	
4	585	12	4.030	1.040	1.221	27.736	1615.75	27.8	12.1	0.38853775	16.172201	59.38	2.37	
5	620	12	5.164	3.274	1.405	25.926	1882.15	20.5	11.3	1.30890186	14.879503	54.70	2.86	
6	655	12	2.041	5.066	0.687	16.486	832.02	29.6	7.2	3.18683073	14.817096	54.48	2.04	
7	700	12	8.878	1.764	2.029	13.5	2888.69	10.8	5.9	1.35436174	23.081534	84.16	8.78	
8	750	12	2.170	0.880	0.682	8.63	726.886	14.1	3.8	1.05682452	11.704218	43.17	3.27	
9	850	12	2.464	1.154	0.785	5.555	773.859	8.2	2.4	2.15375348	11.247561	41.50	4.95	
10	1000	12	3.421	1.471	1.214	8.205	1125.28	12.1	3.6	1.8585309	16.413969	60.25	5.34	
11	1200	12	8.894	2.817	4.621	18.294	2947.13	12.4	8.0	1.59617172	19.777279	72.35	6.36	
12	1400	12	34.04	4.149	14.142	38.287	11478.21	13.8	16.7	1.12313448	41.380797	148.20	11.19	
								Cumulative % $^{39}\text{Ar}$ released =	100.0			<b>Plateau age</b> <b>(steps 1-6)</b>	56.61	1.93
												<b>Isochron age</b> <b>(steps 2-7)</b>	50.90	2.20

note: isotope beams in mV, rlsd = released, error in age includes J error, all errors 1 sigma

 $^{36}\text{Ar}$  through  $^{40}\text{Ar}$  are measured beam intensities, corrected for decay for the age calculations

TABLE 3: Major and trace element compositions of Iranian Paleogene volcanic rocks

Sample	AN3	AN5	AR3	AR5	DV1	DV4	QM2	QM6	QZ2	SA5	SA7
Latitude (WGS84)	33.12397	33.13792	34.30428	34.31207	35.78198	35.73080	34.08575	34.87202	35.98157	36.22677	35.41140
Longitude (WGS84)	52.53003	52.54782	51.17087	51.23790	51.95788	51.87353	50.52168	49.90792	50.79127	50.58443	51.30395
Lithology	<i>Basaltic andesite</i>	<i>Andesite</i>	<i>Andesite</i>	<i>Trachy-basalt</i>	<i>Basalt</i>	<i>Basalt</i>	<i>Andesite</i>	<i>Basalt</i>	<i>Basalt</i>	<i>Basalt</i>	<i>Basalt</i>
SiO <sub>2</sub> (%)	53.02	59.27	59.31	46.87	47.38	49.07	58.04	48.56	46.65	50.00	49.49
TiO <sub>2</sub> (%)	1.09	1.10	1.32	1.73	0.42	1.04	0.97	1.42	1.97	1.09	1.04
Al <sub>2</sub> O <sub>3</sub> (%)	17.77	16.20	15.21	16.52	11.63	15.37	17.43	19.08	15.34	18.84	18.69
Fe <sub>2</sub> O <sub>3</sub> (%)	8.41	8.31	10.38	11.30	10.15	9.94	7.68	11.41	12.75	10.12	10.13
MnO (%)	0.15	0.15	0.21	0.26	0.19	0.17	0.12	0.20	0.20	0.17	0.17
MgO (%)	6.13	2.81	2.92	6.80	15.98	9.85	3.43	4.29	8.31	4.95	5.78
CaO (%)	8.42	5.48	3.72	10.49	12.75	10.43	7.84	9.93	10.20	10.06	10.13
Na <sub>2</sub> O (%)	3.46	3.78	3.72	3.11	0.85	1.76	3.00	3.98	3.25	2.80	2.71
K <sub>2</sub> O (%)	1.13	2.18	2.43	2.16	0.37	1.70	1.31	0.65	0.65	1.34	1.28
P <sub>2</sub> O <sub>5</sub> (%)	0.33	0.31	0.39	0.51	0.05	0.32	0.17	0.18	0.44	0.31	0.33
Total (%)	99.91	99.59	99.61	99.75	99.77	99.65	99.99	99.70	99.76	99.68	99.75
Nb (ppm)	14.6	9.2	11.3	46.7	1.0	4.9	2.4	8.6	14.5	7.0	6.0
Zr (ppm)	115	157	257	126	18	66	56	134	119	84	73
Y (ppm)	21.6	26.4	47.0	20.5	10.1	16.5	23.2	25.8	25.3	20.1	19.0
Sr (ppm)	426	444	190	866	424	552	365	220	878	642	699
U (ppm)	0	1	2	0	0	0	0	0	0	0	0
Rb (ppm)	17.5	62.8	68.4	51.1	10.2	35.5	14.2	36.7	8.4	30.2	26.0
Th (ppm)	2	10	8	3	1	3	1	5	2	2	2
Pb (ppm)	5	11	8	139	2	5	4	7	3	6	1
Ga (ppm)	17	17	17	16	11	15	22	18	17	18	18
Zn (ppm)	72	66	299	231	63	73	89	95	90	81	68
Ni (ppm)	84	4	1	50	296	131	10	6	86	17	23
Cr (ppm)	264	51	11	134	823	478	38	27	193	40	27
V (ppm)	160	151	148	188	147	226	276	186	225	224	209
Ce (ppm)	33	51	52	53	7	33	15	33	43	35	36
Ba (ppm)	363	496	651	1041	91	476	199	450	378	351	393
La (ppm)	14	22	21	26	3	18	2	15	19	14	13

TABLE 3 (continued): Major and trace element compositions of Iranian Paleogene volcanic rocks

Sample	SV4	TA1	TA3	TA5	DEHNAR1	MSHK1	TRD5	HSN1	NA3	7453
Latitude (WGS84)	35.26700	36.24017	36.23063	36.22677	34.30428	36.82298	35.47757	35.40928	32.22457	36.20155
Longitude (WGS84)	50.09178	50.58243	50.58340	50.58443	51.17087	58.12228	54.31718	51.30103	53.25290	51.00782
Lithology	<i>Basaltic trachy-andesite</i>	<i>Basalt</i>	<i>Basanite</i>	<i>Analcime phonotephrite</i>	<i>Basaltic andesite</i>	<i>Basalt</i>	<i>Analcime tephri-phonolite</i>	<i>Basalt</i>	<i>Analcime trachy-andesite</i>	<i>Basanite</i>
SiO <sub>2</sub> (%)	52.48	47.04	45.42	52.21	54.99	48.27	54.04	49.18	55.27	43.59
TiO <sub>2</sub> (%)	1.00	1.08	1.22	0.86	1.44	1.58	0.90	1.06	0.73	1.53
Al <sub>2</sub> O <sub>3</sub> (%)	17.22	16.57	14.22	19.64	16.36	17.13	17.74	19.06	20.66	15.46
Fe <sub>2</sub> O <sub>3</sub> (%)	8.04	10.46	12.23	7.91	9.38	9.56	7.51	10.10	5.77	10.74
MnO (%)	0.15	0.17	0.23	0.16	0.11	0.15	0.14	0.17	0.13	0.17
MgO (%)	7.28	8.95	7.29	2.75	1.62	8.02	2.37	5.30	1.79	8.48
CaO (%)	7.16	11.96	13.38	7.11	10.13	9.21	6.57	10.86	5.05	9.73
Na <sub>2</sub> O (%)	3.96	2.76	4.03	3.89	3.84	4.08	3.73	2.68	4.51	2.62
K <sub>2</sub> O (%)	1.87	0.60	1.36	4.64	1.56	0.93	6.08	1.24	5.24	1.29
P <sub>2</sub> O <sub>5</sub> (%)	0.47	0.36	0.50	0.78	0.33	0.57	0.60	0.28	0.56	0.68
Total (%)	99.63	99.95	99.88	99.95	99.76	99.50	99.68	99.93	99.71	94.29
Nb (ppm)	21.4	3.5	12.7	14.5	8.7	23.0	15.2	6.6	9.4	27
Zr (ppm)	201	36	114	158	200	199	202	73	157	142
Y (ppm)	21.1	17.1	25.4	21.5	36.1	22.5	18.8	18.4	20.0	23
Sr (ppm)	583	738	1247	1235	208	673	1410	646	932	775
U (ppm)	0	0	0	0	2	0	0	0	1	0.69
Rb (ppm)	37.9	12.0	125.2	165.4	46.5	13.4	126.5	26.3	189.6	20
Th (ppm)	7	2	11	14	6	3	12	2	12	2.2
Pb (ppm)	9	8	18	29	5	3	28	6	30	6
Ga (ppm)	16	15	16	17	17	17	19	17	17	NA
Zn (ppm)	70	63	100	69	166	75	70	80	72	108
Ni (ppm)	139	92	32	11	9	82	10	25	5	126
Cr (ppm)	242	230	70	39	63	174	22	50	10	189
V (ppm)	130	242	336	143	243	169	165	230	83	216
Ce (ppm)	59	27	112	87	40	58	82	30	57	71.2
Ba (ppm)	639	451	1402	1616	334	221	819	349	1362	431
La (ppm)	31	11	51	45	16	26	38	15	28	34.4

## Chapter 4

### **Litho- and chemostratigraphy of the Johnnie Formation and Stirling Quartzite, Panamint Range and Funeral Mountains, eastern California: implications for the Death Valley record of Ediacaran ocean chemistry**

#### **ABSTRACT**

New carbon isotope data from thick exposures of the upper Johnnie Fm. in the Panamint Range of eastern California, combined with data from carbonate-rich facies of the Stirling Quartzite in the Funeral Mountains, provide a more complete record of  $\delta^{13}\text{C}$  fluctuations during the middle to late Ediacaran than previously determined from the Death Valley region. These data, coupled with field observations, provide evidence for at least three unconformities in the upper Johnnie Fm.: one at the base of the Johnnie oolite, a second, younger unconformity that is marked by a laterally extensive submarine debris flow in the central and northern Panamint Range, and a third unconformity at the Johnnie-Stirling contact. In the Funeral Mtns., carbonates in the uppermost Johnnie Fm. and in the lower part of the Stirling Quartzite have  $\delta^{13}\text{C}_{\text{PDB}}$  values near 0‰, suggesting that the Shuram anomaly is recorded entirely within the upper Johnnie Fm. and that previously recognized negative  $\delta^{13}\text{C}$  values from the middle to upper part of the Stirling Quartzite postdate the Shuram anomaly and predate the Precambrian-Cambrian boundary. Similarities in C isotope compositions suggest that incision of km-deep canyons in the Wonoka Fm. of South Australia could have been time equivalent with the submarine debris flow exposed in the Panamint Range.

## INTRODUCTION

The Johnnie Formation and Stirling Quartzite were deposited along the Cordilleran continental margin after the Marinoan cap carbonates of the underlying Noonday Dolomite (Prave, 1999, Petterson et al., 2007) and prior to the Precambrian-Cambrian boundary in the overlying Wood Canyon Fm. (Corsetti and Hagadorn, 2000). This time interval corresponds with the breakup of Rodinia and the development of the western Laurentian passive margin (e.g., Hoffman, 1991, Prave, 1999) and to some of the most significant geobiological events in earth history, including the radiation of multicellular organisms and the final stage in the oxygenation of the oceans (e.g., Fike et al., 2006, Kaufman et al., 2007, McFadden et al., 2008). Extremely light  $\delta^{13}\text{C}$  values from the upper part of the Johnnie Fm. (Corsetti and Kaufman, 2003) may record this final oxidation stage, and have been used to correlate the upper Johnnie Fm. with strata in Australia, Oman, and China (Halverson et al., 2005, Fike et al., 2006). Although it seems clear that previous geochemical studies in the Death Valley region have accurately located the stratigraphic position corresponding with the onset of this isotope excursion (e.g., Corsetti and Kaufman, 2003), a complete Death Valley C isotope record of the recovery from this event, which would include data from the upper Johnnie Fm. and possibly the overlying Stirling Quartzite, has not been assembled. Furthermore, the best Death Valley isotope data that do exist for this period come from one of the thinnest, most platformal settings in the region, raising the possibility that existing data do not fully capture  $\delta^{13}\text{C}$  fluctuations that may be recorded in thicker, more basinal settings. The association of older Neoproterozoic negative carbon isotope excursions with glaciations (e.g., Hoffman et al., 1998) coupled with geochronological evidence from

Newfoundland of a post-Marinoan glacial event (Bowring et al., 2003) has led to speculation of glacially-influenced sedimentation within the Johnnie Fm. (e.g., Abolins et al., 2000) which further motivates this study.

This paper reports the results of field and analytical work on the Johnnie Fm. and Stirling Quartzite conducted in the Panamint Range and Funeral Mountains of eastern California (Fig. 1). In the Panamint Range, the Johnnie Fm. is exposed continuously along strike for ~100 km, in contrast to more isolated exposures east of Death Valley where most studies of the Johnnie Fm. have been conducted. Field mapping and measured sections, as well as carbon isotope chemostratigraphy, from a ~30 km long transect in the Panamint Range (Fig. 2) were used to investigate along-strike facies changes within the upper Johnnie Fm. We also present new  $\delta^{13}\text{C}$  data from the uppermost Johnnie Fm. and lower Stirling Quartzite from carbonate-rich facies in the Funeral Mtns.

## **STRATIGRAPHIC AND TECTONIC SETTING**

The oldest Proterozoic stratigraphy in the southern Great Basin is the 3-4 km thick Pahrump Group, consisting of the Crystal Spring, Beck Spring, and Kingston Peak Formations (Fig. 3). U-Pb dates of 1.08 Ga from diabase sills that intrude the Crystal Spring Fm. (Heaman and Grotzinger, 1992) are the only reliable radiometric ages that have been determined from the Death Valley Proterozoic section, but correlations with other radiometrically dated sections worldwide have been facilitated by C isotope stratigraphy. Overlying the Kingston Peak Formation is the Noonday Dolomite, which was correlated by Prave (1999) to Marinoan cap carbonates (e.g., Kennedy, 1998) that

have subsequently been radiometrically dated at ~635 Ma in Namibia (Hoffmann et al., 2004) and China (Condon et al., 2005). Above the Noonday Dolomite are the Johnnie Formation, Stirling Quartzite, and Wood Canyon Formation. The trace fossil *Treptichnus pedum*, which first occurs in the lower Wood Canyon Fm., establishes the Precambrian-Cambrian boundary at this interval (Corsetti and Hagadorn, 2000). Deposition of the Noonday Dolomite to Lower Wood Canyon succession therefore may have occurred over as much as 90 to 100 My.

These sediments record the rifting history of southwest Laurentia and the subsequent development of a passive margin sequence. Structural and stratigraphic evidence of tectonism within the Kingston Peak Fm. (e.g., Walker et al., 1986) is generally considered to mark a period of rifting that was preceded by stable cratonic conditions and followed by development of the Cordilleran miogeocline (e.g., Stewart, 1972, Heaman and Grotzinger, 1986). Prave (1999) argued that Sturtian and Marinoan glacial deposits within the Kingston Peak Fm. correspond with two distinct periods of rifting. These field-based studies, which indicate that the “rift to drift” transition took place at approximately the Kingston Peak-Noonday contact, contrast with tectonic subsidence models which suggest that post-rift cooling began near 560 Ma (e.g., Bond et al., 1985), approximately 75 My after the Marinoan glaciation. Based on stratigraphic evidence from the Johnnie Fm., Summa (1993) concluded that it was deposited in subsiding basins related to extensional deformation, suggesting significantly younger rifting than previously thought and potentially reconciling the discrepancy between previous field

observations and subsidence models. Similarly, Clapham and Corsetti (2005) argued that there is evidence for tectonic activity at the Johnnie-Stirling contact.

The Panamint Range is an east-tilted fault block along the western margin of Death Valley that contains extensive exposures of all of the Proterozoic formations described above (e.g., Hunt and Mabey, 1966). The northern part of the range consists of a central area of greenschist to lower-amphibolite facies metamorphic rocks that is flanked on the east and west by normal faults carrying unmetamorphosed to greenschist-facies Proterozoic to Tertiary strata in their hanging walls (e.g., Hodges et al., 1990). The structurally lowest and regionally most persistent fault on the east side of the range where our work is concentrated is the middle Miocene Harrisburg Fault (Fig. 2), which typically places unmetamorphosed to weakly metamorphosed upper Johnnie Fm. onto higher-grade and stratigraphically lower units including the Kingston Peak Fm., Noonday Dolomite, and lower Johnnie Fm. (Wernicke et al., 1988, Hodges et al., 1990).

## **STRATIGRAPHY OF THE JOHNNIE FORMATION AND STIRLING QUARTZITE**

### **Background**

The Johnnie Fm., originally named by Nolan (1929) for exposures near Johnnie Wash in the Spring Mtns. (Fig. 1), lies disconformably on the underlying Noonday Dolomite (Summa, 1993). It varies in thickness from about 30 to 1600 m within the southern Great Basin (Stewart, 1970) and is comprised of siltstone, sandstone, dolostone, limestone and conglomerate. Stewart (1970) divided the Johnnie Fm. into the following six members,

listed in ascending order: transitional, quartzite, lower carbonate-bearing, siltstone, upper carbonate-bearing, and Rainstorm (Fig. 3). The uppermost of these, the Rainstorm Member (originally named by Barnes et al., 1965, for outcrops near the Rainstorm Mine in southern Nevada), is the most widespread across the southern Great Basin (Stewart, 1970) and is the primary focus of this study. As defined by Stewart (1970), the Rainstorm Member consists of basal siltstone overlain by a 1 to 2 m-thick oolite bed of regional extent (the so-called "Johnnie oolite") which is the most distinctive lithological feature within the Johnnie Fm. Overlying the Johnnie oolite is a thin siltstone interval that is typically followed by several meters of conspicuous pale red limestones and 50 to 80m of limey siltstones. Above this, the upper part of the Rainstorm Member varies widely in thickness from 15 to 200 m in previously described sections and is composed of siltstone, fine-grained sandstone, and occasional carbonates (Stewart, 1970). Summa (1993) conducted a detailed sequence stratigraphic study of the Johnnie Fm. which supplements the lithostratigraphic observations of Stewart (1970). She places a sequence boundary at the base of the Johnnie oolite, a flooding surface within the siltstones above the oolite, and another sequence boundary at the Johnnie-Stirling contact, as discussed below. She concluded from her work in the southern Nopah Range (Fig. 1) that the Johnnie Fm. there is comprised of a combination of shallow-marine and fluvial sediments and was deposited in an inner shelf basin. Rainstorm Member isopachs (Fig. 1, Stewart, 1970) illustrate NW or WNW thickening in three regions: 1) within the area immediately north of Las Vegas, 2) in an area that stretches along the Nevada-California border from approximately Clark Mtn. in the SE to the northern part of the Resting Spring Range in the NW, and 3) within the Panamint Range.

The contact relationship between the Johnnie Fm. and the overlying Stirling Quartzite has been the subject of some disagreement. Most early studies concluded that the contact is conformable (e.g., Stewart, 1970, Benmore, 1978), but in more recent investigations, Christie-Blick and Levy (1989) and Summa (1993) interpreted it as a sequence boundary and described incised valleys which locally removed as much as 150 m of the underlying Rainstorm Member before being filled with breccia and siltstone prior to deposition of the overlying Stirling Quartzite. Abolins et al. (2000) suggested that this canyon incision was related to glacioeustatic sea-level fall and that some of the clasts within the valley fill were derived from cap carbonates deposited subsequent to glaciation. Clapham and Corsetti (2005) argued against a glacial origin for the incised valleys and suggested that their locations were controlled by syndimentary normal faults.

Corsetti and Kaufman (2003) measured C isotopes in the Johnnie Fm. from sections in the southern Nopah Range, Alexander Hills, and Winters Pass Hills (Fig. 1). Their results revealed extremely light  $\delta^{13}\text{C}_{\text{PDB}}$  within Rainstorm Member carbonates (as negative as  $-11.5\text{‰}$ ), values which have subsequently been correlated with the early part of the so-called “Shuram anomaly” C isotope excursion in Oman, which is also known from several other sections worldwide (e.g., Halverson et al., 2005, Le Guerroué et al., 2006, Fike et al., 2006). The anomaly is manifest in most sections by an apparent rapid decline (relative to deposition rate) from positive values of  $\delta^{13}\text{C}$  to some of the lowest values ever recorded in the marine record, significantly below the mantle value of approximately  $-6\text{‰}$ . The values then gradually and monotonically recover to positive

values. The Shuram anomaly has been interpreted as the result of oxidation of large volumes of organic carbon in the deep ocean (Rothman et al., 2003, Fike et al., 2006, McFadden et al., 2008). In sections in Oman, South Australia, and China,  $\delta^{13}\text{C}_{\text{PDB}}$  of carbonates steadily increases from a nadir of about -12‰ up to 0‰ (Calver, 2000, Condon et al., 2005, Fike et al., 2006, McFadden et al., 2008). In contrast,  $\delta^{13}\text{C}_{\text{PDB}}$  from Rainstorm Member carbonates in the Winters Pass Hills (Corsetti and Kaufman, 2003; the most detailed data previously published from the Rainstorm Member) recover to only -9.2‰ below the contact with the Stirling Quartzite, suggesting that a significant part of the Shuram anomaly may be missing along the disconformity at the Johnnie-Stirling contact. The coincidence of the Johnnie oolite, which was probably deposited as a transgressive sheet following a period of erosion or non-deposition (Benmore, 1978, Summa, 1993, Kaufman et al., 2007), with the onset of the Shuram anomaly suggests that the events responsible for significantly altering the C isotope chemistry of the oceans at this time were associated with a rise in sea-level (Kaufman et al., 2007), not a fall as would be predicted from a glacial origin of the anomaly.

Global correlations of the Shuram anomaly, coupled with geochronological data from the Doushantuo Fm. in China and the Nafun Group in Oman, place some constraints on the age of the upper Johnnie Fm. and, in particular, the Johnnie oolite. Detrital zircons as young as 600 Ma from the Khufai Fm. in Oman (Le Guerroué et al., 2006) place a maximum age constraint on the onset of the Shuram anomaly and, by extension, deposition of the Johnnie oolite. A U-Pb date of  $551.1 \pm 0.7$  Ma from an ash bed in the upper part of the anomaly in the Doushantuo Fm. (Condon et al., 2005) provides a

minimum age constraint. Therefore, if correlations between these regions are valid, the implication is that the Johnnie oolite is between 551 and 600 My old. However, the most limiting U-Pb geochronological data from a single region are those of Condon et al. (2005) from China, which only bracket the age of the Shuram anomaly, and therefore the lower Rainstorm Member, between 551 and 633 Ma.

Much like the underlying Rainstorm Member, the Stirling Quartzite thickens to the NW or WNW and reaches a maximum thickness of >1600 m in southern Nevada (Fig. 9 of Stewart, 1970). It has been divided into five members, named, in ascending order, the A Member through E Member (Stewart, 1966, Stewart, 1970). Because carbonate beds are relatively rare in the Stirling Quartzite, C isotope data are sparse compared with other Neoproterozoic/Cambrian units in the region.  $\delta^{13}\text{C}$  data have previously been collected from the D Member in the Grapevine Mtns. and Bare Mtn. (Fig. 1, Corsetti and Hagadorn, 2000, Corsetti and Kaufman, 2003) and from the “middle member” in the southern Nopah Range and Salt Spring Hills (Fig. 1, Corsetti and Kaufman, 2003). Taken together, these data seem to suggest moderately negative values in the middle part of the formation which cross into positive values within the D Member (Corsetti and Hagadorn, 2000 and Corsetti and Kaufman, 2003).

### **Lithostratigraphy and C isotope data from the Panamint Range**

In the central and northern Panamint Range, the upper part of the Johnnie Fm. is lithostratigraphically distinct from the Rainstorm Member in the eastern Death Valley region. Although it contains siltstone and carbonate, it lacks the Johnnie oolite, pale red

limestones and abundant ripple marks and flute casts in fine-grained sandstones that distinguish the Rainstorm Member in the eastern Death Valley region and the southern Panamint Range. These dissimilarities have led to variable lithostratigraphic correlations and interpretations for these strata amongst previous workers (Hunt and Mabey, 1966, McDowell, 1967, Stewart, 1970, Benmore, 1978, Abolins et al., 2000).  $\delta^{13}\text{C}$  data from the Rainstorm Member, which reach primary values significantly lighter than at any other time in earth history, are particularly useful in this case for correlating various sections that have eluded definitive lithostratigraphic correlation. Here we describe 10 measured stratigraphic sections and accompanying C isotope data from the Panamint Range that span a total along-strike distance of 30 km. These data are presented in order from south to north, which also corresponds with lithofacies that are progressively unlike more thoroughly described sections of the Rainstorm Member to the east of Death Valley. C and O isotopic measurements were conducted in the stable isotope laboratories at Stanford University and the University of Michigan.

### ***Johnson Canyon***

In Johnson Canyon (Fig. 2), the upper Johnnie Formation is lithologically quite similar to exposures in the southern Nopah Range and many other locations east of Death Valley. Stewart (1970) recognized all six members of the Johnnie Fm in this area. The top and bottom of the Johnnie oolite contain rip-up clasts in outcrops examined in Johnson Canyon (Figs. 4 A and B), consistent with previous interpretations that the base of the oolite disconformably overlies the lower Rainstorm Member siltstones and marks the onset of a marine transgression (Summa, 1993, Kaufman et al., 2007), and possibly

suggesting another disconformity at the top of oolite. Scanning-electron microscope analysis of the oolite revealed numerous small (<100  $\mu\text{m}$ ) apatite crystals within both the ooids and micrite matrix. Attempts to measure U-Pb ages of these grains using isotope dilution-thermal ionization mass spectrometry were unsuccessful, however, because of insufficient radiogenic Pb. Immediately above the oolite are 5 m of siltstones overlain by 6.5 m of distinctive pale red limestones (Fig. 4C) similar in appearance to those described from the southern Nopah Range (e.g., Stewart, 1970, Summa, 1993, Corsetti et al., 2004). Above these are ~150m of siltstone and sandstone with rare, thin carbonate beds.

The total thickness of the Rainstorm Member in Johnson Canyon is ~160 m (Fig. 5), approximately 2-3 times greater than in sections from the southern Nopah Range and Winters Pass Hills where previous C isotope studies have been conducted (Corsetti and Kaufman, 2003).  $\delta^{13}\text{C}_{\text{PDB}}$  within the upper carbonate bearing member vary somewhat but are generally 1 to 3‰ in the stratigraphically lowest samples (Fig. 5, Table 1). Values decrease up section and reach a value of -3.7‰ at the base of the Johnnie oolite. Within slightly over a meter, values decrease to -5.3‰ at the top of the Johnnie oolite (Fig. 5). In the overlying pale red limestones  $\delta^{13}\text{C}_{\text{PDB}}$  becomes even lighter, reaching a nadir of -11.6‰ near the top of these beds, nearly identical to the lightest values from dolostones above the Johnnie oolite in the Winters Pass Hills (Corsetti and Kaufman, 2003).  $\delta^{13}\text{C}_{\text{PDB}}$  values from Johnson Canyon show a slight overall increase in the overlying ~45 m of section, reaching a value of -9.4‰. Siltstone and sandstone predominate in the upper ~100m of section, but thin dolostone beds record values no heavier than -7.3‰ beneath the contact with the Stirling Quartzite.

### ***South Fork of Hanaupah Canyon***

Along the South Fork of Hanaupah Canyon (Fig. 2), ~500m of limestone, dolostone, and siltstone underlie the Stirling Quartzite and overlie siltstones of the middle Johnnie Fm. (Fig. 6). McDowell (1967) was the first to describe the geology of this area in detail and defined this part of the section as the “limey argillite” member of the Johnnie Fm.

Within this interval and 180 m below the contact with the Stirling Quartzite are ~7 m of edgewise conglomerate (Fig. 4D), previously noted by McDowell (1967) and Stewart (1970). Three lithostratigraphic correlations have been proposed for this section of the upper Johnnie Fm. Stewart (1970) and Benmore (1978) interpreted it as the Rainstorm Member, a suggestion which is supported by previous descriptions of a 1.4 m-thick oolite bed at the base of the section (Benmore, 1978). Although we did not find oolite in the section we measured, we have observed isolated exposures of probable Johnnie oolite as far north as Trail Canyon (described below) and suspect the oolite could have easily been omitted by erosion or non-deposition over much of the central and northern Panamints.. McDowell (1967) made the same correlation but suggested that the edgewise conglomerate, located in the upper half of the limey argillite member, was equivalent to the Johnnie oolite, which normally occurs near the base of the Rainstorm Member (e.g., Stewart, 1970). Abolins et al. (2000) suggested that the edgewise conglomerate was deposited within a canyon that was incised into the top of the Rainstorm member.

$\delta^{13}\text{C}_{\text{PDB}}$  values from carbonates within this section are approximately -10‰ at the bottom and decrease fairly regularly up section to about -5‰ near the top (Fig. 5). Three

samples from the matrix of the edgewise conglomerate have  $\delta^{13}\text{C}_{\text{PDB}}$  ranging from -7.6 to -8.5‰. The similarity of these limey argillite member values with data from the Rainstorm Member in Johnson Canyon support the interpretation of Stewart (1970) and Benmore (1978) that the entire ~500 m of section is equivalent to the Rainstorm Member. These data also suggest that deposition of the edgewise conglomerate postdates the Johnnie oolite, which has  $\delta^{13}\text{C}_{\text{PDB}}$  of -3.7 to -5.3‰ in Johnson Canyon and corresponds with the rapidly decreasing part of the Shuram anomaly, not the gradually increasing part. The absence of a discernable change in  $\delta^{13}\text{C}$  within the matrix of the edgewise conglomerate or within overlying sediments argues against the interpretation of Abolins et al. (2000) that the conglomerate was deposited above a major unconformity. It is also noteworthy that  $\delta^{13}\text{C}_{\text{PDB}}$  of carbonates reach values as heavy as -5.2‰ at the top of this section, compared with the heaviest value of -7.3 ‰ from Johnson Canyon.

#### ***North Fork of Hanaupah Canyon***

From Hanaupah Canyon to the Wildrose Peak area (Fig. 2), unusual occurrences of carbonates at the Johnnie-Stirling contact were noted by Hunt and Mabey (1966) and mapped by Albee et al. (1981) but have not previously been investigated in detail. The largest and best exposed outcrop of these is found in the north fork of Hanaupah Canyon, where ~100 m of dolostone is situated between fine-grained sandstones and siltstones of the Johnnie Fm. below and sandstones of the Stirling Quartzite above (Fig. 7A). In detail, this outcrop consists of cross-bedded dolostone and carbonate breccia in the lower 2.5 m (Fig. 8A), overlain by 0.5 m of stromatolitic fine-grained dolostones (Fig. 8B) which, in some ways, resemble the tubestones of the underlying Noonday Dolomite (e.g.,

Cloud et al., 1974). Lying above the stromatolitic dolostone are 11 m of carbonate breccia, sandstone, and conglomerate and an additional 11 m of laminated dolostone and siltstone. The remainder of the section is comprised of 75 m of sandy dolostone containing stromatolites with up to 0.5m of synoptic relief (Fig. 8C). The top of the carbonate section is brecciated, and the contact with the overlying Stirling Quartzite is sharp.

The contact of this carbonate unit with underlying sandstones and siltstones is well exposed in the north fork of Hanaupah Canyon. A thin, white sandstone in the area is a useful marker bed for illustrating the stratigraphic relationship between the carbonate unit and underlying and overlying strata. Along the south wall of the canyon (Figs. 7B and C) this marker bed is separated from the overlying Stirling Quartzite by 2 m of sandy, cross-bedded dolostone. Tracing the marker bed to the east, it is down-dropped by a steeply east-dipping normal fault which also offsets beds in the overlying Stirling Quartzite. Just to the east of this fault, the carbonate unit is significantly thicker than in the footwall and reaches its full thickness of 100 m within a couple of hundred meters to the north where the white quartzite bed is still present at the base (Fig. 7A). The carbonate unit appears to thin to almost zero thickness farther to the north before intersecting another fault (Fig. 7A). The overall picture is therefore of a lens-shaped carbonate unit, 2.5 km in length, thickest in the middle and tapering to zero thickness to the north and south.

$\delta^{13}\text{C}$  values are significantly different in this 100 m-thick section than in sections of upper Rainstorm Member described previously (Fig. 5). The stratigraphically lowest

sample has carbonate  $\delta^{13}\text{C}_{\text{PDB}}$  of -4.5‰, and values increase in the overlying 20 m of section to -3.3‰ before increasing suddenly to ~0‰. In the uppermost 80 m of section they increase slightly to as much as 1.2‰. These values thus contrast with  $\delta^{13}\text{C}$  from the upper Johnnie Fm. in the south fork of Hanaupah Canyon and in Johnson Canyon, being wholly greater than even the heaviest isotopes in the uppermost Johnnie Fm in the other sections.

### ***Wildrose Peak area***

Albee et al. (1981) mapped a thin dolostone unit at the top of the Johnnie Fm. from the north fork of Hanaupah Canyon to the vicinity of Wildrose Peak (Fig. 2). This unit, “jud: Johnnie upper dolostone” on the map of Albee et al. (1981), includes the thick carbonate unit in the north fork of Hanaupah Canyon described above as well as thinner dolostones to the north that are at a similar stratigraphic position. We mapped the northern reaches of the dolostone along strike for about 4 km, starting 0.5 km east of the Thorndike campground and proceeding north (Figs. 2 and 9). In the southern part of this transect, the dolostone is overlain by sandstones of the Stirling Quartzite, and to the north siltstones pinch in between it and the Stirling Quartzite. The dolostone becomes discontinuous in the northernmost km of the transect, either from faulting, overall poor exposure, or stratigraphic pinch out.

This unit generally consists of light grey to white, laminated dolostone and lesser limestone, and becomes sandier up section. Where we measured it, the unit is 40m thick, although this seems to vary somewhat along-strike. Where exposed, the base is

frequently brecciated, and breccias occur throughout the section. In one particularly good exposure of the upper 4 m of the unit, the lower 2m consists of brecciated sandy dolostone overlain by laminated dolostone and siltstone. Above this is 1 m of dolostone with domal stromatolites, followed by 50 cm of planar laminated dolostone. Overlying the dolostone are several tens of meters of dark grey siltstone followed by sandstone of the Stirling Quartzite. In another good exposure of the top of the carbonate unit 1 km to the north, the overall stratigraphy is similar, consisting of a laminated uppermost part underlain by carbonate intraformational breccia. In this area, giant ooids (Sumner and Grotzinger, 1993), ~1 cm in diameter (Fig. 8D), occur in a thin interval between the breccia and overlying laminated dolostone.

Carbon isotope samples were collected from several locations within this unit, and we have combined the results to create a composite chemostratigraphy (Fig. 5).  $\delta^{13}\text{C}_{\text{PDB}}$  of carbonate at the base of the unit is -3.5‰, increases sharply to near 0‰ within the middle, and then increases more gradually to values as great as 1.8‰ in the upper portion. The two exposures of the top of the unit described above yield similar results:  $\delta^{13}\text{C}_{\text{PDB}}$  of carbonate from the brecciated portion are between 1.2 and 1.7‰, and values are -0.1 to 1.5‰ in the overlying laminated and oolitic dolostones. The giant ooids have a  $\delta^{13}\text{C}_{\text{PDB}}$  value of 0.2‰. Although thinner than the carbonate unit described from the north fork of Hanaupah Canyon,  $\delta^{13}\text{C}$  values of these dolostones are generally similar.

### *Trail Canyon*

The majority of our work was conducted in Trail Canyon (Figs. 2 and 10), where the Johnnie Fm. is well exposed along strike for 8 km in an area of high relief. For the purpose of mapping, the Johnnie Fm. in this area is best divided into three members. The lower member (Zjl) consists predominantly of dark-grey siltstone with lesser carbonate and is separated from the underlying Noonday Dolomite by a fault in most of Trail Canyon. Based on our mapping (Fig. 11), we estimate a thickness of 330 m for this member. Above Zjl are some 200m of light-green siltstones and orange- to brown-weathering, laminated, silty dolostones comprising the middle member (Zjm).

The contact between Zjm and the overlying upper member (Zju) is defined by a carbonate breccia horizon that can be followed nearly continuously from the road leading to Aguerberry Point in the north to the southern end of the south fork of Trail Canyon, a distance of at least 8 km (Fig. 11). The most common clast type within the breccia is a distinctive bluish grey limestone. During reconnaissance in Blackwater Wash (Fig. 2), located an additional 5 km to the north, the breccia bed was found at the same stratigraphic position and with similar clast composition (Figs. 12A and B). Blocks within the breccia that have discernable edges at outcrop scale can reach up to 10m in diameter (Fig. 13), and the largest blocks are at least 10s of meters in length. In many places, 3 m of laminated, sandy dolostone occurs within the breccia (Fig. 14A). The presence of limestone clasts both above and below this laminated dolostone make it difficult to determine whether the laminated dolostone beds are themselves large clasts. Bedding in the laminated dolostone is always parallel to bedding above and below the

breccia, however, providing some indication that it may be autochthonous and was deposited synchronously with the allochthonous blocks in the breccia bed. To the south the breccia bed becomes thicker and very sandy, reaching a thickness of 85 m in the south fork of Trail Canyon.

Above the breccia bed, Zju is composed almost entirely of dark-grey siltstone with occasional thin dolomitic beds. In places we have observed thin-bedded alternations of siltstone and fine-grained sandstone within Zju, which we interpret as turbidites (Fig. 14B). Two thin conglomerate beds occur in the uppermost part of Zju (Stewart, 1970, Abolins et al., 2000) and are usually composed of quartz granules and pebbles (Fig. 14C), although they may also contain siltstone clasts. We measured a thickness of 281 m for Zju, and our estimate for the combined thickness of Zjm, the breccia bed, and Zju within the northern part of Trail Canyon is 490 m. The abrupt change in lithology across the breccia bed, from siltstones and thin-bedded carbonates in Zjm to almost entirely siltstones in Zju, suggests an unconformity between these units at the level of the breccia bed. As described below, all previously published C isotope data from the Johnnie Fm. come from stratigraphic positions significantly below this intra-Rainstorm unconformity.

The central and eastern portions of Trail Canyon comprise an east-dipping homocline of the units described above and the overlying Stirling Quartzite, Wood Canyon Formation, Zabriskie Quartzite, and Carrera Fm. (Fig. 11). It is cut by numerous, relatively small, generally south-dipping normal faults that cut at high angles across bedding, as well as shallowly north-dipping normal faults with greater offset. The western part of the area is

made up of highly deformed Noonday Dolomite and, in places, overlying Zjl siltstone. In the western area the Noonday-Johnnie contact is offset by a series of east-dipping, high-angle normal faults (Figs. 10 and 11). Separating the western area from the central and eastern areas is an east-dipping normal fault of considerable offset which, according to the generalized geologic maps of Hodges et al. (1987) and Hodges et al. (1990), is the southern continuation of the Harrisburg Fault. In the northern part of the Trail Canyon area this fault juxtaposes Zjl and the Noonday Dolomite; in the middle part it drops Zjm onto the Noonday, and in the southern part it separates Zjm in the hanging wall from Zjl in the footwall (Fig. 11). To the south of the mapped area, vegetation and extremely rugged topography obscure the transition to the upper Johnnie section near Wildrose Peak described in the previous section.

C isotope data were obtained from six measured sections within Trail Canyon. The southernmost section is in the south fork of Trail Canyon (location TC1, Fig. 11), where the lower 39 m are in siltstones and laminated and cross-bedded dolostones of Zjm, and stratigraphically higher samples are from 85 m of carbonate breccia and coarse-grained dolomitic sandstone which underlie siltstones of Zju. Dolostones in the upper part of Zjm have  $\delta^{13}\text{C}_{\text{PDB}}$  values ranging from -10.6 to -11.0‰ (Fig. 15), which are typical for carbonates in the lower part of the Rainstorm Member, above the oolite. Above Zjm,  $\delta^{13}\text{C}_{\text{PDB}}$  in the carbonate breccia/dolomitic sandstone interval are strikingly different, falling between -0.7 and 1.1‰.

The next section to the north begins in Zjm and includes two large limestone blocks from the breccia bed separating Zjm and Zju (location TC2, Figs. 11 and 13). About 25 m below the breccia bed, a dolostone bed records  $\delta^{13}\text{C}_{\text{PDB}}$  of -4.6‰, and ~3m below the breccia bed values reach as heavy as about -2.1‰ (Fig. 15). Above these, one sample was collected from a relatively small breccia block which has a  $\delta^{13}\text{C}_{\text{PDB}}$  value of 1.2‰ (Fig. 15). In the overlying, larger block, seven samples were collected which range from -3.6‰ at the “base” to 1.0‰ at the “top,” although the facing direction within the block could not be determined.

To the north, samples were collected from carbonates overlying the diamictite locality described by Abolins (1999) in the central portion of Trail Canyon (location TC3, Fig. 11). Our mapping indicates that the diamictite, overlying limestones and carbonate breccias in this area are all part of the breccia bed separating Zjm and Zju. The diamictite (Fig. 14D) is underlain by Zjm siltstones and consists of pebble- to boulder-size limestone clasts supported by a silty matrix. It is overlain by 7 m of massive sandy limestone which is brecciated at its base, and which we interpret as an allochthonous block. Above this are 14 m of matrix- and clast- supported carbonate breccia followed by another block of black, sandy limestone that is overlain by Zju siltstones.  $\delta^{13}\text{C}_{\text{PDB}}$  in the lower limestone block is -1.8‰ at the base and increase to -0.4‰ near the middle before decreasing again to -1.9‰ at the top (Fig. 15). The upper limestone has  $\delta^{13}\text{C}_{\text{PDB}}$  of 1.5‰ at the base, decreasing to -2.7‰ at the top. The pattern in this block is similar to that in the block at TC1, except inverted.

An intact section of lower Johnnie Fm. and possibly uppermost Noonday Dolomite is exposed near the detachment fault in the northern part of this area (location TC4, Fig. 11). The basal 12 m of this section is primarily grey, laminated to massive dolostone overlain by dolostone containing thin siltstone beds. It is unclear if these beds are lower Johnnie Fm. or upper Noonday Dolomite. Above these carbonates are 11 m of siltstones followed by a 9 m-thick breccia bed containing carbonate clasts supported in a silty matrix (Fig 16 A and B). Overlying the breccia are 29 m of siltstones with an increasing number of thin dolostone beds up-section. In the 30 m of section above these siltstones, at least 4 rhythmic cycles are developed which each consist of a basal bed of silty, laminated dolostone, an intermediate bed of pure, thin-bedded dolostone, and upper siltstone beds (Fig. 16C), which we interpret as deepening-upward. Overlying the siltstones of the last cycle there is a very distinctive, 6 m-thick horizon of siltstone supporting dispersed rounded carbonate boulders up to 1.5 m in diameter (Fig. 16D). Lying above the “boulder horizon” are ~250 m of siltstone and rare carbonates which make up the majority of Zjl, and these are followed concordantly by Zjm.  $\delta^{13}\text{C}_{\text{PDB}}$  from the basal carbonate part of section TC4 vary from about -2 to -4‰ (Fig. 15), comparable to values from the lower Johnnie Fm. in the southern Nopah Range (Corsetti and Kaufman, 2003) and from the upper Noonday Dolomite (Prave, 1999, Corsetti and Kaufman, 2003).  $\delta^{13}\text{C}_{\text{PDB}}$  of carbonate from the dolostone-siltstone cycles is broadly similar, varying from about -2.5 to -3.7‰.

The northernmost section is just south of the road leading to Aguerberry Point (location TC5, Fig. 11) and includes samples collected from the base of Zjm through the upper part

of Zju (Fig. 15). The two stratigraphically lowest carbonate samples from Zjm have  $\delta^{13}\text{C}_{\text{PDB}}$  of -6 to -9‰, and slightly above these, a thin oolite bed records values of about -10 to -11‰. In the upper part of Zjm,  $\delta^{13}\text{C}_{\text{PDB}}$  of carbonate is as heavy as -4‰, and  $\delta^{13}\text{C}_{\text{PDB}}$  of carbonate in the matrix of the overlying breccia bed is also about -4‰. Carbonate beds are rare within the Zju siltstones, but those that are present indicate that  $\delta^{13}\text{C}_{\text{PDB}}$  values return to more negative values, approximately -6 to -7‰, in the lower part of Zju.

Finally, we collected samples from the lower part of the D member of the Stirling Quartzite near Trail Canyon (location TC6, Fig. 5).  $\delta^{13}\text{C}_{\text{PDB}}$  is -5.2‰ at the base of the D Member (Fig. 15), increases slightly to about -4.2‰, and then decreases to about -6.4‰ in the highest carbonate bed we sampled 30 m above the base of the D member. The total thickness of the D member in this area is approximately 125m (Stewart, 1970).

### **Lithostratigraphy and C isotope data from the Funeral Mountains**

With the exception of the upper dolostone unit in Hanaupah Canyon, the uppermost Johnnie Fm. and most of the Stirling Quartzite are siliciclastic in the Panamint Range, in the Funeral Mtns. (Fig. 1) more abundant carbonate beds in this interval provide an opportunity to measure  $\delta^{13}\text{C}_{\text{carb}}$  above and below the Johnnie-Stirling contact. We collected samples from two locations: near Indian Pass in the northern part of the Funeral Mtns. and near Lees Camp in the central part (Fig. 1). In the Indian Pass area, a 2 m-thick bed of sandy dolostone is situated in the uppermost part of the Johnnie Fm. (Wright and Troxel, 1993). Unlike the dolostone at the Johnnie-Stirling contact in the central

Panamint Range described above, the dolostone bed near Indian Pass is not brecciated and has gradational upper and lower contacts. We have seen no evidence that it is allochthonous. Near Indian Pass another dolostone interval, approximately 13 m thick, is used as a marker horizon within the A Member of the Stirling Quartzite (Wright and Troxel, 1993). In the Lees Camp area, a sandy dolostone bed of comparable thickness is found in the A Member (Stewart, 1970, Wright and Troxel, 1993), and is presumed to be equivalent to the bed near Indian Pass. Near Lees Camp, the middle and upper parts of the Stirling Quartzite contain much more carbonate than in most other locations. Both Stewart (1970) and Wright and Troxel (1993) mapped at least portions of the Lees Camp area, and they differ somewhat in their conventions for identifying various members of the Stirling Quartzite. Below, we follow the descriptions and mapping of Stewart (1970) when referring to the C and D Members.

$\delta^{13}\text{C}_{\text{PDB}}$  from the upper Johnnie Fm. dolostone near Indian Pass ranges from -0.7 to 1.6‰, and the Stirling A marker horizon in this area records broadly similar values of -1.7 to 0.2‰ (Fig. 17A). In the Lees Camp area, the Stirling A carbonate marker bed has  $\delta^{13}\text{C}_{\text{PDB}}$  values of -2 to 0.3‰, essentially indistinguishable from values to the north.  $\delta^{13}\text{C}_{\text{PDB}}$  of carbonate from the overlying C and D members of the Stirling Quartzite are significantly different from these values, however. Values in the lower part of the C member are -3.6 to -4.3‰ and become heavier upsection, crossing 0‰ in the D member (Fig. 17B), consistent with previous data from the Grapevine Mtns. (Corsetti and Hagadorn, 2000).

## **DISCUSSION AND CONCLUSIONS**

### **Correlations within the Panamint Range**

Sections of the upper Johnnie Fm. in Johnson Canyon (the “conventional” Rainstorm Member lithologically similar to the type section in Nevada and sections in the eastern Death Valley region), the south fork of Hanaupah Canyon (the limey argillite member), and the northernmost part of Trail Canyon (Zjm and Zju) are lithologically quite dissimilar and therefore difficult to correlate based strictly on lithostratigraphy.

However, distinctive C isotope data from these areas may be used to establish correlation between various sections.

Based on our C isotope data, we correlate the 160 m of typical Rainstorm Member lithologies exposed in Johnson Canyon with the upper 500 m of the Johnnie Fm in the north fork of Hanaupah Canyon and with Zjm from section TC4 in Trail Canyon (Fig. 18). Because our data from Hanaupah Canyon do not definitively record the onset of the Shuram anomaly, we cannot confidently correlate the base of the Rainstorm Member to these areas. Furthermore, Stewart (1970) measured a thickness of only 280 m for the Rainstorm Member in the south fork of Hanaupah Canyon. He noted that because of numerous small faults, his estimate for the true thickness was uncertain, and it is unclear if he measured his section in the same location we did. Our measured thickness also suffers from uncertainty due to faulting and should be treated with some caution.

We interpret the breccia bed in Trail Canyon as a submarine gravity flow or “olistostrome” (e.g., Krause and Oldershaw, 1979). Relatively heavy  $\delta^{13}\text{C}$  values from within the breccia bed in the southern part of Trail Canyon (locations TC1-3, Figs. 5 and 11) contrast markedly with values measured in strata immediately below (locations TC1, 2 and 4) and above (location TC4) the breccia. The original stratigraphic positions of the large blocks are difficult to ascertain because their C isotope values, though rapidly changing through the two mlarger blocks, are non-unique. The prevalence of fine-grained siliclastics, turbidites, and debris flows within the Johnnie Fm. in Trail Canyon suggest deeper water deposition than at localities to the southeast such as the southern Nopah Range (Summa, 1993).

Our mapping near the Thorndike campground suggests that the dolostones and breccias found at the Johnnie-Stirling contact from the north fork of Hanaupah Canyon to near Wildrose Peak, i.e., the “Johnnie upper dolostone” unit of Albee et al. (1981), are equivalent to the breccia bed in Trail Canyon. In the area of our map transect near the campground, the dolostone unit is overlain by sandstone of the Stirling Quartzite to the south and progressively more siltstone (equivalent to Zju) to the north (Fig. 9). In Trail Canyon, the thickness of Zju siltstone overlying the breccia bed reaches 280 m and becomes even thicker in the northernmost Panamint Range. If these beds are, in fact, equivalent, one implication is that the limey argillite member in the south fork of Hanaupah Canyon correlates with Zjm in Trail Canyon. C isotope data from these locations (Figs. 5 and 15) are consistent with this interpretation:  $\delta^{13}\text{C}_{\text{PDB}}$  of carbonate from the limey argillite member range from -10.5‰ at the base to approximately -5‰ at

the top, while in the TC4 section,  $\delta^{13}\text{C}_{\text{PDB}}$  reaches a nadir of -10.9‰ near the base of Zjm and increases to -4‰ at the top, just below the breccia bed. The difference in thickness between these units can probably be attributed to accumulation rate, which seems to have been significantly greater near Hanaupah Canyon than at Trail Canyon.

Assuming that transport of the gravity flow was roughly north-south, a minimum run out distance of ~22 km is suggested by our field observations, spanning from the north fork of Hanaupah Canyon in the south to Blackwater Wash in the north (Fig. 2). The stratigraphic relationship between the breccia bed and the overlying Stirling Quartzite provides strong evidence that the Johnnie-Stirling contact is a sequence boundary. In the southern Panamint Range and to the southeast of Death Valley, this sequence boundary is a disconformity at the Johnnie-Stirling contact, while in more basinal locations such as Trail Canyon and the Funeral Mtns. it is either a slight disconformity or a correlative conformity. Assuming further that the base of the Stirling Quartzite is isochronous, we can estimate the slope on which the breccia bed was deposited from the along-strike distance between the south fork of Hanaupah Canyon, where the base-of-Stirling unconformity has just eroded through the breccia bed, to the north end of Trail Canyon (location TC4), where 280 m of Zju is present between the breccia bed and the overlying unconformity (Fig. 19). This distance is ~17 km, from which we estimate a northward-dipping slope of approximately 1 degree.

The significance of the 100 m-thick carbonate bed in the north fork of Hanaupah Canyon (Fig. 7) is still a matter of some uncertainty. As described above, this bed has a carbonate

breccia at its base (Fig. 8A), is also brecciated at the top, and forms a discontinuous outcrop that pinches out to the north and south. Based on these observations it is tempting to conclude that it is a giant olistolith, some 2.5 km in length, located in an up-dip position within the breccia bed. Geochemical data from the bed are inconclusive on this matter:  $\delta^{13}\text{C}$  values are entirely heavier than in the limey argillite member in the south fork of Hanaupah Canyon, located only a short distance to the south, and are actually somewhat similar to those from the middle part of the Noonday Dolomite (Pettersen et al., 2007). On the other hand, the slightly positive values from the upper part of the bed are similar to those found in the uppermost Johnnie Fm. near Indian Pass (Fig. 17A), suggesting that the bed could be autochthonous. Regardless, we consider the brecciated upper portion of this bed and the sharp contact with the overlying Stirling Quartzite to be convincing evidence for an unconformity at the top of the unit and note that its thickness may have originally been greater but was eroded prior to deposition of the Stirling Quartzite.

#### **Record of the Shuram anomaly in the Death Valley region**

C isotope data from the Winters Pass Hills (Corsetti and Kaufman, 2003), where the Rainstorm Member is 80 m thick (Stewart, 1970), have been used to correlate the upper Johnnie Fm. with strata in Oman, China, and Australia (Halverson et al., 2005, Fike et al., 2006). In light of the evidence for a sequence boundary at the Johnnie-Stirling contact, it is reasonably clear that only the earliest part of the Shuram anomaly is preserved in the Winters Pass Hills. As one progresses from southeast to northwest across the Death Valley region, a greater proportion of the Shuram anomaly is preserved beneath the

unconformity at the Johnnie-Stirling contact, as illustrated by increasingly heavy  $\delta^{13}\text{C}$  values from the uppermost Johnnie Fm. In the Winters Pass Hills, the Rainstorm Member reaches values no heavier than -9.2‰ beneath the contact with the Stirling Quartzite (Corsetti and Kaufman, 2003). In Johnson Canyon, the heaviest values near the top of the Johnnie Fm. are -7.3‰. In the south fork of Hanaupah Canyon, they become as heavy as -5.2‰. In Trail Canyon, they are -2.3‰. Finally, near Indian Pass, the top of the Johnnie Fm. records  $\delta^{13}\text{C}_{\text{PDB}}$  values of 0 to 1.5‰ (Figs. 1 and 18). Data from the Johnnie Fm. in Trail Canyon and near Indian Pass thus suggest that  $\delta^{13}\text{C}_{\text{PDB}}$  of carbonate returned to values at or near 0‰ prior to deposition of the Stirling Quartzite, a conclusion which is supported by some slightly positive  $\delta^{13}\text{C}$  values from the Stirling A member in the Indian Pass and Lees Camp areas of the Funeral Mtns. If one assumes relatively isochronous deposition of individual members of the Stirling Quartzite across the Death Valley region, negative values from the Stirling C and D members documented in this paper and by Corsetti and Hagadorn (2000) and Corsetti and Kaufman (2003) suggest that an additional negative isotope excursion occurred during deposition of the lower part of the Stirling Quartzite.

Our data from Zju at location TC4 indicates that following the recovery of  $\delta^{13}\text{C}_{\text{PDB}}$  to about -4‰ during deposition of Zjm, values decreased to about -6 to -7‰ at the base of Zju, just above the breccia bed, and recovered to at least -2.3‰ in overlying Zju sediments. This spike does not seem to have been recognized in any other sections worldwide, and unfortunately the evidence for it in the Panamint Range is quite limited due to the lack of carbonate in Zju. At location TC2, two dolostone beds in the upper

part of Zjm have carbonate  $\delta^{13}\text{C}_{\text{PDB}}$  of -4.6 and -2.1‰, providing additional evidence of recovery to relatively heavy values prior to emplacement of the breccia bed. Some corroborating evidence for an additional recovery prior to deposition of the Stirling Quartzite is provided by  $\delta^{13}\text{C}_{\text{PDB}}$  values of 2.6 to 2.9‰ in samples of a thin limestone bed deposited within incised channels at the Johnnie-Stirling contact in the southern Nopah Range (Corsetti and Kaufman, 2003). These values, which postdate the Johnnie oolite and predate the Stirling Quartzite, suggest that the recovery of the Shuram anomaly to positive values ended before deposition of the Stirling Quartzite. In the following section we discuss the only other known section with clear evidence for an unconformity at a similar stratigraphic position.

### **Comparison with the Wonoka Formation, South Australia**

The Shuram anomaly has also been identified in the Wonoka Fm. in the Adelaide Geosyncline of South Australia (Calver, 2000). In this area, incised valleys, up to ~1 km deep, were eroded into the lower Wonoka Fm. and underlying strata and were subsequently filled prior to deposition of the overlying Bonney Sandstone (e.g., von der Borch, 1982). Whether the incision and filling of these canyons required subaerial exposure has been the matter of some debate (e.g., von der Borch et al., 1989), as have the origin of the canyons. Explanations for canyon incision include lowering of sea-level in a restricted basin due to evaporation (e.g., Christie-Blick et al., 1990) and uplift related to a mantle plume (Williams and Gostin, 2000).

C isotope data from Calver (2000) can be utilized to investigate the relative timing of incision and filling of the Wonoka canyons. In the central part of the Flinders Ranges in South Australia, where there is no evidence of canyon incision,  $\delta^{13}\text{C}_{\text{PDB}}$  of carbonate is slightly less than 0‰ at the base of the Wonoka Fm., decreases rapidly to a nadir of -11.2‰ 90 m up section, and then recovers back to 0‰ near the top of the formation (Fig. 20, Calver, 2000). This overall pattern is very similar to that recognized in the Shuram and Buah Fms. in Oman (Fike et al., 2006). The stratigraphic position of the unconformity that correlates with the base of the canyons has been estimated to be at one of two levels within this section (Fig. 20, Christie-Blick et al., 1990, Christie-Blick et al., 1995). Importantly, if either of these correlations is correct, it implies that the most negative values of the Shuram anomaly preceded the incision of the Wonoka Canyons and  $\delta^{13}\text{C}_{\text{PDB}}$  of carbonate subsequently recovered to at least -8‰ before incision of the canyons. In the northern part of the Flinders Ranges, where the Wonoka canyons are developed,  $\delta^{13}\text{C}_{\text{PDB}}$  of carbonate ranges from -6.7 to -8.2‰ in the lower ~1100 m of canyon fill (Fig. 20, Calver, 2000).

Comparison of C isotope data from the Wonoka Fm. with our new data from the Panamint Range illustrates an interesting possible correlation.  $\delta^{13}\text{C}_{\text{PDB}}$  of carbonate at the top of the limey argillite member in the south fork of Hanaupah Canyon reaches values as heavy as -5.2‰ beneath the contact with the Stirling Quartzite (Fig. 5). As outlined above, our mapping suggests that the top of this member is equivalent to the top of Zjm in Trail Canyon, which reaches values as heavy as about -4‰.  $\delta^{13}\text{C}_{\text{PDB}}$  values from the base of Zju are -6.5 to -7.2‰ (Fig. 15), comparable to values from the fill within

the Wonoka Canyons. We note that based on available data, it is possible that the unconformity and breccia bed within the Rainstorm Member identified during this study correlate with the unconformity marking the base of the Wonoka canyons. In this scenario, Zjm preserves a slightly later record of C isotope compositions than has been measured below the sub-canyon unconformity in the Wonoka Fm., while the bottom part of Zju and the base of the canyon fill are at least roughly isochronous.

## REFERENCES

- Abolins, M.J., 1999, I. Stratigraphic constraints on the number of discrete Neoproterozoic glaciations and the relationship between glaciation and Ediacaran evolution. II. The Kwichup Spring thrust in the northwestern Spring Mountains, Nevada: implications for large-magnitude extension and the structure of the Cordilleran thrust belt [Ph.D. thesis]: Pasadena, California Institute of Technology, 340 p.
- Abolins, M., Oskin, R., Prave, T., Summa, C., and Corsetti, F., 2000, Neoproterozoic glacial record in the Death Valley region, California and Nevada, *in* Lageson, D.R., Peters, S.G., and Lahren, M.M., eds., Great Basin and Sierra Nevada: Boulder, Geological Society of America Field Guide 2, p. 319-335.
- Albee, A.L., Labotka, T.C., Lanphere, M.A., and McDowell, S.D., 1981, Geologic map of the Telescope Peak quadrangle, California: U.S. Geological Survey Geologic Quadrangle Map GQ-1532, scale 1:62,500, 1 sheet.

Barnes, H., Christiansen, R.L., and Byers, F.M. Jr., 1965, Geologic map of the Jangle Ridge quadrangle, Nye and Lincoln Counties, Nevada: U.S. Geological Survey Geologic Quadrangle Map GQ-363, scale 1:24,000, 1 sheet.

Benmore, W.C., 1978, Stratigraphy, sedimentology, and paleoecology of the late Paleophytic or earliest Phanerozoic Johnnie Formation, eastern California and southwestern Nevada [Ph.D. thesis]: Santa Barbara, University of California, 243 p.

Bond, G.C., Christie-Blick, N., Kominz, M.A., and Devlin, W.J., 1985, An early Cambrian rift to post-rift transition in the Cordillera of western North America: *Nature*, v. 315, p. 742-746.

Bowring, S.A., Myrow, P.M., Landing, E., Ramezani, J., and Grotzinger, J.P., 2003, Geochronological constraints on terminal Neoproterozoic events and the and the rise of metazoans: *Geophysical Research Abstracts*, 5, 13219.

Calver, C.R., 2000, Isotope stratigraphy of the Ediacarian (Neoproterozoic III) of the Adelaide Rift Complex, Australia, and the overprint of water column stratification: *Precambrian Research*, v. 100, p. 121-150.

Calver, C.R., and Lindsay, J.F., 1998, Ediacarian sequence and isotope stratigraphy of the Officer Basin, South Australia, *Australian Journal of Earth Sciences*, v. 45, p. 513-532.

Christie-Blick, N., Dyson, I.A., and von der Borch, C.C., 1995, Sequence stratigraphy and the interpretation of Neoproterozoic earth history: *Precambrian Research*, v. 73, p. 3-26.

Christie-Blick, N., and Levy, M., 1989, Stratigraphic and tectonic framework of upper Proterozoic and Cambrian rocks in the western United States, *in* Christie-Blick, N., and Levy, M., eds., *Late Proterozoic and Cambrian tectonics, sedimentation, and record of Metazoan radiation in the western United States*: Washington, D.C., American Geophysical Union, Field Trip Guidebook T331, p. 7-21.

Christie-Blick, N., von der Borch, C.C., and DiBona, P.A., 1990, Working hypotheses for the origin of the Wonoka Canyons (Neoproterozoic), South Australia: *American Journal of Science*, v. 290A, p. 295-323.

Clapham, M.E., and Corsetti, F.A., 2005, Deep valley incision in the terminal Neoproterozoic (Ediacaran) Johnnie Formation, eastern California, USA: tectonically or glacially driven?: *Precambrian Research*, v. 141, p. 154-164.

Cloud, P., Wright, L.A., Williams, E.G., Diehl, P., and Walter, M.R., 1974, Giant stromatolites and associated vertical tubes from the upper Proterozoic Noonday Dolomite, Death Valley region, eastern California: *Geological Society of America Bulletin*, v. 85, p. 1869-1882.

Condon, D., Zhu, M., Bowring, S., Wang, W., Yang, A., and Jin, Y., 2005, U-Pb ages from the Neoproterozoic Doushantuo Formation, China: *Science*, v. 308, p. 95-98.

Corsetti, F.A., and Hagadorn, J.W., 2000, Precambrian-Cambrian transition: Death Valley, United States: *Geology*, v. 28, p. 299-302.

Corsetti, F.A., and Kaufman, A.J., 2003, Stratigraphic investigations of carbon isotope anomalies and Neoproterozoic ice ages in Death Valley, California: *Geological Society of America Bulletin*, v. 115, p. 916-932.

Corsetti, F.A., Lorentz, N.J., and Pruss, S.B., 2004, Formerly-aragonite seafloor fans from Neoproterozoic strata, Death Valley and southeastern Idaho, United States: implications for “cap carbonate” formation and snowball Earth, *in* Jenkins, G.S., et al., eds., *The Extreme Proterozoic: Geology, Geochemistry, and Climate*. American Geophysical Union Geophysical Monograph Series, v. 146, Washington, DC, p. 33–44.

Eickhoff, K.-H., von der Borch, C.C., and Grady, A.E., 1988, Proterozoic canyons of the Flinders Ranges (South Australia): submarine canyons or drowned river valleys?: *Sedimentary Geology*, v. 58, p. 217-235.

Fike, D.A., Grotzinger, J.P., Pratt, L.M., and Summons, R.E., 2006, Oxidation of the Ediacaran ocean: *Nature*, v. 444, p. 744-747.

Halverson, G.P., Hoffman, P.F., Schrag, D.P., Maloof, A.C., and Rice, A.H.N., 2005, Toward a Neoproterozoic composite carbon-isotope record: Geological Society of America Bulletin, v. 117, p. 1181-1207.

Harding, M.B., 1987, The geology of the Wildrose Peak area, Panamint Mountains, California [Ph.D. thesis]: Laramie, University of Wyoming, 207 p.

Heaman, L.M., and Grotzinger, J.P., 1992, 1.08 Ga diabase sills in the Pahrump Group, California: implications for development of the Cordilleran miogeocline: Geology, v. 20, p. 637-640.

Hodges, K.V., Walker, J.D., and Wernicke, B.P., 1987, Footwall structural evolution of the Tucki Mountain detachment system, Death Valley region, southeastern California, *in* Coward, M.P., et al., eds., Continental Extensional Tectonics: Oxford, Geological Society Special Publication No. 28, p. 393-408

Hodges, K.V., McKenna, L.W., and Harding, M.B., 1990, Structural unroofing of the central Panamint Mountains, Death Valley region, southeastern California, *in* Wernicke, B.P., ed., Basin and Range extensional tectonics near the latitude of Las Vegas, Nevada: Geological Society of America Memoir 176, Boulder, p. 377-390.

Hoffman, P.F., 1991, Did the breakout of Laurentia turn Gondwanaland inside-out?: Science, v. 252, p. 1409-1412.

Hoffman, P.F., Kaufman, A.J., Halverson, G.P., and Schrag, D.P., 1998, A Neoproterozoic snowball Earth: *Science*, v. 281, p. 1342-1346.

Hoffmann, K.-H., Condon, D.J., Bowring, S.A., and Crowley, J.L., 2004, U-Pb zircon date from the Neoproterozoic Ghaub Formation, Namibia: constraints on Marinoan glaciation: *Geology*, v. 32, p. 817-820.

Hunt, C.B., and Mabey, D.R., 1966, Stratigraphy and structure, Death Valley, California: U.S. Geological Survey Professional Paper 494-A, 162 p.

Kaufman, A.J., Corsetti, F.A., and Varni, M.A., 2007, The effect of rising atmospheric oxygen on carbon and sulfur isotope anomalies in the Neoproterozoic Johnnie Formation, Death Valley, USA: *Chemical Geology*, v. 237, p. 47-63.

Kennedy, M.J., Runnegar, B., Prave, A.R., Hoffmann, K.-H., and Arthur, M.A., 1998, Two or four Neoproterozoic glaciations?: *Geology*, v. 26, p. 1059-1063

Krause, F.F., and Oldershaw, A.E., 1979, Submarine carbonate breccia beds-a depositional model for two-layer sediment gravity flows from the Sekwi Formation (Lower Cambrian), Mackenzie Mountains, Northwest Territories, Canada: *Canadian Journal of Earth Sciences*, v. 16, p. 189-199.

Le Guerroué, E., Allen, P.A., Cozzi, A., Etienne, J.L., and Fanning, M., 2006, 50 Myr recovery from the largest negative  $\delta^{13}\text{C}$  excursion in the Ediacaran ocean: *Terra Nova*, v. 18, p. 147-153.

McDowell, S.D., 1967, The intrusive history of the Little Chief granite porphyry stock, central Panamint Range, California: I. Structural relationships. II. Petrogenesis, based on electron microprobe analyses of the feldspars [Ph.D. thesis]: Pasadena, California Institute of Technology, 282 p.

McFadden, K.A., Huang, J., Chu, X., Jiang, G., Kaufman, A.J., Zhou, C., Yuan, X., and Xiao, S., 2008, Pulsed oxidation and biological evolution in the Ediacaran Doushantuo Formation: *Proceedings of the National Academy of Sciences*, v. 105, p. 3197-3202.

Nolan, T.B., 1929, Notes on the stratigraphy and structure of the northwest portion of Spring Mountain, Nevada: *American Journal of Science*, v. 17, p. 461-472.

Petterson, R., Prave, A., Wernicke, B., and Fallick, A.E., 2007, New stratigraphic and isotopic constraints on the Cryogenian-Ediacaran strata of Death Valley region, *Geological Society of America Abstracts with Programs*, v. 39, no. 6, p. 222.

Prave, A.R., 1999, Two diamictites, two cap carbonates, two  $\delta^{13}\text{C}$  excursions, two rifts: the Neoproterozoic Kingston Peak Formation, Death Valley, California: *Geology*, v. 27, p. 339-342.

Rothman, D.H., Hayes, J.M., and Summons R.E., 2003, Dynamics of the Neoproterozoic carbon cycle: Proceedings of the National Academy of Sciences, v. 100, p. 8124-8129.

Stewart, J.H., 1966, Correlation of lower Cambrian and some Precambrian strata in the southern Great Basin, California and Nevada: U.S. Geological Survey Professional Paper 550C, p. C66-C72.

Stewart, J.H., 1970, Upper Precambrian and lower Cambrian strata in the southern Great Basin, California and Nevada: U.S. Geological Survey Professional Paper 620, 206 p.

Stewart, J.H., 1972, Initial deposits in the Cordilleran geosyncline: evidence of a late Precambrian (<850 m.y.) continental separation: Geological Society of America Bulletin, v. 83, p. 1345-1360.

Summa, C.L., 1993, Sedimentologic, stratigraphic, and tectonic controls of a mixed carbonate-siliciclastic succession: Neoproterozoic Johnnie Formation, southeast California [Ph.D. thesis]: Cambridge, Massachusetts Institute of Technology, 332 p.

Sumner, D.Y., and Grotzinger, J.P., 1993, Numerical modeling of ooid size and the problem of Neoproterozoic giant ooids: Journal of Sedimentary Petrology, v. 63, p. 974-982.

von der Borch, C.C., Grady, A.E., Eickhoff, K.H., Dibona, P., and Christie-Blick, N., 1989, Late Proterozoic Patsy Springs Canyon, Adelaide geosyncline: submarine or subaerial origin?: *Sedimentology*, v. 36, p. 777-792.

von der Borch, C.C., Smit, R., and Grady, A.E., 1982, Late Proterozoic submarine canyons of Adelaide geosyncline, South Australia: *American Association of Petroleum Geologists Bulletin*, v. 66, p. 332-347.

Walker, J.D., Klepacki, D.W., and Burchfiel, B.C., 1986, Late Precambrian tectonism in the Kingston Range, southern California: *Geology*, v. 14, p. 15-18.

Wernicke, B.P., Walker, J.D., and Hodges, K.V., 1988, Field guide to the northern part of the Tucki Mountain fault system, Death Valley region, California, *in* Weide, D.L., and Faber, M.L., eds., *This extended land, geological journeys in the southern Basin and Range*, Geological Society of America Cordilleran Section Field Trip Guidebook, p. 58-63.

Williams, G.E., and Gostin, V.A., 2000, Mantle plume uplift in the sedimentary record: origin of kilometre-deep canyons within late Neoproterozoic successions, South Australia: *Journal of the Geological Society, London*, v. 157, p. 759-768.

Wright, L.A., and Troxel, B.W., 1993, Geologic map of the central and northern Funeral Mountains and adjacent areas, Death Valley region, southern California: U.S. Geological Survey, Miscellaneous Investigations Series Map I-2305, scale 1:24,000, 1 sheet.

**FIGURE CAPTIONS**

**Figure 1.** Shaded relief map of part of the southern Great Basin showing locations mentioned in text and thickness (in feet) of the Rainstorm Member of the Johnnie Fm. Isopachs from Stewart (1970).

**Figure 2.** Shaded relief map of the Panamint Range showing study locations, Miocene detachment faults, and location of the Johnnie Fm. Sources of mapping: Hunt and Mabey (1966), McDowell (1967), Albee et al. (1981), Harding (1987), this study, and unpublished mapping from R. Petterson, C. Verdel, and B. Wernicke. Fault locations from Hodges et al. (1990). Abbreviations: EF-Emigrant Fault, HF-Harrisburg Fault.

**Figure 3.** Generalized Proterozoic to earliest Cambrian stratigraphy of the Death Valley region.

**Figure 4.** Photographs from Johnson Canyon and the south fork of Hanaupah Canyon. (A) Breccia at the base of the Johnnie oolite, Johnson Canyon. (B) Breccia at the top of the Johnnie oolite, Johnson Canyon. (C) Pink limestones above the Johnnie oolite, Johnson Canyon. (D) Edgewise conglomerate in upper Johnnie Fm., south fork of Hanaupah Canyon.

**Figure 5.** C isotope data for the upper Johnnie Fm. from sections measured in Johnson Canyon, Hanaupah Canyon, and near Wildrose Peak. Datum for Johnson Canyon section is within the upper carbonate-bearing member. N. fork Hanaupah Canyon and Wildrose

Peak data are from dolostones in the uppermost Johnnie Fm. Position of the Johnnie oolite in the N. fork of Hanaupah Canyon is approximated from the description of Benmore (1978). Note differences in vertical scales. Abbreviations: jud-Johnnie upper dolostone, Zj-undifferentiated Johnnie Fm., Zju-upper Johnnie Fm., Zsa-A member, Stirling Quartzite.

**Figure 6.** North-looking photograph of upper Johnnie Fm. and lower Stirling Quartzite along the south fork of Hanaupah Canyon. Width of view in the foreground is approximately 1.6 km.

**Figure 7.** Upper Johnnie Fm. dolostone in the N. fork of Hanaupah Canyon. (A) Photograph looking northeast into the N. fork. Dashed line marks the contact between the dolostone and the overlying Stirling Quartzite. Note white marker bed below the dolostone. (B) Photograph looking south at the south wall of the N. fork of Hanaupah Canyon showing the southern termination of the dolostone. Width of view in the middle ground is ~250 m. (C) Sketch illustrating stratigraphic relationships between the dolostone, underlying Johnnie Fm., and overlying Stirling Quartzite. Abbreviations: jud-Johnnie upper dolostone, Zs-Stirling Quartzite, Zj-Johnnie Fm.

**Figure 8.** Photographs of upper Johnnie Fm. carbonates, Hanaupah Canyon to Wildrose Peak. (A) Breccias at base of the dolostone in the N. fork of Hanaupah Canyon. (B) Stromatolites (tubes?) near base of dolostone unit, N. fork of Hanaupah Canyon. (C)

Stromatolites in the upper part of dolostone unit, N. fork Hanaupah Canyon. (D) Giant ooids in upper Johnnie Fm. carbonates, near Wildrose Peak.

**Figure 9.** Geologic map of the Johnnie-Stirling contact near Wildrose Peak.

**Figure 10.** Photograph looking north into Trail Canyon. Detachment fault is probably the continuation of the Harrisburg Fault. Fig. 11 is a geologic map of this area.

Abbreviations: Zn-Noonday Dolomite, Zjl-lower Johnnie Fm., Zjm-middle Johnnie Fm., Zju-upper Johnnie Fm., Zs-Stirling Quartzite, CZw-Wood Canyon Fm., Cz-Zabriskie Quartzite.

**Figure 11.** Geologic map of the Trail Canyon area showing locations of measured sections TC 1 through 6. Contour interval is 50 meters.

**Figure 12.** Johnnie Fm. breccia bed in Blackwater Wash. (A) Photograph looking north at section of Johnnie Fm. and lower Stirling Quartzite. Width of view in foreground is approximately 300 meters. (B) Breccia clast of blue-grey limestone.

**Figure 13.** Giant limestone breccia clasts in Trail Canyon at location TC2. Circle around ~1.8m-tall person for scale.

**Figure 14.** Photographs of the upper Johnnie Fm. in Trail Canyon. (A) Laminated dolostone within breccia bed, near location TC5. (B) Thin-bedded alternations of

siltstone and fine-grained sandstone, interpreted as turbidites, near location TC3. (C) Quartz granules and pebbles in upper Johnnie Fm. (D) Carbonate clasts in siltstone matrix, near base of section measured at location TC3.

**Figure 15.** Carbon isotope data from sections measured in the Trail Canyon area. We interpret carbonates in the TC3 section and upper parts of the TC1 and TC2 sections as allochthonous blocks. Note that vertical scale of TC4 and TC5 sections is different than other sections.

**Figure 16.** Photographs of the lower Johnnie Fm. in Trail Canyon. (A) Limestone clasts in breccia near base of Zjl. (B) Matrix-supported carbonate clasts, same breccia near base of Zjl. (C) Deepening-upward cycles, as indicated by arrows. Circle around rock hammer for scale. (D) Rounded carbonate boulders supported in a silty matrix.

**Figure 17.** Carbon isotope data from sections measured in the Funeral Mtns.

**Figure 18.** Johnnie Fm. carbon isotope data from the Winters Pass Hills, Johnson Canyon, the S. fork of Hanaupah Canyon, and the northern part of the Trail Canyon area. Datum for Winters Pass Hills section is the base of the Noonday Dolomite (Corsetti and Kaufman, 2003). Position of the Johnnie oolite in the N. fork of Hanaupah Canyon is approximated from the description of Benmore (1978). Position of the Johnnie oolite at location TC5 is taken as the oolite bed near the base of the section.

**Figure 19.** Scale drawing of Zjm/Zju/breccia illustrating possible correlation between middle and upper Johnnie Fm. sediments in Hanaupah Canyon and Trail Canyon.

**Figure 20.** Summary of carbon isotope data from the Wonoka Fm., south Australia.

Figure 1

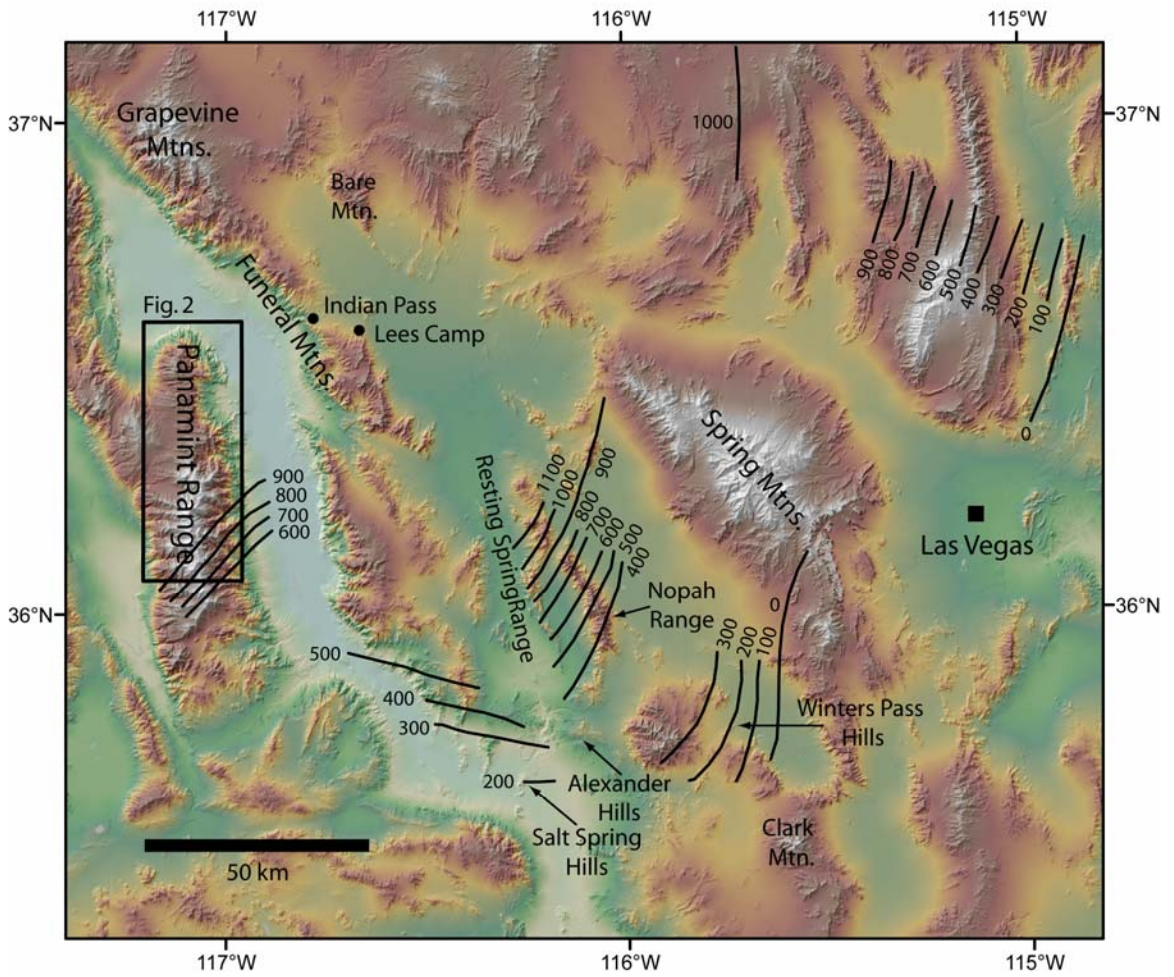


Figure 2

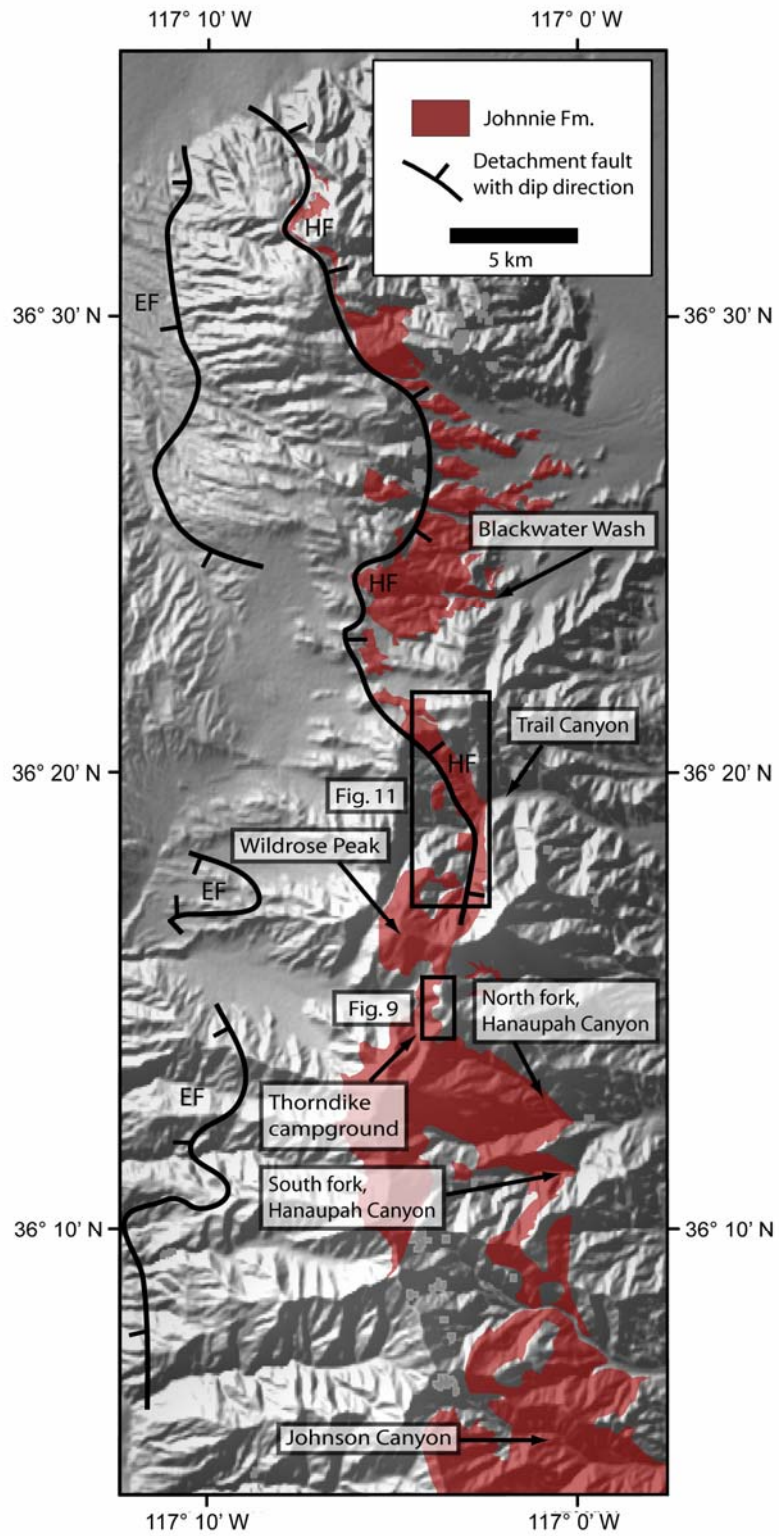


Figure 3

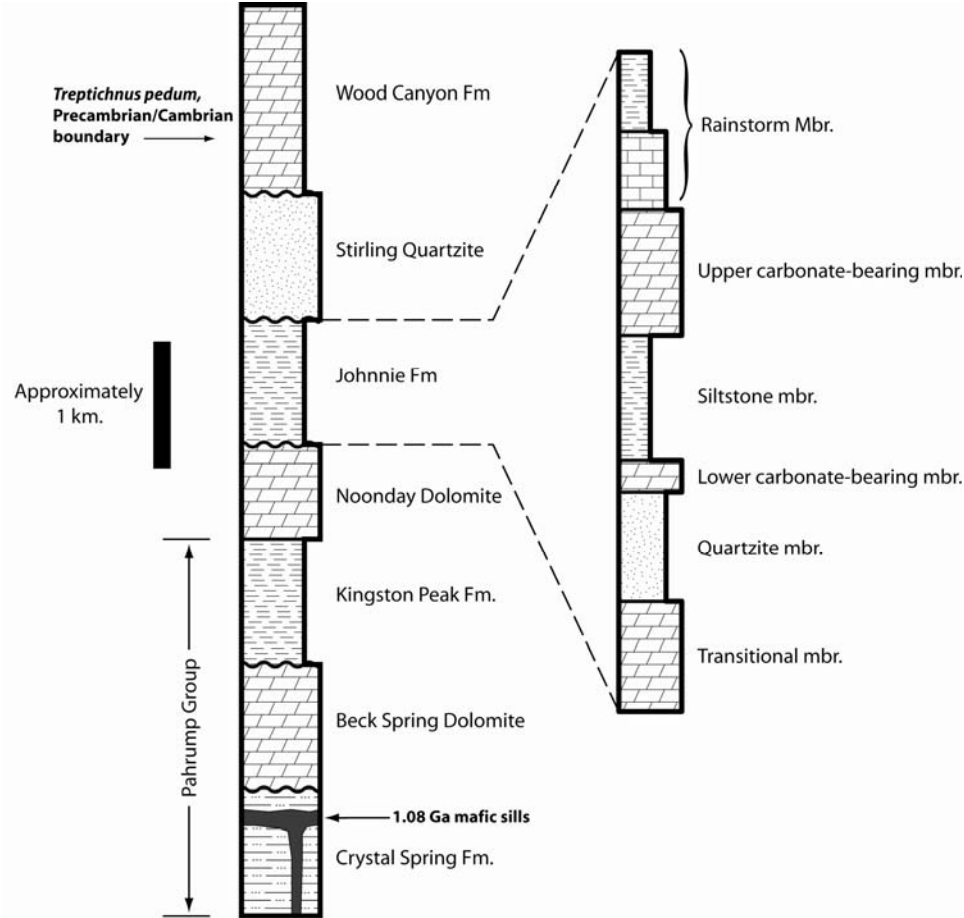


Figure 4

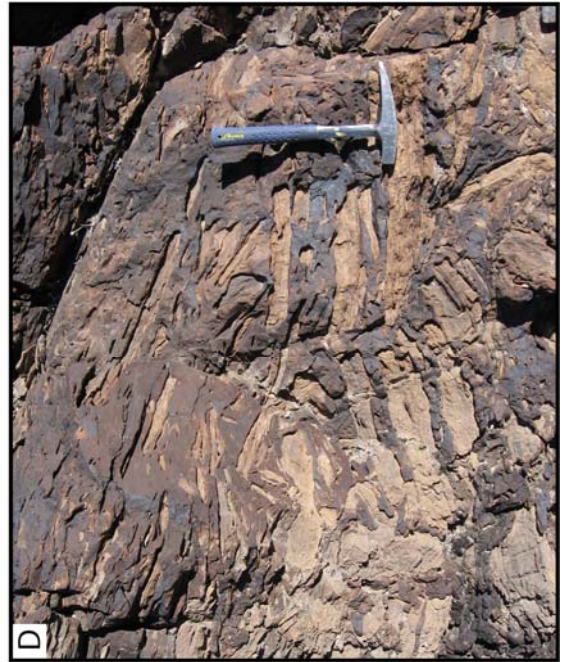
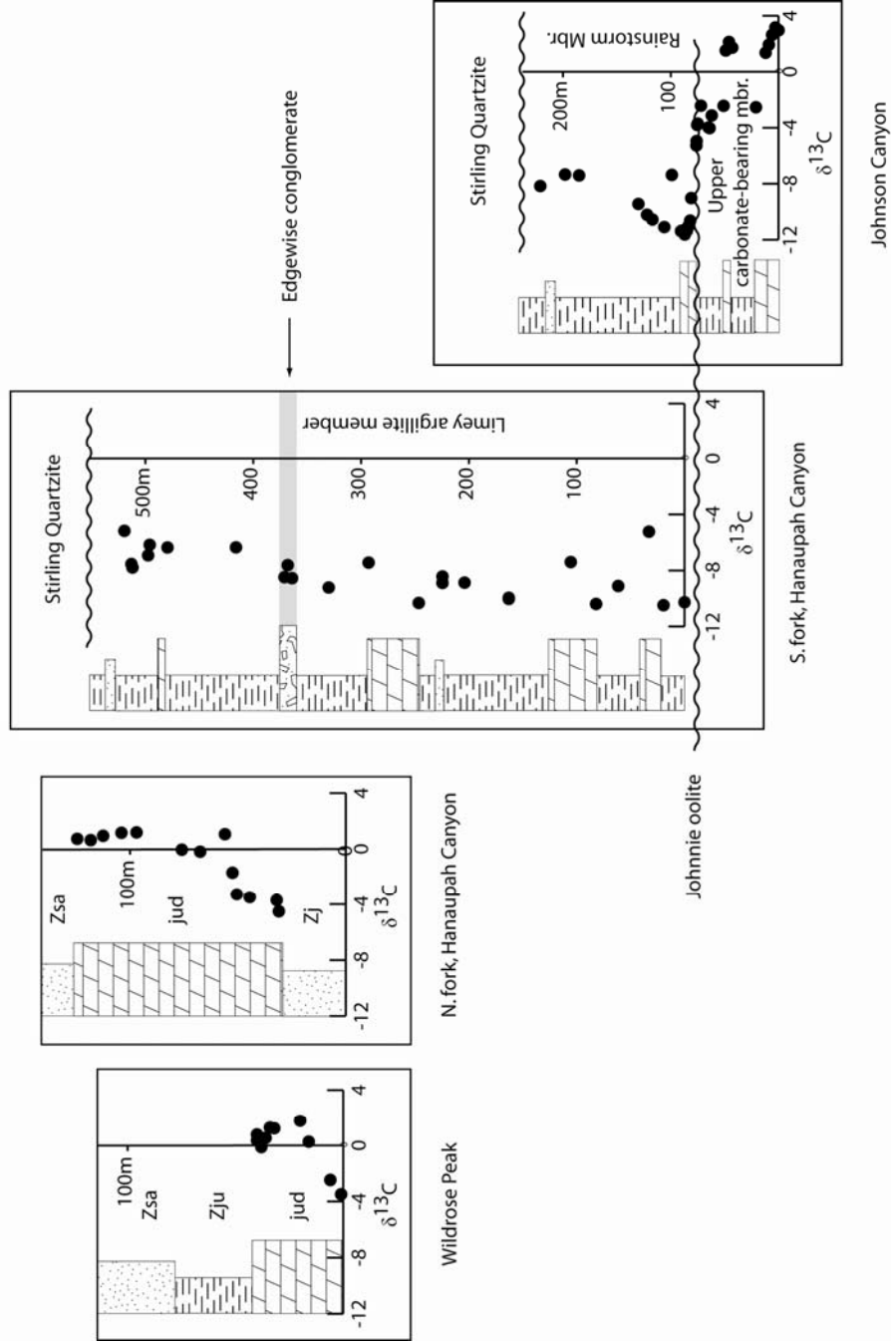


Figure 5



**Figure 6**

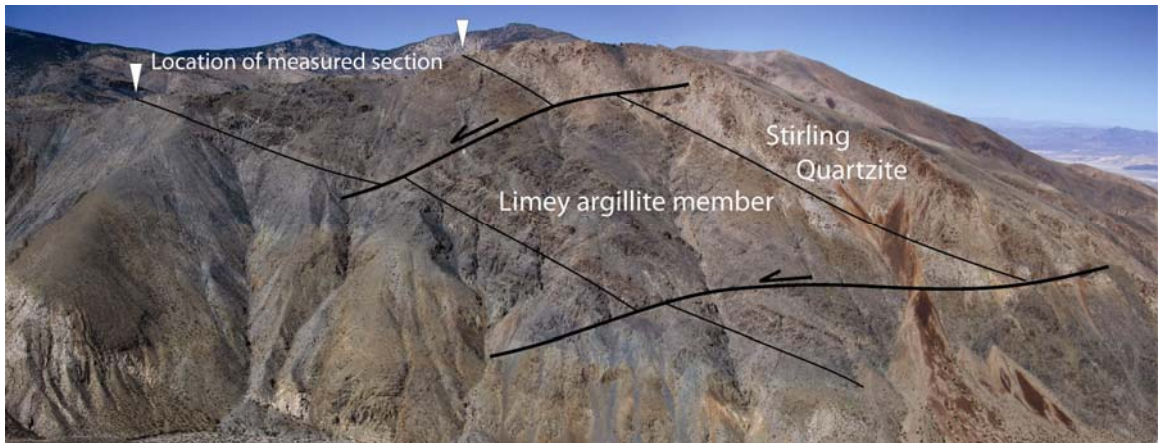


Figure 7

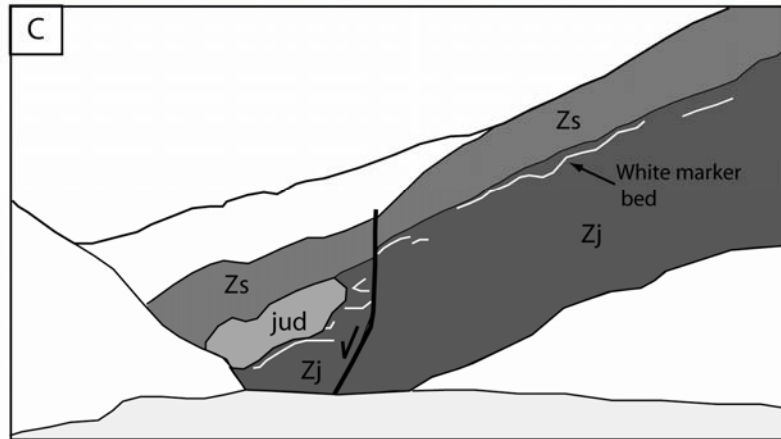
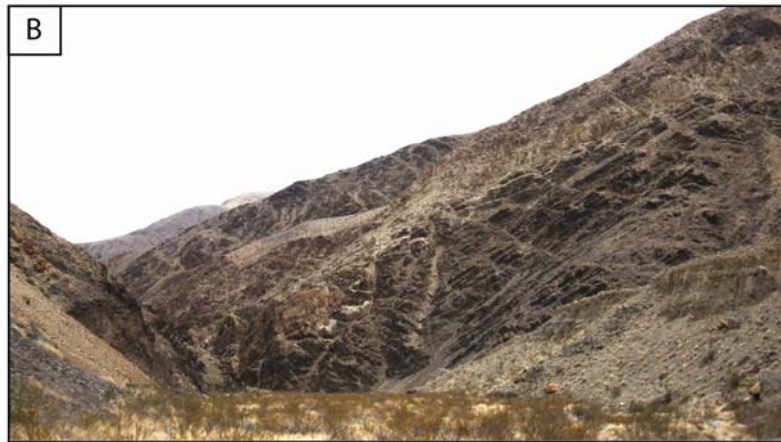
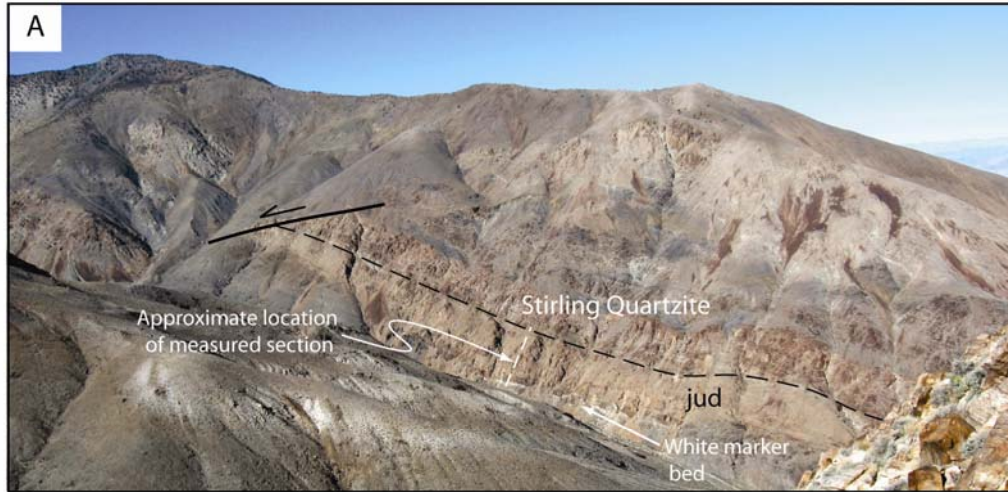


Figure 8

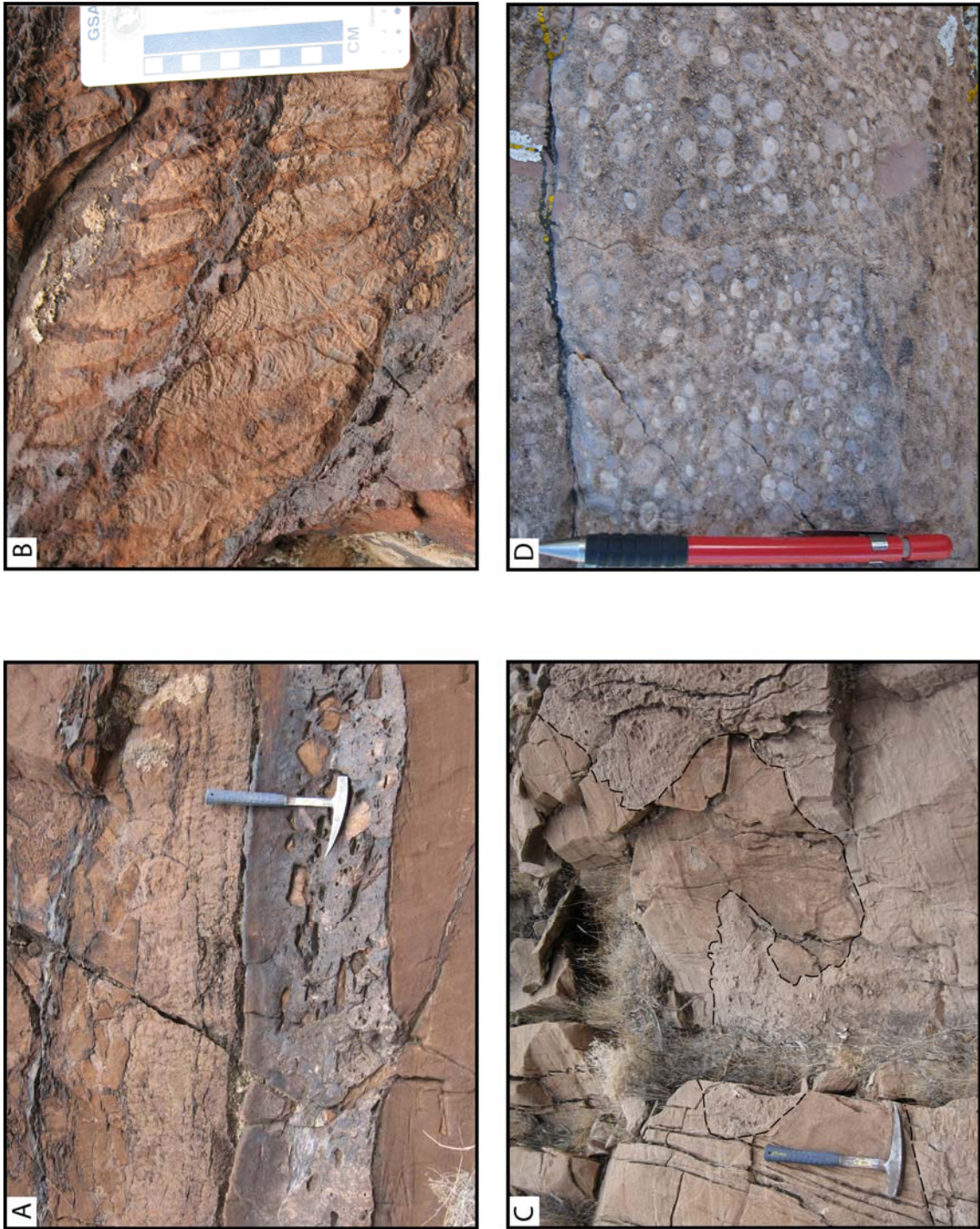


Figure 9

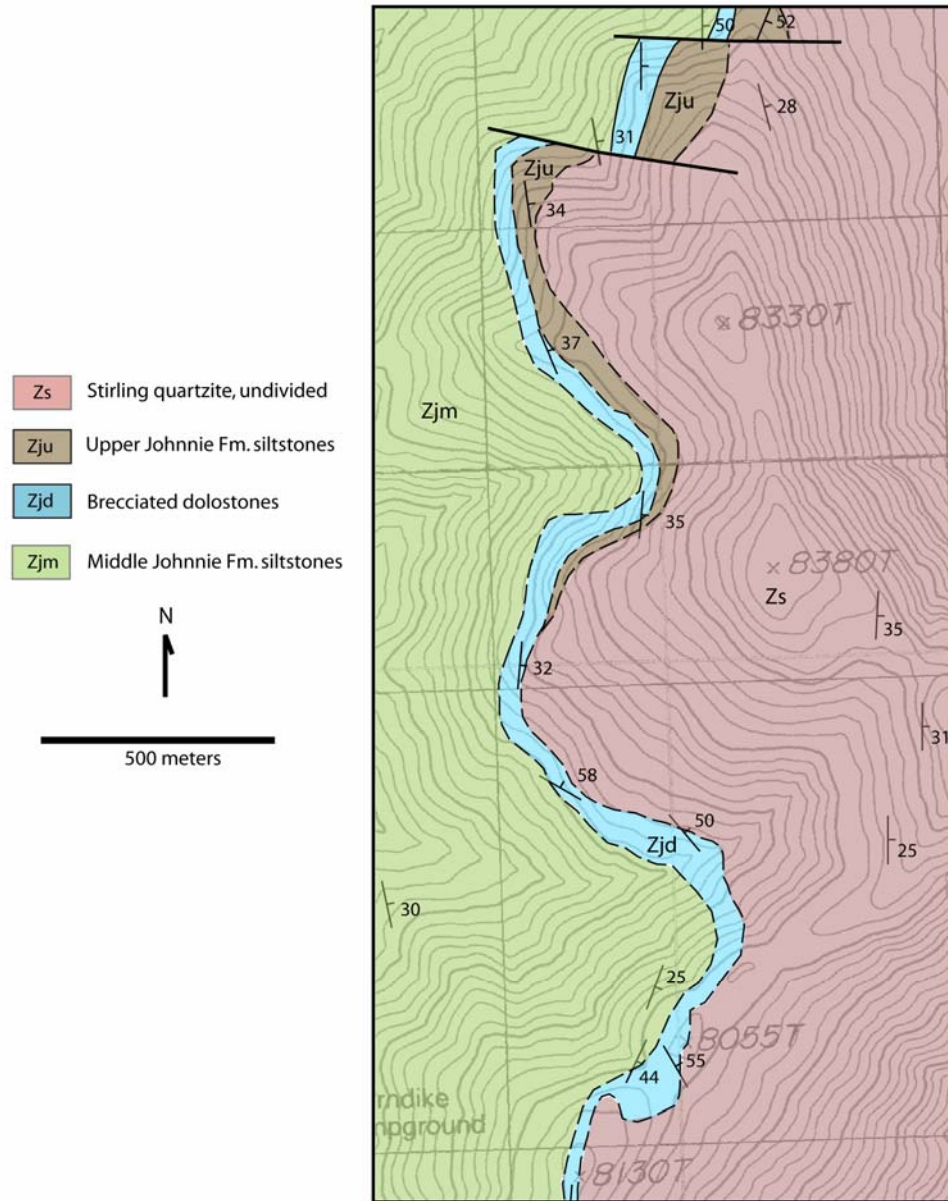


Figure 10

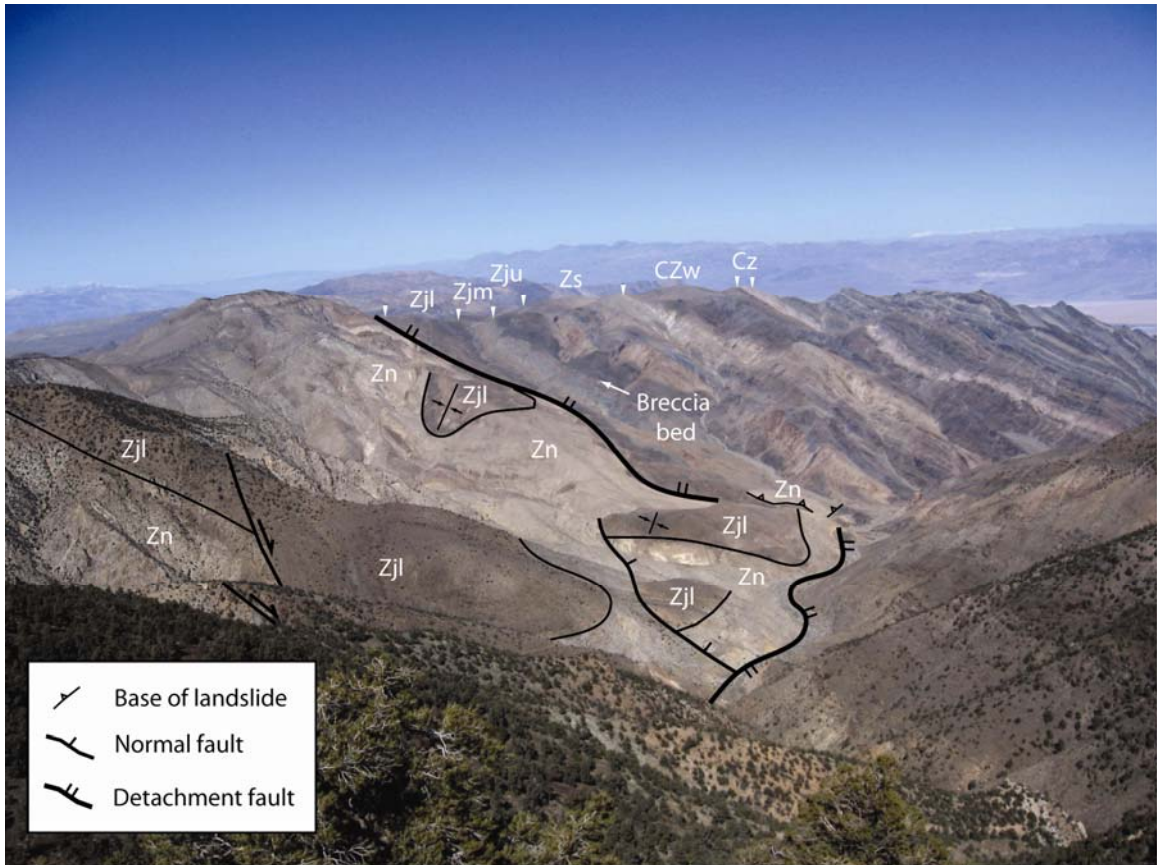


Figure 11

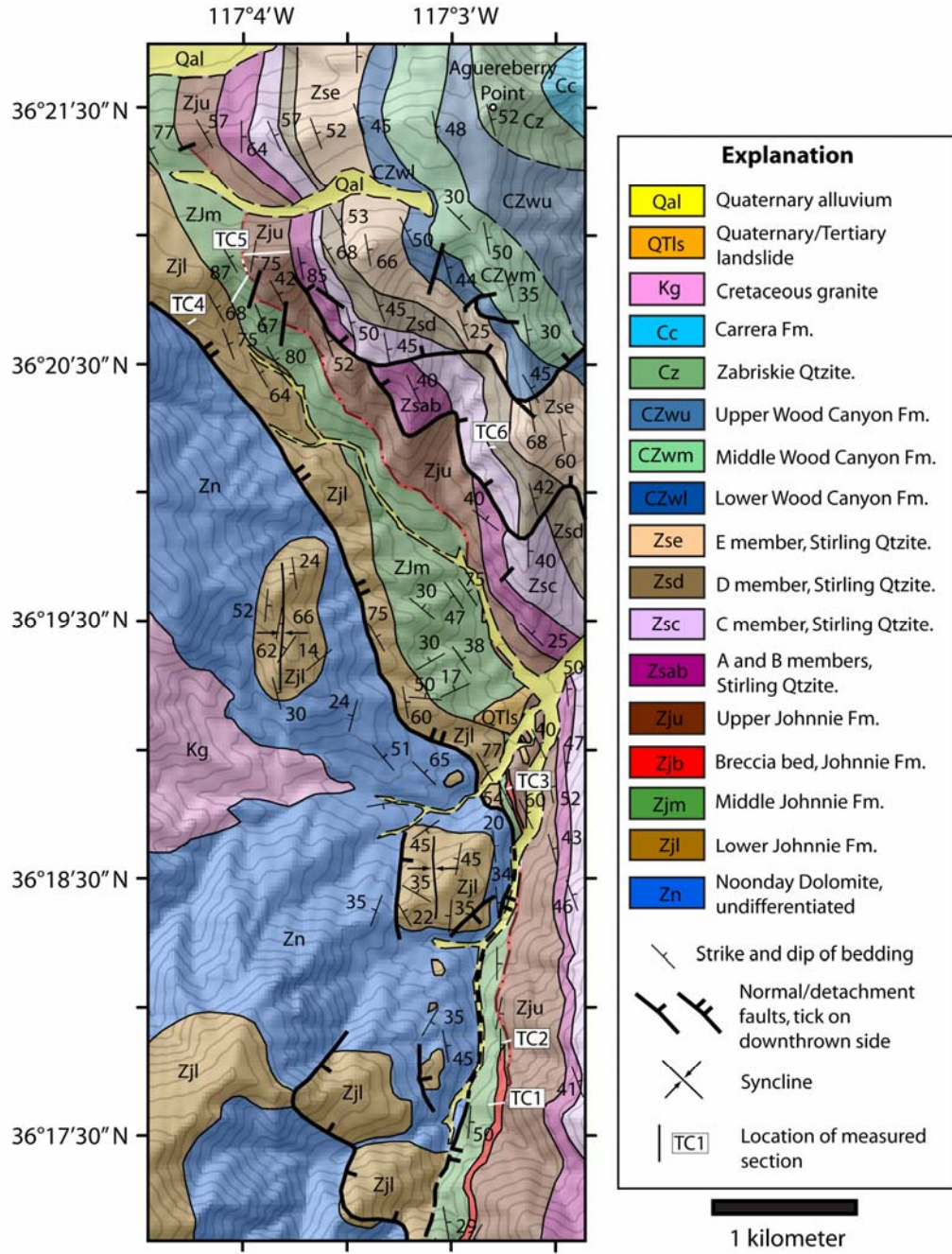
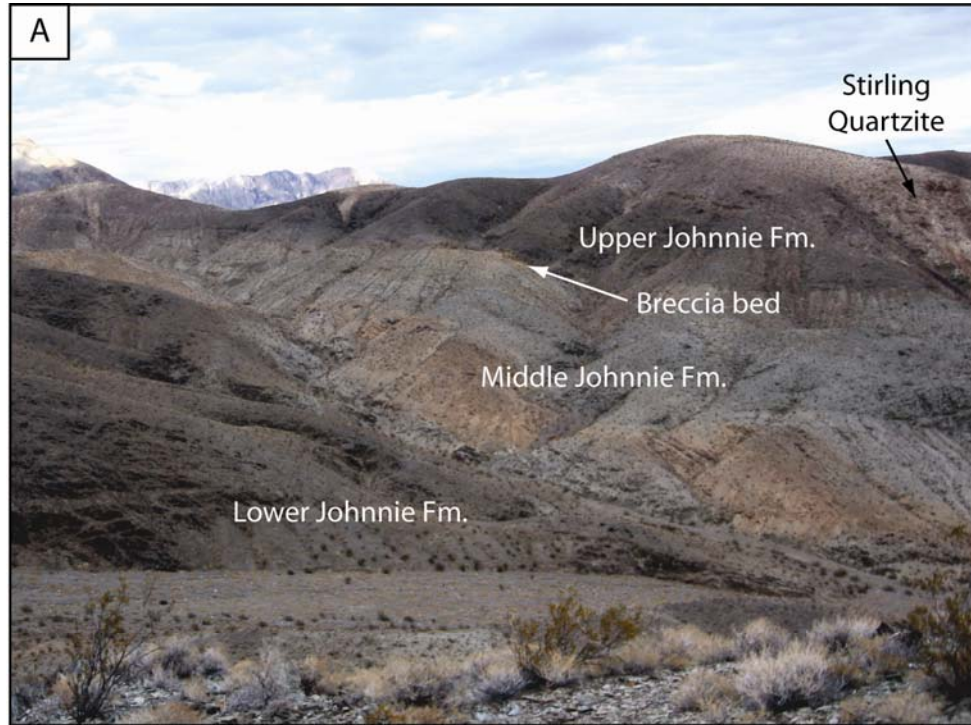


Figure 12



IV-58

**Figure 13**

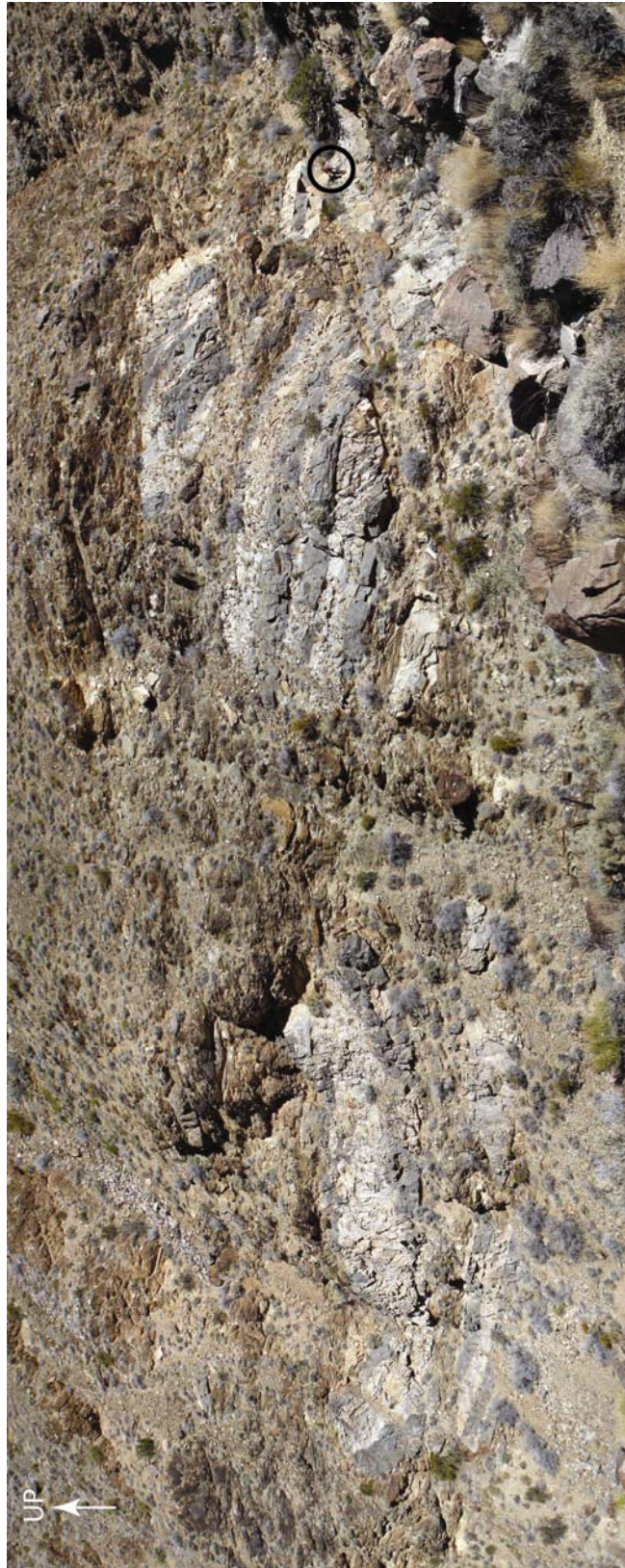


Figure 14

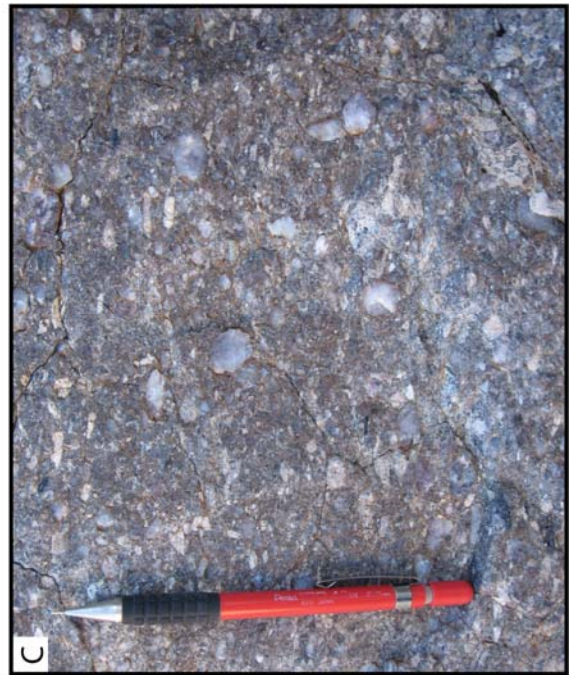
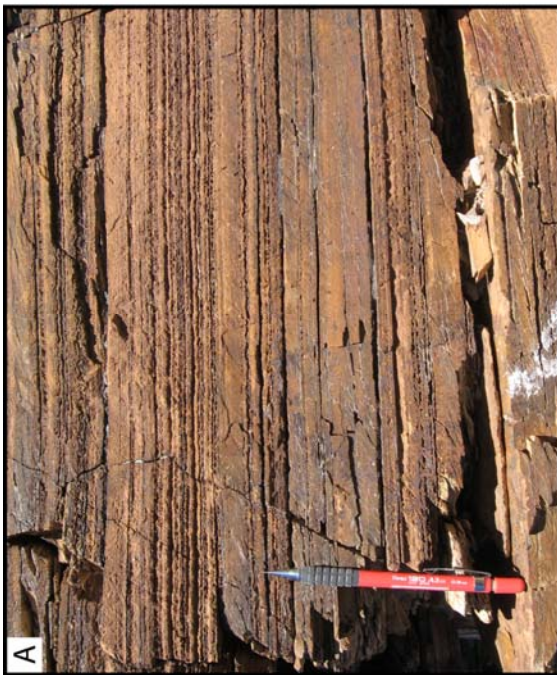


Figure 15

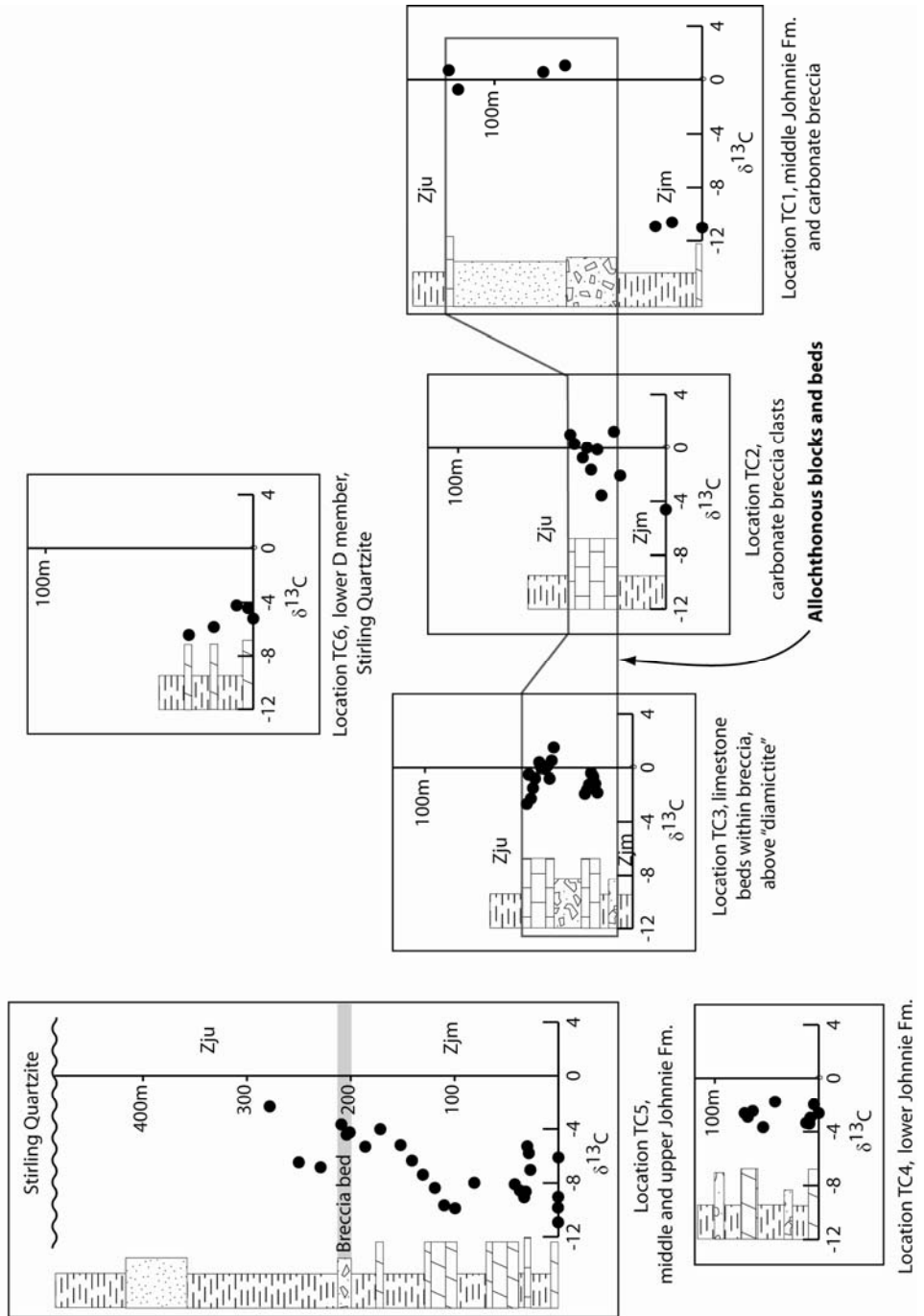


Figure 16

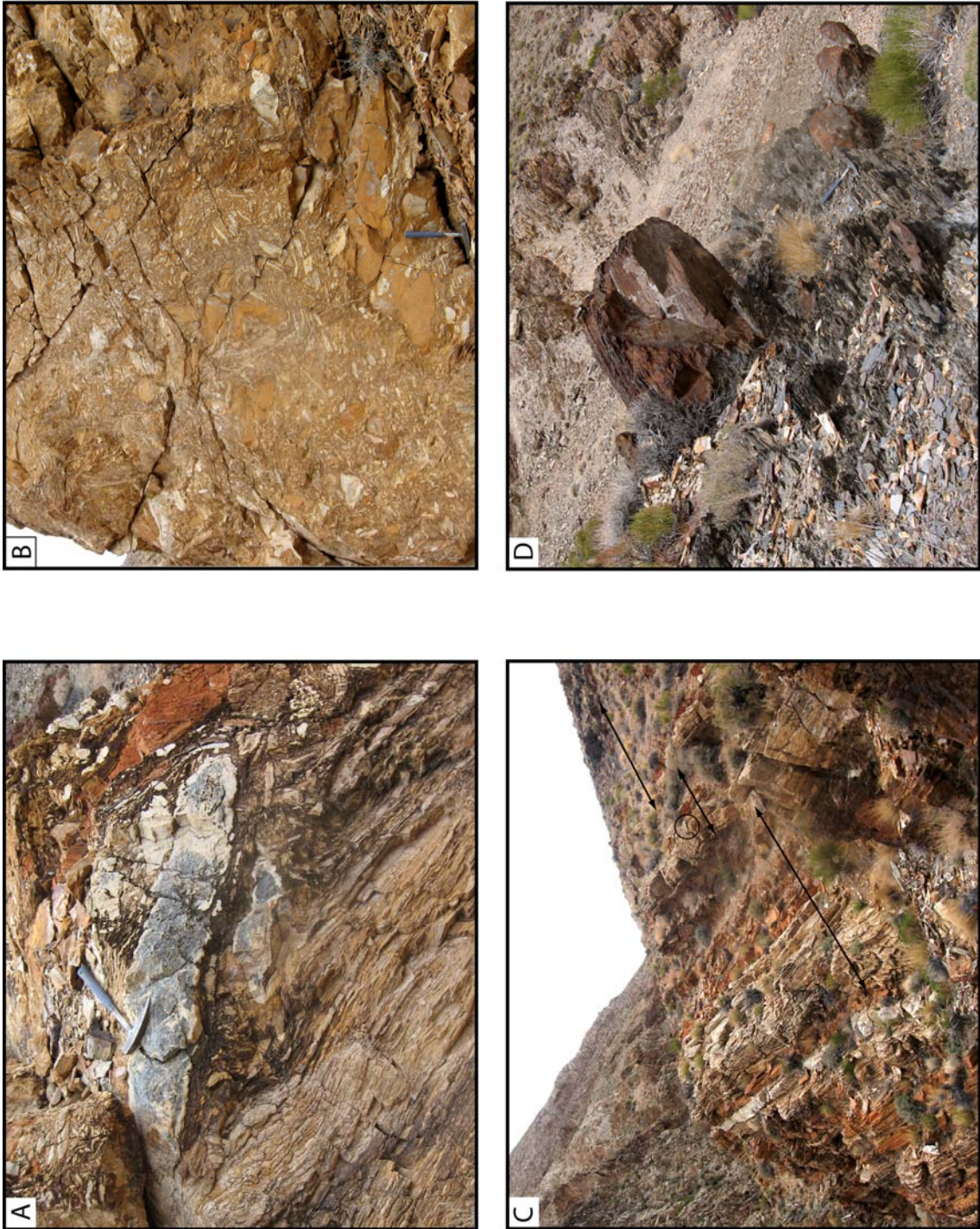


Figure 17

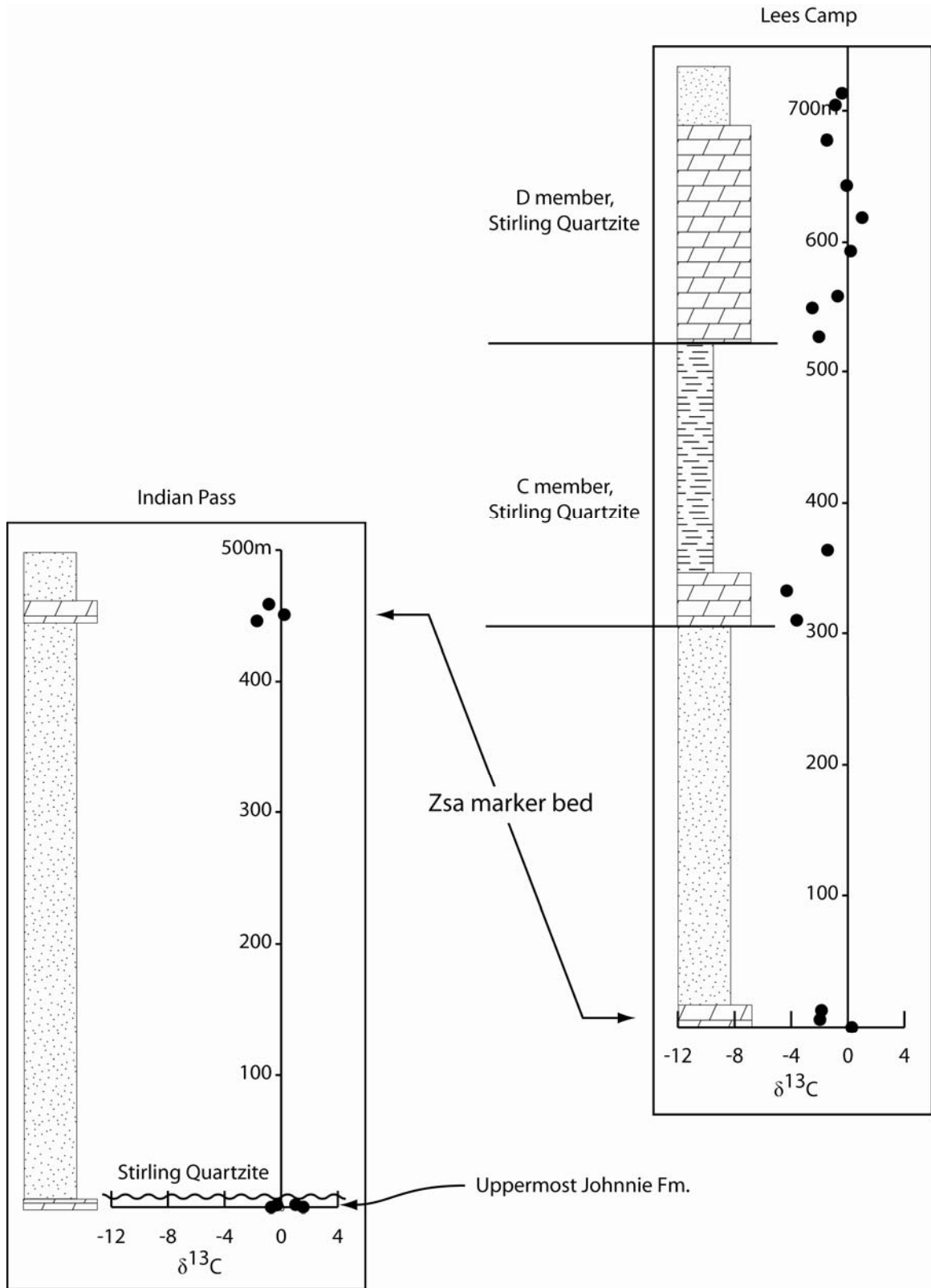


Figure 18

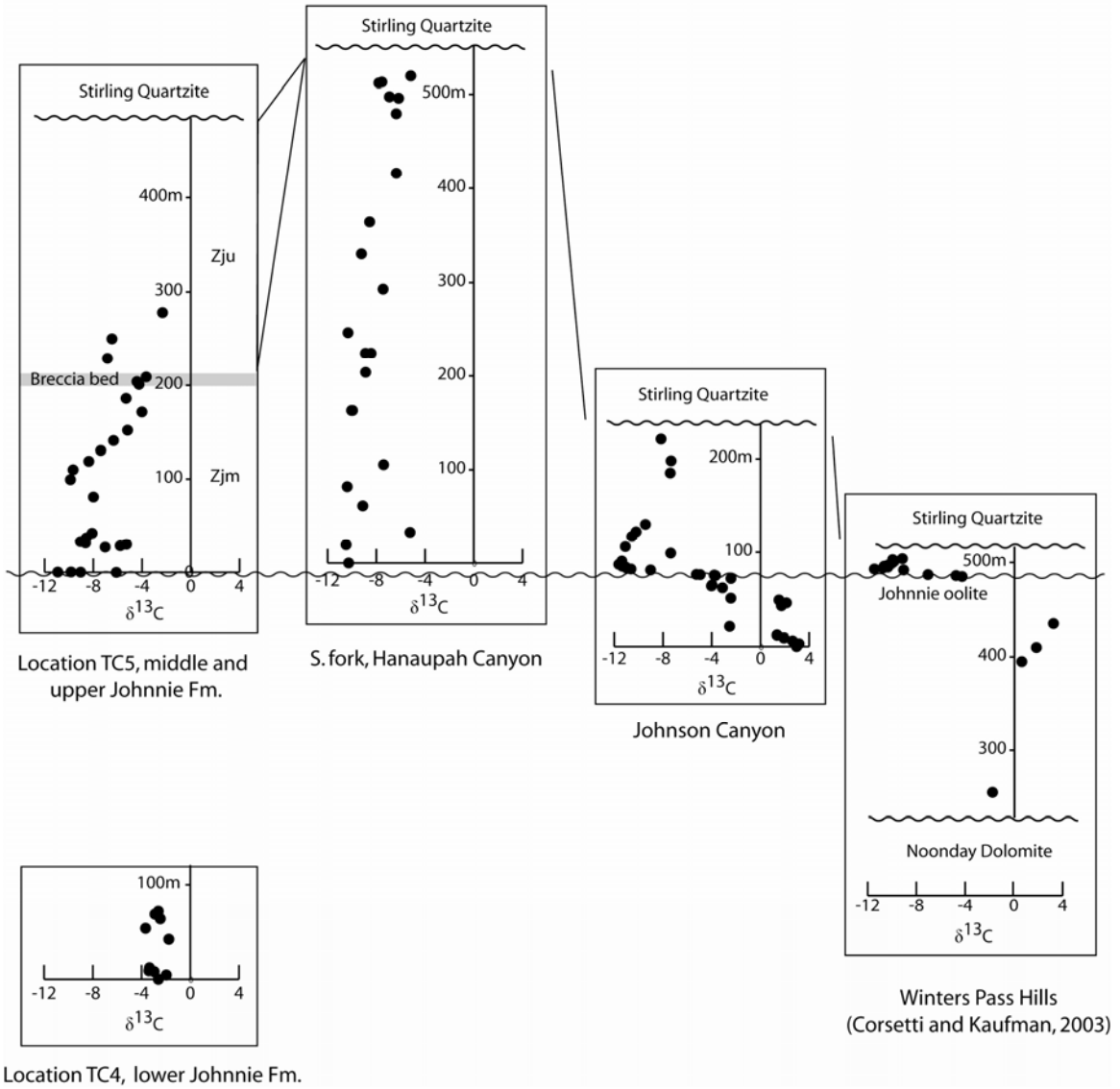


Figure 19

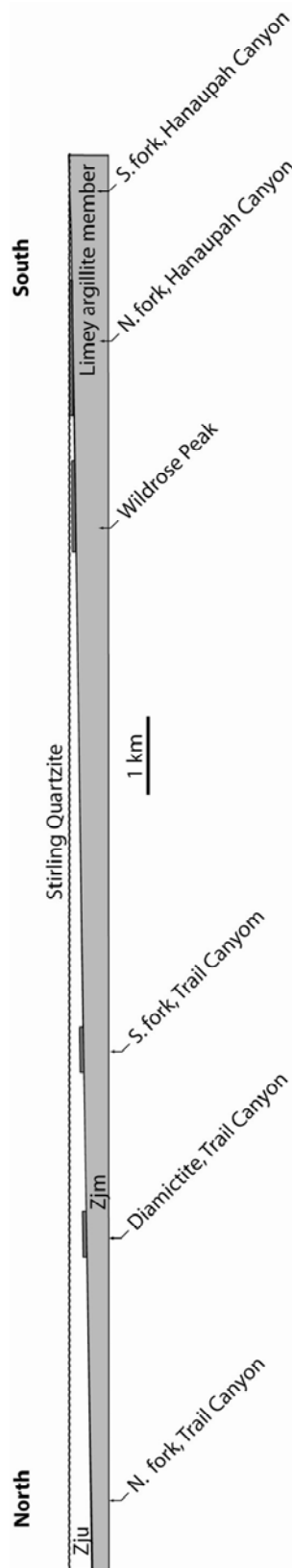
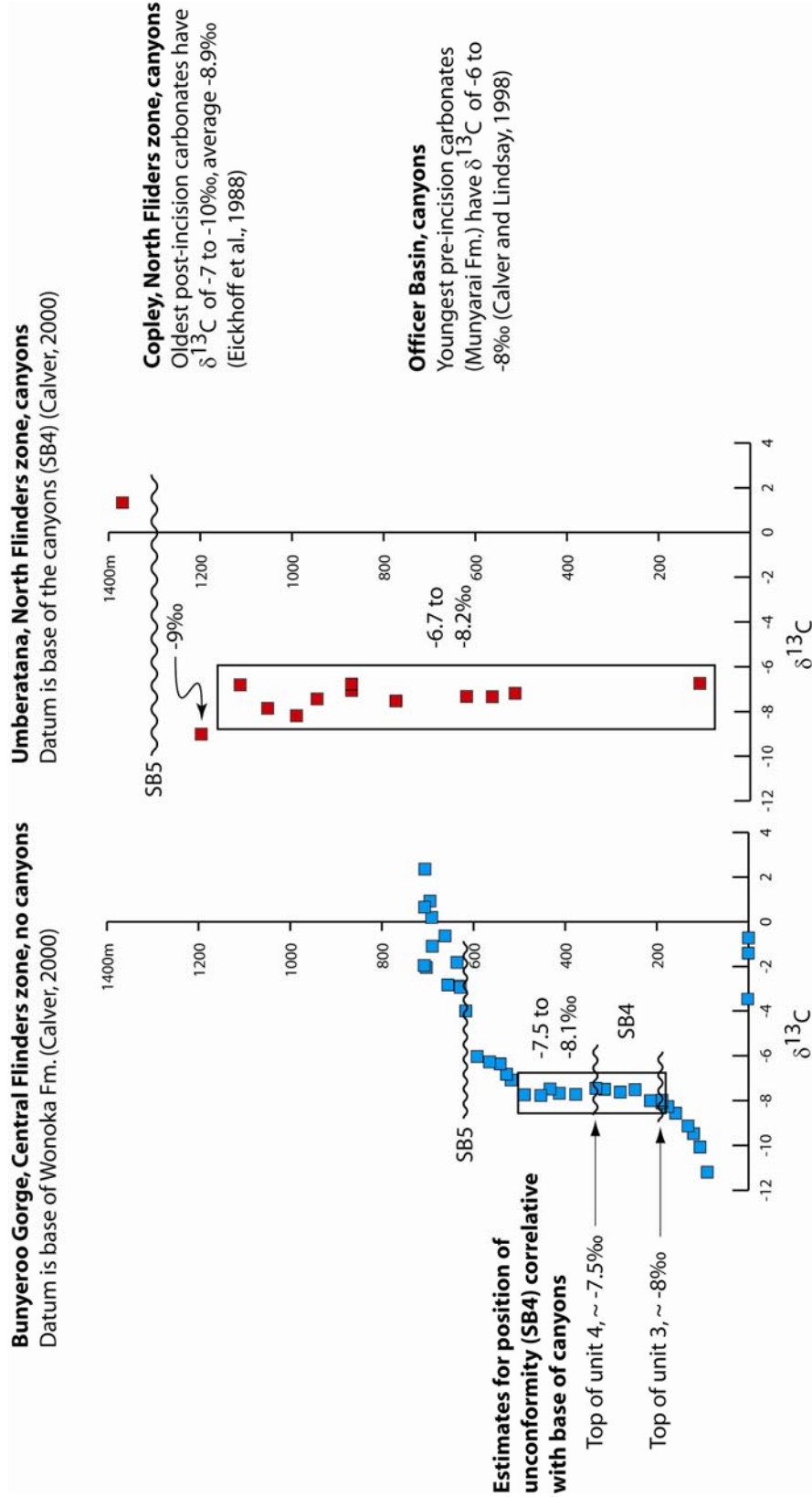


Figure 20



**Table 1: C and O isotope data tables**

<i>Johnson Canyon</i>				
<b>Sample</b>	<b>Stratigraphic position (m)</b>	<b>d<sup>13</sup>C<sub>PDB</sub></b>	<b>d<sup>18</sup>O<sub>PDB</sub></b>	<b>Notes</b>
JC1	0.0	2.96	-8.31	
JC2	3.0	3.16	-7.21	
JC3	6.0	2.63	-5.21	
JC4	9.0	1.93	-4.00	
JC5	12.0	1.36	-3.31	
JC6	21.0	-2.53	-7.12	
JC7	43.0	1.72	-8.97	
JC8	46.0	2.13	-6.14	
JC9	49.0	1.52	-5.26	
JC10	51.0	-2.43	-6.38	
JC11	62.0	-3.12	-9.58	
JC12	65.0	-3.97	-6.34	Break in section at prominent reddish brown dolostone below oolite
JC13	64.0	-4.02	-6.17	
JC14	72.0	-2.43	-10.47	
JC15	75.0	-3.70	-8.65	Base of Johnnie oolite
JC16	75.5	-3.80	-8.57	
JC17	76.0	-4.95	-8.55	
JC18	76.2	-5.26	-8.60	Top of Johnnie oolite
JC19	81.0	-9.02	-13.97	Base of pink limestones
JC20	82.0	-10.63	-15.87	
JC21	83.0	-10.99	-15.59	
JC22	84.0	-11.06	-14.73	
JC23	85.0	-11.35	-16.02	
JC24	87.0	-11.63	-16.04	
JC25	87.5	-11.47	-15.81	Top of pink limestones
JC26	90.5	-11.38	-15.45	
JC27	99.0	-7.37	-11.52	
JC28	106.0	-11.09	-16.26	
JC29	117.0	-10.56	-15.93	
JC30	122.0	-10.21	-15.54	
JC31	130.0	-9.44	-16.20	
JC32	185.0	-7.41	-12.35	
JC33	198.0	-7.34	-9.14	
JC34	221.0	-8.16	-9.60	Stirling contact at 235m

<i>South fork, Hanaupah Canyon</i>				
<b>Sample</b>	<b>Stratigraphic position (m)</b>	<b>d<sup>13</sup>C<sub>PDB</sub></b>	<b>d<sup>18</sup>O<sub>PDB</sub></b>	<b>Notes</b>
LA1	0.0	-10.27	-24.65	
LA2	19.5	-10.48	-19.91	
LA3	33.0	-5.23	-12.82	
LA4	61.5	-9.11	-22.50	
LA5	82.0	-10.39	-27.45	
LA6	105.5	-7.40	-15.97	
LA7	163.0	-10.03	-19.85	
HC1	163.0	-9.95	-18.77	
HC3	204.0	-8.87	-19.68	
HC4	224.5	-8.89	-18.88	
LA8	224.5	-8.43	-16.73	
HC5	246.5	-10.32	-17.50	
HC7	293.0	-7.44	-20.56	
LA9	330.0	-9.22	-21.49	
HC14	364.0	-8.55	-24.67	Base of edgewise conglomerate
HC13	368.0	-7.62	-20.67	Top of edgewise conglomerate
HC12	371.0	-8.48	-18.99	
HC8	416.0	-6.35	-29.49	
LA10	479.5	-6.36	-10.85	
LA11	497.5	-6.92	-12.02	
LA12	496.0	-6.17	-10.06	
LA13	512.0	-7.79	-12.05	
LA14	513.0	-7.54	-12.90	
LA15	519.5	-5.17	-9.04	Stirling contact at ~563m
<i>North fork, Hanaupah Canyon</i>				
<b>Sample</b>	<b>Stratigraphic position (m)</b>	<b>d<sup>13</sup>C<sub>PDB</sub></b>	<b>d<sup>18</sup>O<sub>PDB</sub></b>	<b>Notes</b>
CVNHC1	31.0	-4.51	-11.05	White marker bed at 22 to 27.5m
CVNHC5	32.0	-3.70	-8.46	
CVNHC2	44.5	-3.49	-7.52	
CVNHC3	50.5	-3.27	-8.87	
CVNHC4	52.5	-1.70	-6.36	
CVNHC6	56.0	1.06	-8.58	
CVNHC7	67.5	-0.19	-4.57	
CVNHC8	76.0	-0.05	-4.96	
CVNHC10	97.0	1.19	-4.00	
CVNHC11	104.0	1.16	-5.28	
CVNHC12	112.5	0.94	-7.75	
CVNHC13	118.3	0.63	-5.60	
CVNHC14	124.5	0.73	-4.35	Stirling contact at 126m

*Johnnie upper dolostone, near Wildrose Peak*

<b>Sample</b>	<b>Stratigraphic position (m)</b>	<b>d<sup>13</sup>C<sub>PDB</sub></b>	<b>d<sup>18</sup>O<sub>PDB</sub></b>	<b>Notes</b>
PM23	1.0	-3.49	-7.44	
PM32	6.0	-2.47	-6.81	
PM33	16.0	0.27	-5.52	
PM34	20.0	1.78	-3.19	
PM28	32.0	1.23	-5.46	
PM29	34.0	1.28	-5.02	
PM30	36.0	0.54	-7.37	
PM31	38.0	-0.12	-7.34	
PM27	40.0	0.36	-6.71	
PM35	40.0	0.78	-3.93	

*TC1*

<b>Sample</b>	<b>Stratigraphic position (m)</b>	<b>d<sup>13</sup>C<sub>PDB</sub></b>	<b>d<sup>18</sup>O<sub>PDB</sub></b>	<b>Notes</b>
PM73	0.0	-11.01	-17.07	
PM74	14.5	-10.62	-16.37	
PM75	22.5	-10.92	-16.28	
PM76	66.0	1.06	-11.56	Zjm/breccia contact at ~39m
PM77	76.5	0.57	-13.29	
PM78	117.5	-0.73	-12.34	
PM79	122.0	0.70	-9.05	Breccia/Zju contact at ~122.5m

*TC2*

<b>Sample</b>	<b>Stratigraphic position (m)</b>	<b>d<sup>13</sup>C<sub>PDB</sub></b>	<b>d<sup>18</sup>O<sub>PDB</sub></b>	<b>Notes</b>
PM37	0.0	-4.62	-15.63	Dolostone in Zjm
PM38	22.0	-2.08	-10.99	Dolostone in Zjm
PM39	25.0	1.22	-12.29	Lower block
PM40	31.0	-3.56	-14.20	Base of upper block
PM41	33.0	-0.12	-14.03	
PM42	36.0	-1.63	-14.15	
PM43	38.0	0.00	-11.32	
PM44	40.0	-0.73	-12.81	
PM45	44.0	0.29	-12.85	
PM46	46.0	0.98	-13.49	Top of upper block

<i>TC3</i>				
<b>Sample</b>	<b>Stratigraphic position (m)</b>	<b>d<sup>13</sup>C<sub>PDB</sub></b>	<b>d<sup>18</sup>O<sub>PDB</sub></b>	<b>Notes</b>
TC2	17.0	-1.82	-13.88	Base of blue-grey limestone
TC3	18.0	-1.17	-14.34	
TC4	19.0	-0.65	-14.81	
TC5	20.0	-0.38	-13.37	
TC6	21.0	-1.22	-13.71	
TC7	22.0	-1.62	-14.61	
TC8	23.0	-1.92	-13.98	1m below top of blue-grey limestone
TC9	38.0	1.50	-14.12	Base of black limestone
TC10	39.0	0.53	-14.03	
TC11	40.0	-0.79	-11.50	
TC12	41.0	0.13	-13.20	
TC13	42.0	-0.08	-14.13	
TC14	43.0	0.03	-14.48	
TC15	44.0	-0.02	-14.19	
TC16	45.0	0.40	-14.60	
TC17	47.0	-0.77	-13.67	
TC18	48.0	-1.48	-13.58	
TC19	49.0	-2.26	-13.18	
TC20	50.0	-0.49	-15.31	
TC21	51.0	-2.66	-13.58	Top of black limestone
<i>TC4</i>				
<b>Sample</b>	<b>Stratigraphic position (m)</b>	<b>d<sup>13</sup>C<sub>PDB</sub></b>	<b>d<sup>18</sup>O<sub>PDB</sub></b>	<b>Notes</b>
JL1	0.0	-2.62	-12.70	
JL2	4.5	-1.97	-11.87	
JL3	8.0	-2.96	-14.64	
JL4	9.0	-3.40	-13.46	
JL5	12.0	-3.35	-13.31	
JL6	42.0	-1.76	-16.72	
JL7	53.5	-3.67	-14.81	
JL8	63.5	-2.46	-13.53	Near base of deepening-upward cycles
JL9	68.3	-2.90	-13.23	
JL10	71.3	-2.62	-13.60	

<i>TC5</i>				
<b>Sample</b>	<b>Stratigraphic position (m)</b>	<b>d<sup>13</sup>C<sub>PDB</sub></b>	<b>d<sup>18</sup>O<sub>PDB</sub></b>	<b>Notes</b>
AP1	0.0	-6.11	-11.42	Base of Zjm
AP2	0.2	-9.04	-12.21	
AP3	0.3	-10.92	-12.79	Oolitic dolostone
AP4	0.4	-9.83	-12.36	Oolitic dolostone
AP5	27.0	-7.03	-11.61	
AP6	28.5	-5.79	-10.16	
AP7	30.0	-5.28	-10.78	
AP8	31.5	-8.64	-12.72	Pink, thin-bedded limestone
AP9	33.0	-9.06	-15.64	Pink, thin-bedded limestone
AP10	37.0	-8.57	-13.45	Pink, thin-bedded limestone
AP11	42.0	-8.10	-13.77	
AP12	81.0	-7.99	-13.07	
AP13	99.5	-9.88	-14.53	
AP14	110.0	-9.66	-15.47	
AP15	119.0	-8.37	-13.67	
AP16	130.5	-7.39	-13.15	
AP17	141.0	-6.34	-13.84	
AP18	152.0	-5.19	-11.72	
AP19	171.5	-4.01	-7.84	
AP20	186.0	-5.31	-11.35	
AP21	201.0	-4.25	-11.46	Pink thin-bedded dolostone at base of breccia interval
AP22	204.0	-4.42	-11.71	
AP23	209.0	-3.66	-9.16	Dolostone at top of breccia
AP24	229.0	-6.84	-11.39	
AP25	250.0	-6.47	-11.22	
AP26	278.0	-2.32	-3.42	Stirling contact at ~490m
<i>TC6</i>				
<b>Sample</b>	<b>Stratigraphic position (m)</b>	<b>d<sup>13</sup>C<sub>PDB</sub></b>	<b>d<sup>18</sup>O<sub>PDB</sub></b>	<b>Notes</b>
SD1	0.0	-5.20	-11.31	At base of Stirling D member
SD2	2.5	-4.42	-8.39	
SD3	8.0	-4.22	-11.30	
SD4	19.0	-5.83	-7.97	
SD5	31.0	-6.42	-12.31	
<i>Indian Pass</i>				
<b>Sample</b>	<b>Stratigraphic position (m)</b>	<b>δ<sup>13</sup>C<sub>PDB</sub></b>	<b>δ<sup>18</sup>O<sub>PDB</sub></b>	<b>Notes</b>
FM1	0.0	-0.70	-13.55	Upper Johnnie Fm.
FM2	0.2	1.56	-14.30	Upper Johnnie Fm.
FM3	1.7	-0.30	-14.20	Upper Johnnie Fm.
FM4	2.0	1.02	-10.24	Upper Johnnie Fm.
IP1	446.0	-1.71	-15.29	Stirling A member marker bed
IP2	450.8	0.22	-13.54	Stirling A member marker bed
IP3	458.8	-0.87	-7.07	Stirling A member marker bed

*Lees Camp*

<b>Sample</b>	<b>Stratigraphic position (m)</b>	$\delta^{13}\text{C}_{\text{PDB}}$	$\delta^{18}\text{O}_{\text{PDB}}$	<b>Notes</b>
LC1	0.0	0.28	-5.45	Stirling A member marker bed
LC2	6.0	-1.97	-5.71	Stirling A member marker bed
LC3	13.0	-1.86	-3.62	Stirling A member marker bed
LC4	310.0	-3.61	-2.54	Base of Stirling C member
LC5	332.5	-4.32	-5.41	
LC6	363.5	-1.43	-4.71	
LC7	526.5	-2.04	-7.14	Base of Stirling D member
LC8	548.5	-2.51	-10.29	
LC9	557.5	-0.72	-6.19	
LC10	592.5	0.20	-5.61	
LC11	618.0	1.01	-4.62	
LC12	642.5	-0.08	-7.99	
LC13	677.0	-1.48	-7.28	
LC14	703.5	-0.88	-7.70	
LC15	712.5	-0.41	-8.52	

## **Chapter 5**

### **Geochemistry of the Ediacaran Browns Hole basalt, Utah: implications for the timing of western Laurentian rifting.**

#### **ABSTRACT**

Trace element and U-Pb apatite data from the Ediacaran Browns Hole basalt in northern Utah, coupled with new regional correlations based on existing C isotope data from underlying strata, provide strong evidence that the basalt is rift-related and was erupted after deposition of Marinoan cap carbonates within the Cordilleran continental margin, providing some of the youngest geological evidence yet documented for the rifting of western Laurentia. Paleomagnetic data from the basalt and sedimentary rocks above and below it fail a fold test, indicating that the original magnetic orientation of these rocks was overprinted during or after Mesozoic to early Cenozoic folding.

#### **INTRODUCTION**

In the ~90 My following the last of the Snowball Earth events, the earth underwent some of the most remarkable changes in its history, including the radiation of multicellular organisms (e.g., Knoll and Carroll, 1999), the continued breakup of a supercontinent (e.g., Hoffman, 1991), the final stage in the oxidation of the oceans (Rothman et al., 2003), the largest negative C isotope excursion in earth history (e.g., Fike et al., 2006), an additional glaciation (Bowring et al., 2003), and possibly an episode of true polar wander (Kirschvink et al., 1997). Significant uncertainty surrounds the relative timing of these events and how they may relate to one another. The final stage in the rifting of western

Laurentia has been variously estimated at ca. 635 Ma based on geological evidence (e.g., Prave, 1999) and 550-600 Ma based on tectonic subsidence models (e.g., Bond et al., 1985). The Gaskiers glaciation, which followed what seem to be the more widespread Sturtian and Marinoan glaciations (i.e., the “Snowball Earth” events), has been radiometrically dated at 580 Ma (Bowring et al., 2003). Paleomagnetic data from the Sept. Iles intrusion in Quebec have been interpreted as indicative of an episode of inertial interchange true polar wander (IITPW) between 561 and 564 Ma (Kirschvink et al., 2005). Estimates for the onset of the Shuram anomaly C isotope excursion, which may have resulted from oxidation of a large reservoir of organic carbon (Fike et al., 2006), include before (Abolins et al., 2000, Halverson et al., 2007) and after (Condon et al., 2005, Fike et al., 2006) the Gaskiers glaciation, and available radiometric data constrain it only between ~551 and 600 Ma (Condon et al., 2005, Le Guerroué et al., 2006). Incision of km deep canyons into the syn-Shuram anomaly Wonoka Fm. of South Australia (e.g., Calver, 2000) may be related to sea-level drawdown resulting from the 580 Ma Gaskiers glaciation or ca. 560 Ma IITPW (Kirschvink et al., 2005).

Neoproterozoic strata in northern Utah, which include glacial diamictites (e.g., Ojakangas and Matsch, 1980) preserved in paleocanyons (Crittenden et al., 1978, Christie-Blick et al., 1989) and a basalt flow (Crittenden and Wallace, 1973) possibly related to the rifting of Laurentia, hold some promise for shedding light on this debate. Because these rocks are generally unmetamorphosed, they also have the potential for providing paleomagnetic data pertinent to discussions of late Precambrian true polar wander.

We collected samples of late Neoproterozoic strata from the Browns Hole quadrangle (Crittenden, 1972) just east of Huntsville, Utah (Fig. 1). Stratigraphic relationships and a new analysis of pre-existing C isotope data from the Ediacaran strata of northern Utah and southern Idaho in light of new chemostratigraphic data from the Death Valley region (Pettersen et al., 2007) confirm that the Browns Hole basalt is younger than Marinoan cap carbonates. The Mineral Fork Tillite of northern Utah is almost certainly pre-Gaskiers in age based on our geochronology data from the basalt and the stratigraphic relationship between it and the tillite, a conclusion which is in agreement with regional stratigraphic studies (Crittenden et al., 1971, Crittenden et al., 1983).

#### **NORTHERN UTAH NEOPROTEROZOIC-CAMBRIAN STRATIGRAPHY**

Proterozoic strata in northern Utah and southern Idaho were part of a westward thickening wedge of rift-related and passive margin sediments (Stewart, 1970). East-vergent thrusting during the Mesozoic and Early Cenozoic disrupted the original distribution of sediments within this wedge such that the thickest, most basinal sections can now be found in the upper plates of regional thrust sheets and the most platformal sections are preserved within the autochthon (Crittenden et al., 1983). Our work is concentrated in the Browns Hole quadrangle which, except for a small area at the southern edge of the quadrangle, is situated in the hanging wall of the Willard-Paris thrust (Crittenden, 1972). Precambrian strata in this area include, in ascending order, the Maple Canyon Fm., Kelley Canyon Fm., Caddy Canyon Quartzite, Inkom Fm., Mutual Fm., and Browns Hole Fm. Above these units is the Precambrian(?) to Cambrian Geersten Canyon Quartzite (Fig. 2). The Precambrian-Cambrian boundary has not been

definitively located within this section, but *Skolithos* burrows have been found at the top of the Geersten Canyon Quartzite (Crittenden et al., 1971). These Neoproterozoic through Cambrian strata are predominantly sandstones and siltstones; the only mapped carbonates are thin layers in the Kelley Canyon Fm. These units and overlying Paleozoic sediments are folded into a NNE- plunging anticline in the Browns Hole quadrangle and are unconformably overlain by Upper Cretaceous to Paleogene conglomerates (Fig. 3, Crittenden, 1972).

Our study is focused on the interval from the Inkom Fm. to the Geersten Canyon Quartzite. The Inkom Fm. is comprised almost entirely of siltstone and is about 120 to 150m thick within the quadrangle (Crittenden, 1972). Disconformably overlying it are coarse-grained sandstones of the Mutual Fm., which range from approximately 150 to 400m in thickness across the area. The volcanic member of the Browns Hole Fm. conformably overlies the Mutual Fm. (Christie-Blick and Levy, 1989) and consists of ~60 to 150m of volcanic breccia, basalt, and sandstone. Above this is the Terra cotta quartzite member of the Browns Hole Fm., made up of roughly 30 to 50m of cross-bedded sandstone with frosted quartz grains and wind ripples that has been interpreted as an eolian or very shallow water deposit (Crittenden et al., 1971, Christie-Blick et al., 1989). Disconformably overlying the Browns Hole Fm. are ~400m of sandstone comprising the lower member of the Geersten Canyon Quartzite.

To the northwest of Huntsville, and also in the hanging wall of the Willard-Paris thrust, the Maple Canyon Fm. overlies the formation of Perry Canyon (Sorensen and Crittenden,

1976, and Crittenden et al., 1983), which contains two diamictites separated by siltstone, greywacke, and limestone. The lower diamictite unconformably overlies rocks of presumed Paleoproterozoic age, varies from 0 to 365m in thickness, and contains metavolcanic rocks near its base (Crittenden et al., 1983).

To the south in Big Cottonwood Canyon (Fig. 1), the Mutual Fm. disconformably overlies the Mineral Fork Tillite, which is filling a canyon eroded into the underlying Big Cottonwood Fm (Crittenden et al., 1978). Although the Browns Hole basalt is absent in this section, stratigraphic relationships indicate that it is younger than the Mineral Fork Tillite. The previous age determined for the basalt of  $580 \pm 16$  Ma ( $2\sigma$ ) (discussed in detail below) thus leaves open the possibility that the tillite is Gaskiers in age. However, this location is within the autochthon and is one of the thinnest exposures of Neoproterozoic glacial stratigraphy in the region (Crittenden et al., 1983). Previous work has concluded that the Mutual Fm. disconformably overlies the tillite (Crittenden et al., 1983) implying that significant time may have elapsed between glaciation and deposition of the Mutual Fm.

## **ANALYTICAL DATA**

### **Trace element data, Browns Hole basalt**

Major and trace element data were obtained for a sample of the Browns Hole basalt using X-ray fluorescence (XRF) at the Ronald B. Gilmore XRF laboratory at the University of Massachusetts (Table 1). Details of the analytical procedure can be found in Rhodes (1996). The basalt is porphyritic and consists of clinopyroxene and plagioclase

phenocrysts in a groundmass of plagioclase. It contains 43.5 wt.% SiO<sub>2</sub>, 6.09 wt.% MgO, 38 ppm Ni, and 33 ppm Cr, and has an olivine-diopside-nepheline normative assemblage. Relatively low Cr and Ni contents, as well as the absence of olivine phenocrysts, suggest that the basalt has probably undergone some degree of assimilation and fractional crystallization. On a total alkali-silica diagram it plots in the tephrite/basanite field (Fig. 4A), and because it contains >10 wt.% normative olivine it is classified as a basanite (Le Maitre et al., 1989). Although technically not a basalt, the term “Browns Hole basalt” is established in the literature, and we use the term “basalt” throughout this paper for the sake of clarity.

As illustrated on a MORB-normalized trace element diagram (Fig. 4B), the basalt is strongly enriched in the most incompatible trace elements, particularly Rb and Ba. As expected, the data provide no indication of a subduction zone environment, e.g. there is no Nb-depletion, the most common characteristic of arc volcanism (Gill, 1981). Continental basalts with enriched incompatible element concentrations relative to mid-ocean ridge basalts are frequently ascribed to low degrees of partial melting accompanying rifting (e.g., Fitton and Dunlop, 1985). Trace element compositions of the Browns Hole basalt are quite reminiscent of significantly older basalts within the formation of Perry Canyon and equivalent units in northern Utah and southern Idaho that are associated with earlier phases of the break-up of Rodinia (Harper and Link, 1986).

## Geochronology

The Browns Hole basalt is one of the few Ediacaran volcanic units in North America, and its age is therefore of considerable interest. Crittenden and Wallace (1973) obtained an  $^{40}\text{Ar}/^{39}\text{Ar}$  hornblende total gas age of  $570\pm 7$  Ma ( $1\sigma$ ) from a clast within volcanic breccia underlying the Browns Hole basalt. This age was subsequently re-calculated to  $580\pm 8$  Ma ( $1\sigma$ ) using new Ar decay constants (Christie-Blick and Levy, 1989). Because of uncertainties in the validity of this age, including the fact that the date was obtained from a clast underlying the basalt flow and not the flow itself, we collected new samples of the basalt to attempt a modern geochronological study. We recovered no zircon or baddeleyite, but apatite is relatively common within the basalt. U-Pb ages were determined on apatite grains using the isotope dilution thermal ionization mass spectrometry (ID-TIMS) method in the geochronology laboratory at the Massachusetts Institute of Technology. Because of low U concentrations ( $<2$  ppm) within these apatites, the U-Pb age is very sensitive to the common-Pb correction, making it useless to rely on modeled initial Pb ratios such as those from Stacey and Kramers (1975). In order to precisely estimate the initial common-Pb of apatite, we step-leached Pb from  $\sim 75$  hand-picked plagioclase grains using a method modified from Housh and Bowring (1991) and determined isotopic ratios of this nonradiogenic Pb. Our best estimate for the age of the apatites thus determined is the weighted mean  $^{206}\text{Pb}/^{238}\text{U}$  age of two multi-grain analyses, which is  $609\pm 25$  Ma ( $2\sigma$ ) (Fig. 5, Table 2). However, one of these analyses is slightly discordant, and both multi-grain fractions may be on a mixing line defined by two single-grain analyses, one concordant and one discordant, in which case

the actual age may be older. In either case, it would seem that the previous radiometric date of  $580 \pm 16$  Ma ( $2\sigma$ ) is a slight underestimate of the age of the basalt.

### **Paleomagnetic data**

We collected 33 oriented block samples from the Inkom Fm. through the lower Geersten Canyon Quartzite (Fig.2) in the Browns Hole quadrangle. In order to conduct a paleomagnetic fold test, samples were collected from both the north and south limbs of the plunging anticline in the quadrangle (Fig. 3). Following measurements of natural remanent magnetization (NRM), each sample was cooled in LN<sub>2</sub> to unlock multi-domain magnetite and then underwent alternating field demagnetization to 10 mT followed by about 15 to 30 thermal demagnetization steps from 60 to  $\sim 680^\circ\text{C}$ .

Paleomagnetic directions were determined from principal component analysis of these demagnetization data (Kirschvink, 1980) and primarily reveal two magnetization components (Fig. 6). The low temperature component, which is present in almost all of the samples, has an orientation close to that of the present-local magnetic field (PLF, Fig. 6A and B). Removal of this component with AF and relatively low temperature thermal demagnetization reveals a higher temperature component in many of the samples that we have denoted the B component. It is present in all of the basalt samples (Fig. 6C) and in many from the overlying and underlying sediments (Fig. 6D). When plotted in geographic (i.e., in situ, or non tilt-corrected) coordinates, the orientations of B components from samples from the north and south limbs of the fold overlap (Fig. 6E). When plotted in tilt-corrected coordinates, however, orientations of samples from the two

limbs clearly fall into different groups according to the limb from which they were collected (Fig. 6F). It is clear that this component fails a fold-test, i.e., the B component magnetization was acquired during or after folding and is thus not the primary remanence of the samples.

In a few (~5) of the samples there appears to be an additional, still higher temperature component. Orientations of this component are uniformly low-inclination (Fig 6 G and H), but declinations are scattered. Because of the scatter in declination and the limited number of samples with evidence for this component, a fold test is inconclusive. The low-inclination component is present in some of the sedimentary rocks but not in any samples from the basalt, suggesting that it is carried only by hematite (Curie temperature $\approx$ 675°C), which is present in many of the sandstones, and has been completely overprinted in magnetite (Curie temperature=578°C), which is the overwhelming ferromagnetic mineral in the basalt. It is very doubtful that strata of the Huntsville area ever reached temperatures this high (which probably would have reset the hornblende  $^{40}\text{Ar}/^{39}\text{Ar}$  age from the volcanic clast), but chemical alteration could have overprinted the primary magnetic orientation at much lower temperature. Of the 5 samples in which we observe the low-inclination component, four are from the Mutual Fm. and the other is from the Terra cotta quartzite member of the Browns Hole Fm., so any future paleomagnetic studies of the area should probably focus on these units.

## DISCUSSION

### Correlations with Death Valley

Although Neoproterozoic through Cambrian strata in northern Utah and southern Idaho are predominantly siliciclastic, C isotope compositions have previously been measured for many of the carbonate beds that are present.  $\delta^{13}\text{C}_{\text{carb}}$  data are available for the Scout Mountain member of the Pocatello Fm. (Smith et al., 1994, Lorentz et al., 2004), the Blackrock Canyon Limestone (Smith et al., 1994, Corsetti et al., 2007), and carbonates within the Caddy Canyon Quartzite (Smith et al., 1994). As explained below, although these analyses are limited, it is nevertheless possible to confidently correlate these strata with equivalent units in the Death Valley region through a combination of lithologic similarities and C isotope chemostratigraphy. Our conclusions differ significantly from previous comparisons between the northern Utah/southern Idaho and Death Valley Neoproterozoic sections (e.g., Corsetti et al., 2007) and are made possible by new lithostratigraphic and C isotope data from the Noonday Dolomite (Petterson et al., 2007).

Corsetti et al. (2007) noted that carbonates overlying the upper of two diamictites in the Scout Mt. member of the Pocatello Fm. are lithologically quite similar to the Ibex Fm. in the Death Valley region (Corsetti and Kaufman, 2005), which, based on the work of Petterson et al. (2007) is equivalent to the Sentinel Peak and Radcliff members of the Noonday Dolomite.  $\delta^{13}\text{C}_{\text{carb}}$  from carbonates immediately above diamictite in the Pocatello Fm. are about -3.0 to -3.5‰ (Fig. 7, Smith et al., 1994), values which are nearly identical to previously determined  $\delta^{13}\text{C}_{\text{carb}}$  for the Sentinel Peak and lower Radcliff members of the Noonday Dolomite (Corsetti and Kaufman, 2005, Petterson et al., 2007).

~100m above these carbonates in the Pocatello Fm. are an additional ~25m of carbonate with  $\delta^{13}\text{C}$  values ranging from about -4 to -6‰ (Smith et al., 1994, Lorentz et al., 2004), identical to values from the lower Radcliff member (Petterson et al., 2007). Based on these lithological and chemical similarities, we suggest that these lower and upper carbonates overlying diamictite in the Scout Mt. member are equivalent to the Sentinel Peak and Radcliff members, respectively, of the Noonday Dolomite.

C isotope values from the Middle Carbonate member of the Caddy Canyon Quartzite range from 3.9 to 8.8‰ (Smith et al., 1994), some of the heaviest values reported from Cordilleran Neoproterozoic carbonates. Corsetti et al. (2007) suggest that these beds are equivalent with the middle Johnnie Fm. in the Death Valley area, but the heaviest C isotope values from the Johnnie Fm. are only 3.3‰ (Corsetti and Kaufman, 2003).

Current compilations of Neoproterozoic C isotope data (Halverson et al. 2005) indicate that  $\delta^{13}\text{C}$  values became as heavy as 8.8‰ at only one point in the Ediacaran Period, at a time corresponding with deposition of the Mahogany Flats member of the upper Noonday Dolomite (Petterson et al., 2007). Based on this observation we suggest that the Middle Carbonate member of the Caddy Canyon Quartzite correlates with the upper Noonday Dolomite. C isotope values from the Blackrock Canyon Limestone, situated between the Pocatello Formation and Caddy Canyon Quartzite and correlated with carbonates in the Kelley Canyon Fm. by Crittenden et al. (1971), are generally -1.5 to 0‰ in the lower part and about 0 to 1‰ in the upper part (Fig. 7, Smith et al., 1994, Corsetti et al., 2007).

Although these values are not unique to any particular time, they are consistent with data from the middle to upper part of the Noonday Dolomite (Petterson et al., 2007).

We thus conclude from pre-existing C isotope data that the Noonday Dolomite is equivalent to strata ranging from carbonates in the upper part of the Scout Mt. member of the Pocatello Fm. through at least the Middle Carbonate member of the Caddy Canyon Quartzite (Fig. 7). By this interpretation, Scout Mt. member carbonate overlying the younger of two diamictites in the Pocatello Fm. are cap dolostones, and the interval above this, to at least the Middle Carbonate member of the Caddy Canyon Quartzite, if not to the contact with the Upper Fluvial member, is a “cap-carbonate sequence” as defined by Hoffman and Schrag (2002). If this interpretation is correct, it would suggest that the Shuram anomaly is present somewhere in overlying strata below the *Skolithos*-bearing beds in the upper part of the Camelback Mt. Quartzite. Unfortunately, carbonates beds are rare to completely absent in this interval and C isotope data are unavailable.

Christie-Blick and Levy (1989) correlated the contact between the Inkom and Mutual Fms. with a sequence boundary at the Johnnie Fm.-Stirling Quartzite contact in the Death Valley region. If this correlation is valid, it would suggest that the Shuram anomaly is present within the Inkom Fm., unless it has been removed by erosion as it almost was in sections of the Johnnie Fm. to the southeast of Death Valley (Chapter 4). In terms of lithostratigraphy, this is the most obvious correlation: the contact between Inkom Fm. siltstones and overlying Mutual Fm. sandstones is lithologically quite reminiscent of the contact between Johnnie Fm. siltstones and overlying Stirling Quartzite sandstones, and the unconformity within the upper part of the Caddy Canyon Quartzite may correlate with karst developed at the Johnnie-Noonday contact (Summa, 1993). However, the Shuram anomaly can be no older than ~600 Ma. based on U-Pb dates from detrital

zircons near the base of the anomaly in Oman (Le Guerroué et al., 2006). Given our best estimate for the age of the Browns Hole basalt ( $609\pm 25$  Ma), it is unlikely that the Inkom Fm., located at least 150m below the basalt and separated from it by what may be a significant unconformity at the base of the Mutual Fm., could be as young as 600 Ma, although we cannot entirely rule out this possibility because of the large uncertainties associated with the apatite U-Pb age. This reasoning would suggest, however, that the Shuram anomaly corresponds with some part of the Mutual Fm., Browns Hole Fm., and/or lower part of the Geersten Canyon Quartzite, or has been removed along an unconformity within this interval.

## **CONCLUSIONS**

Regardless of the exact position of the Shuram anomaly, if our correlation of carbonates in the Caddy Canyon Quartzite with the upper Noonday Dolomite is correct, it implies that the Browns Hole basalt is distinctly post-Noonday. Coupled with trace element data which indicate that the basalt is probably related to extension, this observation suggests that in at least one place, the rifting of western Laurentia continued later than estimated by most geological studies (e.g., Prave, 1999), a conclusion which is consistent with the results from tectonic subsidence models (e.g., Bond et al., 1985). U-Pb data from the basalt indicate that it is older than proposed latest Proterozoic (ca. 560 Ma) IITPW (Kirschvink et al., 2005).

**REFERENCES**

Abolins, M., Oskin, R., Prave, T., Summa, C., and Corsetti, F., 2000, Neoproterozoic glacial record in the Death Valley region, California and Nevada, *in* Lageson, D.R., Peters, S.G., and Lahren, M.M., eds., Great Basin and Sierra Nevada: Boulder, Geological Society of America Field Guide 2, p.319-335.

Bond, G.C., Christie-Blick, N., Kominz, M.A., and Devlin, W.J., 1985, An early Cambrian rift to post-rift transition in the Cordillera of western North America, v. 315, p. 742-746.

Bowring, S.A., Myrow, P.M., Landing, E., Ramezani, J., and Grotzinger, J.P., 2003, Geochronological constraints on terminal Neoproterozoic events and the rise of metazoans: *Geophysical Research Abstracts*, 5, 13219.

Calver, C.R., 2000, Isotope stratigraphy of the Ediacaran (Neoproterozoic III) of the Adelaide Rift Complex, Australia, and the overprint of water column stratification: *Precambrian Research*, v. 100, p. 121-150.

Christie-Blick, N., and Levy, M., 1989, Stratigraphic and tectonic framework of upper Proterozoic and Cambrian rocks in the western United States, *in* Christie-Blick, N., and Levy, M., eds., Late Proterozoic and Cambrian tectonics, sedimentation, and record of Metazoan radiation in the western United States: Washington, D.C., American Geophysical Union, Fieldtrip Guidebook T331, p. 7-21.

Christie-Blick, N., Mount, J.F., Levy, M., Philip W. Signor, and Link, P.K., 1989, Description of stops, *in* Christie-Blick, N., and Levy, M., eds., Late Proterozoic and Cambrian tectonics, sedimentation, and record of Metazoan radiation in the western United States: Washington, D.C., American Geophysical Union, Fieldtrip Guidebook T331, p. 55-113.

Condon, D., Zhu, M., Bowring, S., Wang, W., Yang, A., and Jin, Y., 2005, U-Pb ages from the Neoproterozoic Doushantuo Formation, China: *Science*, v. 308, p. 95-98.

Corsetti, F.A., and Kaufman, 2003, Stratigraphic investigations of carbon isotope anomalies and Neoproterozoic ice ages in Death Valley, California: *Geological Society of America, Bulletin*, v.115, p. 916-932.

Corsetti, F.A., and Kaufman, A.J., 2005, The relationship between the Neoproterozoic Noonday Dolomite and the Ibex Formation: new observations and their bearing on 'snowball Earth': *Earth-Science Reviews*, v. 73, p. 63-78.

Corsetti, F.A., Link, P.K., and Lorentz, N.J., 2007,  $\delta^{13}\text{C}$  chemostratigraphy of the Neoproterozoic succession near Pocatello, Idaho, U.S.A.: implications for glacial chronology and regional correlations: *SEPM Special Publication No. 86*, p. 193-205.

Crittenden, M.D., Jr., 1972, Geologic map of the Browns Hole Quadrangle, Utah: U.S. Geological Survey Geologic Quadrangle Map GQ-968, scale 1:24,000, 1 sheet.

Crittenden, M.D., Jr., Calkins, F.C., Sharp, B.J., Baker, A.A., and Bromfield, C.S., 1978, Geology of Big Cottonwood mining district: Utah Geological and Mineral Survey Map 49, scale 1:24,000, 1 sheet.

Crittenden, M.D., Jr., Christie-Blick, N., and Link, P.K., 1983, Evidence for two pulses of glaciation during the late Proterozoic in northern Utah and southeastern Idaho: Geological Society of America Bulletin, v. 94, p. 437-450.

Crittenden, M.D., Jr., Schaeffer, F.E., Trimble, D.E., and Woodward, L.A., 1971, Nomenclature and correlation of some upper Precambrian and basal Cambrian sequences in western Utah and southeastern Idaho: Geological Society of America Bulletin, v. 82, p. 581-602.

Crittenden, M.D., Jr., and Wallace, C.A., 1973, Possible equivalents of the Belt supergroup in Utah, *in* Belt Symposium: Moscow, Idaho, Department of Geology, University of Idaho and Idaho Bureau of Mines and Geology, v. 1, p. 116-138.

Fike, D.A., Grotzinger, J.P., Pratt, L.M., and Summons, R.E., 2006, Oxidation of the Ediacaran ocean: Nature, v. 444, p. 744-747.

Fitton, J.G., and Dunlop, H.M., 1985, The Cameroon line, West Africa, and its bearing on the origin of oceanic and continental alkali basalt: *Earth and Planetary Science Letters*, v. 72, p. 23-38.

Gill, J.B., 1981, *Orogenic andesites and plate tectonics*: Springer-Verlag, 390 p.

Halverson, G.P., Hoffman, P.F., Schrag, D.P., Maloof, A.C., and Rice, A.H.N., 2005, Toward a Neoproterozoic composite carbon-isotope record: *Geological Society of America Bulletin*, v. 117, p. 1181-1207.

Harper, G.D., and Link, P.K., 1986, Geochemistry of Upper Proterozoic rift-related volcanics, northern Utah and southeastern Idaho: *Geology*, v. 14, p. 864-867.

Hintze, L.F., Willis, G.C., Laes, D.Y.M., Sprinkel, D.A., and Brown, K.D., 2000, *Digital Geologic map of Utah*: Utah Geological Survey, scale 1:500,000, 2 sheets.

Hoffman, P.F., 1991, Did the breakout of Laurentia turn Gondwanaland inside-out?: *Science*, v. 252, p. 1409-1412.

Hoffman, P.F., and Schrag, D.P., 2002, The snowball Earth hypothesis: testing the limits of global change: *Terra Nova*, v. 14, p.129-155.

Housh, T., and Bowring, S.A., 1991, Lead isotopic heterogeneities within alkali feldspars: implications for the determination of initial lead isotopic compositions: *Geochemica et Cosmochimica Acta*, v. 55, p. 2309-2316.

Johnson, B.R., and Raines, G.L., 1996, Digital representation of the Idaho state geologic map: a contribution to the Interior Columbia River Basin Ecosystem Management Project: U.S. Geological Survey Open-File Report 95-690, 22 p.

Kirschvink, 1980, The least-squares line and plane and the analysis of paleomagnetic data: *Geophysical Journal of the Royal Astronomical Society*, v. 62, p. 699-218.

Kirschvink, J.L., Mound, J., Mitrovitca, J.X., Raub, T.D., Evans, D.A.D., and Kopp, R.E., 2005, Rapid inertial-interchange true polar wander during Ediacaran time induced by intrusion of the Sept-Îles intrusive suite, Quebec, Canada: a possible trigger for massive sea-level and carbon isotopic excursions: *Proceedings of the Gondwana XII conference*, Mendoza, Argentina, Nov. 2005.

Kirschvink, J.L., Ripperdan, R.L., and Evans, D., 1997, Evidence for a large-scale reorganization of early Cambrian continental masses by inertial interchange true polar wander: *Science*, v. 277, p. 541-545.

Knoll, A.H., and Carroll, S.B., 1999, Early animal evolution: emerging views from comparative biology and geology: *Science*, v. 284, p. 2129-2137.

Le Guerroué, E., Allen, P.A., Cozzi, A., Etienne, J.L., and Fanning, M., 2006, 50 Myr recovery from the largest negative  $\delta^{13}\text{C}$  excursion in the Ediacaran ocean: *Terra Nova*, v. 18, p. 147-153.

Le Maitre, R.W., Bateman, D., Dudek, A., and Keller, J., 1989, A classification of igneous rocks and glossary of terms: recommendations of the International Union of Geological Sciences Subcommittee on the Systematics of Igneous Rocks: Oxford, Boston, Blackwell, 193 p.

Lorentz, N.J., Corsetti, F.A., and Link, P.K., 2004, Seafloor precipitates and C-isotope stratigraphy from the Neoproterozoic Scout Mountain member of the Pocatello Formation, southeast Idaho: implications for Neoproterozoic earth system behavior: *Precambrian Research*, v. 130, p. 57-70.

Ojakangas, R.W., and Matsch, C.L., 1980, Upper Precambrian (Eocambrian) Mineral Fork Tillite of Utah: a continental glacial and glaciomarine sequence: *Geological Society of America Bulletin*, v. 91, p. 495-501.

Petterson, R., Prave, A., Wernicke, B., and Fallick, A.E., 2007, New stratigraphic and isotopic constraints on the Cryogenian-Ediacaran strata of Death Valley region, *Geological Society of America Abstracts with Programs*, v. 39, no. 6, p. 222.

Prave, A.R., 1999, Two diamictites, two cap carbonates, two  $\delta^{13}\text{C}$  excursions, two rifts: the Neoproterozoic Kingston Peak Formation, Death Valley, California: *Geology*, v. 27, p. 339-342.

Rhodes, J.M., 1996, Geochemical stratigraphy of lava flows sampled by the Hawaii Scientific Drilling Project: *Journal of Geophysical Research*, v. 101, p. 11729-11746.

Rothman, D.H., Hayes, J.M., and Summons R.E., 2003, Dynamics of the Neoproterozoic carbon cycle: *Proceedings of the National Academy of Sciences*, v. 100, p. 8124-8129.

Smith, L.H., Kaufman, A.J., Knoll, A.H., and Link, P.K., 1994, Chemostratigraphy of predominantly siliciclastic Neoproterozoic successions: a case study of the Pocatello Formation and Lower Brigham Group, Idaho, USA: *Geological Magazine*, v. 131, p. 301-314.

Sorensen, M.L., and Crittenden, M.D., Jr., 1976, Preliminary geologic map of the Mantua Quadrangle and part of the Willard Quadrangle, Box Elder, Weber, and Cache Counties, Utah: U.S. Geological Survey, Miscellaneous Field Studies Map MF-720, scale 1:24,000.

Stacey, J.S., and Kramers, J.D., 1975, Approximation of terrestrial lead isotope evolution by a two-stage model, *Earth and Planetary Science Letters*, v. 26, p. 207-221.

Stewart, J.H., 1970, Upper Precambrian and lower Cambrian strata in the southern Great Basin, California and Nevada: U.S. Geological Survey Professional Paper 620, 206 p.

Summa, C.L., 1993, Sedimentologic, stratigraphic, and tectonic controls of a mixed carbonate-siliciclastic succession: Neoproterozoic Johnnie Formation, southeast California [Ph.D. thesis]: Cambridge, Massachusetts Institute of Technology, 332 p.

Sun, S.S., and McDonough, W.F., 1989, Chemical and isotopic systematics of oceanic basalts; implications for mantle composition and processes, *in* Saunders, A.D., and Norry, M.J., eds., *Magmatism in the oceanic basins*: Geological Society of London Spec. Pub. 42, p. 313-345.

**FIGURE CAPTIONS**

**Figure 1.** Shaded relief map of northern Utah and southern Idaho showing distribution of Neoproterozoic sediments. Geology of Utah and Idaho after Hintze et al. (2000) and Johnson and Raines (1996), respectively.

**Figure 2.** Part of the Late Proterozoic to Cambrian stratigraphy of the Browns Hole Quadrangle (Crittenden, 1972) and stratigraphic positions of samples discussed in text.

**Figure 3.** Geologic map of the Browns Hole quadrangle (Crittenden, 1972) showing sample locations. Abbreviations: pCga-Maple Canyon Fm., pCk-Kelley Canyon Fm., pCc-Caddy Canyon Quartzite, pCi-Inkom Fm., pCm-Mutual Fm., pCb-Volcanic member of the Browns Hole Fm., pCt-Terra Cotta member of the Browns Hole Fm., CpCgl-Lower member of the Geertsen Canyon Quartzite, CpCgu-Upper member of the Geertsen Canyon Quartzite, TKwe-Cretaceous to Eocene Wasatch and Evanston Fms., Qal-Quaternary alluvium.

**Figure 4.** Geochemical data from the Browns Hole basalt. (A) Primitive mantle normalized trace element diagram. Oceanic island basalt (OIB) and primitive mantle compositions from Sun and McDonough (1989). (B) Total alkali-silica diagram.

**Figure 5.** U-Pb concordia diagram for Browns Hole basalt apatites. Multi-grain analyses shown as filled ellipses.

**Figure 6.** Paleomagnetic data from the Browns Hole quadrangle. (A) Vector component, equal area, and magnetic intensity ( $J/J_0$ ) diagrams for sample SF5 from the volcanic member of the Browns Hole Fm. in the south limb of the fold. The only magnetic component discernable from this sample is parallel to the present-local magnetic field (PLF), marked by a star at the center of the cluster of data points. The PLF component vector is drawn as a blue arrow in this and subsequent plots. D=declination; I=inclination. (B) Equal area plot showing the orientations of all PLF components as well as the mean inclination and declination of these individual measurements. (C) Summary of data for sample MF10 from the Browns Hole basalt in the north limb of the fold. This sample displays evidence for two magnetic components: a low-temperature PLF component that dominates the NRM, and a higher temperature, high-inclination B component that trends to the NW in both geographic and tilt-corrected coordinates. Note that the magnetic intensity ( $J_0$ ) of this sample (the only basalt sample shown on the figure) is ~1000x greater than the other samples. On this and subsequent plots, the B vector is shown as a green arrow. (D) Data for sample MF19 from the Inkom Fm. in the south limb of the fold. This sample also shows evidence for both PLF and a high-inclination B component. The B components from this sample (south limb) and MF10 (north limb, panel C) plot in similar locations on geographic equal area plots but in different locations on tilt-corrected plots, suggesting that the B component was acquired after folding. (E) All measured B components plotted in geographic coordinates. Note that orientations from samples in both limbs overlap. (F) B components plotted in tilt-corrected coordinates. On this plot, the orientations from either limb diverge, providing strong evidence that the B component fails a fold test, i.e., the B component was acquired

after folding. (G) Data for sample MF4 from the upper Mutual Fm. in the north limb of the fold. The lowest temperature component identifiable from the data is the high-inclination B component. Note the similarity with the B component from sample MF10 (also from the north limb, panel C). In addition to the B component, there is evidence for a higher temperature, low-inclination C component. On this and the following plot, the C vector is shown as a purple arrow. (H) Data for sample SF12 from the Mutual Fm. in the south limb of the fold. This sample also has evidence for the B and C components. Taken together, the data from this sample and MF4 (panel G) suggest that the C component trends SW-NE and plunges slightly to the SW.

**Figure 7.** Existing C isotope data from Neoproterozoic carbonates in northern Utah and southern Idaho. Lithostratigraphy after Christie-Blick et al. (1989) and Corsetti et al. (1987) based on thicknesses near Pocatello. Datum is top of the upper diamictite of the Pocatello Fm. (Smith et al., 1994).

Figure 1

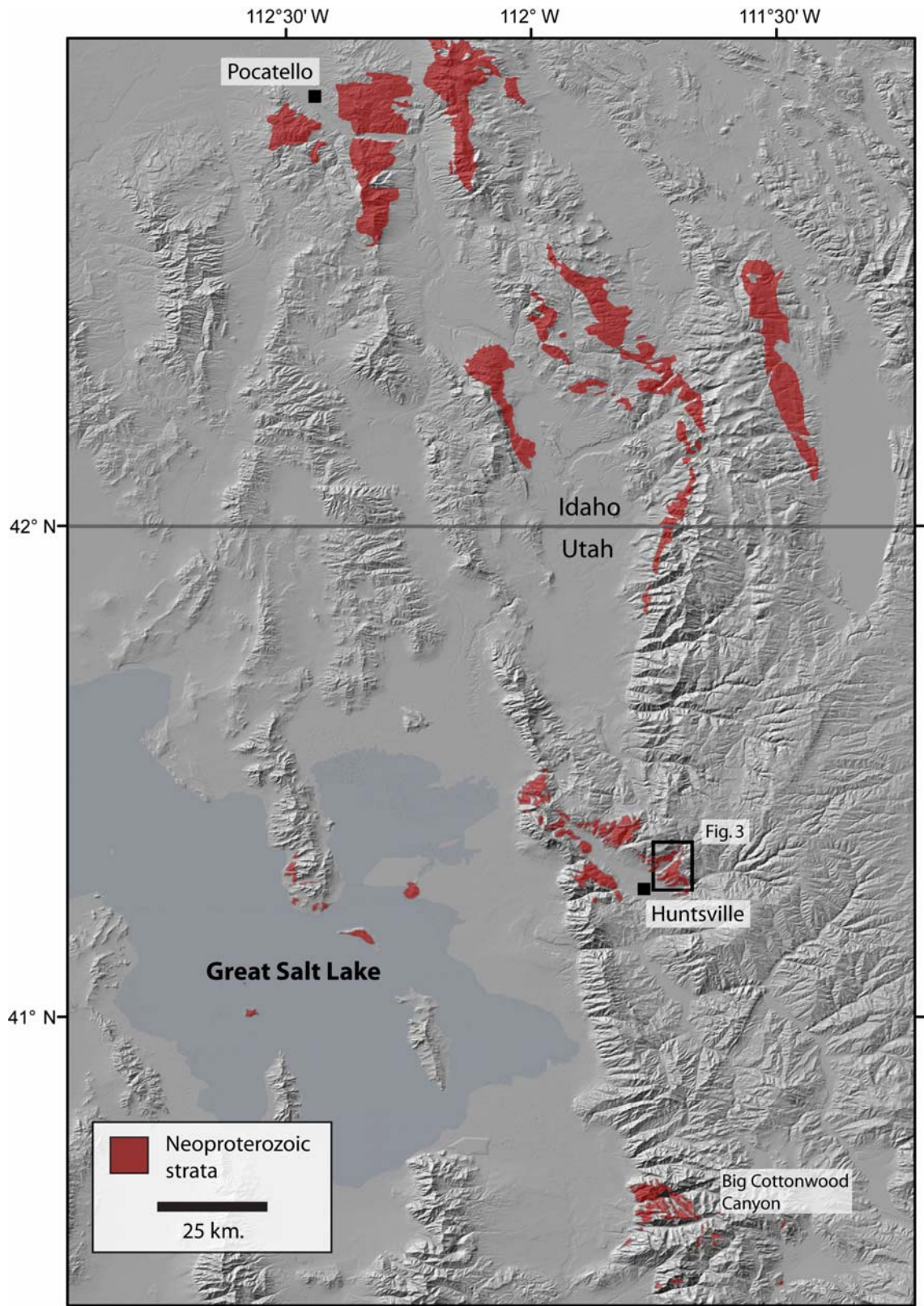


Figure 2

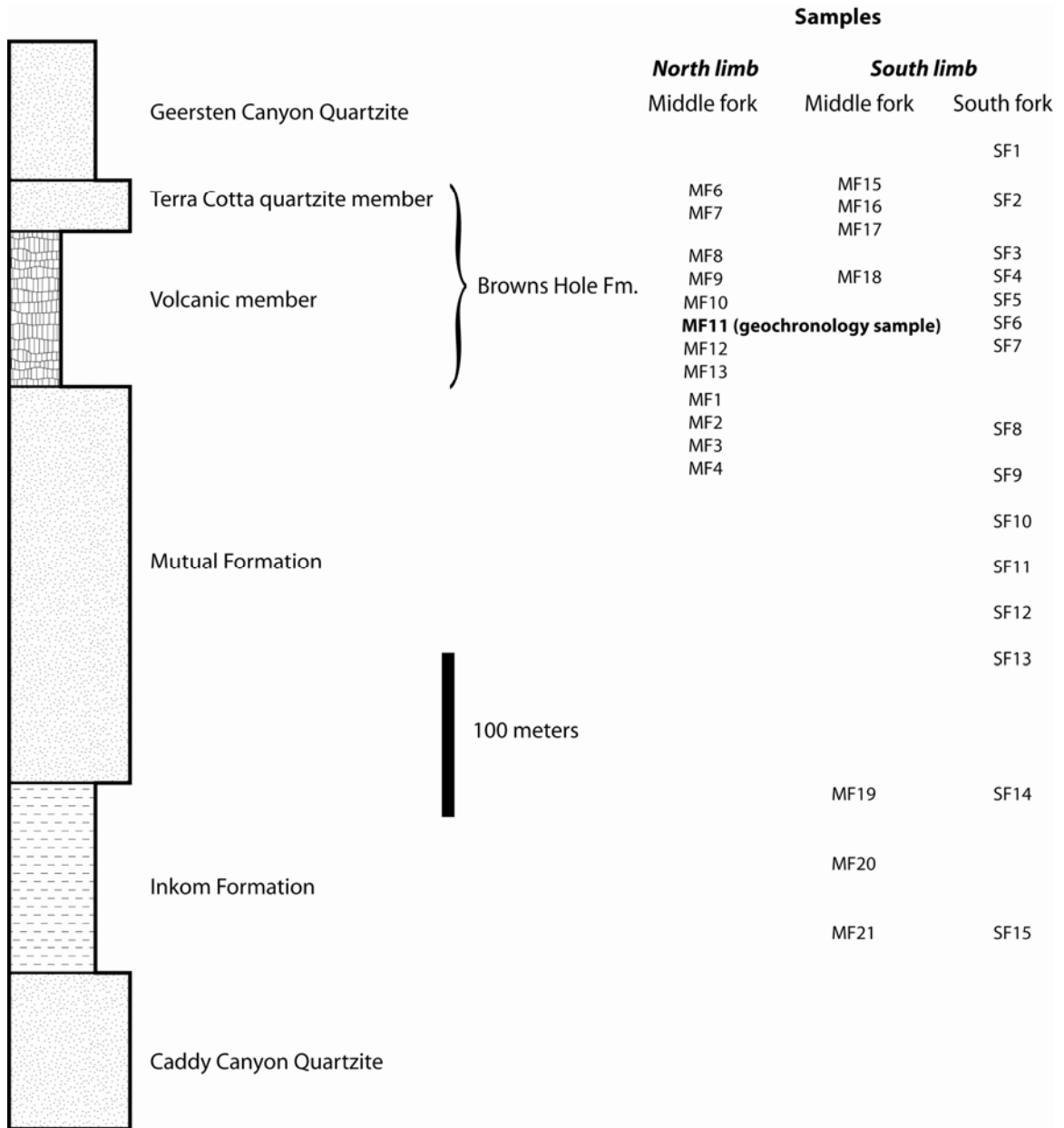


Figure 3

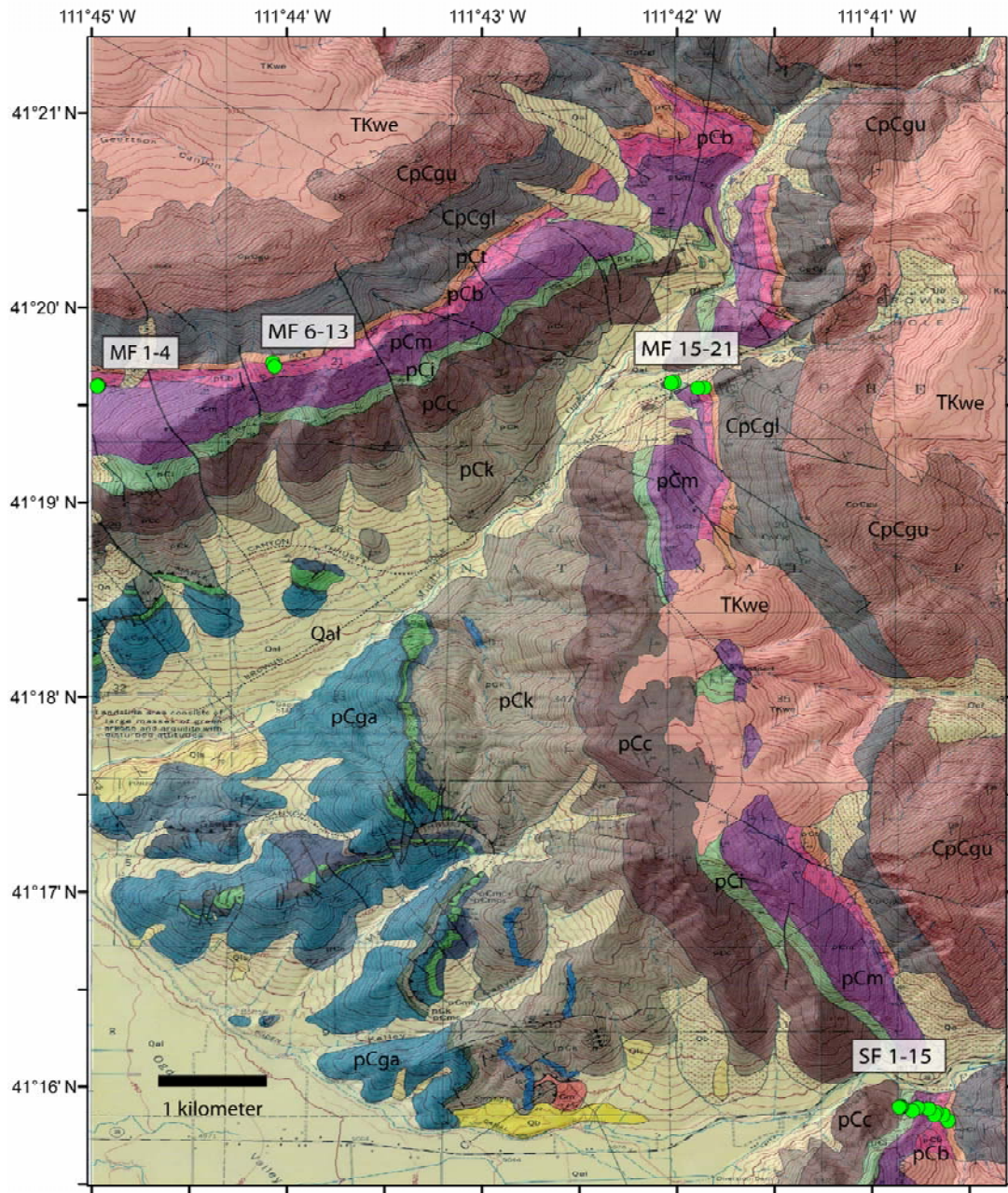


Figure 4

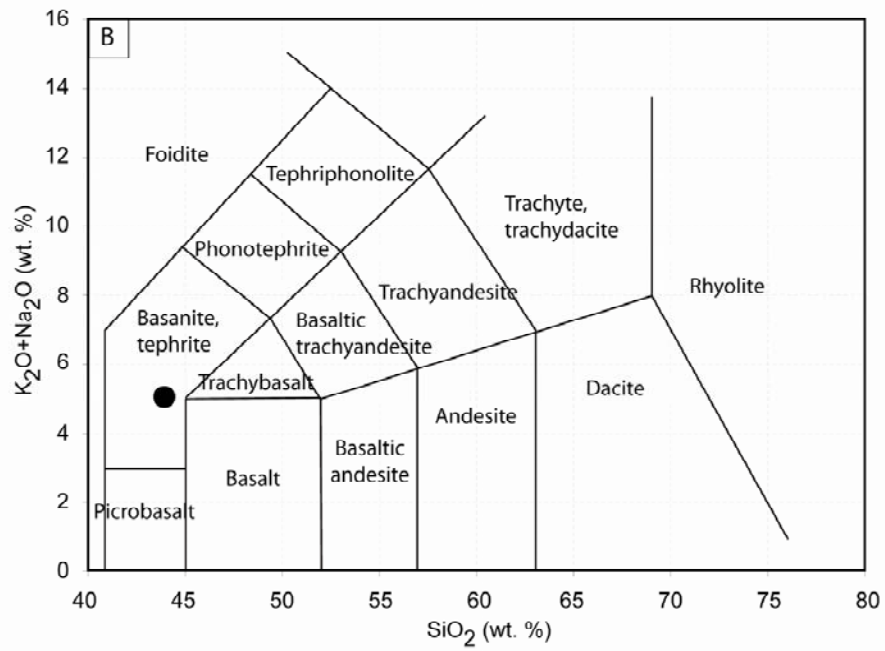
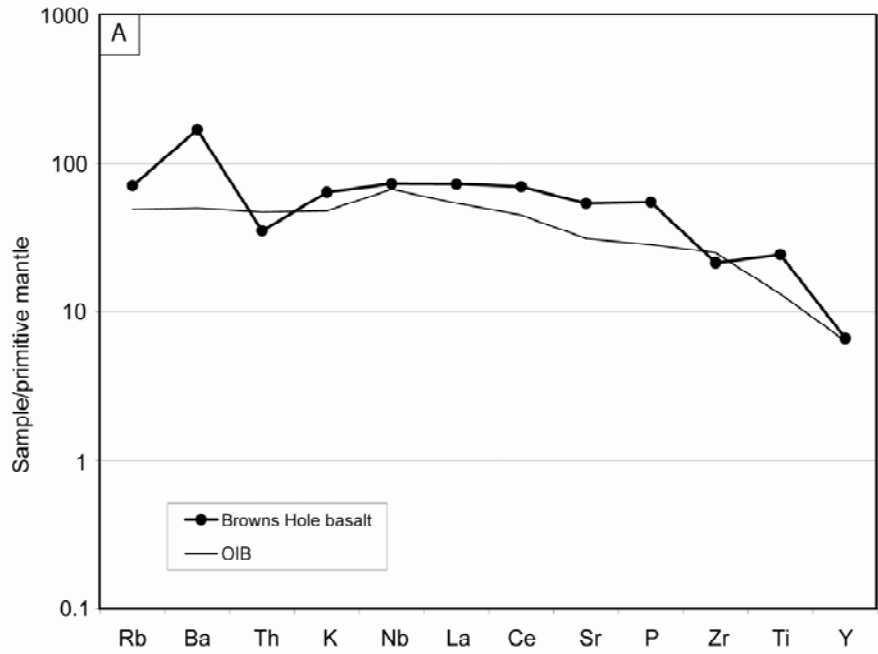


Figure 5

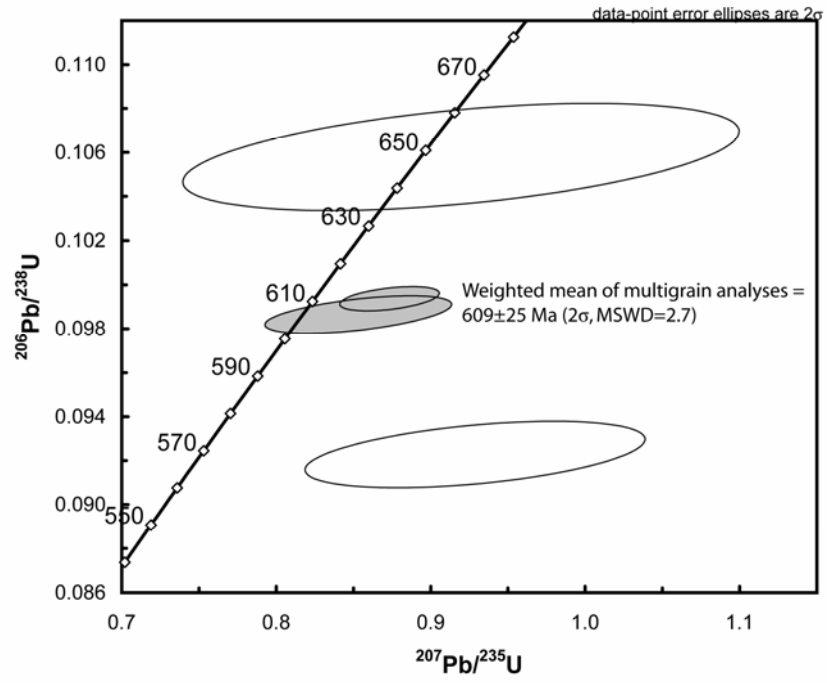


Figure 6

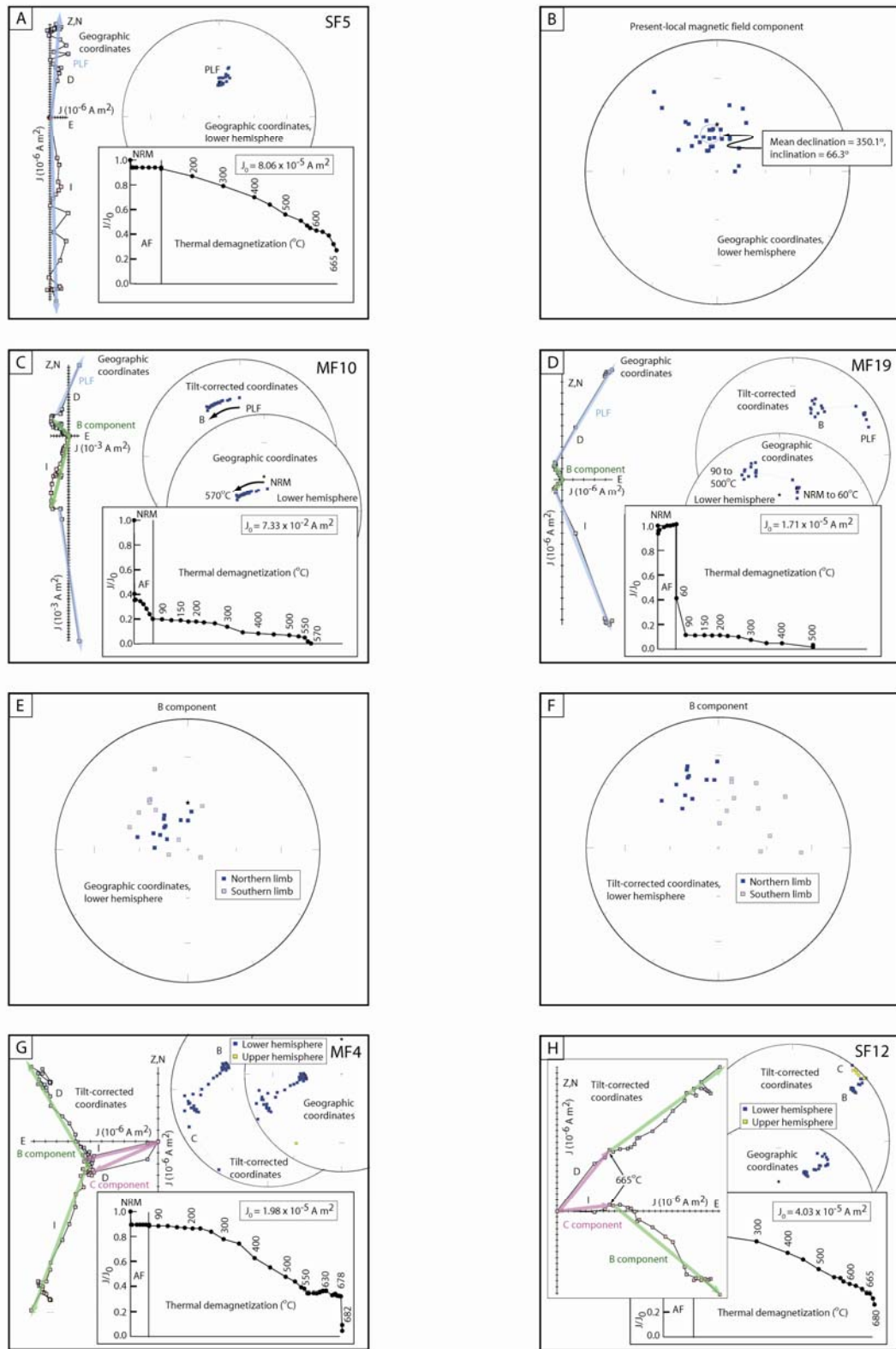


Figure 7

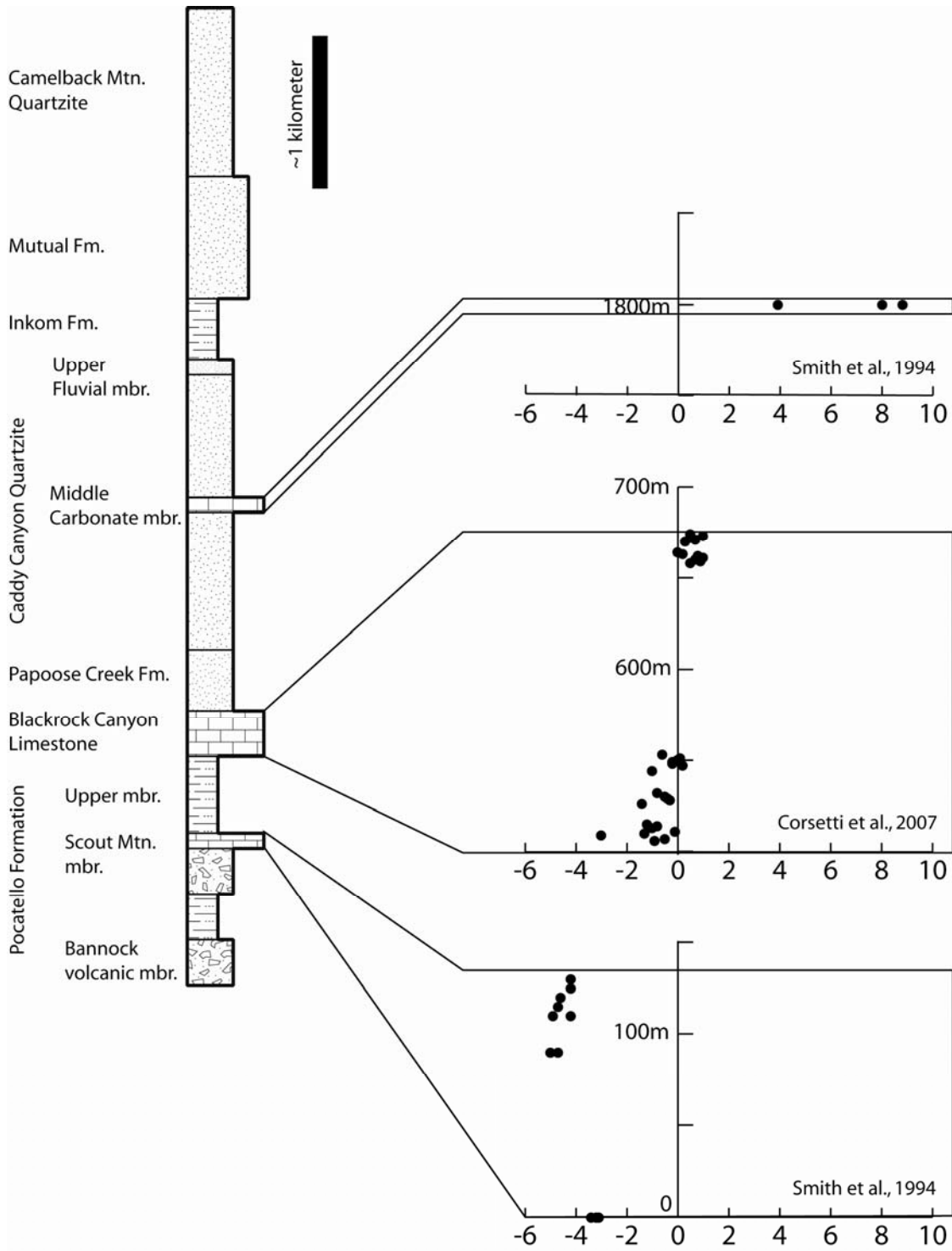


TABLE 1: XRF major and trace element data from the Browns Hole basalt

SiO <sub>2</sub> (%)	43.53
TiO <sub>2</sub> (%)	5.26
Al <sub>2</sub> O <sub>3</sub> (%)	14.10
Fe <sub>2</sub> O <sub>3</sub> (%)	14.99
MnO (%)	0.42
MgO (%)	6.09
CaO (%)	9.17
Na <sub>2</sub> O (%)	3.08
K <sub>2</sub> O (%)	1.93
P <sub>2</sub> O <sub>5</sub> (%)	1.20
Total (%)	99.77
Rb (ppm)	45
Ba (ppm)	1181
Th (ppm)	3
Nb (ppm)	52
La (ppm)	50
Ce (ppm)	124
Sr (ppm)	1138
P (ppm)	5217
Zr (ppm)	240
Y (ppm)	30
Cr (ppm)	33
Ni (ppm)	38

TABLE 2: U-Pb geochronology of the Browns Hole basalt

*Apatite U-Pb data*

Sample/ Fractions	Number of grains	Wt. ( $\mu\text{g}$ ) (a)	Pb(c) (pg) (b)	Pb*/ Pb(c)	Th/U	Concentrations		Ratios						Age (Ma)			Corr. coef.		
						U (ppm)	Pb (ppm)	$^{206}\text{Pb}/$ $^{204}\text{Pb}$	$^{208}\text{Pb}/$ $^{206}\text{Pb}$	$^{206}\text{Pb}/$ $^{238}\text{U}$	err ( $2\sigma\%$ )	$^{207}\text{Pb}/$ $^{235}\text{U}$	err ( $2\sigma\%$ )	$^{207}\text{Pb}/$ $^{206}\text{Pb}$	err ( $2\sigma\%$ )	$^{206}\text{Pb}/$ $^{238}\text{U}$		$^{207}\text{Pb}/$ $^{235}\text{U}$	$^{207}\text{Pb}/$ $^{206}\text{Pb}$
CVMF11	apatite																		
a1	1	3.7	1.5	0.3	3.591	0.64	0.30	28.30	1.220	0.105784	(1.90)	0.91900	(16.14)	0.06301	(15.33)	<b>648.21</b>	<b>661.83</b>	<b>708.5</b>	0.473
a2	1	3.6	1.6	0.5	2.355	1.08	0.39	32.36	1.326	0.09215	(1.35)	0.92813	(9.76)	0.07305	(9.21)	<b>568.24</b>	<b>666.65</b>	<b>1015.3</b>	0.461
a3	5	7.9	2.7	0.8	3.568	1.40	0.51	42.62	1.280	0.098576	(.71)	0.85194	(5.83)	0.06268	(5.47)	<b>606.06</b>	<b>625.71</b>	<b>697.4</b>	0.549
a4	8	12.6	3.3	1.0	3.344	1.25	0.44	47.45	1.251	0.09930	(.47)	0.87221	(3.04)	0.06370	(2.85)	<b>610.31</b>	<b>636.76</b>	<b>731.8</b>	0.456

Weighted mean of a3 and a4 =  **$609 \pm 25$  Ma ( $2\sigma$ )**, MSWD = 2.7, probability = 0.10

- (a) Sample weights are estimated from grain images.  
 (b) Total common-Pb in analyses.  
 (c) Measured ratio corrected for spike and fractionation only.  
 (d) Radiogenic Pb.  
 (e) Corrected for fractionation, spike, blank, and initial common Pb.

Mass fractionation correction of  $0.25\%/amu \pm 0.04\%/amu$  (atomic mass unit) was applied to single-collector Daly analyses and  $0.07\%/amu \pm 0.04\%$  for dynamic Faraday-Daly analyses. Total procedural blank less than 0.3 pg for Pb and less than 0.1 pg for U.

Blank isotopic composition:  $^{206}\text{Pb}/^{204}\text{Pb} = 18.27 \pm 0.1$ ,  $^{207}\text{Pb}/^{204}\text{Pb} = 15.59 \pm 0.1$ ,  $^{208}\text{Pb}/^{204}\text{Pb} = 38.12 \pm 0.1$ .

Corr. coef. = correlation coefficient.

Age calculations are based on the decay constants of Steiger and Jäger (1977).

Common-Pb corrections were calculated by using the model of Stacey and Kramers (1975) and the interpreted age of the sample.

## References:

1. Stacey, J.S. and Kramers, J.D., Earth and Planetary Science Letters 26, 207, 1975.
2. Steiger, R.H., and Jäger, E., Earth Planetary Science Letters 36, 359, 1977.

TABLE 2 (continued): U-Pb geochronology of the Browns Hole basalt

*Plagioclase step leaching results.*

Common Pb composition from step 2 used in subsequent calculations.

Step	Reagent	$^{206}\text{Pb}/$ $^{204}\text{Pb}$	2 $\sigma$ abs. error	$^{207}\text{Pb}/$ $^{204}\text{Pb}$	2 $\sigma$ abs. error	$^{208}\text{Pb}/$ $^{204}\text{Pb}$	2 $\sigma$ abs. error
1	12N HCl	19.4722	0.0052	15.7771	0.0045	37.302	0.012
2	conc. HF 1	17.4701	0.0084	15.4989	0.0075	37.266	0.018
3	conc. HF 2	17.9631	0.0056	15.5572	0.0058	37.670	0.014
	SRM 981*	16.9418	0.0006	15.5000	0.0006	36.727	0.002

\* Baker et al. (2004) Chem Geol 211, p.275-303